

University of Southampton Research Repository

Copyright © and Moral Rights for this thesis and, where applicable, any accompanying data are retained by the author and/or other copyright owners. A copy can be downloaded for personal non-commercial research or study, without prior permission or charge. This thesis and the accompanying data cannot be reproduced or quoted extensively from without first obtaining permission in writing from the copyright holder/s. The content of the thesis and accompanying research data (where applicable) must not be changed in any way or sold commercially in any format or medium without the formal permission of the copyright holder/s.

When referring to this thesis and any accompanying data, full bibliographic details must be given, e.g.

Thesis: Author (Year of Submission) "Full thesis title", University of Southampton, name of the University Faculty or School or Department, PhD Thesis, pagination.

Data: Author (Year) Title. URI [dataset]



University of Southampton

Faculty of Natural and Environmental Sciences

School and Biological Sciences

Human NMDA receptors: Functional insights into the two isoforms of the human GluN2A subunit.

by

Steven Dennis John Houghton

ORCID ID 0000-0002-9568-3769

Thesis for the degree of Doctor of Philosophy

July 2025

University of Southampton

Abstract

Faculty of Natural and Environmental Sciences
School of Biological Sciences
Thesis for the degree of Doctor of Philosophy

Human NMDA receptors: Functional insights into the two isoforms of the human GluN2A subunit.

by

Steven Dennis John Houghton

Glutamate is a major excitatory neurotransmitter in the central nervous system and plays an essential role in cognition and memory formation. This function is enacted through binding with glutamate receptors found at glutamatergic excitatory synapses. One such receptor is the *N*-methyl-D-aspartate receptor (NMDAR). NMDARs form ion channels and play key roles in neuronal development, synaptic communication, and mechanisms underlying learning and memory. Their function depends on the coincidence of pre- and post-synaptic activity, which relieves the voltage-dependent Mg²⁺ blockade and permits Ca²⁺ influx. While the GluN2A subunit is well-characterised, recent evidence suggests the existence of an alternatively spliced isoform, GluN2A-Short (GluN2A-S), distinguished by a truncated C-terminal domain and a unique C-terminus. Expression of constructs containing cDNA for human GluN2A results in a mixed expression of GluN2A-Long (GluN2A-L) and GluN2A-S isoforms, limiting insight into their individual contributions to function.

This thesis investigates whether the two human GluN2A isoforms can be studied independently to determine their specific functional properties within the NMDAR complex. Using site-directed mutagenesis, we disrupted the splice acceptor site responsible for generating both isoforms, enabling the selective expression of GluN2A-L. Applying this tool, we examined whether GluN2A-S confers distinct functional properties to the NMDAR under both physiological and disease-associated conditions. We studied both wild-type (WT) and mutant forms of human GluN2A-S with association with neurological disease in humans. Using electrophysiology and a bioluminescence-based Ca²⁺ assay, we found that WT GluN2A-S contributes enhanced voltage-dependent Mg²⁺ blockade compared to GluN2A-L. This finding pointing at an isoform-specific function of NMDARs containing either GluN2A-L or GluN2A-S in physiological conditions.

We further assessed how GluN2A-S functions in disease-associated mutations such as the epilepsy-associated *GRIN2A* mutation: L812M. When investigating this gain-of-function mutation, we found that GluN2A-S mitigates the decrease in voltage-dependent Mg²⁺ blockade but does not alleviate the increase in glutamate potency. This suggests an isoform-specific gain-of-function effect of the L812M mutation.

Furthermore, the epilepsy-associated G483R mutation exhibited an isoform-dependent effect, resulting in a loss-of-function in GluN2A-L but a gain-of-function in GluN2A-S. Specifically, while

the G483R mutation caused a strong decrease in Ca²⁺ conductance through GluN2A-L-containing NMDARs, it led to a marked increase in conductance through GluN2A-S-containing receptors.

These findings underscore the clinical relevance of each individual human GluN2A isoforms. Studying them separately may provide deeper insight into their distinct contributions to NMDAR function in both synaptic physiology and neurological disease. In the context of the epilepsy-associated mutations explored in this thesis, upregulation of the human GluN2A-S isoform and/or suppression of GluN2A-L expression could be a potential strategy for managing the dysfunction imposed by L812M. Similarly, increasing GluN2A-S expression in patients carrying the G483R mutation may help rescue the loss-of-function imposed by the mutation.

Table of Contents

Table of Co	ontents	i
Table of Ta	ıbles	vii
Table of Fi	gures	ix
Table of Ed	quations	xiii
Research T	hesis: Declaration of Authorship	xv
Acknowled	lgements	xvii
List of Abb	reviations	xix
Chapter 1	General Introduction	23
1.1 NM	DARs in health and disease	23
1.1.1	Tetrameric composition of NMDARs	23
1.1.2	Ion channel architecture and properties	24
<u> </u>	I.1.2.1 N-terminal domain	25
<u>-</u>	1.1.2.2 Agonist binding domain	26
-	I.1.2.3 Pore domain	28
2	L.1.2.4 Mg ²⁺ block of NMDA receptors	29
	1.1.2.4.1 Kinetics of Mg ²⁺ blockade	30
	1.1.2.4.2 Subtype-dependent variation in Mg ²⁺ blockade	31
2	I.1.2.5 C-terminal domain	32
1.1.3	Mutations in hGluN2A and association with neurological disorders	34
1.2 Glu	N2A-S: A primate-specific NMDA receptor isoform	35
1.2.1	Mechanism and regulation of pre-mRNA splicing	37
1.2.2	Two GRIN2A transcripts are expressed in human and primate brain	39
1.2.3	Translation of the GRIN2A-S transcript into GluN2A-S protein	41
1.3 Нур	oothesis and Aims	43
Chapter 2	Methods	45
2.1 Ma	terials	45
2.1.1	Oligonucleotides	45
2	2.1.1.1 Oligonucleotides for site-directed mutagenesis	45

	2	2.1.1.2 Oligonucleotides for sequencing	. 46
	2	2.1.1.3 Oligonucleotides for PCR	. 46
	2.1.2	DNA plasmids	. 47
	2.1.3	Antibodies	. 48
	2.1.4	Buffers and Solutions	. 49
	2	2.1.4.1 Molecular biology	. 49
	2.	2.1.4.2 Protein analysis	. 50
2.2	Bioir	nformatics	. 52
2.3	Cell	Culture Methods	.52
	2.3.1	Human Embryonic Kidney cell line maintenance	. 52
	2.3.2	Human Embryonic Kidney Cell Transfection	. 53
	2.3.3	Patch clamp electrophysiology	. 54
	2.3.4	Iontophoresis	. 55
	2.3.5	Bioluminescence assay	. 56
2.4	Mole	ecular Biology Techniques	. 57
	2.4.1	Bacterial plasmid DNA transformation	. 57
	2.4.2	Plasmid DNA Mini-Prep	. 57
	2.4.3	Plasmid DNA Maxi-Prep	. 58
	2.4.4	RNA extraction	. 59
	2.4.5	Reverse Transcription of RNA to cDNA	. 60
	2.4.6	Nanodrop Determination of Nucleotide Concentrations	. 60
	2.4.7	End-point PCR	. 61
	2.4.8	Agarose gel electrophoresis	. 61
	2.4.9	Site-directed mutagenesis (SDM)	. 62
	2.4.10	Sequence verification	. 64
2.5	Prot	tein analysis techniques	. 64
	2.5.1	Protein extraction	. 64
	2.5.2	SDS polyacrylamide gel electrophoresis (SDS PAGE)	. 64
	2.5.3	Wet transfer	. 65
	2.5.4	Immunoblotting	. 65
2.6	Data	a Analysis	66

Chapter 3		Generation of a gene expression construct to investigate the function of						
		Human GluN2A and GluN2A-S in isolation	67					
3.1	Intr	oduction	67					
3.2	Aim	s and Objectives	69					
3.3	Res	ults	70					
3	3.3.1	Creating a tool to express the hGluN2A-L in isolation. Step 1: Site direct	ed					
		mutagenesis of hGRIN2A and sequence validation	70					
3	3.3.2	Creating a tool to express the hGluN2A-L in isolation. Step 2: Testing mF	RNA					
		transcripts produced by the mutant	72					
3	3.3.3	Creating a tool to express the hGluN2A-L in isolation. Step 3: Testing pro	otein					
		isoforms produced by the mutant.	75					
3	3.3.4	Creating splice sites in rGluN2A. Step 1: Site directed mutagenesis of rG	rin2A					
		and sequence validation.	77					
3	3.3.5	Creating splice sites in rGluN2A. Step 2: Testing mRNA transcripts produ	ıced					
		by the mutant	79					
3.4	Disc	cussion	82					
3	3.4.1	Conclusions and Key Findings	82					
	3	3.4.1.1 Generating a tool for investigating the functional significance of						
		GluN2A-L in isolation	82					
	3	3.4.1.2 Rat Grin2A splice site mutagenesis suggests more complex						
		mechanisms of splicing for human GluN2A-S generation	84					
3	3.4.2	Future perspectives	85					
Chapt	er 4	Investigating differences in the current-voltage relationship between						
-		Human GluN2A, Rat GluN2A, and Human GluN2A-S	87					
4.1	Intr	oduction						
4.2		s and Objectives						
4.3		ults						
4	1.3.1	, 3 11						
,	ופיו	via iontophoresis Analysis of voltage-dependence of rGluN2A, h(r)GluN2A-L and hGluN2A						
4	+.3.∠	containing NMDARs during instantaneous Mg ²⁺ unblock	N-S- 91					

	ependence of Mg ²⁺ Block and Conductance-Voltage Analysis
	93
4.3.2.2 Current-v	oltage relationship of NMDARs under low Mg ²⁺ conditions . 96
4.3.3 Investigation of	Mg ²⁺ blockade in hGluN2A-S-containing NMDARs during non-
instantaneous b	lock and unblock99
4.4 Discussion	107
4.4.1 Conclusions and	Key Findings107
4.4.1.1 hGluN2A	S increases magnesium sensitivity of exogenous NMDAR
current ir	HEK293T cells107
	r of h(r)GluN2A-L and hGluN2A-S-containing NMDARs during
non-insta	ntaneous changes in membrane potential108
4.4.1.3 Implication	ons of increased voltage dependence in hGluN2A-S-containing
NMDARs	
4.4.2 Future perspect	ves111
Chapter 5 Investigating th	e isoform-specific effect of disease-associated <i>GRIN2A</i>
	ions on NMDAR function113
E 1 Introduction	113
	113
5.2 Aims and Objectives.	
5.2 Aims and Objectives.5.3 Results	
5.2 Aims and Objectives.5.3 Results5.3.1 Investigating the	e effect of the epilepsy-associated GOF mutation L812M on
5.2 Aims and Objectives.5.3 Results5.3.1 Investigating the	
5.2 Aims and Objectives.5.3 Results5.3.1 Investigating the h(r)GluN2A-L and	e effect of the epilepsy-associated GOF mutation L812M on
5.2 Aims and Objectives.5.3 Results5.3.1 Investigating the h(r)GluN2A-L and 5.3.1.1 Site directions.	e effect of the epilepsy-associated GOF mutation L812M on dhGluN2A-S-containing NMDARs.
 5.2 Aims and Objectives. 5.3 Results 5.3.1 Investigating the h(r)GluN2A-L and 5.3.1.1 Site directivalidation 	
5.2 Aims and Objectives. 5.3 Results 5.3.1 Investigating the h(r)GluN2A-L and 5.3.1.1 Site directival validation 5.3.1.2 Testing many street in the s	
5.2 Aims and Objectives. 5.3 Results 5.3.1 Investigating the h(r)GluN2A-L and 5.3.1.1 Site directival dation validation 5.3.1.2 Testing m 5.3.1.3 Establishing	
5.2 Aims and Objectives. 5.3 Results 5.3.1 Investigating the h(r)GluN2A-L and salidation validation 5.3.1.1 Site direct validation 5.3.1.2 Testing m 5.3.1.3 Establishin activity	
5.2 Aims and Objectives. 5.3 Results 5.3.1 Investigating the h(r)GluN2A-L and validation validation 5.3.1.2 Testing m 5.3.1.3 Establishing activity 5.3.1.4 Analysis of	e effect of the epilepsy-associated GOF mutation L812M on d hGluN2A-S-containing NMDARs
5.2 Aims and Objectives. 5.3 Results 5.3.1 Investigating the h(r)GluN2A-L and salidation validation 5.3.1.1 Site direct validation 5.3.1.2 Testing m 5.3.1.3 Establishing activity 5.3.1.4 Analysis of hGluN2A-like hGluN2A-like hGluN2A-like hGluN2A-like hGluN2A-like has a constant and salidation has been salidated as a constant and salidate	e effect of the epilepsy-associated GOF mutation L812M on d hGluN2A-S-containing NMDARs

	5.3.2	2 Invest	tigating the effect of the disease-associated LOF mutations on hGlu	ıN2A-
		S and	its effect on wild-type receptor function	134
		5.3.2.1	C231Y and C436R	134
		5.3.2.2	G483R	137
5.4	4 Di	scussion		140
	5.4.	1 Concl	usions and Key Findings	140
		5.4.1.1	Bioluminescence-based Ca ²⁺ assay as a suitable method for study	ing
			ion channel function	140
		5.4.1.2	The GOF epilepsy-associated L812M mutation confers an isoform	-
			independent effect on glutamate potency	141
		5.4.1.3	The GOF epilepsy-associated L812M mutation confers an isoform	J -
			specific change in Mg ²⁺ sensitivity	143
		5.4.1.4	Isoform-independent effect of disease-associated C231Y and C43	6R
			LOF mutations	144
		5.4.1.5	The LOF epilepsy-associated G483R mutation confers a GOF effect	t in
			hGluN2A-S	145
	5.4.2	2 Futur	e perspectives	147
Cha	pter 6	Gene	ral discussion and future directions	1/10
	•			
			of findings	149
6.2	2 Fu	iture res	earch directions	150
	6.2.	1 Furth	er investigation of the altered Mg ²⁺ sensitivity in hGluN2A-S	150
	6.2.2	2 Devel	oping rodent models to explore GluN2A-S function	151
	6.2.3	3 Invest	tigating the synaptic localisation of hGluN2A-S	154
Арр	endix	A Biolu	minescence-based calcium assay for the analysis of NMDA recept	or:
		magn	esium pharmacology	157
Α.:	1 In	troductio	on	157
A.2	2 M	ethods		157
	Α 2	1 Biolur	minescence assay	157
			uring resting membrane potential	
Α.				
Α.:	o K€	esuits and	d discussion	158

٦	Γ ¬	h	_	٦f	\sim	n+	ents	
	ıa	U	ю.	OI	U.O	1116	-1115	

ist of References	
-------------------	--

Table of Tables

Table 2.1	List of oligonucleotides used for site-directed mutagenesis PCR	45
Table 2.2	List of oligonucleotides used for sequencing.	46
Table 2.3	List of oligonucleotides used as primers for end-point PCR	46
Table 2.4	List of plasmid DNA constructs used.	47
Table 2.5	List of antibodies and their respective dilutions	48
Table 2.6	Recipe for SDS-PAGE separating gel (1x1.0mm; 7%)	51
Table 2.7	Recipe for SDS-PAGE stacking gel (1x1.0mm; 4%)	51
Table 2.8	HEK293T cell experimental layout	53
Table 2.9	HEK293T cell transfection parameters	54
Table 2.10	Recording pipette puller settings.	55
Table 2.11	Iontophoresis pipette puller settings.	56
Table 2.12	PCR amplification master mix recipe	61
Table 2.13	Thermocycler settings for PCR amplification	61
Table 2.14	Q5 Site-directed mutagenesis master mix recipe	63
Table 2.15	Thermocycler settings for site-directed mutagenesis	63
Table 5.1	GRIN2A missense mutations and clinical presentations	116

Table of Figures

Figure 1.1 - Structural architecture of the NMDA receptor.	.25
Figure 1.2 - Residues involved in glutamate binding to GluN2A.	.27
Figure 1.3 - Residues involved in extracellular Mg2+ binding and blockade of NMDARs	.30
Figure 1.4 – Human GluN2A-S lacks both the C-terminal binding regions for PSD-95	.36
Figure 1.5 - pre-mRNA splicing.	.38
Figure 1.6 - Exon-dependent alternative splicing of human GRIN2A.	.39
Figure 1.7 - Two GRIN2A mRNA transcript variants in human and primate brain but not mo	use
brain.	.40
Figure 1.8 - Two GluN2A isoforms are present in the human brain but not the mouse brain	. 42
Figure 2.1 - The process of incorporating substitution mutations into plasmid DNA using sit	te-
directed mutagenesis.	.62
Figure 2.2 - Assembly of Western Blot transfer sandwich.	.65
Figure 3.1 - Comparison of the donor and acceptor splice sites responsible for the alternati	ve
splicing of hGRIN2A with the equivalent sites in rodent Grin2A	.68
Figure 3.2 - Generation of a plasmid construct to independently express canonical human	
GluN2A using site-directed mutagenesis.	.71
Figure 3.3 - Exogenous expression of eGFP-Human GluN2A ^{A4114G} in HEK293T cells	.72
Figure 3.4 - End-point PCR following RNA extraction and RT-PCR from HEK293T cells expres	ssing
Human GRIN2A ^{A4114G} .	.74
Figure 3.5 - SDS-PAGE and western blot following protein extraction from HEK293T cells	
expressing Human GluN2AA4114G	.76
Figure 3.6 - Generation of pCI-EGFP-NR2a ^{G4114A} using site-directed mutagenesis	.78
Figure 3.7 - Exogenous expression of PCI-eGFP-Rat Grin2A ^{G4114A} in HEK293T cells	.79
Figure 3.8 - End-point PCR following RNA extraction and RT-PCR from HEK293T cells expres	ssing
Rat Grin2A ^{G4114A}	.80

Figure 3.9 - N ı	ucleotide sequence alignr	ment between hum	nan and rat Grin2A co	oding sequences
	surrounding the dono	or and acceptor spli	ice sites	81
Figure 4.1 - Es	tablishing a stationary NI	MDA receptor conc	ductance	90
Figure 4.2 - A ı	nalysis of voltage depend		•	
Figure 4.3 - A ı	nalysis of voltage depend	ence of human and	d rat NMDA receptor	rs: relationship
	between expected lin	near and blocked cu	ırrent	95
Figure 4.4 - A ı	nalysis of voltage depend	ence of human and	d rat NMDA receptor	rs in low
	extracellular magnesi	ium: subtracted and	d normalised	98
Figure 4.5 - N I	MDA-induced currents du	uring voltage-steps.	•	100
Figure 4.6 - N I	MDA-induced currents du	uring action potent	ial waveform stimula	ation: fast somati
	Na+ backpropagating	action potential		102
Figure 4.7 - N I	MDA-induced currents du			
	Na+/Ca+ action poter	ntial		104
Figure 4.8 - N I	MDA-induced currents du	uring action potent	ial waveform stimula	ation: all-or-none
	dendritic Na+ action p	potential (boosted	excitatory postsyna _l	ptic potential.105
Figure 4.9 - N I	MDA-induced current-vol	ltage relationship d	luring either slow vo	ltage ramp or
	during action potentia	al waveform stimu	lation	106
Figure 5.1 - Lo	cations of loss-of-functio	on and gain-of-func	tion epilepsy-associa	ated GRIN2A
	missense mutations			115
Figure 5.2 - G e	eneration of pcDNA3.1+ e	eGFP-h(r)GRIN2A-Lʻ	^{C2434A} using site-direc	ted mutagenesis.
Figure 5.3 - G	eneration of pcDNA3.1+ e	eGFP-Human GRIN2	2A-S ^{C2434A} using site-(directed
	mutagenesis			120
Figure 5.4 - Ex	ogenous expression of e	GFP-h(r)GluN2A-L ^{c2}	^{2434A} and eGFP-hGluN	I2A-S ^{C2434A} in
	HEK293T cells			121
Figure 5.5 - Ex	ogenous expression of re	ecombinant h(r)GRI	IN2A-L ^{C2434A} results in	n a single GRIN2A
	mRNA transcript in H	EK293T cells		123

Figure 5.6 - Establishing parameters for the measurement of calcium influx through NMDA
receptors using a bioluminescence-based assay on HEK293G5A cells with
calcium-sensitive aequorin expression
Figure 5.7 - Analysis of the individual effect of the epilepsy-associated L812M GRIN2A missense
mutation on glutamate pharmacology in hGluN2A-L and hGluN2A-S-containing
NMDA receptors
Figure 5.8 - Analysis of the individual effect of the epilepsy-associated L812M GRIN2A missense
mutation on voltage-dependence in hGluN2A-L and hGluN2A-S-containing
NMDA receptors
Figure 5.9 - Analysis of isoform-dependent effect of the L812M mutation on voltage dependence
of NMDA receptors: relationship between expected linear and blocked
current
Figure 5.10 - Investigating the effect of epilepsy-associated GRIN2A loss-of-function missense
mutations in GluN2A-S and its effect on wild-type receptor function136
Figure 5.11 - Investigating whether the effect of the G483R missense mutation on hGluN2A-S is
isoform-specific139
Figure 6.1 - TKIT design for the generation of a mouse GluN2A-S isoform153
Figure 6.2 - Human GluN2A-S lacks both the C-terminal binding regions for PSD-95

Table of Equations

Equation 4.1 - Boltzmann distribution
--

Research Thesis: Declaration of Authorship

Print name: Steven Dennis John Houghton

Title of thesis: Analysing the functional significance of a primate-specific glutamate receptor subunit

I declare that this thesis and the work presented in it are my own and has been generated by me as the result of my own original research.

I confirm that:

- This work was done wholly or mainly while in candidature for a research degree at this University.
- 2. Where any part of this thesis has previously been submitted for a degree or any other qualification at this University or any other institution, this has been clearly stated.
- 3. Where I have consulted the published work of others, this is always clearly attributed.
- 4. Where I have quoted from the work of others, the source is always given. Except for such quotations, this thesis is entirely my own work.
- 5. I have acknowledged all main sources of help.
- 6. Where the thesis is based on work done by myself jointly with others, I have made clear exactly what was done by others and what I have contributed myself.
- 7. None of this work has been published before submission.

Signature:	

Acknowledgements

I have yet to experience a more emotionally and physically taxing but equally rewarding experience as that imposed by my PhD project. There is a plethora of individuals that have provided academic, pastoral and emotional support during my time at the University of Southampton—without which I do not believe the completion of my PhD would have been possible.

I would like to first express my gratitude to my primary supervisor, Mariana Vargas-Caballero, who has supported my academic journey from my master's to now PhD project. I thank her for providing me with technical and transferable skills alongside her pastoral support. I am additionally appreciative of my secondary supervisory team including Andrew Penn and Katrin Deinhardt, further supporting my professional and personal growth. I would like to thank all members of the laboratory team past and present: Hannah Warming, Lauren Walker, Oreoluwa Fakeye, Lucy Scullard, Kirsten Williamson, Natasha Lebos, Cerys Roberts, Midhun Krishnan and Alexander Lowe for supporting my work and making a positive impact to my experience.

I am also extremely grateful to the South Coast Biosciences Doctoral Training Partnership (SoCoBio DTP) and Institute for Life Sciences for co-funding my PhD project. I would like to send a particularly large thank-you to the Gerald Kerkut Charitable Trust for supporting my extension and nominal registration, allowing me to write my thesis despite mental health setbacks.

To the amazing team of technicians within building 85 Life Sciences, for all your work in supporting the smooth operations of an academic laboratory allowing me to undertake my experimental work.

A huge thank you goes to my friends and family for supporting me emotionally and providing breakaways from the hardships and challenges of my project. I would like finally to thank my darling fiancée—soon to be my wife—Jess Kirby. You have been the guiding light and emotional crutch when I have been stuck between a rock and hard place. I love you so very much and without your selflessness and sacrifices, this would not have been at all possible.

List of Abbreviations

ABDAgonist-binding domain

ABPEatypical benign partial epilepsy AMPARAlpha-amino-3-hydroxyl-5-methyl-4-isoxadole-proprionate receptor BpBase-pair Ca²⁺......Calcium ion CaMKII......Calcium-calmodulin-dependent kinase II cDNAcomplementary DNA CDScoding sequence CNS Central nervous system CSWSScontinuous spike-and-wave during slow-wave sleep syndrome CTDC-terminal domain DMEMDulbecco's Modified Eagle Medium DPBS......Dulbecco's Phosphate Buffered Saline EASEpilepsy-aphasia spectrum ECDExtracellular domain ER Endoplasmic Reticulum ESES Epileptic Encephalopathy related to Status Epilepticus during slow

FBS.....Foetal Bovine Serum

GluN2A-LGluN2A-Long

GluN2A-S......GluN2A-Short

GOFGain of function

gRNA.....guide RNA

G-Vconductance-voltage relationship

Sleep

h(r)GluN2A-Lhuman GluN2A^{R1372G}

H⁺......Hydrogen ion/proton

List of Abbreviations

HEK293..... Human Embryonic Kidney cell

hGluN2A-L.....Human GluN2A-L

hGluN2A-S..... Human GluN2A-S

hGRIN2A Human GRIN2A

IC₅₀ Half-maximal inhibitory concentration

INDELInsertion/Deletion mutations

I-V.....Current-voltage

K⁺......Potassium ion

LKS.....Landau-Kleffner syndrome

LOF Loss of function

M1-4NMDAR transmembrane domains

Mg²⁺ Magnesium ion

mGluN2A mouse GluN2A

mGrin2A..... mouse Grin2A

Na⁺ Sodium ion

NMDAR N-methyl-D-aspartate receptor

NTD N-terminal domain

ORF Open reading frame

P1 Postnatal day 1

PAM Protospacer-adjacent motif

PCR.....polymerase chain reaction

PSD......Postsynaptic density

RE Rolandic epilepsy

rGluN2A rat GluN2A

rGrin2A rat Grin2A

RLU......Relative luminescence units

snRNA Small nuclear RNA

snRNP.....Small nuclear ribonucleoprotein

Chapter 1 General Introduction

Glutamate is the principal excitatory neurotransmitter in the central nervous system (CNS) (Zhou and Danbolt, 2014), playing a crucial role in higher cortical functions such as cognition and memory (Francis, 2003). It is released at specialised neuronal structures called synapses, where it mediates excitatory neurotransmission. Upon release from presynaptic vesicles, glutamate diffuses across the synaptic cleft (~20-30 nm) and exerts its effects through specific channel-forming ionotropic glutamate receptors in the post-synaptic membrane. These include N-methyl-D-aspartate receptor (NMDAR), α -amino-3-hydroxyl-5-methyl-4-isoxadole-proprionate receptor (AMPAR) and kainate receptor. NMDARs are involved in a range of physiological processes, ranging from CNS development (Forrest $et\ al.$, 1994; Hamada $et\ al.$, 2014) to synaptic neurotransmission (Zito and Scheuss, 2009) and the mechanisms underlying learning and memory (Nicoll, 2017).

Beyond their role in normal cognitive function, NMDARs have been implicated in numerous neurological disorders, including Alzheimer's disease (Francis, 2003), ischemic stroke (Bruno *et al.*, 2001), and epilepsy (Meldrum, Akbar and Chapman, 1999). Gaining a deeper understanding of NMDAR function at the synapse, particularly aspects unique to humans, may provide critical insights for developing therapeutic strategies targeting NMDAR-related pathologies.

Prior research had focused on analysing NMDA receptors cloned from rodent DNA (Vicini *et al.*, 1998; Barria and Malinow, 2007), but we now know that humans express two isoforms GluN2A-L (1464 amino acids) and GluN2A-S (1281 amino acids) (Pegasiou, 2018; Warming *et al.*, 2019). This research aims to investigate the functional significance of GluN2A-S and compare that to the function of the canonical GluN2A-L isoform. This chapter will provide an overview of NMDAR structure and function, discuss NMDAR mutations associated with epilepsy-aphasia spectrum (EAS) disorder, and summarise the current understanding of the GluN2A-S isoform.

1.1 NMDARs in health and disease

1.1.1 Tetrameric composition of NMDARs

NMDARs are composed of four co-assembled subunits. To date, seven distinct subunits have been identified: GluN1, GluN2 (GluN2A-D), and GluN3 (GluN3A and GluN3B). In humans these subunits are encoded by the genes: *GRIN1*, *GRIN2A*, *GRIN2B*, *GRIN2C*, *GRIN2D*, *GRIN3A*, and *GRIN3B*, respectively. Similarly, in rodents such as rats, they are encoded by *Grin1*, *Grin2a*, *Grin2b*, *Grin2c*, *Grin2d*, *Grin3a*, and *Grin3b* (Traynelis *et al.*, 2010). These receptors form heterotetrameric

assemblies, which in the forebrain typically consist of two copies of the obligatory GluN1 subunit and two GluN2 subunits (Cull-Candy and Leszkiewicz, 2004; Traynelis *et al.*, 2010; Paoletti, 2011).

Although GluN1 is encoded by a single gene, alternative splicing generates eight distinct isoforms (GluN1-1a to GluN1-4a and GluN1-1b to GluN1-4b) (Rumbaugh *et al.*, 2000; Horak and Wenthold, 2009; Vance, Hansen and Traynelis, 2012). The GluN1 subunit is expressed uniformly throughout the brain from embryonic development to adulthood. In contrast, the expression patterns of GluN2 and GluN3 subunits are developmentally regulated.

In-situ hybridisation studies using oligonucleotide probes for *Grin2a* in fixed mouse and rat brain tissue at various developmental stages have shown that GluN2A is expressed early in postnatal development and gradually increases until reaching a stable level around the third postnatal week (Watanabe *et al.*, 1992; Akazawa *et al.*, 1994). Conversely, the study of *GRIN2A* expression in the human brain reveals an earlier expression profile. Bar-Shira et al. (2015) systematically reviewed microarray and RNA-seq data from human post-mortem tissue from various ages and found that *GRIN2A* expression rises during prenatal embryonic development with a clear switch of expression profile between *GRIN2A* and *GRIN2B* neonatally (Bar-Shira, Maor and Chechik, 2015).

Sheng et al. (1994), using serial immunoprecipitation in rat brain tissue, demonstrated that NMDARs are composed of the obligatory GluN1 subunit, which associates with either GluN2A or GluN2B subunits to form di-heteromeric receptors (GluN1/GluN2A or GluN1/GluN2B). They also found that GluN2A-specific antibodies immunoprecipitated GluN2B and vice versa, suggesting the formation of tri-heteromeric configurations containing both GluN2A and GluN2B subunits (GluN1/GluN2A/GluN2B). (Sheng et al., 1994). Rauner and Köhr (2011) further explored the presence of tri-heteromeric NMDARs in the mouse brain by comparing excitatory post-synaptic currents from hippocampal CA1 synapses in WT mice to those expressing either *Grin2a* or *Grin2b* alone. They identified a subset of NMDARs whose properties could not be explained by a mixture of GluN1/GluN2A and GluN1/GluN2B di-heteromers. These tri-heteromers exhibited deactivation kinetics comparable to GluN2B-containing receptors, but with a voltage-dependence characteristic of GluN2A-containing receptors (Rauner and Köhr, 2011).

1.1.2 Ion channel architecture and properties

NMDAR subunits are composed of four distinct structural domains: the N-terminal domain (NTD), the agonist binding domain (ABD), the pore domain, and the C-terminal domain (CTD) (Figure 1.1) (Paoletti and Neyton, 2007; Karakas and Furukawa, 2014; Lee *et al.*, 2014).

In this chapter, we will examine each of these domains and their roles in NMDAR function. Additionally, we will discuss the voltage-dependent blockade of magnesium ions (Mg²⁺) in the channel pore. Finally, we will explore how mutations in the *GRIN2A* gene are linked to human neurological disorders, particularly epilepsy and neurodevelopmental dysfunction.

1.1.2.1 N-terminal domain

The NTD consists of the first 350 amino acids and plays a role in subunit assembly and allosteric modulation of the NMDAR. Its essential role in subunit assembly has been demonstrated through the generation of truncated NMDAR chimeras, followed by measurement of both cell surface expression and functional activity (Meddows *et al.*, 2001). Structural studies have identified a binding site for the allosteric modulator Zn²⁺ within the cleft of the clamshell-like structure of the NTD (Karakas, Simorowski and Furukawa, 2009). By measuring the effects of extracellular Zn²⁺ on NMDARs with different subunit compositions, Paoletti et al. (1997) found that Zn²⁺ is a more potent inhibitor of NMDAR activation in GluN1/GluN2A di-heteromers (Paoletti, Ascher and Neyton, 1997).

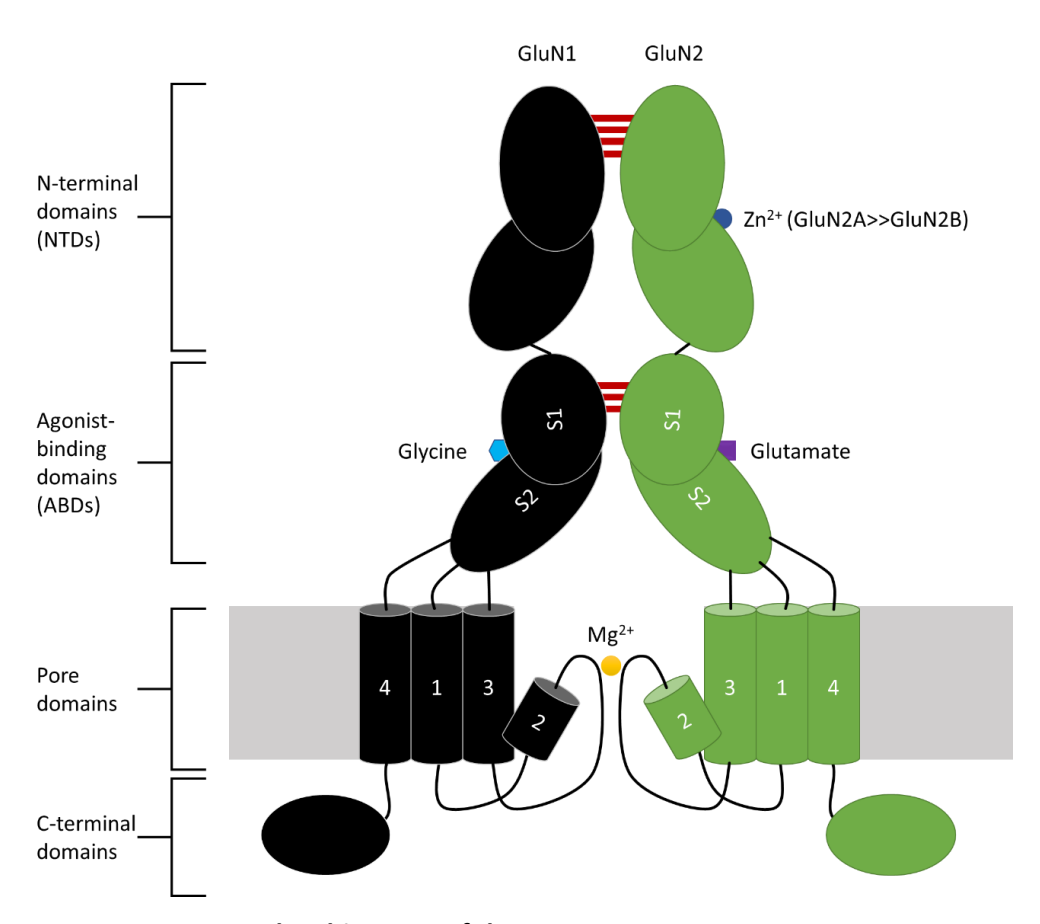


Figure 1.1 - Structural architecture of the NMDA receptor.

One half of the tetrameric assembly is shown for simplicity. The extracellular domain consists of two clamshell-like domains, the N-terminal domain (NTD) and agonist-binding domain (ABD). The subunits dimerise via both the NTDs (predicted) and

ABDs. The endogenous antagonist Zn²⁺ binds to the NTD with strong GluN2A selectivity and inhibits at nanomolar concentrations. The endogenous agonist glutamate binds to the GluN2 subunit ABD whilst the co-agonist glycine (or D-serine) binds to the ABD of the GluN1 subunit. The ion-channel domain consists of 4 transmembrane domains (M1, M3 and M4) with a M2 re-entrant loop. These pore domains contain both the ion-selectivity filter and binding site for endogenous extracellular Mg²⁺ blockade, giving these receptors voltage-dependence. The intracellular CTD plays roles in receptor anchoring, trafficking and downstream signalling pathways via interaction motifs with synaptic scaffolding and signalling proteins.

1.1.2.2 Agonist binding domain

The ABD consists of two segments: S1 and S2. S1, located at the N-terminal, includes the pretransmembrane domain 1 (M1) region, while S2 is positioned between the M3 and M4 transmembrane domains. Together, the S1S2 domain forms a "clamshell-like" structure that serves as the binding site for the agonist glycine on GluN1 and GluN3 subunits, and for glutamate on the GluN2 subunit. Furukawa et al. (2005) resolved the structure of the rat GluN2A S1S2 domain bound to glutamate, as well as the GluN1/GluN2A S1S2 complex bound to both glycine and glutamate through X-ray crystallography. This was made possible by the modular nature of NMDARs, allowing the isolation and preparation of the water-soluble ligand-binding S1S2 domain of the ABD. The study revealed that the subunit dimer-of-dimer interactions are mediated by three subsites. Site II includes residues Y535 and P532 of GluN1, P527 of GluN2A, a disulphide bridge between R755 of GluN1 and E530 of GluN2A, and hydrogen bonding between K531 of GluN1 and the carbonyl oxygen of F524 in GluN2A. Sites I and III consist of hydrophobic residues, including I519, A524, and L777 of GluN1, and I514, V526, L777, and L780 of GluN2A. These interactions contribute to the back-to-back orientation of the GluN1/GluN2A S1S2 heterodimer (Figure 1.1) (Furukawa *et al.*, 2005).

The split S1S2 structure of the ABD allows for hinge-like movement, enabling the lobes to close around the agonist. The crystal structure of the GluN2A ligand-binding core revealed how glutamate binds and triggers receptor activation. Glutamate interacts with residue D731 via its α -amino group while forming hydrogen bonds with E413 and Y761. Additionally, van der Waals interactions occur between the γ -carboxylate of glutamate and the highly conserved GluN2 residue Y730 (Figure 1.2) (Furukawa *et al.*, 2005). Laube et al. (2004) showed that mutation of the equivalent tyrosine residue in the GluN2B (Y705) to alanine reduced glutamate binding affinity by 450-fold, emphasising its critical role in agonist recognition (Laube, Schemm and Betz, 2004).

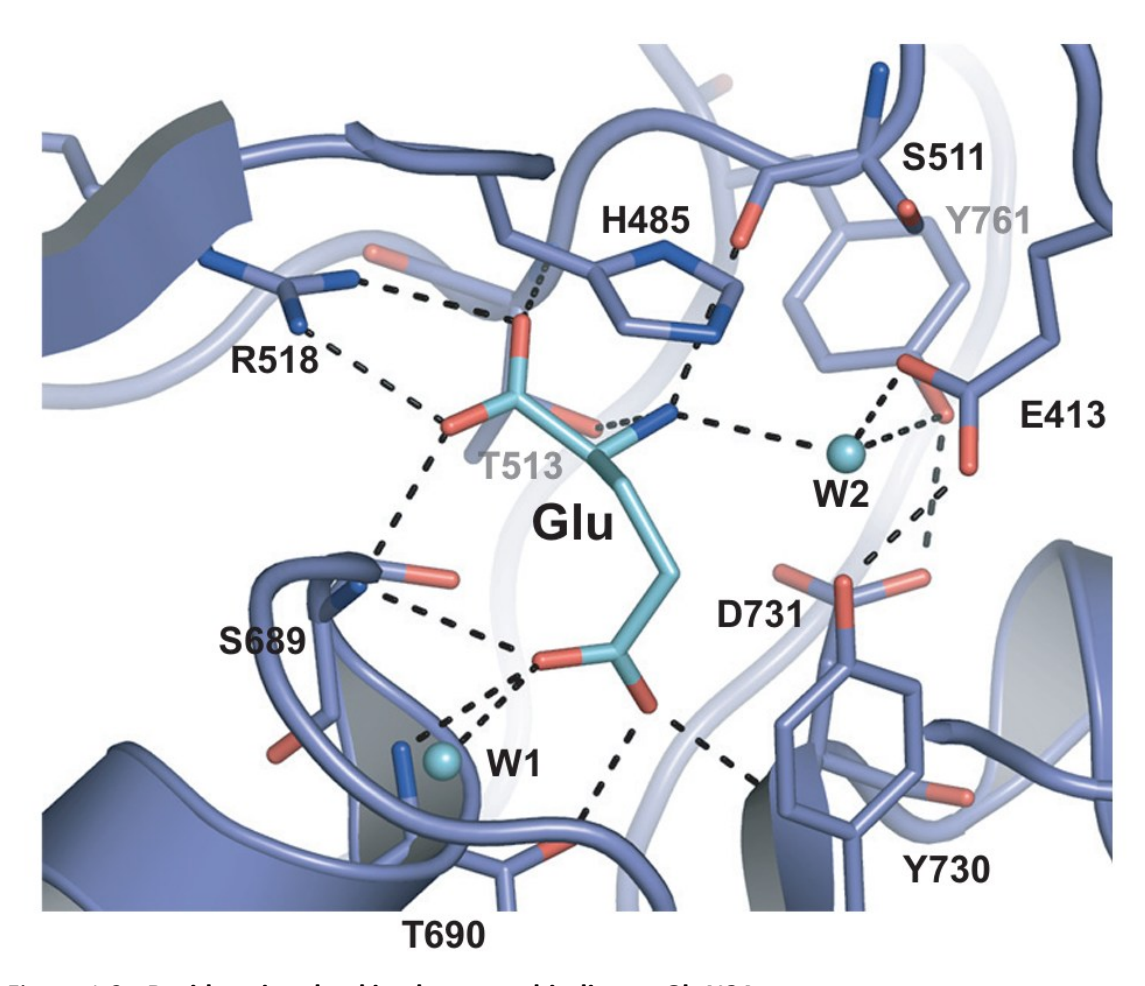


Figure 1.2 - Residues involved in glutamate binding to GluN2A.

Interaction of glutamate with residues of GluN2A and two water molecules (W1 and W2). Dashed lines present either hydrogen bonds or disulphide salt bridges.

Schematic taken from Furukawa et al., 2005.

Studies resolving the crystal structure of AMPAR, NMDARs, and kainate receptors have provided key insights into the shared mechanisms of gating control in these ionotropic glutamate receptors. Work by Sun et al. (2002) combined structural analysis with electrophysiological recordings to propose a mechanistic scheme for how glutamate binding leads to a transition from the resting state to bound, open, or desensitised states. By stabilising a key interface in the dimerisation between the S1S2 domains of the GluR2 AMPAR subunits, they found that desensitisation of the receptor was reduced. Upon agonist binding, conformational strain from S1S2 dimerisation and closure around the agonist leads to tension in the linkers connecting the ABD to the pore domain, resulting in channel opening.

Once activated, NMDARs display relatively slow deactivation kinetics compared to other ionotropic glutamate receptors such as AMPARs. The deactivation time course is heavily dependent on subunit composition. GluN2A-containing receptors deactivate with a weighted

Chapter 1

mean decay time constant (τ_w) of approximately 50 ms at room temperature. In contrast, GluN2B-containing receptors exhibit much slower deactivation kinetics, with a τ_w of around 250 ms at room temperature (Vicini *et al.*, 1998).

During desensitisation, the dimer interface is decoupled from the pore domain, causing channel closure even in the presence of bound glutamate (Sun *et al.*, 2002). This work underscores the importance of the ABD in regulating channel opening and desensitisation, and thus channel conductance.

In NMDARs, mutations in residues within the NTD, ABD and linker regions have been implicated in neurological disorders such as epilepsy. One such mutation, L812M, occurs in the linker region between the S2 domain and the M4 transmembrane domain. This mutation elicits receptor dysfunction through key gating regions, including the M4 domain of GluN2A and the M3 transmembrane domain and pre-M1 helix of GluN1. As a result, glutamate potency, open probability, and charge transfer during synaptic transmission are enhanced (Yuan *et al.*, 2014).

Additional *GRIN2A* mutations include C231Y—located in the NTD—as well as C436R and G483R, both situated within the S1 agonist-binding domain. These mutations have been shown to reduce agonist potency and surface expression (Addis *et al.*, 2017). This highlights the crucial role of residues within the NTD and ABD in the finely tuned mechanisms that control NMDAR gating and conductance. Disruption of these mechanisms through single point mutations can have drastic effects on NMDAR function, thereby influencing the clinical phenotypes of NMDAR-associated neurological disorders.

1.1.2.3 Pore domain

The pore domain of NMDARs shares structural homology with an inverted potassium channel due to the presence of an M2 re-entrant loop and its tetrameric quaternary structure (Wollmuth and Sobolevsky, 2004). The pore domain of NMDARs is responsible for permeability of the channel to sodium (Na⁺), potassium (K⁺) and calcium (Ca²⁺) ions. In addition, deep within the channel pore is a binding site for a magnesium ion (Mg²⁺) which acts as a voltage-dependent receptor antagonist, blocking ion flux. The selectivity filter attributing the ion permeability and Mg²⁺ binding is due to the M2 re-entrant loop of each subunit (Figure 1.1). Mutagenesis studies and glutamate-activated whole cell current measured in *Xenopus* oocytes, including early work by Burnashev et al. (1992) found that a highly conserved asparagine (N598 in GluN1; N614 in GluN2A) is crucial in Na⁺, K⁺, and Ca²⁺ selectivity and Mg²⁺ blockade (Burnashev *et al.*, 1992). More recent modelling by Kumar and Kumar, (2021), suggests that the electronegative side chain of the asparagine residues creates

a 'ring of partial negativity' allowing electrostatic interactions with Na^+ , K^+ , and Ca^{2+} (Kumar and Kumar, 2021).

1.1.2.4 Mg²⁺ block of NMDA receptors

The voltage-dependent blockade of NMDARs by extracellular Mg²⁺ plays a crucial role in synaptic plasticity regulation. This blockade occurs when Mg²⁺ binds within the channel pore, obstructing Na⁺, K⁺, and Ca²⁺ conduction. Under resting membrane conditions, the negative intracellular voltage attracts Mg²⁺ to the pore's blocking site (Mayer, Westbrook and Guthrie, 1984). Upon presynaptic glutamate release and postsynaptic depolarisation—typically triggered by AMPAR activation—Mg²⁺ is expelled, enabling NMDAR ion conduction. This coincidence detection of preand post-synaptic activity allows Ca²⁺ influx which serves as a key signal for synaptic strengthening and memory formation (Dingledine *et al.*, 1999).

The molecular mechanism underlying Mg^{2+} blockade is shaped by receptor structural features. Site-directed mutagenesis studies have identified key residues influencing Mg^{2+} sensitivity, many of which also regulate Ca^{2+} permeability, suggesting a shared electrostatic mechanism. A critical region is the Q/R/N site (N_0) within the M2 re-entrant loop (Figure 1.3). This site, formed by conserved asparagine residues in GluN1 (N598) and GluN2A (N614), creates an electrostatic barrier slowing Mg^{2+} permeability. Mutating N598 to glutamine in GluN1 (N598Q) has minimal impact on Mg^{2+} sensitivity, whereas the equivalent mutation in GluN2A (N614Q) dramatically reduces Mg^{2+} blockade and paradoxically increases Mg^{2+} permeability (Burnashev *et al.*, 1992).

Further evidence for an electrostatic network governing Mg²⁺ blockade comes from the role of the arginine residue at N+1 (Figure 1.3). Mutating this arginine significantly decreases Mg²⁺ sensitivity, highlighting its role in Mg²⁺ binding (Wollmuth, Kuner and Sakmann, 1998). Additionally, hydrophobic interactions contribute to Mg²⁺ binding stability. A tryptophan residue (W607 in GluN2B, W606 in GluN2A) within the pore-forming domain is essential for Mg²⁺ sensitivity. Replacing this tryptophan with non-aromatic residues significantly reduces Mg²⁺ sensitivity, underscoring the role of hydrophobic forces in Mg²⁺ interactions (Williams *et al.*, 1998).

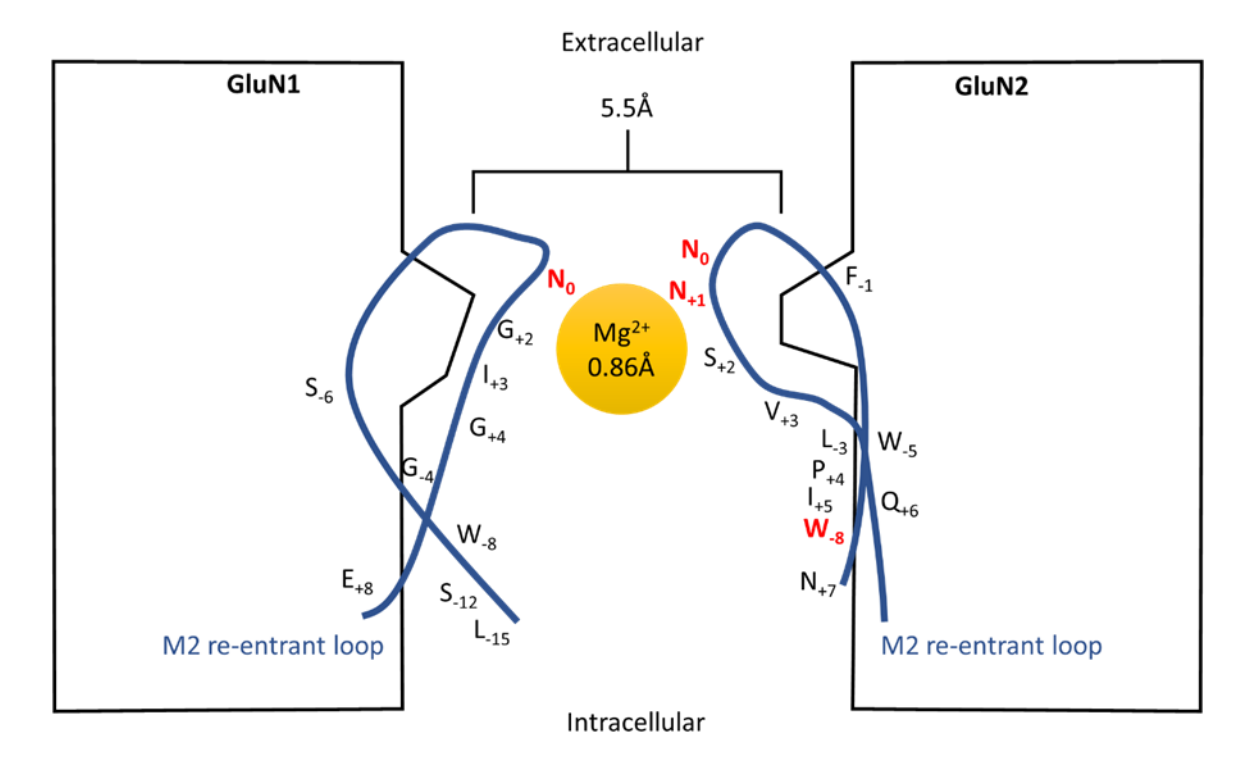


Figure 1.3 - Residues involved in extracellular Mg2+ binding and blockade of NMDARs.

Residues shown for GluN2 are for GluN2A although experiments providing evidence for this schematic are from receptors containing GluN1, GluN2A, GluN2B or GluN2C. This model ignores the possibility that either residues shown could be contributed by single GluN1 and GluN2 subunits or contributed to different subsets of residues from the two copies of GluN1 and GluN2 in the heterotetrameric assembly. Residues that are important for Mg²⁺ binding to the channel pore through mutational studies are shown in red. A particularly important residue contributed by each subunit is represented as N₀ which is within the Q/R/N site (N598 in GluN1; N614 in GluN2A) and carries an important role in Mg²⁺ binding in addition to Na⁺, K⁺ and Ca⁺ selectivity. This cartoon summarises the output from: Burnashev et al., 1992; Kumar and Kumar, 2021; Kuner et al., (1996), Kupper et al., (1996, 1998), Villarroel et al., (1995), Williams et al., (1998) and Wollmuth et al., (1996, 1998). (Figure adapted from Dingeldine et al., 1999).

1.1.2.4.1 Kinetics of Mg²⁺ blockade

Electrophysiological studies provide insight into Mg²⁺ blockade kinetics. Sobolevsky and Yelshansky (2000) demonstrated that Mg²⁺ remains trapped within the pore despite agonist-induced channel opening and closing, maintaining voltage-dependent blockade until sufficient depolarisation occurs. Following depolarisation and NMDAR unblock, as the membrane potential returns to resting levels, residue ion flow can persist briefly as Mg²⁺ re-enters to resting levels.

This re-blocking event can lead to a characteristic 'hooked' tail current—an inward transient preceding full channel blockade (Sobolevsky and Yelshansky, 2000).

Vargas-Caballero and Robinson (2003) further investigated Mg²⁺ unblock kinetics. Using nucleated patch recordings, they identified two unblocking phases: a fast (~1 ms) and a slower (~14-23 ms) component, the latter contributing ~50% of the current at -40 mV. They found that NMDAR currents were minimal during fast Na⁺ action potentials due to slow unblocking kinetics, whereas slower Ca²⁺ action potentials allowed for greater NMDAR activation. These findings suggest that NMDARs do not significantly contribute to the initial phase of fast action potential but play a crucial role in dendritic excitability and slow Ca²⁺-dependent action potentials. Large tail currents during repolarisation indicated a role of NMDARs in spike-timing-dependent plasticity, as NMDARs could extend the window for Ca²⁺ conductance and are therefore well-suited for mechanisms of long-term potentiation (LTP) and synaptic modification (Vargas-Caballero and Robinson, 2003).

Vargas and Robinson (2003) proposed an 'asymmetric trapping block' model, refining the earlier symmetric trapping block model by Sobolevsky and Yelshansky (2000), which could not fully account for the slow Mg²⁺ unblock observed during depolarisation. In this model, Mg²⁺ binding not only physically occludes the channel but also allosterically stabilises the close state, promoting a faster transition to closure once bound. This results in an asymmetric mechanism: slow Mg²⁺ unblock during depolarisation but rapid re-block upon repolarisation. The model better explains NMDAR behaviour during physiological voltage changes, such as during action potential firing. The interplay of slow unblock and fast re-block is crucial for shaping synaptic responses and dendritic voltage dynamics—slow unblock extends NMDAR activity, while rapid re-block ensure efficient termination of channel conductance. This mechanism underpins the essential roles of NMDARs in synaptic plasticity and dendritic integration.

1.1.2.4.2 Subtype-dependent variation in Mg²⁺ blockade

The kinetics of Mg²⁺ unblock vary among NMDAR subtypes, influencing receptor activation and synaptic plasticity. Qian, Buller and Johnson (2005) and Clarke and Johnson (2006) found that GluN2A- and GluN2B-containing NMDARs exhibit stronger Mg²⁺ inhibition and a pronounced slow unblocking component. Conversely, GluN2C- and GluN2D-containing receptors display weaker Mg²⁺ blockade and lack the slow unblocking phase, allowing them to respond more rapidly to transient depolarisations.

Comparing GluN2A and GluN2B, the slow component is more pronounced in GluN2B-containing receptors, which may favour mechanisms of synaptic weakening (long-term depression), whereas

the faster unblocking of GluN2A may facilitate LTP. The speculative possibility of tri-heteromeric configurations yielding intermediate Mg²⁺ block kinetics remains an unsolved area of research, through difficulty in isolating the tri-heteromeric population (Qian, Buller and Johnson, 2005; Clarke and Johnson, 2006).

Additional studies have explored the molecular basis of subtype-dependent Mg²⁺ blockade using mutagenesis. Retchless, Gao, and Johnson (2012) and Clarke, Glasgow, and Johnson (2013) identified a serine/leucine (S/L) site differentiating GluN2A/B from GluN2C/D in Mg²⁺ sensitivity. Mutating the S632L site in GluN2A and S633L in GluN2B reduced Mg²⁺ inhibition (IC₅₀) and diminished slow unblocking kinetics, resembling GluN2C/D-containing receptors. Conversely, introducing L643S in GluN2C and L657S in GluN2D increased Mg²⁺ sensitivity, mimicking GluN2A/B characteristics (Retchless, Gao and Johnson, 2012; Clarke, Glasgow and Johnson, 2013). These findings highlight how structural determinants influence Mg²⁺ blockade, contributing to functional differences among NMDAR subtypes and their roles in synaptic plasticity.

1.1.2.5 C-terminal domain

The CTD occupies the final portion of each subunit of the NMDAR and is involved in receptor modulation, trafficking, and synaptic localisation via binding to intracellular scaffolding molecules. NMDARs are synthesised and folded within the endoplasmic reticulum (ER). Correctly folded and assembled receptors (GluN1/GluN2) are exported while misfolded or misassembled complexes are retained by molecular chaperones and degraded—a mechanism that is implicated in the pathophysiology of certain *GRIN* gene mutations associated with neurological disorders such as epilepsy (Addis *et al.*, 2017; Phillips, Gomez-Navarro and Miller, 2020).

The GluN1 subunit's CTD contains the di-arginine ER-retention signal, RRR, which follows the ER-retention motif (RXR) (Standley *et al.*, 2000). When expressed alone in heterologous cells, the GluN1-1a subunit cannot form a functional NMDAR and thus does not localise to the membrane or synapse (McIlhinney *et al.*, 1998; Barria and Malinow, 2007). Other isoforms of GluN1 can override this retention signal and escape the ER, enabling surface expression (Ehlers, Tingley and Huganir, 1995; Okabe, Miwa and Okado, 1999). For instance, GluN1-3 contains a PDZ-binding motif (STVV) within its C2' splice cassette, which is proposed to override the retention signal via two potential mechanisms. One possibility is that PDZ proteins mask the RXR motif, while another suggests that PDZ proteins assist in the export of GluN1-3 from the ER (Standley *et al.*, 2000).

When expressed alone, GluN2 subunits do not localise to the plasma membrane (McIlhinney *et al.*, 1998), nor do they form functional homodimers in neurons (Hall and Soderling, 1997). As with GluN1, ER retention of GluN2 subunits is CTD-dependent, though the specific sequence

responsible for this retention remains to be identified. Hawkins et al. (2004) studied the ER retention of GluN2B using a chimera composed of the interleukin receptor-2 and the CTD of GluN2B. They found that multiple sites may be responsible for ER retention and export. One sequence of four amino acids (HLFY; 839-842) just downstream of the M4 transmembrane domain, is crucial for ER export. This sequence is present in both GluN2A and GluN2B but absent in GluN1 (Hawkins *et al.*, 2004). After release from the ER, further processing occurs within the Golgi apparatus before the receptors are transported to the plasma membrane via the trans-Golgi network and endosomes.

NMDARs trafficked to the synapse are clustered and stabilised through interactions with proteins of the postsynaptic density (PSD). The PSD is a specialised structure located near the post-synaptic membrane of the dendritic spines, opposite the presynaptic active zone. It is composed of postsynaptic receptors, scaffolding proteins, cytoskeletal elements, and signalling proteins, ensuring that these components are near vesicular transmitter release from the presynaptic membrane. A major role of the PSD is to localise and stabilise AMPARs and NMDARs at the postsynaptic membrane (Vyas and Montgomery, 2016). Key components of the PSD include proteins from the MAGUK family, such as PSD-95, PSD-93, SAP-97, and SAP102 (Barria and Malinow, 2007). PSD-95 has been extensively studied for its interaction with the GluN2A subunit via its SH3 and PDZ domain engaging with the SH3- and PDZ-binding motifs on the CTD of GluN2A (Cousins, Kenny and Stephenson, 2009; Cousins and Stephenson, 2012).

In addition to interacting with the scaffolding proteins within the PSD, the CTD of GluN2A and GluN2B subunits binds to calcium/calmodulin-dependent protein kinase II (CaMKII), a key regulator of NMDAR activity and a crucial mediator of neuronal plasticity (Lisman, Yasuda and Raghavachari, 2012). Upon NMDAR activation, the resulting increase in intracellular Ca²⁺ level promotes CaMKII binding to the CTD of NMDARs. Once bound, CaMKII can modulate other proteins within the PSD. A key consequence of this interaction is the stimulation of actin filament polymerisation, which enables AMPAR recruitment and insertion into the postsynaptic membrane, thereby strengthening synaptic transmission (Chen *et al.*, 2000; Herring and Nicoll, 2016). Furthermore, CaMKII possesses an auto-phosphorylating property, allowing it to provide long-lasting effects on synaptic strengthening and remodelling—underlying learning and memory formation (Bayer *et al.*, 2001).

1.1.3 Mutations in hGluN2A and association with neurological disorders

Mutations in the human GluN2A subunit of the NMDAR are associated with several neurological and neurodevelopmental disorders, primarily affecting cognition, motor function, and epilepsy susceptibility.

Epilepsy is a common neurological disorder, affecting an estimated 50 million individuals worldwide (WHO, 2024). It is characterised by recurrent seizures caused by abnormal electrical activity in the brain. Seizures can range in severity and type, from brief lapses in awareness to convulsions and loss of consciousness. Epilepsy can be focal, originating in a specific brain region, or generalised, affecting the entire brain. The causes of epilepsy are broadly categorised into familial—accounting for a significant portion of cases—and acquired/symptomatic, typically resulting from conditions such as infection, stroke, or traumatic brain injury (Myers et al., 2019).

Epilepsy presents a wide pathological spectrum, with phenotypes that can vary from seizures and cognitive/behavioural deficits to severe intellectual disability and developmental delay (Berg *et al.*, 2010; Lesca *et al.*, 2019). Recent advances in next-generation sequencing have facilitated the identification of several genes strongly associated with epilepsy phenotypes in patients (Myers et al., 2019). One such gene is *GRIN2A*, where numerous genetic alterations have been linked to epilepsy (Lesca et al., 2012, 2013). Studies have identified both *de novo* and familial *GRIN2A* mutations—including nonsense and missense mutations—in patients with conditions such as with Landau-Kleffner syndrome (LKS), Epileptic Encephalopathy related to Status Epilepticus during slow Sleep (ESES) and Rolandic epilepsy (RE) with verbal dyspraxia (Carvill et al., 2013; Lemke et al., 2013b; Lesca et al., 2013).

Missense mutations in *GRIN2A* result in amino acid substitutions that can have varying functional consequences, generally classified as either gain-of-function (GOF) or loss-of-function (LOF). Several studies have examined the impact of *GRIN2A* missense mutations on the NMDAR. For example, Yuan et al. (2014) and Elmasri et al. (2022) investigated the L812M mutation in a child with intractable infantile-onset epilepsy and profound developmental delay. This GOF mutation was found to reduce the voltage-dependent Mg²⁺ blockade, increase glutamate potency, and elevate channel open probability, thereby enhancing charge transfer (Yuan *et al.*, 2014; Elmasri *et al.*, 2022). Such mutations have significant implications for affected individuals, and to date, no anti-epileptic drug has proven effective in treating *GRIN2A*-associated epilepsy (Strehlow *et al.*, 2016). The studies by Elmasri et al. (2022) and Yuan et al. (2014) are crucial for advancing our understanding of the pathophysiology of *GRIN2A*-associated epilepsy and informing future therapeutic interventions.

1.2 GluN2A-S: A primate-specific NMDA receptor isoform

Recent research from the Vargas-Caballero lab has analysed the expression of GluN2A in human brain tissue, identifying a previously unrecognised isoform termed GluN2A-S. Western blot analysis of fresh-frozen human cortical homogenates revealed two distinct protein bands at approximately 180 kDa (Pegasiou, 2018; Warming et al., 2019). Warming et al. (2019) confirmed that the second band resulted from an alternative isoform of hGluN2A with transcripts corresponding to that observed through genome-wide analysis of open-reading frames (ORFs) of human mRNA libraries (Strausberg et al., 2002; Yang et al., 2011) while also providing confirmation via mass spectrometry analysis that the second band corresponded to GluN2A, identifying 14 unique peptides.

Warming et al. (2019) detected both GRIN2A mRNA transcripts in human and primate brain tissue but not in rodent brain tissue. Additionally, we further confirmed the presence of both GluN2A isoforms in an age-independent manner (Warming *et al.*, 2019).

Compared to the canonical GluN2A-Long (GluN2A-L) isoform, which has a predicted molecular weight of ~165 kDa, GluN2A-S is shorter, with an estimated molecular weight of ~144 kDa (Consortium, 2023). This isoform lacks amino acids 1281-1464 and features a unique C-terminal sequence spanning residues 1259-1281. Consequently, GluN2A-S lacks the ESDV PDZ-binding region at the extreme C-terminal tail and the PSDPYK SH3-binding region located further upstream in the C-terminal domain. These binding motifs allow interactions with the synaptic scaffolding protein postsynaptic density protein 95 (PSD-95), a member of the Membrane-Associated Guanylate Kinase (MAGUK) family responsible for clustering and stabilising NMDARs at the synapse (Cousins, Kenny and Stephenson, 2009; Cousins and Stephenson, 2012) (Figure 1.4).

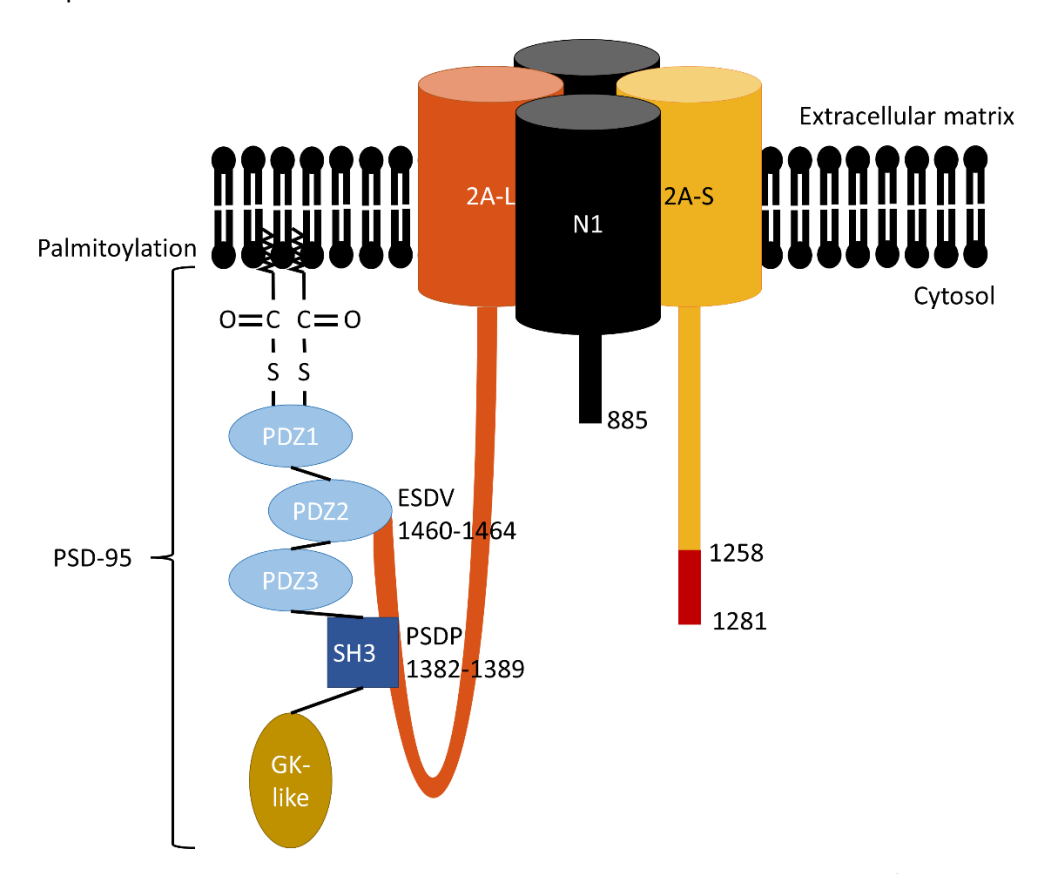


Figure 1.4 – Human GluN2A-S lacks both the C-terminal binding regions for PSD-95.

Human GluN2A-S is lacking both the ESDV PDZ-binding and the PSDPYK SH3-binding regions which bind allow binding of PSD-95 to the C-terminal domain of the canonical human GluN2A.

Additionally, GluN2A-S lacks several serine and tyrosine residues targeted by Src/Fyn kinases and Protein Kinase C (PKC), which modulate NMDAR channel properties, synaptic localisation, and mechanisms of synaptic plasticity (Lussier, Sanz-Clemente and Roche, 2015). The generation of GluN2A-S arises from alternative splicing of GRIN2A pre-mRNA, whereby intra-exon splice recognition sites facilitate the production of two distinct GRIN2A transcripts encoding the two hGluN2A protein isoforms. This chapter will review the mechanisms of pre-mRNA splicing and the current understanding of the GluN2A-S isoform.

GluN2A arises from alternative processing of GRIN2A pre-mRNA – a process known as alternative splicing. This is by recognition of intra-exon splice recognition sites allowing the generation of two distinct GRIN2A transcripts giving rise to two hGluN2A protein isoforms. In this chapter, we will review the mechanisms of pre-mRNA splicing and the current understanding of the GluN2A-S isoform.

1.2.1 Mechanism and regulation of pre-mRNA splicing

RNA and expressed sequence tag (EST) cDNA sequencing estimates that approximately 95% of multiexon genes undergo alternative splicing, a process that generates multiple protein isoforms by incorporating different combinations of exons (Pan et al., 2008). Pre-mRNA splicing occurs cotranscriptionally, as evidenced by early electron microscopy (EM) studies that observed RNA lariat structures—intronic splicing intermediates—while transcripts remained attached to chromatin (Beyer and Osheim, 1988). Further supporting this, Wetterberg et al. (2001) used EM combined with immunolocalisation to identify the U2 small nuclear RNA-protein complex (snRNP)—a key mediator of pre-mRNA splicing—colocalised with RNA polymerase II (Wetterberg et al., 2001).

Splicing follows a sequential phosphodiester transfer process catalysed by the spliceosome—a large ribonucleoprotein complex. This complex consists of more than 100 core proteins and five snRNPs: U1, U2, U4, U5, and U6—which function as trans-acting splicing factors (Zhou *et al.*, 2002; Jurica and Moore, 2003; Nilsen, 2003)

Additionally, splicing requires recognition of cis-regulatory elements, including three core splicing signals. The 5' splice site (donor site) is located at the exon-intron junction and is typically a conserved guanine (G)-uracil (U) dinucleotide, initially recognised by the U1 small nuclear ribonucleoprotein (snRNP). The 3' splice site (acceptor site) is found at the intron-exon junction and is identified by the U2 auxiliary factor (U2AF) due to the presence of a polypyrimidine tract followed by an adenine (A)-G dinucleotide. U2AF then recruits the U2 snRNP to the branch point upstream of the acceptor splice site. This branch point contains a crucial adenine, which facilitates lariat formation during splicing (Figure 1.5A).

Beyond these core splicing signals, pre-mRNA splicing is tightly regulated by splicing regulatory elements (SREs), which include exonic and intronic splicing enhancers or silencers. These elements modulate splice site recognition and spliceosome assembly by recruiting trans-acting splice factors that either promote or inhibit splicing (Wang and Burge, 2008).

Splicing occurs in two catalytic steps. First, the 2' hydroxyl of the branch point attacks the donor splice site, cleaving the phosphodiester bond and forming a 2'-5' phosphodiester bond between the branch point and the 5' terminal nucleotide of the intron. This results in an intron/3' exon lariat and a free 5' exon. In the second step, the newly released 3' hydroxyl of the 5' exon attacks the acceptor splice site, cleaving the phosphodiester bond and ligating the 5' and 3' exons. The final products are the spliced exons and a free intron lariat (Nilsen, 2003) (Figure 1.5A).

Alternative splicing can generate multiple mRNA isoforms through events such as exon skipping, intron retention, and alternative exon usage (Figure 1.5B). In the case of hGRIN2A, there exists

intra-exonic splice junctions at positions p13.2 chr16:9,763,428 and p13.2 chr16:9,763,771. This leads to exon-dependent alternative splicing resulting in both hGluN2A-L and hGluN2A-S isoforms. Exon-dependent splicing causes a 343-nucleotide deletion (exitron) from exon 13, causing a frameshift and premature stop codon (Figure 1.6). Consequently, this truncates 183 amino acids from the CTD and generates a unique 23-amino acid C-terminus (Strausberg *et al.*, 2002; Yang *et al.*, 2011; Herbrechter *et al.*, 2021)

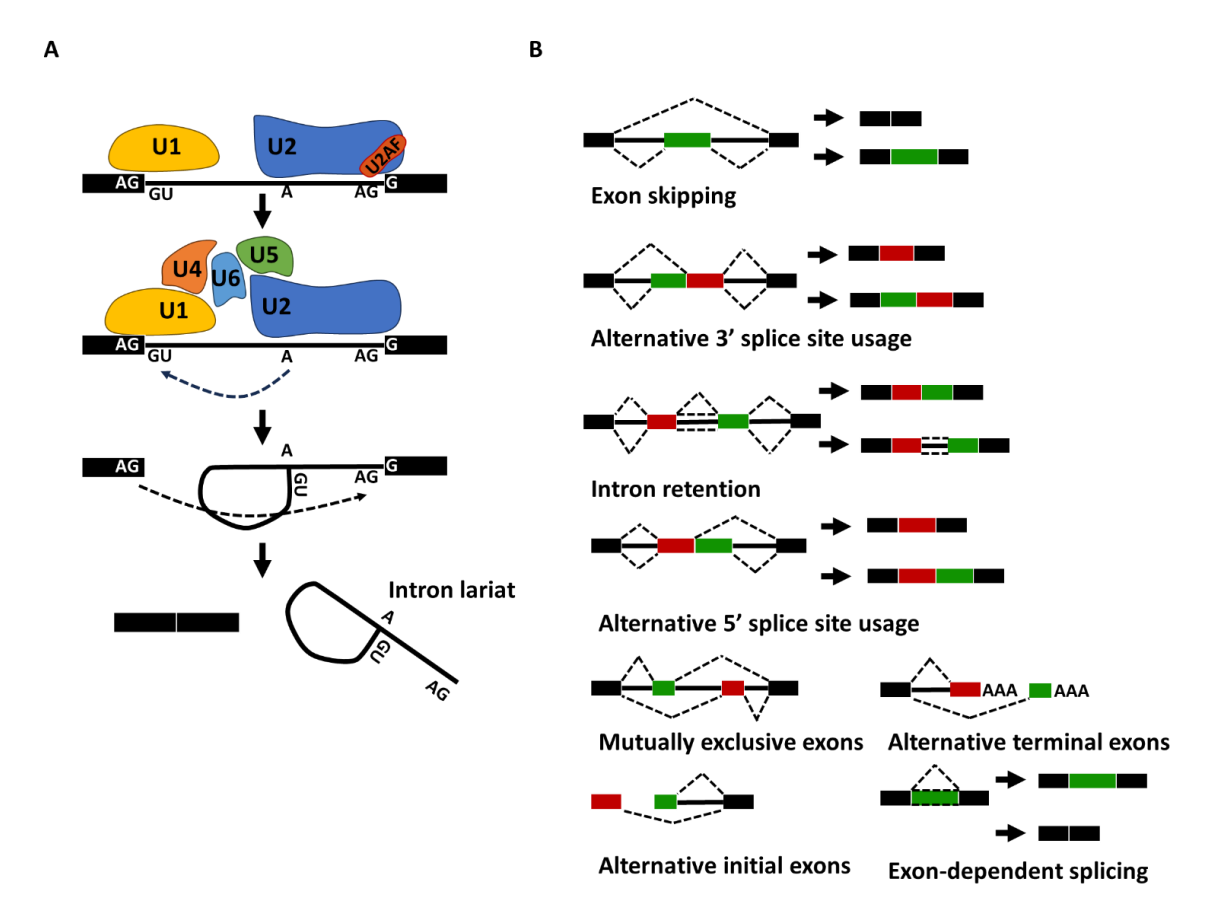


Figure 1.5 - pre-mRNA splicing.

A) Core features of splicing. Spliceosome recognition occurs due to the presence of cis-acting elements at the 5' exon (GU), the branch point (A) and the 3' intron-exon junction (AG). The spliceosome is formed of multiple ribonucleoproteins that mediate intron excision and exon ligation. U1 snRNP recognises the 5' intron boundary and the U2 snRNP recognises the 3' intron boundary and branch point mediated by U2 auxiliary factors (U2AF). Splicing follows a two-step catalytic event where phosphodiester bonds are cleaved at the 5' splice site allowing ligation with the branch point, followed by cleavage of the 3' splice site. This liberates an intron lariat and allows exon-exon ligation. B) Forms of alternative splicing. Due to the recognition of intra-exon splice sites, hGluN2A-S is formed because of exondependent splicing.

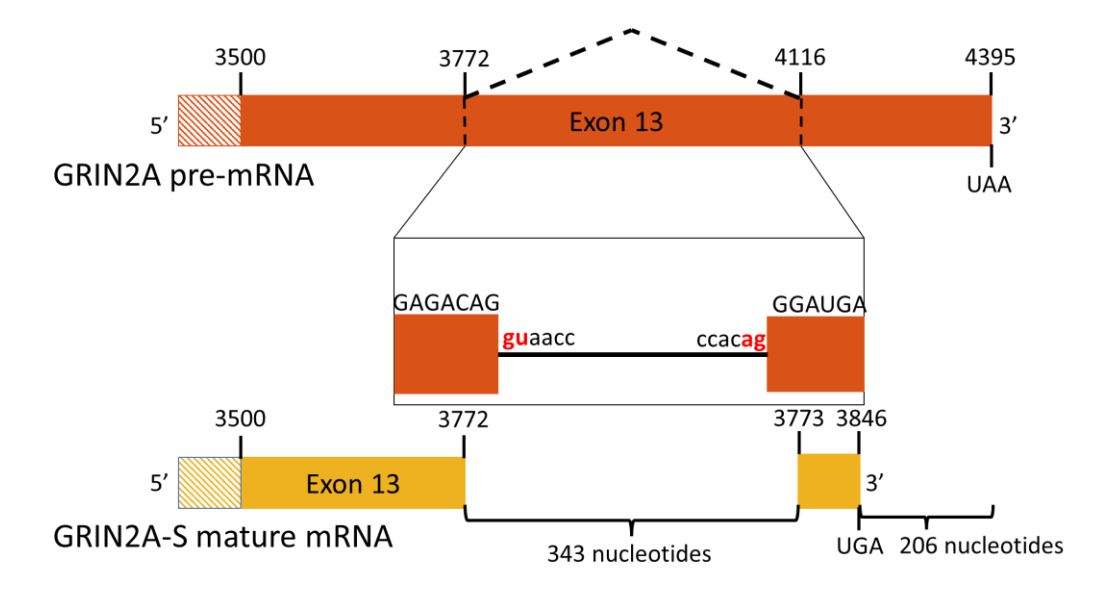


Figure 1.6 - Exon-dependent alternative splicing of human GRIN2A.

Site of alternative splicing of human GRIN2A pre-mRNA. The hGRIN2A transcript contains an intra-exon junction at positions p13.2 chr16:9,763,428 and p13.2 chr16:9,763,771, leading to exon-dependent splicing. Donor and acceptor splice site dinucleotides are displayed in red. Recognition of these sites results in a 343-nucleotide deletion (exitron) from exon 13, leading to a frameshift and premature stop codon.

1.2.2 Two GRIN2A transcripts are expressed in human and primate brain

To investigate the presence of GluN2A-S mRNA transcripts in the human brain, Warming et al. (2019) performed PCR using primer flanking a unique region within the GRIN2A transcript. A ~131 base-pair (bp) amplicon was detected in cDNA extracted from the human brain, consistent with the shorter GRIN2A-S transcript. In contrast, PCR of mouse cDNA yielded a ~474 bp amplicon, indicating the presence of only the longer GRIN2A transcript. Further validation using an additional reverse primer specific to the longer GRIN2A transcript confirmed the presence of both transcripts in the human brain. GRIN2A-S expression was also detected in multiple adult human brains as well as in foetal brain tissue. Consistent with its predicted primate specificity, GRIN2A-S mRNA was also identified in cDNA from the Rhesus macaque brain (Warming *et al.*, 2019) (Figure 1.7).

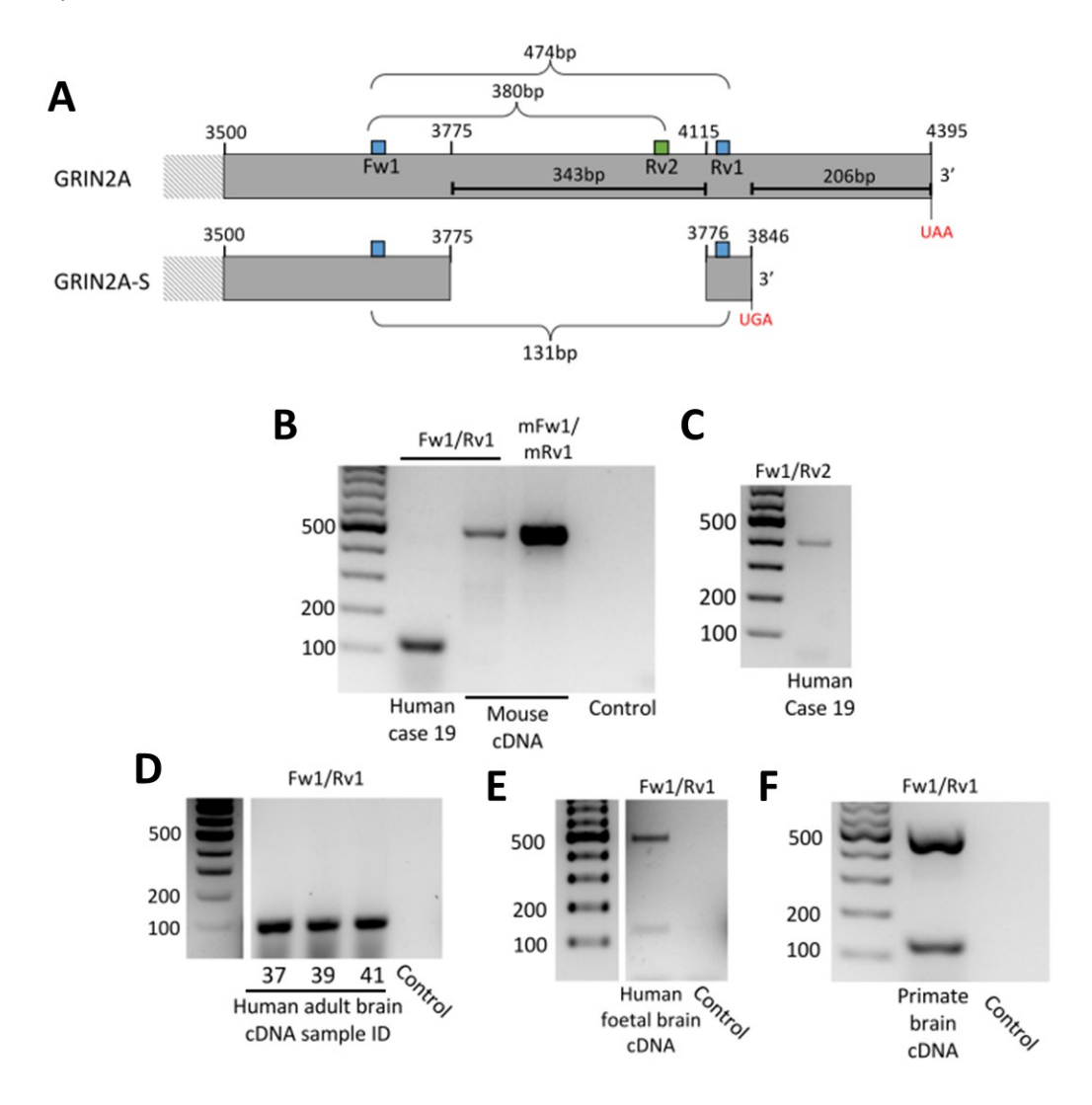


Figure 1.7 - Two GRIN2A mRNA transcript variants in human and primate brain but not mouse brain.

A) Primers were designed to amplify the region of variation between the two isoforms. The Fw1/Rv1 primer pair produced a 474 bp amplicon for GRIN2A and a 131 bp amplicon for GRIN2A-S. A second reverse primer (Rv2) selectively amplified canonical GRIN2A with a 380 bp product. B-F) RT-PCR analysis of transcript variants. Control lanes indicate no-template conditions. B) In human cDNA, only the short isoform (GRIN2A-S) was detected, likely due to preferential amplification, whereas in mouse cDNA—using mouse-specific primers—only the 474 bp GRIN2A amplicon was observed. C) The Fw1/Rv2 primer pair confirmed canonical GRIN2A expression. D) GRIN2A-S was detected in three additional human samples. E) Both transcripts variants were observed in human foetal cDNA. F) GRIN2A-S was also detected in primate (Rhesus) brain cDNA. Figure taken from (Warming et al., 2019).

1.2.3 Translation of the GRIN2A-S transcript into GluN2A-S protein

Warming et al. (2019) investigated whether the GRIN2A-S transcript is translated into protein. Using immunoblot analysis of human brain homogenates with an antibody targeting a conserved epitope shared by both GluN2A-Long (GluN2A-L) and GluN2A-S, they observed two distinct protein bands. In contrast, only a single brand corresponding to the canonical GluN2A protein was detected in mouse brain lysates. To further characterise the lower molecular weight band, human brain protein extracts were subjected to mass spectrometry, which identified 14 unique peptides within GluN2A. Most notably, quantification of immunoreactivity revealed that GluN2A-S accounts for approximately one-third of the total GluN2A protein in the human brain, with this ratio remaining stable across different ages (Figure 1.8). The detection of a second band in fresh tissue supports the existence of the GluN2A-S protein (Warming *et al.*, 2019).

To assess whether GluN2A-S can form functional NMDARs, Warming et al. (2019) co-transfected Human Embryonic Kidney (HEK293) cells with recombinant GluN1 and GluN2A-S subunits. A ramp stimulus was applied by voltage clamping the cell from -70 to +50 mV during local perfusion with 40 μ M NMDA and 10 μ M glycine. This allowed us to record the current-voltage (I-V) relationship of GluN2A-S-containing receptors. We observed an I-V relationship with the characteristic J-shape—due to voltage-dependent Mg²+ blockade of NMDARs—with a reversal potential around 0 mV (Figure 1.8). This therefore confirmed that GluN2A-S can assemble with GluN1 to form functional NMDARs capable of trafficking to the plasma membrane in HEK293 cells 1.1.2.4(Warming et al., 2019).

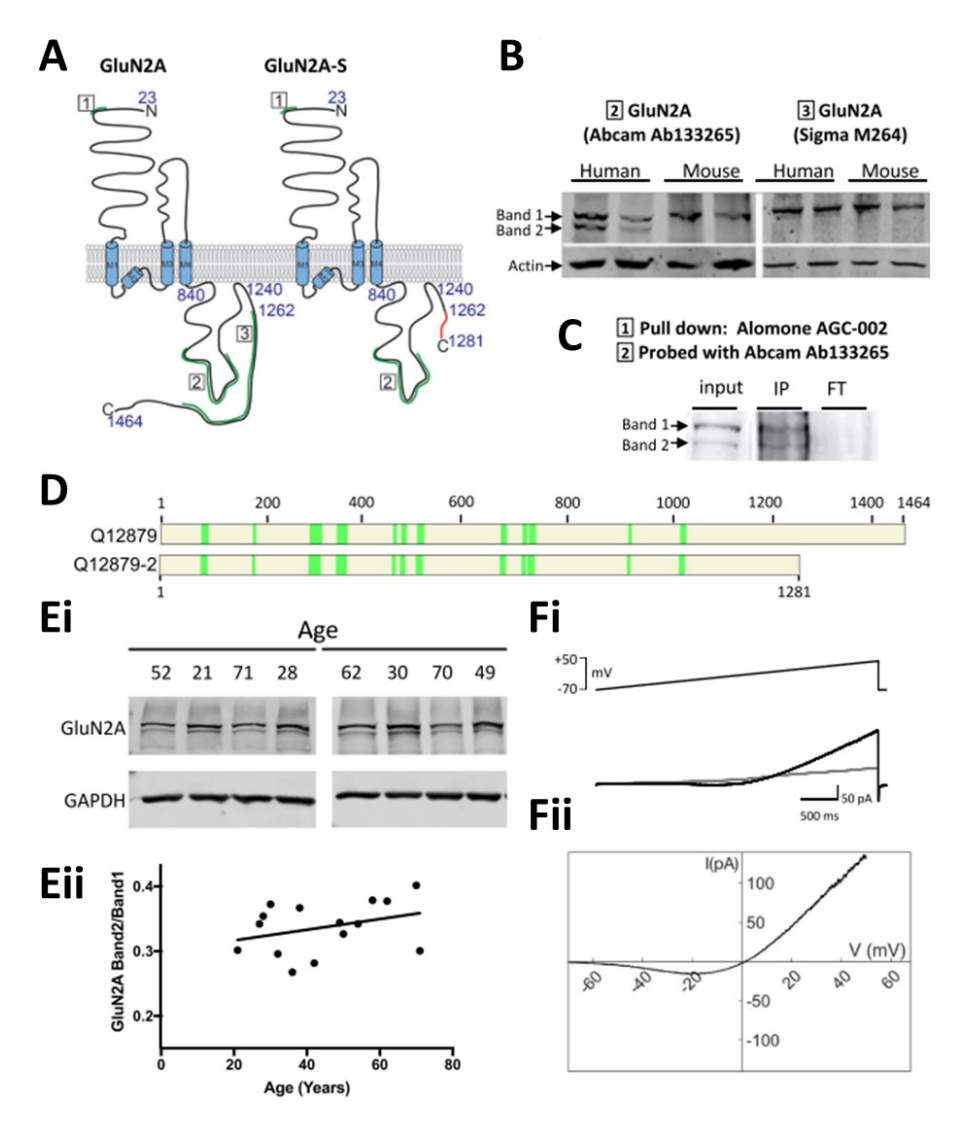


Figure 1.8 - Two GluN2A isoforms are present in the human brain but not the mouse brain.

A) Predicted topology of human GluN2A-S NMDAR subunit based on mRNA sequence data. Alternative splicing results in the truncation of 183 amino acids and the inclusion of a unique 23-amino-acid region within the C-terminal domain (red). Epitopes form the antibodies used are shown in green and numbered. B) Immunoblots using specific antibodies against canonical GluN2A and the putative GluN2A-S protein in human and mouse cortical lysates. C) GluN2A proteins were immunoprecipitated using an N-terminal antibody. Band 2 was excised from a Coomassie-stained polyacrylamide gel and analysed by mass spectrometry. IP, immunoprecipitate; FT, flowthrough. Ei) Immunoblot of homogenised fresh-frozen human cortical tissue probed with the GluN2A antibody Abcam 133265. Eii) Quantification of GluN2A-S/GluN2A immunoreactivity. F) Recombinant GluN2A-S coexpressed with GluN1 in HEK293T cells forms functional NMDA receptors, as indicated by a characteristic J-shaped current-voltage relationship in response to 40

 μ M NMDA during a slow voltage ramp (-70 to + 50 mV, 3 s). Figure taken from (Warming *et al.*, 2019).

1.3 Hypothesis and Aims

The aims of this project are:

- To generate a gene expression construct to investigate the function of human GluN2A-L and GluN2A-S in isolation.
- To investigate whether human GluN2A-L and GluN2A-S contribute different functional properties to NMDA receptors.
- To examine the isoform-specific effect of epilepsy-associated GRIN2A missense mutations on NMDAR function

Chapter 2 Methods

In this thesis, we employed site-directed mutagenesis to modify expression vectors for human and rat GluN2A NMDAR subunits. Plasmid expression was assessed using end-point polymerase chain reaction (PCR) and immunoblotting. To investigate NMDAR function in transfected HEK293 cells, we performed patch-clamp electrophysiological recordings or bioluminescence-based Ca²⁺ assay for higher throughput screening. This chapter details the materials and methods used to examine the function of the two isoforms of the human GluN2A subunit.

2.1 Materials

2.1.1 Oligonucleotides

Oligonucleotides were sourced from Eurofins at $0.01\mu mol$ synthesis scale and were delivered lyophilised. Oligonucleotides were resuspended in $18.2M\Omega$ water to the desired concentration.

2.1.1.1 Oligonucleotides for site-directed mutagenesis

Table 2.1 List of oligonucleotides used for site-directed mutagenesis PCR.

Name	Sequence (5'-3')	T _a (°C)
Q5SDM_HumanGRIN2A- A4114G_F	CCACTCCCACGGGGATGACCA	68
Q5SDM_HumanGRIN2A- A4114G_R	AGGAAAGGGTTATCGGAGGTG	
Q5SDM_RatGrin2A-G4114A_F	CCACACGTATAGGGATGACCAAC	62
Q5SDM_RatGrin2A-G4114A_R	AGGAAAGGATTATCGGAGG	
Q5SDM_HumanGRIN2A- C2434A_F	GAGCAGCCAGATGGACATTGA	65
Q5SDM_ HumanGRIN2A- C2434A_R	ATCACCTCGTTCTTCTCGTTG	-0

2.1.1.2 Oligonucleotides for sequencing

Table 2.2 List of oligonucleotides used for sequencing.

Name	Sequence (5'-3')
CMVfor (eurofins)	CGCAAATGGGCGTAGGCGTG
Seq_Primer_Fwd_A	ATGGGCAGAGTGGGCTATTGGAC
Seq_Primer_Rev_B	CTTGTGCCCCAGGATGTTGC
Seq_Primer_Fwd_C	CTGAGCAAAGACCCCAACGAGAAG
Seq_Primer_Fwd_D	GCTCTACTGTTCCAAAGACGAGG
Seq_Primer_Fwd_E	GATATTCTGAAGAAGCTTTCCAGAACTGTG
Seq_Primer_Fwd_F	CGGAATAACTATCCCTACATGCATCAG
Seq_Primer_Fwd_G	GTTCCCTCATCATGGACATGGTTTCAG
Seq_Primer_Fwd_H	GGACTCCACGCTGCCAATGAAC
Seq_Primer_Fwd_I	GCGGTGAATGACAGCTATCTTCG
RatGrin2A_SeqPrimer_Fwd_A	ATGGGCAGATTGGGCTACTGGAC
RatGrin2A_SeqPrimer_Fwd_D	GCTCTACTGCTCCAAAGACGAGG
RatGrin2A_SeqPrimer_Fwd_E	GACATCCTCAAGAAGCTGTCCAGAACTGTG
RatGrin2A_SeqPrimer_Fwd_F	GGGACGGTACCCAATGGAAGTAC
RatGrin2A_SeqPrimer_Fwd_G	GAGCTACTGACTTCATTCAAAGAGGGTCAC
RatGrin2A_SeqPrimer_Fwd_H	GGACTCCACACTGCCCATGAAC
RatGrin2A_SeqPrimer_Fwd_I	CCAAGGTCTGGAGGACAGCAAGAG

2.1.1.3 Oligonucleotides for PCR

Table 2.3 List of oligonucleotides used as primers for end-point PCR.

Name	Sequence (5'-3')	Amplicon length (kb)	T _a (°C)	
GRIN2A Human F	ATTCAGGCCACTTCACCATGAG	0 474/0 121	64.3	
GRIN2A Human R1	ATCTCCCAATAACCAAGCGTTG	0.474/0.131	04.5	
GRIN2A Human R2	CTTGCTGTCCTCCAGACCTTGG	0.386	64.3	

Name	Sequence (5'-3')	Amplicon length (kb)	T _a (°C)
GRIN2A Rat F	ACTCAGGCCACTTTACCATGAG	0.474	
GRIN2A Rat R	ATCTCCCGATAACTAAGCGTTGGTC		
GAPDH Human F	TGAACGGGAAGCTCACTGG	0.207	(2.2
GAPDH Human R	TCCACCACCCTGTTGCTGTA	0.307	62.3

2.1.2 DNA plasmids

Table 2.4 List of plasmid DNA constructs used.

Name	Backbone	Product	Resistance	Source
eYFP-Rat Grin1-1a	pcDNA3.1(+)	N-terminally eYFP-tagged rat GluN1-1a	Ampicillin (100μg/μL)	Addgene 17928
Human GRIN1-4a	pcDNA3.1(+)	N-terminally FLAG-tagged human GluN1-4a	Ampicillin (100μg/μL)	GenScript
eGFP-Human GRIN2A	pcDNA3.1(+)	N-terminally eGFP-tagged human GluN2A	Ampicillin (100μg/μL)	GenScript
eGFP-Human GRIN2A-A4114G	pcDNA3.1(+)	N-terminally eGFP-tagged human GluN2A- R1372G	Ampicillin (100μg/μL)	Site-directed mutagenesis
eGFP-Human GRIN2A-C2434A, A4114G	pcDNA3.1(+)	N-terminally eGFP-tagged human GluN2A- L812M, R1372G	Ampicillin (100μg/μL)	Site-directed mutagenesis
Human GRIN2A	pcDNA3.1(+)	Human GluN2A	Ampicillin (100μg/μL)	GenScript
eGFP-Human GRIN2A-S	pcDNA3.1(+)	N-terminally eGFP-tagged human GluN2A-S	Ampicillin (100μg/μL)	GenScript
eGFP-Human GRIN2A-S-C2434A	pcDNA3.1(+)	N-terminally eGFP-tagged human GluN2A-S- L812M	Ampicillin (100μg/μL)	Site-directed mutagenesis
Human GRIN2A-S	pcDNA3.1(+)	Human GluN2A-S	Ampicillin (100μg/μL)	GenScript
mCherry-Human GRIN2A-S	pcDNA3.1(+)	N-terminally mCherry-tagged human GluN2A-S	Ampicillin (100μg/μL)	GenScript

Name	Backbone	Product	Resistance	Source
mCherry-Human GRIN2A-S-G692A	pcDNA3.1(+)	N-terminally mCherry-tagged human GluN2A-S- C231Y	Ampicillin (100μg/μL)	GenScript
mCherry-Human GRIN2A-S-T1306C	pcDNA3.1(+)	N-terminally mCherry-tagged human GluN2A-S- C436R	Ampicillin (100μg/μL)	GenScript
mCherry-Human GRIN2A-S- G1447A	pcDNA3.1(+)	N-terminally mCherry-tagged human GluN2A-S- G483R	Ampicillin (100μg/μL)	GenScript
Human GRIN2A-S	pDONR223	Human GluN2A-S	Spectinomycin(10 0μg/μL)	Broad Institute
eGFP-Rat Grin2A	pCl	N-terminally eGFP-tagged rat GluN2A	Ampicillin (100μg/μL)	Addgene 45445
eGFP-Rat Grin2A- G4114A	pCl	N-terminally eGFP-tagged rat GluN2A-G1372R	Ampicillin (100μg/μL)	Site-directed mutagenesis
eGFP	pEGFP-N1	Green Fluorescent	Kanamycin (50μg/μL)	Addgene 6085-1
RFP	mRFP1-N1	Red Fluorescent	Kanamycin (50μg/μL)	Addgene 54635

2.1.3 Antibodies

Table 2.5 List of antibodies and their respective dilutions

	Name	Company and Cat No.	Species	Dilution
1°	GluN2A	Abcam, ab133265	Rabbit	1:1000
	α-tubulin	Merck, T9028	Mouse	1:1000
2°	Rabbit 680nm	LI-COR, 926-68021	Goat	1:10000
_	Mouse 800nm	LI-COR, 926-32210	Goat	1:10000

2.1.4 Buffers and Solutions

2.1.4.1 Molecular biology

LB agar

For 1L;

- 37g Luria Agar (3.7% (w/v), Cat# L24022):
 - 10g/L Casein Digest Peptone
 - 5g/L Yeast Extract
 - o 10g/L NaCl
 - o 12g/L Agar
- Supplement with 1mL antibiotic (100μg/mL Ampicillin, 100μg/mL Spectinomycin or 50ug/mL Kanamycin) before pouring.

LB media

For 1L;

- 20g LB broth (2% (w/v) LB broth Cat# L24066):
 - o 10g/L Casein Digest Peptone
 - o 5g/L NaCl
 - 5g/L Yeast Extract
- ddH₂O to 1L
- Supplement with 1mL antibiotic (100μg/mL Ampicillin, 100μg/mL Spectinomycin or 50ug/mL Kanamycin) before use.

SOC (Outgrowth) Media (Invitrogen, Cat# 15544034)

- 2% (w/v) Tryptone
- 0.5% (w/v) Yeast Extract
- 10mM NaCl
- 2.5mM KCl
- 10mM MgCl₂
- 10mM MgSO₄
- 20mM glucose

50X TAE electrophoresis buffer

For 500mL;

- 121g Tris base
- 28.55mL acetic acid
- 18.6g EDTA sodium salt
- ddH₂O up to 500mL

1X PBS

For 100mL;

- 1 PBS tablet (Cat# P32080):
 - o 137mM NaCl
 - o 2.7mM KCl
 - o 11.9mM phosphate buffer
- ddH₂O up to 100mL

DEPC-treated water

For 1L;

- 1mL Diethyl pyrocarbonate (DEPC; Cat#D5758)
- 999mL ddH₂O
- Incubated overnight followed by autoclaving to decompose DEPC

DEPC-treated 70% ethanol

For 1L;

- 300mL 100% ethanol
- 700mL DEPC-treated water

2.1.4.2 Protein analysis

5X Sample Buffer

- 350mM Tris (HCl) pH 6.8
- 30% (v/v) glycerol
- 10% (w/v) Sodium dodecyl sulfate (SDS)
- 600mM DL-Dithiothreitol (DTT)
- 0.012% (w/v) Bromophenol Blue (BPB)

SDS-PAGE Gels

Table 2.6 Recipe for SDS-PAGE separating gel (1x1.0mm; 7%)

Component	Vol (μL)
4X ProtoGel Resolving buffer (National Diagnostics, Cat# EC-892)	2500
Acrylamide 30% solution (Cat# A3449)	2330
10% (w/v) ammonium persulphate (APS) (Cat #A3678)	100
Tetramethylethylenediamine (TEMED) (Cat# 17919)	10
ddH₂O	5060

Table 2.7 Recipe for SDS-PAGE stacking gel (1x1.0mm; 4%)

Component	Vol (μL)
4X Stacking buffer (Thermo, Cat# J63450.K2)	1250
Acrylamide 30% solution	650
10% (w/v) APS	50
TEMED	5
ddH₂O	3050

5x SDS-PAGE loading buffer

- 350mM Tris (HCl) pH 6.8
- 30% (v/v) Glycerol
- 10% (w/v) SDS
- 600mM DTT
- 0.012% (v/v) Bromophenol blue

10X Laemmli buffer

For 1L;

- 144g Glycine
- 30.3g Tris base
- 10g SDS
- ddH₂O up to 1L

10X Tris Glycine buffer

For 1L;

- 29g Glycine (386mM)
- 58g Tris Base (479mM)
- ddH₂O up to 1L

Transfer buffer

For 1L;

- 100mL 10X Tris Glycine buffer
- 200mL Methanol
- 700mL ddH₂O

TBS-T

For 1L;

- 100mL 10X TBS (Bio-rad, Cat #1706435)
- 900mL ddH₂O
- 1mL Tween-20 (Agros Organics, Cat #WZ-88248-22) (0.1% v/v).

2.2 Bioinformatics

Sequence alignment was performed using MAFFT v7 local pairwise alignment (Katoh and Standley, 2013). Analysis of annotated human genomic transcripts was performed using the UCSC Genome Browser. Human (GRCh38/hg38) was displayed and GENCODE V47, NCBI RefSeq and CCDS tracks were selected (Frankish *et al.*, 2023).

2.3 Cell Culture Methods

2.3.1 Human Embryonic Kidney cell line maintenance

For this study, two derivatives of the original Human Embryonic Kidney parent cell line were used: HEK293T (ATCC; Cat# CRL-3216) expressing the SV40 large T antigen and HEK293G5A (kindly provided by Luis A. Yanez-Guerra) that stably express the chimeric GFP-Aequorin protein G5A (Cat# cAP-0200GFP-AEQ-Cyto). HEK cells were maintained in either T25, T75 culture flasks or 100mm cell culture dishes in high glucose, pyruvate, Dulbecco's Modified Eagle Medium (DMEM) (Gibco, Cat#41966-029) supplemented with 10% (v/v) foetal bovine serum (FBS) (Gibco,

Cat#10270-106). When the confluency reached 80-90%, the media was removed and the cells were washed once with 5mL prewarmed (37°C) 1X Dulbecco's Phosphate Buffered Saline (DPBS) (Gibco, Cat#14190-094). 1mL of prewarmed 1X 0.25% Trypsin-EDTA (Gibco, Cat#25200-056) was added and cells were incubated at 37°C for 2 minutes. Trypsin-EDTA was inactivated by the addition of 9 mL of fresh DMEM with 10% FBS. Detached cells were resuspended and then diluted into fresh DMEM with 10% FBS and 1% (v/v) PenStrep (Cat# 15140-122) in a T75/100mm dish at a ratio of either 1:5 or 1:10 (cells: media) before being incubated at 37°C and 5% CO₂. Media for HEK293G5A was additionally supplemented with 8μg/mL puromycin (Cat# P4512) to maintain GFP-Aequorin expression.

During plating, detached cells were passed through a $40\mu m$ cell strainer and counted for density following resuspension during passage using a haemocytometer. Cells were then plated according to experimental design (see Table 2.8). For some experiments, cells were plated on 13mm (Cat# NPC13/13) circular glass coverslips. Coverslips were first prepared by washing in 1M HCl for 1 hour followed by 5 washes with ddH₂O. They were then washed in 1M NaOH, followed by 5 washes with ddH₂O. They were then washed with 70% ethanol overnight before being coated with 0.1mg/mL PolyDLysine (PDL, Cat# P7886) at 37°C overnight. The PDL was then removed, and coverslips underwent 3 washes with ddH₂O before being air-dried and stored at -20°C until use.

Table 2.8 HEK293T cell experimental layout

Experiment	Number of cells plated per well/dish	Culture dish	Coverslip size (mm)	The volume of media (mL)
PCR and western blot	500'000	6 well plate	n/a	1
Electrophysiology	60'000	35mm dish	13	1
Bioluminescence	28'000	96 well plate	n/a	0.1

2.3.2 Human Embryonic Kidney Cell Transfection

At least 3 hours after plating, cells were transfected using polyethyleneimine (PEI 25K™, Polysciences, Cat# 23966-1). Plasmid DNA (see Table 2.9) was diluted in opti-MEM (Gibco Cat# 11058-021) and mixed by gentle flicking of the tube. Following this, PEI 25K™ (3:1 PEI: DNA; see Table 2.9) was added to the DNA-optiMEM mixture, mixed by gentle flicking of the tube, and incubated for 10-15 minutes at room temperature. The DNA-PEI-optiMEM mixture was collected at the bottom of the tube by pulse centrifugation and added dropwise to the plated cells. The plate was then returned to 37°C and 5% CO₂. For PCR, western blot, and electrophysiology

experiments, the media was changed after 3 hours for 2mL fresh DMEM with 10% FBS. For bioluminescence assay experiments, the media was removed and replaced with DNA-PEI-optiMEM mixture added to optiMEM supplemented with 5% (v/v) FBS and not subjected to a media change.

For electrophysiology or bioluminescence assay, the post-transfection media was supplemented with 200 μ M APV. For the study of GluN2 subunits containing the L812M missense mutation, the media was supplemented with 300 μ M APV and 3 mM MgCl₂ to counteract enhanced cytotoxicity. Cells were allowed to express for 48h-72h before experimental manipulation.

Table 2.9 HEK293T cell transfection parameters

Experiment	Number of plasmids	Total pDNA (μg)	Amount of PEI (μg)	Volume of optiMEM
PCR and western blot	1	1	3	100
Electrophysiology	2	1.5	4.5	100
Bioluminescence	1	0.06	0.35	120
	2	0.12	0.35	120
	3	0.18	0.35	120

2.3.3 Patch clamp electrophysiology

Data sampling for electrophysiology is at 20 kHz. Thick-walled glass capillaries (World Precision Instruments, Cat# 1B150F-4) were pulled using a Sutter instrument P-97 Flaming/Brown type micropipette puller to achieve a tip of approximately 1 μ m and resistance of 5-8 M Ω (Table 2.10). Pipettes were placed on a silver chloride electrode after being filled with a caesium-based intracellular solution containing, in mM, 70 gluconic acid, 10 CsCl, 5 NaCl, 10 BAPTA, 10 HEPES, 10 QX-314, 0.3 GTP, 4 Mg-ATP and pH balanced to 7.3 using CsOH. The osmolarity was measured at approx. 270mOsm using a Löser Micro-Digital Osmometer Type 15. HEK293T cells on 13mm circular glass coverslips were placed in a microscope-associated bath perfused with a HEPES-based extracellular solution containing, in mM, 140 NaCl, 2 CaCl $_2$, 10 glucose, 2 MgSO $_4$, 3 KCl, 0.1mM glycine, 10mM HEPES and pH balanced to 7.4 using 1M NaOH. For the low magnesium electrophysiological recordings, the extracellular solution contained 0.1 mM MgSO $_4$. Cells were perfused at a rate of 2.5mL/min and bath temperature was maintained at 20±2°C by a Warner Electric TC-324B Single Channel Automatic Heater Controller and SH27B inline heater.

Table 2.10 Recording pipette puller settings.

Line	Heat	Pull	Velocity	Time
1	Ramp	0	26	250
2	Ramp	0	50	250
3	Ramp – 11	0	40	250
4	Ramp – 11	0	40	250

Cells were visualised using an upright DIC microscope (Zeiss AxioSkop) on a vibration table with a Faraday cage. A monitor connected to a monochromatic camera allowed visualisation of the cells during the patch-clamp procedure. Cells were visualised using a 40X water immersion objective and a micromanipulator used to control the recording micropipette. Exogenously expressing cells were identified using a CoolLED pE-300 lite white light LED illumination system and fluorescence filters for 488nm/507nm excitation/emission of GFP-tagged proteins. Cells were whole-cell patchclamped in voltage-clamp mode and electrophysiological recordings were subjected to a low-pass filter at 5 kHz using an Axopatch 700B amplifier controlled via Axon MultiClamp Commander software and acquired at 20 kHz using a National Instruments board analogue to digital converter. Data was displayed and recorded on MATLAB (The MathWorks) using custom software (Ginj2, Hugh P.C. Robinson). Recording with holding currents beyond -200 pA was excluded. The series resistance was monitored but not compensated for electronically during voltage-clamp measurements. The resting membrane potential upon achieving a whole-cell patch clamp was recorded manually in bridge mode displayed by Axon MultiClamp Commander software. A liquid junction potential of approximately -12mV was measured and corrected for during data analysis. For all electrophysiological recordings, data were collected from several independent HEK cell cultures.

2.3.4 Iontophoresis

Iontophoresis pipettes were pulled to achieve a tip with resistance of 25-35 M Ω (Table 2.11) Pipettes were placed on a silver chloride electrode after being filled with a solution containing 150mM NMDA, 100 μ M Alexa Fluor 488 Hydrazide (Cat# A10436) or Lucifer Yellow (Sigma, Cat# L0259) and 30mM NaOH to adjust the pH to ~7.0. A current of 10nA was applied using an MVCS-C-02C micro-iontophoresis amplifier to prevent leakage of the NMDA from the iontophoresis pipette. Electrode stray capacitance was compensated using a Tektronix TDS 210 two-channel digital real-time oscilloscope. For rapid local application of NMDA onto cells, an eject current of -60nA was applied causing repulsion of the NMDA from the pipette tip. During local application of

NMDA, a custom voltage ramp stimulus was applied where the cell was voltage-clamped in increments from -80mV to +50mV over 3.7 seconds.

Table 2.11 Iontophoresis pipette puller settings.

Line	Heat	Pull	Velocity	Time
1	Ramp	45	73	200

2.3.5 Bioluminescence assay

Media from HEK293G5A cells were removed and the cells gently washed with a magnesium-free HEPES-based extracellular solution containing, in mM, 140 NaCl, 2 CaCl₂, 10 glucose, 3 KCl, 0.1mM glycine, 10mM HEPES and pH balanced to 7.4 using 1M NaOH. A solution of the magnesium-free HEPES-based extracellular solution with 3mM Coelenterazine h (Cat# BT10110-2) was then added to the cells and the 96 well plate was incubated at 37°C wrapped in aluminium foil to protect it from light for 2 hours.

A reagent plate was made using glutamate diluted in a magnesium-free HEPES-based extracellular solution. For dose-response curves, glutamate was diluted at the following concentrations, in μ M: 0.1, 0.5, 1, 5, 10, 50, 100, 500 and 1000. A glutamate-free condition was included as a negative control. A condition containing 1mM ATP was included as a positive control activating endogenous P2Y1 and P2Y2 purinoceptors. Experiments following the dose-response pilot experiment were performed using 50 μ M glutamate.

After 2 hours, bioluminescence via calcium influx in response to agonist exposure was measured using a FlexStation 3 Multi-Mode Microplate Reader. Bioluminescence was measured in relative luminescence units (RLU) which represents a relative measure of light intensity produced by the reaction of calcium-bound aequorin and coelenterazine h substrate. The RLU are proportional to the amount of calcium binding to aequorin and therefore provide an indication of intracellular increases in calcium concentration; in this case via glutamate-induced NMDAR activation.

The results were exported as a definite integral which represents a cumulative value reflecting the total calcium response over the 76 second recording time. This data was then subtracted from the bioluminescence readings from cells transfected with RFP. Assays were performed across 2-3 plates and contained 16-64 well repeats for each condition.

2.4 Molecular Biology Techniques

2.4.1 Bacterial plasmid DNA transformation

Bacterial transformation was performed in proximity to a Bunsen burner to generate a sterile heat updraft. Solid agar was melted using a microwave and supplemented with 0.1% (v/v) 100 mg/ml ampicillin, 100 mg/mL spectinomycin or 50 mg/ml kanamycin to a final concentration of 100\mug/ml or 50\mug/ml respectively depending on the plasmid being transformed. The agar was poured into 100 mm dishes and allowed to cool. Plates were then pre-warmed to 37°C .

DH5 α competent cells (Invitrogen, Cat# 18265017), stored at -80°C were thawed on wet ice for 15 mins. 10ng of plasmid DNA was added to 50 μ L component cells, mixed by gently flicking the tube and incubated on wet ice for 30 minutes. Cells were then heat shocked at 42°C in a water bath for 20 seconds before returning to ice for 2 minutes. Cells were then recovered in 250 μ L prewarmed S.O.C. medium (Invitrogen, Cat#15544034) and incubated at 37°C with vigorous shaking (225rpm) for 60 minutes. 200 μ L was then spread onto the prewarmed agar antibiotic selection plates until soaked in and incubated at 37°C overnight.

Following site-directed mutagenesis (chapter 2.4.9) transformation of resultant plasmid DNA was performed using NEB 5-alpha competent $E.\ coli$ (High Efficiency) (Cat# C2987H) stored at -80°C. Competent cells were thawed on wet ice for 15 mins before $5\mu L$ of KLD-treated sample was added and mixed by gentle flicking of the tube. Cells were incubated on ice for 30 minutes before being heat shocked at 42°C for 30 seconds in a water bath. Cells were returned to ice for 5 mins followed by recovery in $150\mu L$ of prewarmed S.O.C. medium and incubation at $37^{\circ}C$ with vigorous shaking (225rpm) for 60 mins. $100\mu L$ was spread onto prewarmed agar antibiotic selection plates until soaked in and incubated at $37^{\circ}C$ overnight.

2.4.2 Plasmid DNA Mini-Prep

Single colonies from selection plates were picked using sterile pipette tips and cultured in 5mL LB media—supplemented with appropriate selective antibiotic—overnight at 37°C with vigorous shaking (225rpm). For preparation of plasmid DNA using mini-prep, bacteria were harvested by centrifugation at 6800xg for 2 mins at RT and LB media was subsequently removed. Either the Qiagen Plasmid Mini Kit (Cat#10023) or GeneJET Plasmid Miniprep Kit (Cat#K0502) was used, following the manufacturer's protocol:

Using the Qiagen Plasmid Mini Kit, cell pellets were re-suspended in 0.3mL buffer P1 (RNase A and LyseBlue). 0.3mL buffer P2 (SDS detergent) was added and mixed thoroughly before being

incubated at room temperature for 5 mins. Upon the addition of buffer P2, the solution should turn blue before reverting to colourless upon the addition of pre-chilled 0.3 mL buffer P3 (neutralisation). The solution was mixed thoroughly and incubated on ice for 5 minutes. The supernatant following centrifugation at 16'000 xg for 10 mins, was added to a QBT buffer-equilibrated Qiagen-tip filter. The DNA bound to the silica membrane was washed twice with QC buffer before being eluted using 0.8 mL buffer QF. The DNA was then precipitated using 0.56 mL room temperature isopropanol, mixed and centrifuged at 16,000 xg for 30 mins. The supernatant was removed, and the pellet was washed with 1 mL 70% ethanol and centrifuged at 16'000 xg for 10 mins. The supernatant was removed, and the pellet was air-dried for 10 mins before being resuspended in $30 \mu L$ ddH₂O.

Using the GeneJET Plasmid Miniprep Kit, cell pellets were re-suspended in 0.25mL of resuspension solution (RNase A). 0.25mL of lysis solution was added and mixed thoroughly before being incubated at room temperature for 5 mins. 0.35mL of neutralisation solution was added and mixed thoroughly before centrifugation at 16'000xg for 5 mins to pellet cell debris and chromosomal DNA. The supernatant was added to a GeneJET spin column and centrifuged at 16'000xg for 1 min. The DNA bound to the silica membrane was washed twice using 0.5mL of wash solution with 16'000xg 1 min centrifugations before being eluted with 0.05mL elution buffer and incubated at RT for 2 mins before being spun at 16'000xg for 2 mins. Yield and purity were determined by spectrophotometric measurement using the Nanodrop as outlined in 2.4.6.

Purified plasmid DNA was sent for sequencing with Eurofins Genomics to confirm the correct plasmid has been amplified and single plasmid purity, as outlined in chapter 2.4.10.

2.4.3 Plasmid DNA Maxi-Prep

Single colonies from selection plates were picked using sterile pipette tips and cultured in 5mL LB media—supplemented with appropriate selective antibiotic—overnight at 37°C with vigorous shaking (225rpm). For the preparation of plasmid DNA using maxi-prep, the 5mL LB starter culture was added to 200-250mL of LB media—supplemented with appropriate selective antibiotic—overnight at 37°C with vigorous shaking (225rpm). Bacteria were harvested by centrifugation at 5000xg for 10 mins at 4°C and LB media was removed. Either the Qiagen Plasmid Maxi Kit (Cat#12162) or GeneJET Plasmid Maxiprep Kit (Cat#K0492) was used, following the manufacturer's protocol:

Using the Qiagen Plasmid Maxi Kit, cell pellets were re-suspended in 10mL buffer P1 (RNase A and LyseBlue). 10mL buffer P2 (SDS detergent) was added and mixed thoroughly before being incubated at room temperature for 5 mins. Upon the addition of buffer P2, the solution should

turn blue before reverting to colourless upon the addition of pre-chilled 10mL buffer P3 (neutralisation). The solution was mixed thoroughly and incubated on ice for 5 minutes. The solution was centrifuged at 20'000xg for 30 mins at 4°C. The supernatant was transferred into a fresh tube and 20,000xg for 15 mins at 4°C. The supernatant was then added to a QBT buffer-equilibrated Qiagen-tip filter. The DNA bound to the silica membrane was washed twice with 60mL QC buffer before being eluted using 15mL buffer QF. The DNA was then precipitated using 10.5mL room temperature isopropanol, mixed and centrifuged at 16'000xg for 30 mins at 4°C. The supernatant was removed, and the pellet was washed with 5mL RT 70% ethanol and centrifuged at 16'000xg for 10 mins. The supernatant was removed, and the pellet was air-dried for 10 mins before being resuspended in 50μ L ddH₂O.

Using the GeneJET Plasmid Miniprep Kit, cell pellets were re-suspended in 6 mL of resuspension solution (RNase A). 6mL of lysis solution was added and mixed thoroughly before being incubated at room temperature for 3 mins. 6mL of neutralisation solution was added and mixed thoroughly followed by 0.8mL of endotoxin binding reagent—after which the solution was incubated at RT for 5 mins. 6mL of 96% ethanol was added and mixed thoroughly before centrifugation at 5'000xg for 40 mins to pellet cell debris and chromosomal DNA. The supernatant was transferred into a 50mL tube and 6mL 96% ethanol was added and mixed thoroughly. The solution was added to a GeneJET spin column and centrifuged at 2'000 xg for 3 min. The DNA bound to the silica membrane was washed using 8mL of wash solution I and centrifuged at 3'000xg for 2 mins. The DNA was then washed twice using 8mL of wash solution II and centrifuged at 3'000xg for 2 mins before being eluted with 1mL elution buffer, incubated at RT for 2 mins before being spun at 3'000xg for 5 mins. Yield and purity were determined by spectrophotometric measurement using the Nanodrop as outlined in 2.4.6.

Purified plasmid DNA was sent for sequencing with Eurofins Genomics to confirm the correct plasmid has been amplified and single plasmid purity, as outlined in chapter 2.4.10.

2.4.4 RNA extraction

RNA was extracted from transfected cells at 48 hours post-transfection using the Qiagen RNeasy Mini Kit (Cat#74104) following the manufacturer's protocol, all centrifugations were performed at 11'000xg unless otherwise stated:

Media was removed and 500µL buffer RLT was added to each well. Cells were scraped from the culture dish well using a pipette tip and the lysate was transferred into a tube. Lysates were homogenised by vortex for 1 min before addition of 500µL DEPC-treated 70% ethanol (see 2.1.4). The solution was mixed thoroughly and then added to a RNeasy Mini spin column and centrifuged

for 30 seconds. The RNA bound in the spin column was washed using 350 μ L RW1 and centrifuged for 30 secs. A solution containing 10 μ L DNase I and 70 μ L RDD buffer was added to the spin column membrane and incubated at RT for 15 mins prior to a subsequent wash with 350 μ L RW1 and centrifuged for 30 secs. The spin column was subsequently washed with 500 μ L RPE buffer, centrifuged for 30 seconds, and 500 μ L RPE buffer centrifuged for 2 mins. The RNA was then eluted using 30 μ L RNase-free water, centrifuged for 1 min. Yield and purity were determined by spectrophotometric measurement using the Nanodrop as outlined in 2.4.6.

2.4.5 Reverse Transcription of RNA to cDNA

RNA isolated as described in chapter 2.4.4 was analysed for concentration via Nanodrop UV absorption as outlined in chapter 2.4.6. RNA was treated with DNase and then reverse transcribed to cDNA using the BIO-RAD iScript gDNA Clear cDNA Synthesis Kit (Cat#172-5034).

 2μ L of DNase master mix—containing 0.5μL iScript DNase and 1.5μL iScript DNase Buffer—was added to 200ng of RNA in 14μL. DNase treatment was performed as follows:

- DNA digestion at 25°C for 5 mins.
- DNase inactivation at 75°C for 5 mins.

The $16\mu L$ of DNase-treated RNA template was then added to $4\mu L$ of iScript Reverse Transcription Supermix and reverse transcription was carried out as follows:

- Annealed at 25°C for 5 mins.
- Extended at 46°C for 20 mins.
- Enzymatic inactivation at 95°C for 1 min.

2.4.6 Nanodrop Determination of Nucleotide Concentrations

Measurement of pDNA, cDNA and RNA concentrations was made using a Thermo Fisher NanoDrop 2000c UV-Vis spectrophotometer. A blank reading was first made using 1μ L of elution buffer/ddH₂O, dependent on the sample being analysed. 1μ L of the sample was then loaded onto the spectrophotometer platform. Nucleic acid concentration was calculated by measurement of absorbance at 260nm (absorbance of 1 at 260 nm = 50μ g/mL pure dsDNA). The measurement was displayed as a subtraction of absorbance from the blank measurement. The quality of the sample was determined by $260/280 \mu$ nm and $260/230 \mu$ nm absorbance ratios.

2.4.7 End-point PCR

End-point PCR was used to detect mRNAs of interest from samples of RNA that underwent reverse transcription into cDNA. REDTaq ReadyMix PCR Reaction Mix (Cat#R2523) was used for all PCR reactions and set up as below:

Table 2.12 PCR amplification master mix recipe.

Component	Volume (μL)
RedTaq ReadyMix	12.5
10 μM Forward Primer	1
10 μM Reverse Primer	1
Template DNA	1
Nuclease Free Water	9.5
Total	25

Samples were briefly vortexed and centrifuged at 11,000 xg for 30 seconds before being loaded into a thermocycler with the following settings:

Table 2.13 Thermocycler settings for PCR amplification

Step	Temperature (°C)	Time (sec)
Initial denaturing	94	120
35 cycles of:		
Denaturing	94	60
Annealing	62.3-64.3	30
Extension	72	60 per kb DNA
Final Extension	72	600
Hold	10	∞

2.4.8 Agarose gel electrophoresis

1% (w/v) agarose gels were made by dissolving 1.2 g agarose (Cat#10766834) in 120 mL 1X TAE buffer (chapter 2.1.4) and heating in a microwave until completely dissolved. 6 μ L 10′000X GelRed (Cat#41003) to stain nucleic acids. The gel was then poured into a cassette with a 20-well comb and allowed to set for 10-20 mins. Once cooled, the comb was removed, and the gel cassette was submerged in 1X TAE buffer. 5 μ L of Quick-Load Purple 1 kb Plus DNA Ladder (Cat#N0550S) as a

reference guide for DNA size and 10 μ L of each sample was loaded into the appropriate wells and the gel was run at 100V for 100 mins before being imaged using a UV transilluminator.

2.4.9 Site-directed mutagenesis (SDM)

Site-directed mutagenesis was used for the substitution of nucleotide bases within plasmid DNA. Specific primers (Table 2.1) were designed using New England Biolabs NEBaseChanger to amplify existing plasmid DNA through PCR (chapter 2.4.7) and introduce sequence substitutions via the primer amplification sequence. Following amplification, the PCR product was phosphorylated, ligated, and circularised whilst the non-modified template plasmid DNA was degraded.

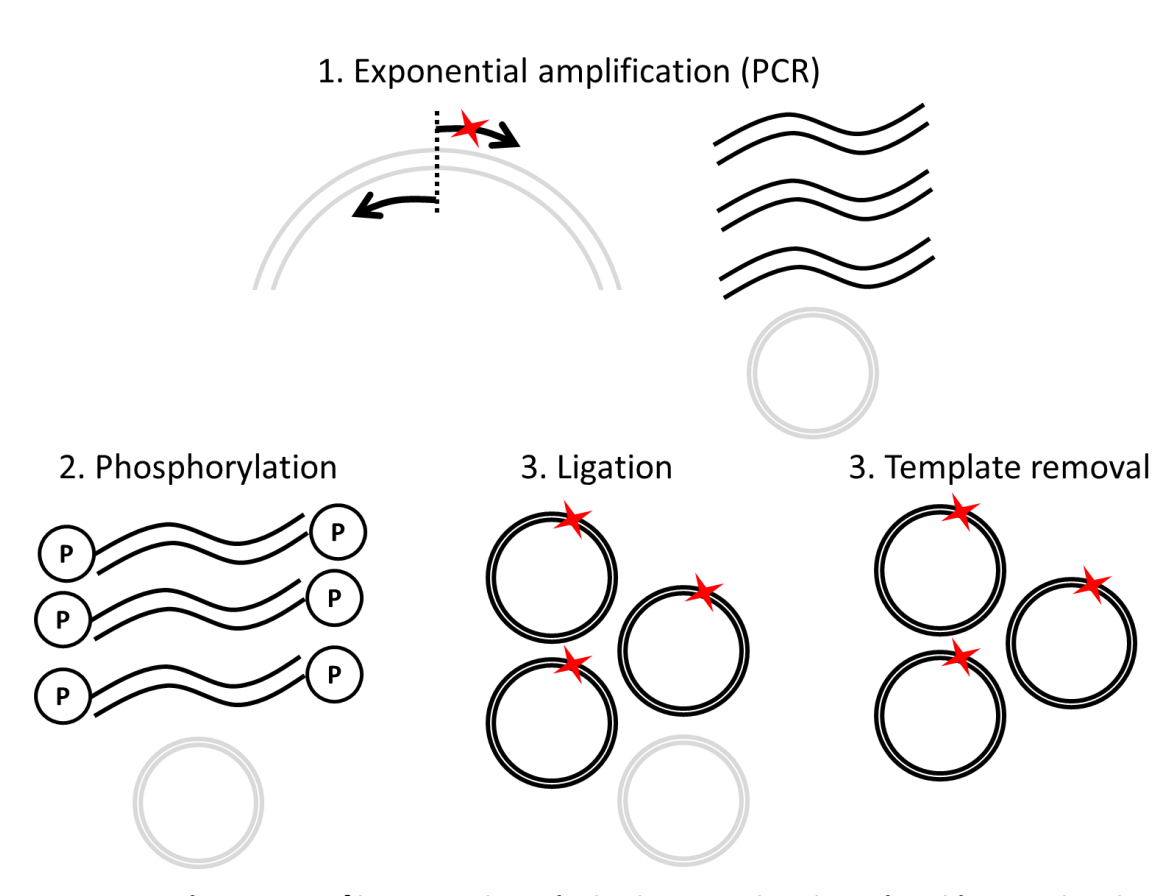


Figure 2.1 - The process of incorporating substitution mutations into plasmid DNA using sitedirected mutagenesis.

A primer pair containing the intended substitution (red star) are used to exponentially amplify the template plasmid DNA, incorporating the mutation. This is followed by incubation with a mixture containing a kinase, ligase and DpnI to phosphorylate, ligate and remove the template plasmid DNA.

Site-directed mutagenesis was performed using the NEB Q5 site-directed mutagenesis kit following the manufacturer protocol:

Table 2.14 Q5 Site-directed mutagenesis master mix recipe

Reagent	Volume (μL)
Q5 Hot Start High Fidelity 2X Master Mix	12.5
10μM Forward Primer	1.25
10μM Reverse Primer	1.25
Template DNA (100ng/μL)	1
Nuclease-free water	9

Samples were briefly vortexed and centrifuged at 11,000 xg for 30 seconds before being loaded into a thermocycler with the following settings:

Table 2.15 Thermocycler settings for site-directed mutagenesis

Step	Temperature (°C)	Time (sec)
Initial denaturing	98	30
25 cycles of:		
Denaturing	98	10
Annealing	62-68	20
Extension	72	30 per kb DNA
Final Extension	72	600
Hold	10	8

Following PCR, the reaction mixture was incubated with Kinase, Ligase, and DpnI enzyme mix (KLD) to phosphorylate and ligate amplified DNA and degrade template plasmid DNA via DpnI bacterial plasmid methylation recognition. The KLD mixture was set up as follows:

Reagent	Volume (μL)
2X KLD Reaction Buffer	5
10X KLD Enzyme Mix	1
PCR product	1
Nuclease-free water	3

Samples were briefly vortexed and incubated at RT for 45 mins before being transformed into NEB 5-alpha Competent E. coli (High Efficiency) for amplification and purification, as outlined in chapters 2.4.1 and 2.4.2.

Purified plasmid DNA was sent for sequencing with Eurofins Genomics to confirm correct substitution at the target site and the absence of off-site mutagenesis as outlined in the chapter 2.4.10.

2.4.10 Sequence verification

Following amplification and purification, plasmid DNA was sent for sequence verification with Eurofins Genomics via the TubeSeq Supreme service using either custom primers or Eurofins standard vector primers (Table 2.2). Four-colour chromatogram sequencing data was analysed and aligned to reference sequences using MAFFT v7 local pairwise alignment in Benchling (Katoh and Standley, 2013).

2.5 Protein analysis techniques

2.5.1 Protein extraction

Protein was extracted from transfected cells at 48 hours post-transfection. 6-well plates containing transfected HEK293T cells were placed on ice and the culture media was removed. $100\mu L$ of prechilled 5X sample buffer (chapter 2.1.4.2) was added to each well and lysed cells were scraped using a pipette tip before being transferred into a tube and stored at -20°C until used.

2.5.2 SDS polyacrylamide gel electrophoresis (SDS PAGE)

Protein lysates were separated by sodium dodecyl sulphate-polyacrylamide gel electrophoresis (SDS-PAGE). Samples were incubated at 95°C for 5 mins before $25\mu L$ was loaded into the SDS PAGE gels in a tank containing 1X Laemmli buffer (chapter 2.1.4.2). $5\mu L$ of Precision Plus Protein All Blue Prestained Protein Standards (Bio-rad, Cat# 1610373) was loaded as a reference guide for protein size. Samples were run at 100V at 4°C until the 50 kDa protein ladder band was near the bottom of the gel for better resolution of protein isoforms between the 250kDa-150kDa protein markers.

2.5.3 Wet transfer

Following protein separation by SDS PAGE, proteins were transferred from the gel to $0.22\mu m$ nitrocellulose membranes (Bio-rad, Cat# 1620097). Transfer sandwiches were assembled and soaked in 1X transfer buffer (chapter 2.1.4.2) prechilled to 4°C and bubbles were removed using a roller as depicted below:

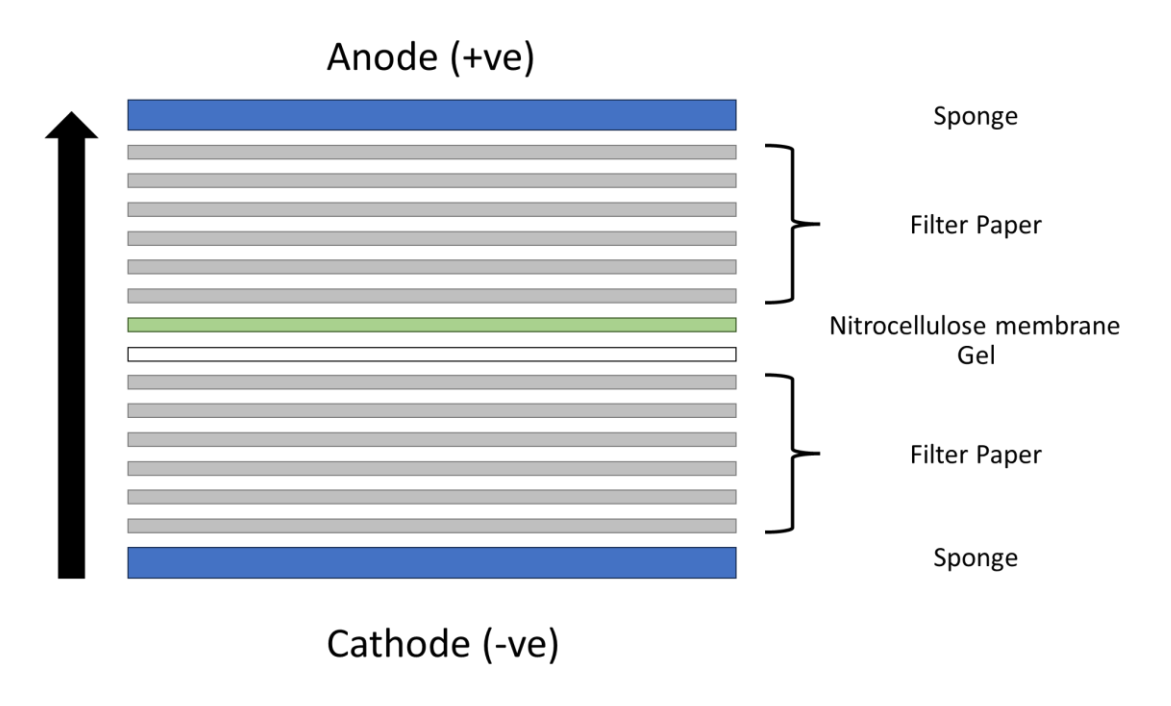


Figure 2.2 - Assembly of Western Blot transfer sandwich.

Transfer sandwiches were assembled within a BioRad transfer tank submerged in 1X transfer buffer (chapter 2.1.4.2) prechilled to 4°C. The wet transfer was performed at 4°C at 30V overnight (approx. 16hrs) with transfer buffer constantly circulating the tank using a magnetic stirrer and stirring bar (flea). Following the transfer, the membrane was blocked in 2% (w/v) bovine serum albumin (BSA) in 1X TBS-T (chapter 2.1.4.2) for 1 hour on an orbital shaker.

2.5.4 Immunoblotting

After blocking, membranes were incubated in primary antibody (Table 2.5) diluted in 2% (w/v) BSA TBS-T, for either 1 hr at RT or overnight (approx. 16 hrs) at 4°C on a roller shaker. Primary antibodies were then removed, and the membrane was washed of excess antibody 3 times in TBS-T for 5 mins at RT on an orbital shaker. The membranes were then incubated in fluorescent secondary antibody (Table 2.5) diluted in 2% (w/v) BSA TBS-T, for 1 hr at RT on an orbital shaker in a light-proof box to prevent fluorophore photobleaching. Secondary antibodies were then removed, and the membrane was washed of excess antibody 3 times in TBS-T for 5 mins at RT on

an orbital shaker. Membranes were subsequently imaged using a Licor Odyssey CLx machine at 700 nm and 800 nm. Images were analysed using ImageStudio Lite software.

2.6 Data Analysis

Data were analysed for quantitative experiments using GraphPad Prism (Version 10) or MatLab R2018b (MathWorks). Statistical analysis was performed using GraphPad; tests and parameters are discussed within figure legends for each results figure. 2D image processing and analysis were performed using FIJI (FIJI is just ImageJ).

Chapter 3 Generation of a gene expression construct to investigate the function of Human GluN2A and GluN2A-S in isolation

3.1 Introduction

We have established that the GRIN2A gene produces at least two protein isoforms in humans and primates (Warming *et al.*, 2019). Prior studies utilising GRIN2A expression in mammalian cells have not distinguished between these isoforms, which makes it essential to isolate their expression and study them independently. The hGRIN2A transcript contains an intra-exon junction at positions p13.2 chr16:9,763,428 and p13.2 chr16:9,763,771, which results in exondependent splicing. This splicing leads to a 343-nucleotide deletion (exitron) from exon 13 and the generation of a new exon 14, producing the primate-specific GluN2A-S protein.

Following the expression of the hGluN2A plasmid, we observed two PCR products corresponding to hGluN2A-Long (hGluN2A-L) and hGluN2A-Short (hGluN2A-S). This suggests that the intra-exon splice site present in the cDNA enables splicing in the presence of the hGRIN2A expression plasmid, despite the absence of intronic regions. Consequently, exogenous expression of hGRIN2A is expected to produce a mixture of two protein isoforms—hGluN2A-L and hGluN2A-S—complicating their independent study.

Developing a tool to study hGluN2A-L and hGluN2A-S in isolation could provide crucial insights into the functional consequences of differences in their C-terminal domains. These differences include the absence of key phosphorylation sites, PDZ- and SH3-binding motifs, and a dileucine motif involved in clathrin-mediated internalisation. Such functional differences have not been fully addressed in existing studies on hGluN2A. For example, Elmasri et al. (2022) investigated the mechanisms by which GOF mutations (including K669N and L812M) and LOF mutations (such as R518H, T531M, and C436R) in hGRIN2A lead to synaptic dysfunction. However, their study did not differentiate the roles of exogenous hGluN2A-L and hGluN2A-S expression in mouse CA1 neurons, which could potentially contribute different properties, such as Mg²⁺ sensitivity, decay kinetics, or charge transfer to NMDARs (Elmasri et al., 2022).

As discussed in Chapter 1.2, GluN2A-S is a primate-specific isoform, and the corresponding splice sites are absent in rats and mice. In the comparison between human and rat Grin2A, the donor recognition site is conserved, but a single nucleotide difference exists at the acceptor recognition

site: adenine in humans and guanine in rats. Both rat and mouse Grin2A transcripts generate only a single GluN2A isoform (Warming *et al.*, 2019; Herbrechter *et al.*, 2021).

By isolating the expression of hGluN2A-L, we would enable more detailed investigations into the functional consequences of hGluN2A-S lacking a portion of the C-terminal domain. This could lead to a better understanding of how the absence of key functional motifs in hGluN2A-S impacts its role in synaptic signalling and its potential involvement in neurological disorders.



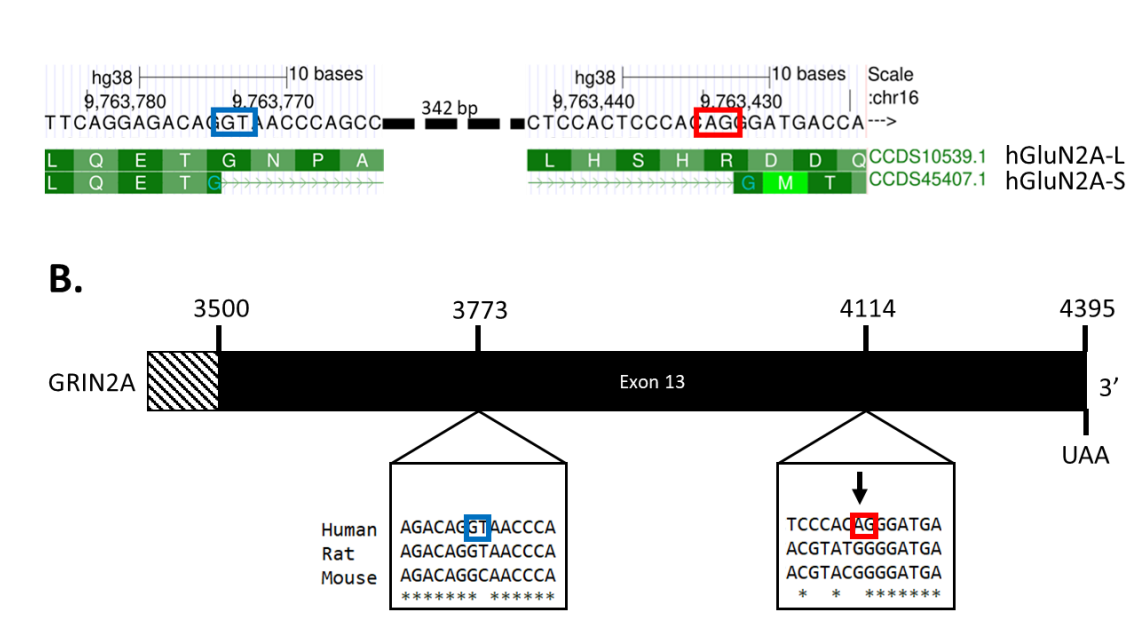


Figure 3.1 - Comparison of the donor and acceptor splice sites responsible for the alternative splicing of hGRIN2A with the equivalent sites in rodent Grin2A.

A) Display of the UCSC Genome Browser showing positions p13.2 chr16:9,763,419-9,763,442 and p13.2 chr16:9,763,760-9,763,783. The donor (boxed in blue) and acceptor splice sites (boxed in red) are suggested to generate the GluN2A-S protein annotated with accession number: CCDS45407.1. Figure adapted from UCSC Genome Browser. B) Diagram depicting the nucleotide sequence of exon 13 of GRIN2A. In boxes are multiple sequence alignments of human, rat, and mouse GRIN2A nucleotide sequences located at the 5' (boxed in blue) and 3' (boxed in red) splice sites responsible in humans for the generation of GluN2A-S. The 5' dinucleotide is conserved between human and rat whilst a single nucleotide mismatch at position 3774 (T vs. C) site can be observed between human/rat and mouse sequences respectively. The 3' dinucleotide is conserved between rat and mouse whilst a single nucleotide mismatch at position 4114 (A vs. G) can be observed between human and rat/mouse sequences respectively. The arrow depicts the position in Human GRIN2A and Rat GRIN2A to undergo site-directed mutagenesis (A4114G and G4114A

respectively). Sequences were aligned using EMBL-EBI, Clustal Omega, Multiple Sequence Alignment; asterisks denote sequence matches.

3.2 Aims and Objectives

The overarching aim of this chapter is to create construct that allows the independent study of hGluN2A-L in isolation from hGluN2A-S expression. Based on our understanding of the splice sites involved in the generation of hGluN2A-S, and by comparing these sequences to that of rodents, which generate only a single canonical isoform, we sought to determine whether removing the acceptor recognition site would be sufficient to prevent the alternative splicing of hGRIN2A. By substituting the adenine in the hGRIN2A acceptor splice site dinucleotide with the guanine found in rat Grin2A, we aimed to generate exclusively the hGluN2A-L protein isoform. We hypothesised that by removing the recognition site, we could prevent the generation of hGluN2A-S, thus providing a tool to study hGluN2A-L in isolation.

A secondary aim of this chapter is to explore whether the determinants of hGRIN2A alternative splicing—absent in rodent Grin2A—are solely attributable to the nucleotide differences within the donor and acceptor splice sites. This work could open new avenues for studying a second, shorter GluN2A isoform in rodent models, such as mice or rats. To this end, we focussed first on performing the G4114A substitution in rat Grin2A (rGrin2A) to attempt to create an acceptor splice site and investigate whether this single nucleotide change is sufficient to generate two rat GluN2A isoforms.

The objectives for this chapter are as follows:

- Substitute the adenine in the acceptor splice site of hGRIN2A for guanine found in rGrin2A using site-directed mutagenesis (A4114G).
- 2. Determine whether the A4114G substitution was sufficient to prevent the formation of the short hGRIN2A mRNA transcript and hGluN2A-S protein.
- 3. Perform the opposing substitution in rGrin2A and determine whether this is sufficient to generate a second shorter rGrin2A mRNA transcript and GluN2A protein.

3.3 Results

3.3.1 Creating a tool to express the hGluN2A-L in isolation. Step 1: Site directed mutagenesis of hGRIN2A and sequence validation.

To generate a tool that enables the study of hGluN2A-L in isolation, we targeted the pcDNA3.1+ eGFP-hGRIN2A plasmid for site-directed mutagenesis. Primers were designed (Table 2.1) to introduce a substitution of the adenine at position 4114 within the acceptor splice site to guanine, matching the sequence found in rGrin2A (Figure 3.1B). We hypothesised that this modification would remove the acceptor splice site, thereby preventing the generation of hGluN2A-S and producing only hGluN2A-L, as rGrin2A generates a single GluN2A protein isoform.

We performed site-directed mutagenesis via PCR using primers designed to amplify the template plasmid while incorporating the A4114G substitution (Table 2.1). PCR products were ligated and transformed into DH5 α *Escherichia coli*, which we then screened for ampicillin resistance (Figure 2.1).

To confirm the successful introduction of the substitution, we screened bacterial colonies by sequencing using the Seq_Primer_Fwd_H sequencing primer, which was designed to cover the SDM target site (Table 2.2). The sequencing chromatogram (Figure 3.2A) confirmed the successful substitution of A4114G in the modified plasmid. Additional sequencing primers (Table 2.2) were designed to provide full coverage of the hGRIN2A^{A4114G} coding sequence, ensuring no off-target mutations had occurred. Sequence alignment confirmed a 100% match between the query sequence and the reference sequence, validating the accuracy of the mutagenesis process.

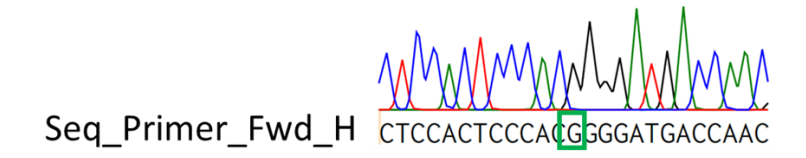
Figure 3.2B illustrates the final pcDNA3.1+ eGFP-hGRIN2A^{A4114G} plasmid construct. This plasmid includes ampicillin and neomycin resistance genes, as well as the coding sequence of eGFP-hGluN2A protein. Sequence analysis confirmed the intended A4114G substitution and revealed a corresponding amino acid change at position 1372 from arginine to glycine. However, we do not expect this amino acid substitution to have functional consequences, as position 1372 in rGluN2A is naturally occupied by glycine. Rodent and human NMDARs share highly conserved sequences and exhibit near-identical pharmacological properties (Hedegaard *et al.*, 2012).

To confirm successful expression, we transfected HEK293T cells with the pcDNA3.1+ eGFP-hGRIN2A^{A4114G} plasmid. Expression was verified by visualisation of the eGFP tag under 480 nm fluorescent excitation at 48 hours post-transfection (Figure 3.3).

pcDNA3.1+ eGFP-Human GRIN2A CTCCACTCCCACAGGGGATGACCAAC Α.







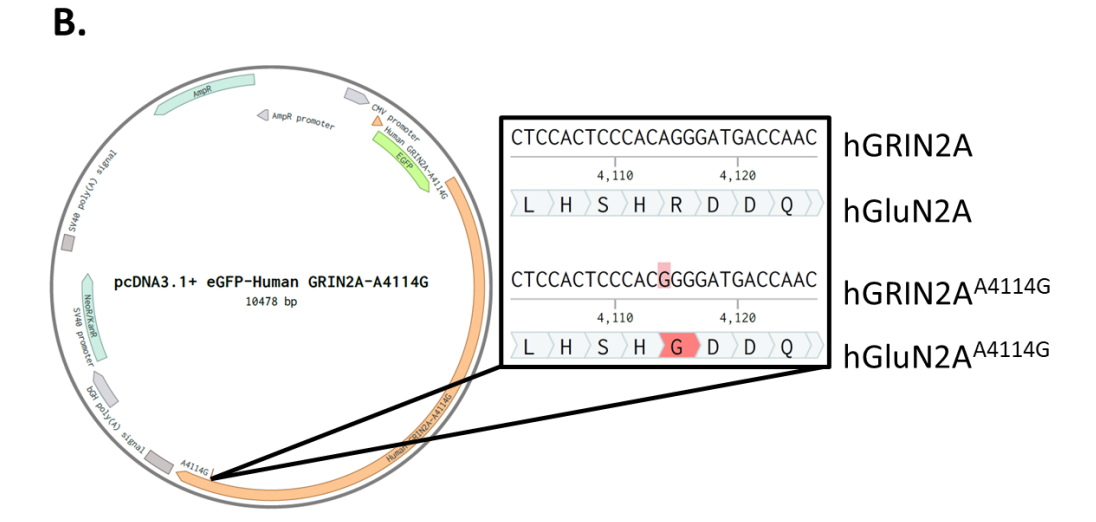


Figure 3.2 - Generation of a plasmid construct to independently express canonical human GluN2A using site-directed mutagenesis.

A) pcDNA3.1+ eGFP-Human GRIN2A and pcDNA3.1+ eGFP-Human GRIN2A^{A4114G} plasmids were sequenced using the Seq_Primer_Fwd_H primer to validate the success of the A4114G substitution. Sequencing chromatogram showing the presence of an adenine (red box) in pcDNA3.1+ eGFP-Human GRIN2A which was mutated to a guanine in pcDNA3.1+ eGFP-Human GRIN2AA4114G resultant from substitution of A4114G via site-directed mutagenesis (green box). B) (Left) Plasmid map of pcDNA3.1+ eGFP-Human GRIN2AA4114G indicating locations of antibiotic resistance, promoter regions and polyA signal sequences. (Right top) Pairwise sequence alignment of the coding sequence of human GRIN2A and human GRIN2A^{A4114G}. As intended, a nucleotide mismatch can be observed at position 4114 due to A4114G substitution (red box). (Right bottom) Pairwise sequence alignment of the amino acid sequence of human GluN2A and human GluN2A^{A4114G}. A mismatch can be observed at position 1372, arginine for glycine respectively (red box). Sequences were aligned using local pairwise, MAFFT v7.

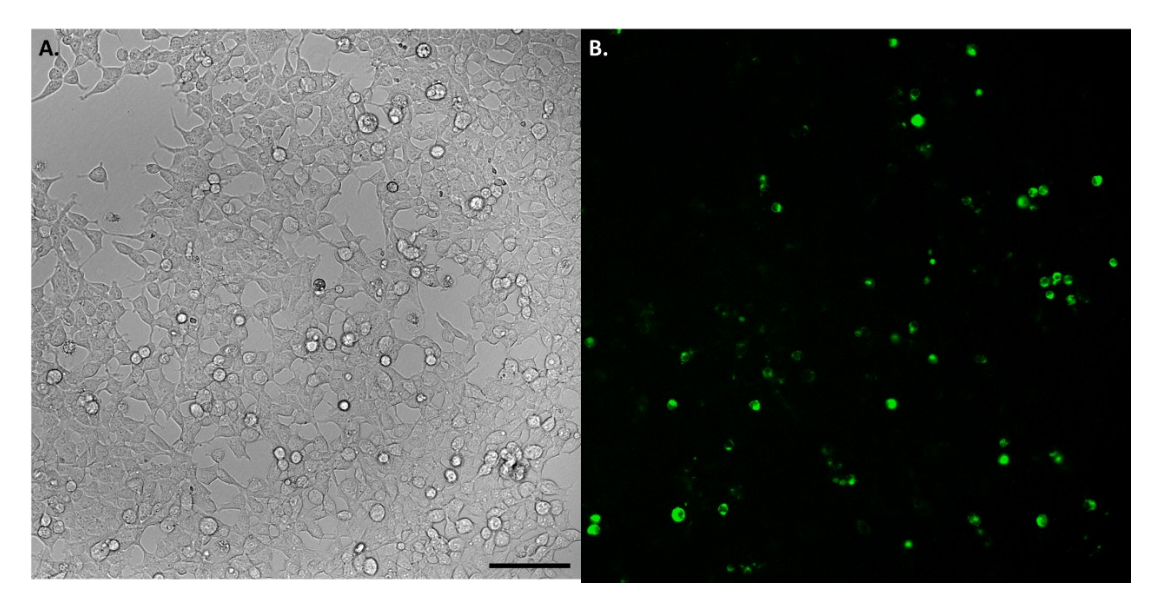


Figure 3.3 - Exogenous expression of eGFP-Human GluN2A^{A4114G} in HEK293T cells.

A) Representative brightfield image of HEK293T cells plated and transfected in a 6-well plate with pcDNA3.1+ eGFP-Human GRIN2A^{A4114G} plasmid. B) As in A, fluorescence image at 488 nm excitation of eGFP-tagged protein. Images were taken at 48 hours post-transfection. Scale bar = 100μ M. Images are representative of 6 independent repeats.

3.3.2 Creating a tool to express the hGluN2A-L in isolation. Step 2: Testing mRNA transcripts produced by the mutant.

Following the successful generation of a plasmid construct containing the A4114G nucleotide substitution, we aimed to determine whether this mutation effectively prevents the generation of the shorter hGRIN2A-S mRNA transcript when exogenously expressed in HEK293T cells.

To test this, we utilised primers previously validated by Warming et al. (2019) to specifically amplify the hGRIN2A and GRIN2A-S transcripts (GRIN2A Human F/GRIN2A Human R1, Table 2.3). These primers were designed to generate distinct amplicons: a 0.474 kb product corresponding to the hGRIN2A-L transcript and a 0.131 kb product corresponding to the hGRIN2A-S transcript (Figure 3.4A).

As expected, PCR of cDNA from cells transfected with the pcDNA3.1+ eGFP-hGRIN2A plasmid produced two distinct bands: an upper band between the 0.4 and 0.5 kb markers, corresponding

to the hGRIN2A-L transcript, and a lower band between the 0.1 and 0.2 kb markers, corresponding to the hGRIN2A-S transcript. The smaller band was consistent in size with the 0.131 kb band observed in cell transfected with the pcDNA3.1+ eGFP-hGRIN2A-S plasmid.

In contrast, PCR of cDNA from cells transfected with the pcDNA3.1+ eGFP-hGRIN2A^{A4114G} plasmid produced only a single band of 0.474 kb, corresponding to the hGRIN2A-L transcript (Figure 3.4B). This indicated that the A4114G mutation successfully abolished the generation of the hGRIN2A-S transcript.

To account for potential preferential amplification of shorter cDNA products, as noted by Warming et al. (2019), we employed an alternative primer pair (GRIN2A Human F/GRIN2A Human R2) that specifically amplified the hGRIN2A-L transcript (Table 2.3) (Warming *et al.*, 2019). Using this primer pair, we observed a single 0.386 kb product from cDNA of cells transfected with either pcDNA3.1+ eGFP-hGRIN2A or pcDNA3.1+ eGFP-hGRIN2A^{A4114G} plasmids, with no amplification from cells transfected with pcDNA3.1+ eGFP-hGRIN2A-S (Figure 3.4B). This confirmed that the A4114G mutation did not disrupt the production of hGRIN2A-L.

To ensure observed amplicons originated from exogenous cDNA rather than endogenous off-target amplification, we included negative controls. Cells transfected with a plasmid expressing soluble eGFP did not yield PCR products. Similarly, no bands were observed in non-template control reactions where cDNA was excluded, confirming that the observed bands were not due to reagent contamination (Figure 3.4B). These results were consistent across three independent experiments.

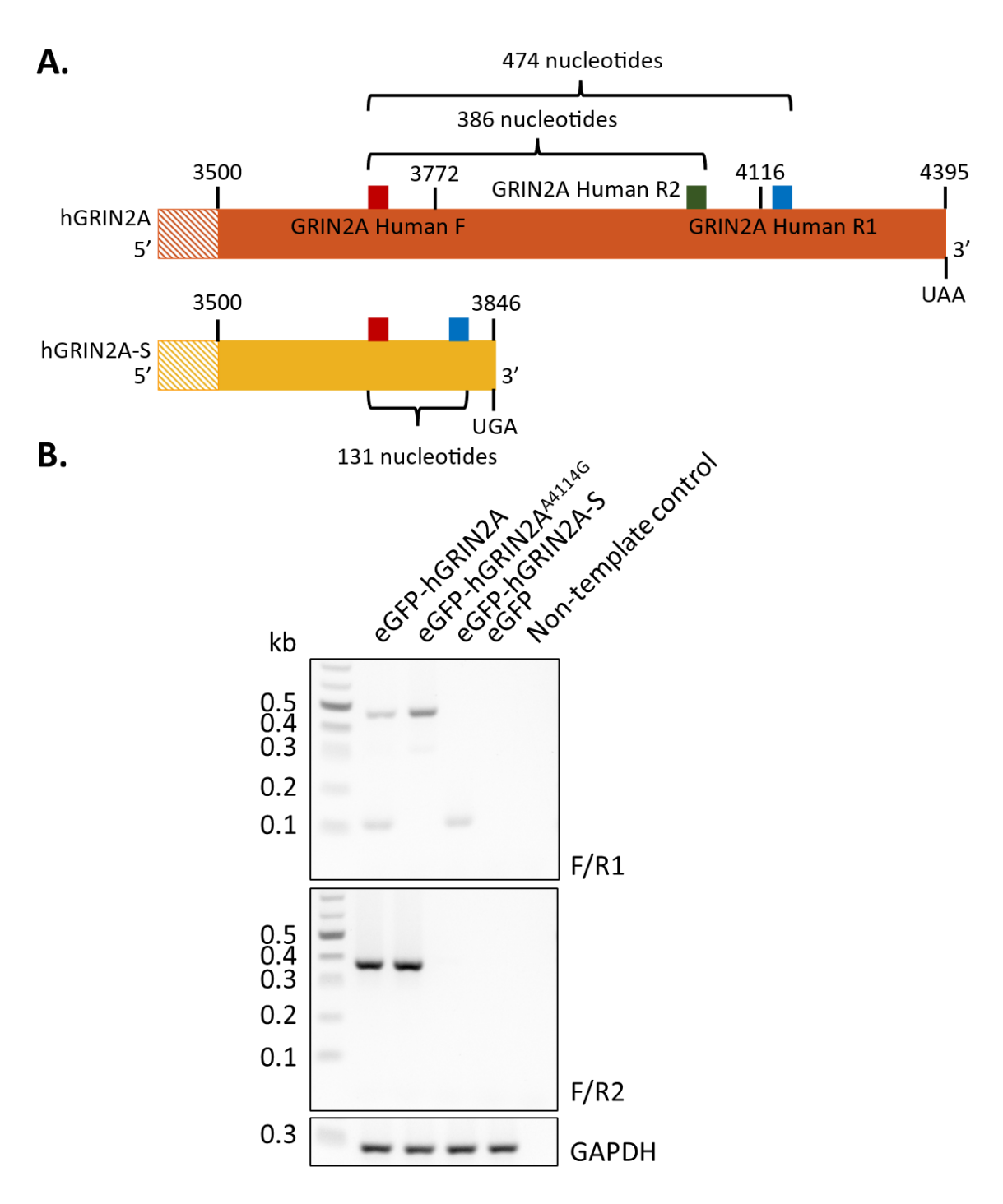


Figure 3.4 - End-point PCR following RNA extraction and RT-PCR from HEK293T cells expressing Human GRIN2A^{A4114G}.

A) Diagram depicting the Human GRIN2A and GRIN2A-S transcripts and the annealing locations of PCR primers (GRIN2A Human F – red; GRIN2A Human R1 – blue; GRIN2A Human R2– green) with their respective expected amplicon sizes. **B)** Gel electrophoresis of PCR products from amplification of cDNA from RNA extracted from HEK293T cells exogenously expressing plasmids encoding human GRIN2A, human GRIN2A^{A4114G}, human GRIN2A-S or eGFP. (top) Primers GRIN2A Human F and GRIN2A Human R1 were used for the specific amplification of human GRIN2A and/or

GRIN2A-S transcripts. (middle) Primers GRIN2A Human F and GRIN2A Human R2 for the specific amplification of Human GRIN2A transcripts. (bottom) GAPDH Human forward (F) and reverse (R) primers were used to control for the presence of cDNA. Image representative of three independent repeats.

3.3.3 Creating a tool to express the hGluN2A-L in isolation. Step 3: Testing protein isoforms produced by the mutant.

To determine whether the A4114G substitution prevented the formation of the hGluN2A-S protein, we analysed the protein products exogenously expressed in HEK293T cells. Total protein was extracted from cells co-transfected with the plasmids encoding eYFP-rGluN1-1a and either eGFP-hGRIN2A, hGRIN2A^{A4114G} or hGRIN2A-S.

Given the potential for recombinant cDNA splicing in HEK293T cells despite the lack of intronic regions, we hypothesised that cells transfected with eGFP-hGRIN2A would produce a mixture of hGluN2A-L and hGluN2A-S protein isoforms. According to UniProt predictions, the molecular weight (MW) of hGluN2A-L is 165.3 kDa, while hGluN2A-S is 144.4 kDa (Consortium, 2023). The internal eGFP tag adds a predicted MW of 26.7 kDa, resulting in expected band sizes of 192 kDa for hGluN2A-L and 171.1 kDa for hGluN2A-S (Figure 3.5B).

We performed western blot analysis using an antibody specific to an epitope common to the C-terminal domain of both hGluN2A-L and hGluN2A-S (ab133265), as previously validated by Warming et al. (2019) to detect both isoforms in human and primate tissue. We also used an anti- α -tubulin antibody (T9028) as a loading control (Figure 3.5A).

To enhance the resolution of the hGluN2A-L and hGluN2A-S immunoreactive bands, protein samples were separated on a 7% polyacrylamide gel until the 75 kDa marker reached the bottom of the gel. Western blotting of protein extracted from cells transfected with eGFP-hGRIN2A revealed four immunoreactive bands between 150-250 kDa. The lower two bands were consistent with the two immunoreactive bands observed in protein extracted from cells transfected with eGFP-hGRIN2A-S, corresponding to the predicted size of the hGluN2A-S isoform.

In contrast, protein extracted from cells transfected with eGFP-hGRIN2A^{A4114G} displayed two immunoreactive bands corresponding only to the higher molecular weight forms, consistent with hGluN2A-L and the absence of hGluN2A-S (Figure 3.5C).

Additionally, we consistently observed a band between 75-100 kDa in protein extracted from cells expressing eGFP-hGluN2A and eGFP-hGluN2A^{A4114G} (Figure 3.5C). As expected, no protein bands were detected in samples from cells transfected with the soluble eGFP control plasmid.

The observed banding patterns were consistent across three independent replicates, suggestive of an impact of the A4114G substitution on hGluN2A-S protein expression.

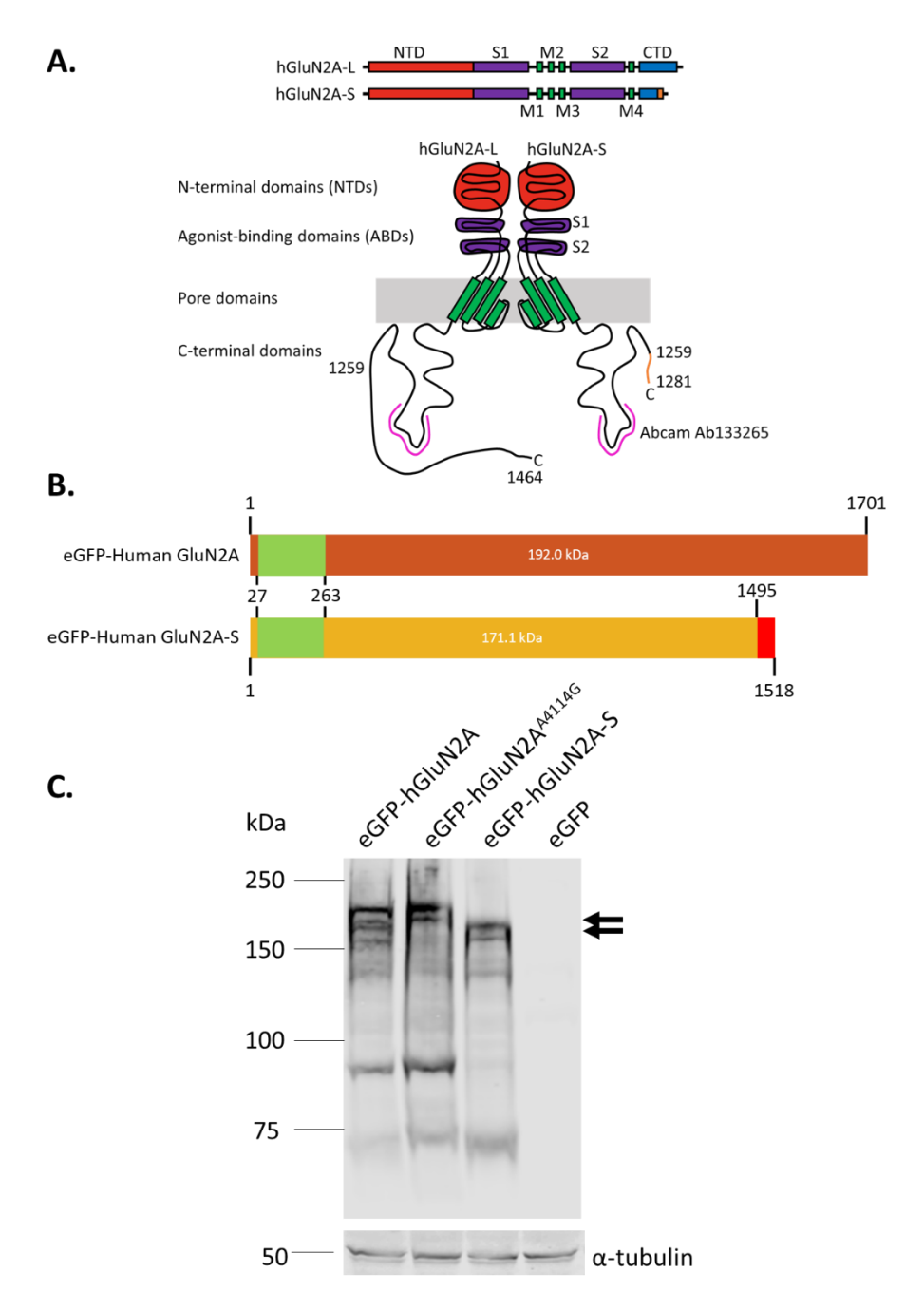


Figure 3.5 - SDS-PAGE and western blot following protein extraction from HEK293T cells expressing Human GluN2A^{A4114G}.

A) Cartoon depicting the structural architecture of a hGluN2A-L and hGluN2A-S NMDA receptors in linear (top) and assembled/native (bottom) formats. One half of the tetrameric assembly in the absence of the obligatory GluN1 subunit is shown for simplicity. The plasma membrane is depicted as a grey box. The epitope of the anti-GluN2A antibody: ab133265 (pink) on the c-terminal domain of the hGluN2A and hGluN2A-S protein allows the specific visualisation of protein extract from transfect

B) Cartoon depicting the expected molecular weight of recombinant eGFP-tagged human GluN2A and human GluN2A-S. The eGFP tag is shown in green, and the unique region of GluN2A-S is shown in red. C) 7% SDS-PAGE western blot of HEK293T cell lysates transfected with plasmids encoding human GluN2A, human GluN2A^{A4114G}, human GluN2A-S, or eGFP at 48 hours. (top) SDS-PAGE gel was run until the 75kDa marker bands were near the bottom to allow clear separation between bands corresponding to each protein isoform. Membrane was blotted with an anti-GluN2A antibody (ab133265). Extra bands were observed between 75-100 kDa from the anti-GluN2A antibody. (bottom) Membrane was blotted with an anti-α-tubulin antibody (T9028) as loading control. N=3 biological replicates. Arrows depict the expected band positions based on predicted molecular weight.

3.3.4 Creating splice sites in rGluN2A. Step 1: Site directed mutagenesis of rGrin2A and sequence validation.

The final aim of this chapter was to introduce the G4114A substitution into the rGrin2A sequence to attempt the creation of an acceptor splice site. This would allow us to determine whether a single nucleotide change was sufficient to generate two distinct rGluN2A isoforms and advance our understanding of GluN2A splicing determinants.

We designed primers (Table 2.1) to target the PCI-eGFP-rGrin2A plasmid for site-directed mutagenesis, substituting the guanine as position 4114 with adenine (Figure 3.1B). Site-directed mutagenesis was performed as described in chapter 2.4.9, with the resulting PCR products ligated and transformed into *E. coli*. We screened transformants for ampicillin resistance, and we selected colonies for sequencing of the mutagenesis target site using the RatGrin2A_SeqPrimerFwd_H primer (Table 2.2).

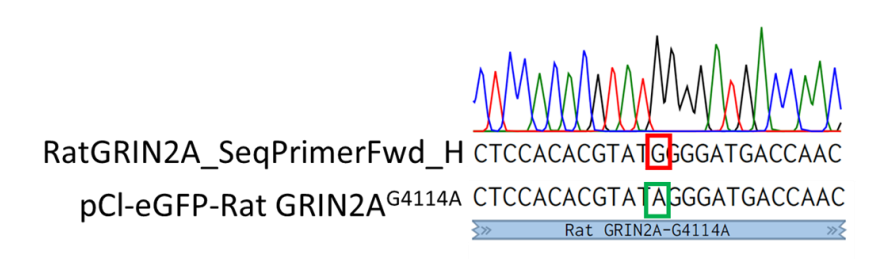
Sequencing chromatograms (Figure 3.6A) confirmed the successful G4114A substitution. To ensure the site-directed mutagenesis did not result in off-target substitutions, insertions, or deletions, we used additional sequencing primers to achieve full coverage of the rGrin2A^{G4114A} coding sequence (Table 2.2). Pairwise alignment of the resulting sequences revealed a 100% match between the query and reference sequence, confirming the integrity of the construct.

The resultant plasmid construct (Figure 3.6B) encodes rGrin2A with an internal eGFP tag near the 5'-end, designed to express an eGFP-tagged rGluN2A protein. Sequence alignment of the rGrin2A and rGrin2A^{G4114A} coding sequences confirmed the G4114A substitution. Alignment of the

respective amino acid sequences further revealed a resultant amino acid substitution from glycine to arginine at position 1372.

We next transfected HEK293T cells with the PCl-eGFP-Rat Grin2A^{G4114A} plasmid to test for expression. At 48 hours post-transfection, successful expression was confirmed by visualising the eGFP tag at 480 nm fluorescent excitation (Figure 3.7).





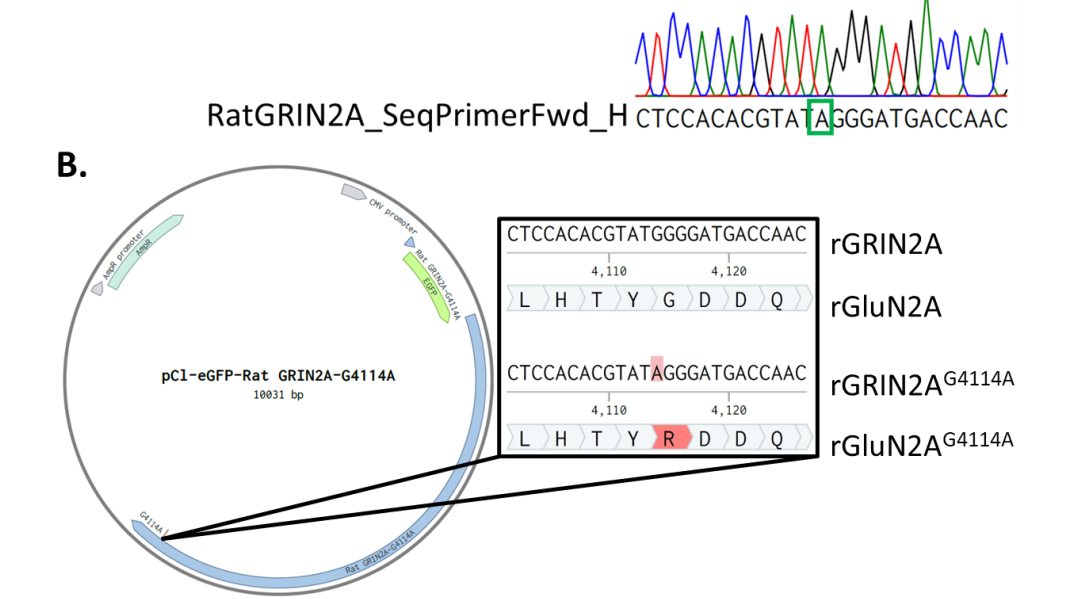


Figure 3.6 - Generation of pCI-EGFP-NR2a^{G4114A} using site-directed mutagenesis

A) pCl-eGFP-Rat Grin2A and pCl-eGFP-Rat Grin2A^{G4114A} plasmids were sequenced using the RatGrin2A_SeqPrimerFwd_H primer to validate the success of the G4114A substitution. Sequencing chromatogram showing the presence of a guanine (red box) in pCl-eGFP-Rat Grin2A which was mutated to an adenine in pCl-eGFP-Rat Grin2A^{G4114A} resultant from substitution of G4114A via site-directed mutagenesis (green box). **B)** (Left) Plasmid map of pCl-eGFP-Rat Grin2A^{G4114A} indicating locations of antibiotic resistance, promoter regions and polyA signal sequences. (Right top)

Pairwise sequence alignment of the coding sequence of Rat Grin2A and Rat Grin2A^{A4114G}. As intended, a nucleotide mismatch can be observed at position 4114 due to G4114A substitution (red box). (right bottom) Pairwise sequence alignment of the amino acid sequence of Rat GluN2A and Rat GluN2A^{G4114A}. A mismatch can be observed at position 1372, glycine for arginine respectively (red box). Sequences were aligned using local pairwise, MAFFT v7.

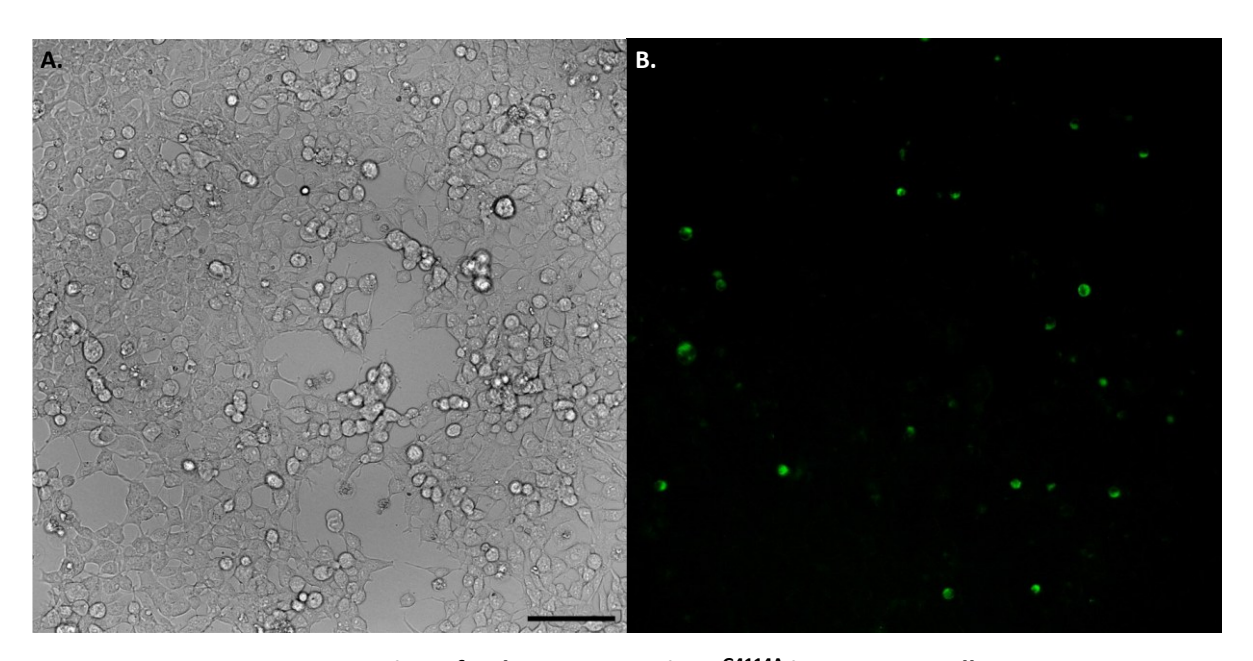


Figure 3.7 - Exogenous expression of PCI-eGFP-Rat Grin2A^{G4114A} in HEK293T cells.

A) Representative brightfield image of HEK293T cells plated and transfected in a 6-well plate with PCl-eGFP-Rat Grin2A^{G4114A} plasmid. B) As in A, fluorescence image at 480 nm excitation of eGFP-tagged protein. Images were taken at 48 hours post-transfection. Scale bar = $100\mu M$. Images are representative of 6 independent repeats.

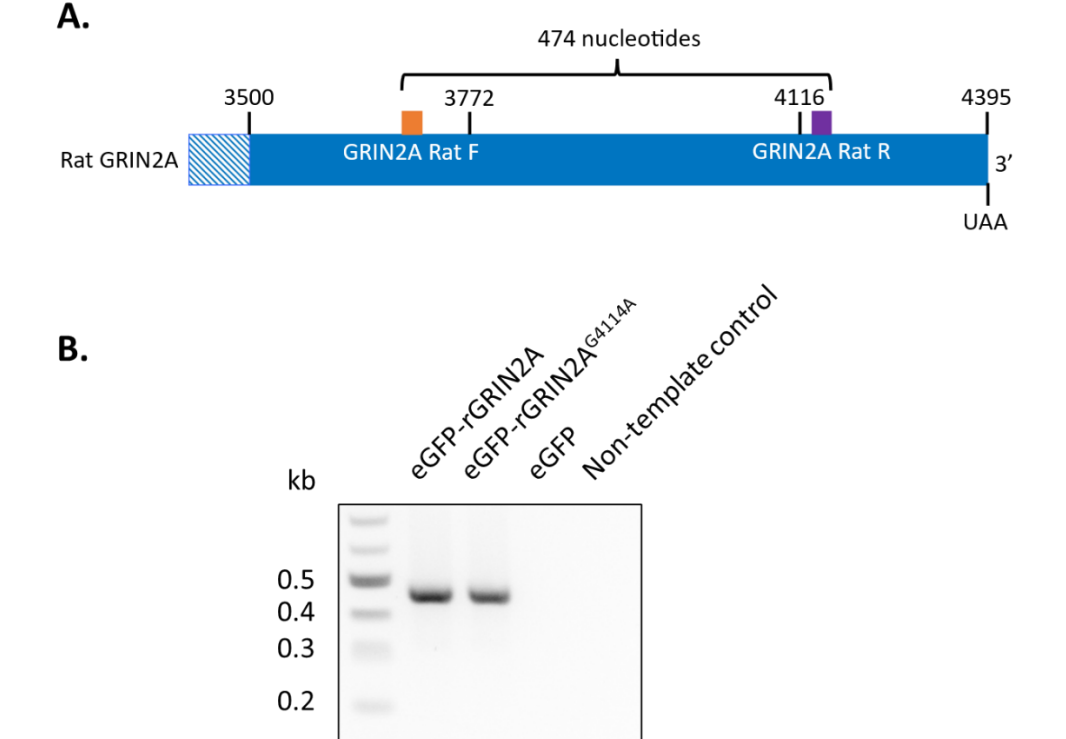
3.3.5 Creating splice sites in rGluN2A. Step 2: Testing mRNA transcripts produced by the mutant.

To determine whether the G4114A substitution was sufficient to generate two distinct rGrin2A mRNA transcripts, we transfected HEK293T cells with either the pCl eGFP-rGrin2A or pCl eGFP-rGrin2A^{G4114A} plasmids. Following RNA extraction and reverse transcription, we subjected the resulting cDNA to end-point PCR.

To ensure specific amplification of rGrin2A, we modified primers previously used by Warming and colleagues (2019) for mouse Grin2A to align with rGrin2A (Table 2.3). For cells transfected with pCl eGFP-rGrin2A, we predicted a single amplicon of 0.474 kb corresponding to rGrin2A transcript (Figure 3.8A).

As expected, a single band was observed between the 0.4-0.5 kb ladder marker, matching the predicted size of the rGrin2A amplicon. Similarly, a single band was observed in cells transfected with pCl-eGFP-rGrin2A^{G4114A}. Importantly, no additional amplicon corresponding to a second rGrin2A transcript of 0.131 kb—indicative of a predicted shorter isoform—was observed (Figure 3.8C).

These results were consistent across three independent repeats, demonstrating that the G4114A substitution did not result in the generation of a second shorter rGrin2A mRNA transcript.



0.1

0.3

Figure 3.8 - End-point PCR following RNA extraction and RT-PCR from HEK293T cells expressing Rat Grin2A^{G4114A}.

A) Diagram depicting the Rat Grin2A transcript and the annealing locations of PCR primers (GRIN2A Rat F – orange; and GRIN2A Rat R – purple) with the resultant expected amplicon size. **B)** Gel electrophoresis of PCR products from amplification of cDNA from RNA extraction of HEK293T cells exogenously expressing plasmids encoding Rat Grin2A, Rat Grin2A^{A4114G} or eGFP. The X depicts the absence of a second band in the eGFP-Rat Grin2A^{G4114A} condition. Primers GRIN2A Rat F and GRIN2A Rat R were used for the specific amplification of the Rat Grin2A transcript. GAPDH Human

GAPDH

forward (F) and reverse (R) primers were used to control for the presence of cDNA. Image representative of three independent repeats.

The data above suggest that the G4114A mutation in rGrin2A is not sufficient to generate both long and short isoforms at the mRNA level. To further investigate potential reasons for this, we performed pairwise sequence alignment of the coding sequences (CDS) of hGRIN2A and rGrin2A as well as their corresponding amino acid sequences.

The sequence alignment revealed an 89.2% identity between the hGRIN2A and rGrin2A CDS, with 475 sequence mismatches. However, these mismatches corresponded to only 42 conservative and 27 semi-conservative substitutions at the amino acid level, resulting in 95.3% identity and 98.2% similarity between hGluN2A and rGluN2A.

Figure 3.9 highlights the region of the CDS surrounding the donor and acceptor splice sites for hGRIN2A and rGrin2A^{G4114A}. Despite the introduction of the G4114A mutation to create an acceptor splice site, there are additional sequence mismatches in this region between the human and rat CDS. These mismatches may alter interactions with the splicing machinery, potentially explaining why the rat sequence does not produce two distinct isoforms as observed for hGRIN2A (Wang and Burge, 2008).

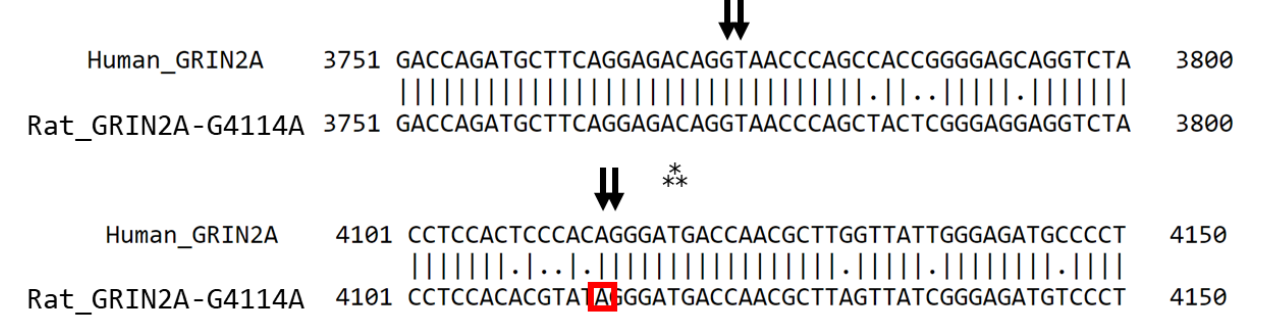


Figure 3.9 - Nucleotide sequence alignment between human and rat Grin2A coding sequences surrounding the donor and acceptor splice sites.

Pairwise sequence alignment of the coding sequence of human GRIN2A and rat Grin2A. Arrows depict the 5' and 3' splice site dinucleotides, respectively. Sequences were aligned using EMBL-EBI, EMBOSS Needle, Pairwise Sequence Alignment; full-stops denote sequence mismatches.

3.4 Discussion

3.4.1 Conclusions and Key Findings

3.4.1.1 Generating a tool for investigating the functional significance of GluN2A-L in isolation

In this chapter, we aimed to develop a means of specifically investigating the functional and dysfunctional differences between hGluN2A-L and hGluN2A-S. By creating a tool that enables the independent study of hGluN2A-L in isolation from hGluN2A-S expression, we sought to address the limitations of prior studies, which inadvertently examined a mixture of these protein isoforms.

Here, we demonstrate that expressing hGRIN2A from a pcDNA3.1+ plasmid in HEK293T cells generates both the long and short isoforms of hGluN2A. Despite the absence of the intronic sequences, the hGRIN2A cDNA is transcribed and processed into two mRNA transcripts corresponding to hGluN2A-L and hGluN2A-S. While it is possible to express hGluN2A-S using a plasmid encoding the spliced transcript, there has been no prior method to study hGluN2A-L in isolation. Through our efforts, we have now generated a tool to study hGluN2A-L in isolation, complementing previous work (Warming *et al.*, 2019) that allows for the independent investigation of hGluN2A-S.

HEK293T cells recognise the intra-exon donor and acceptor splice sites conserved within exon 13 of hGRIN2A, enabling the generation of hGluN2A-L and hGluN2A-S isoforms. As discussed in chapter 1.2.1, alternative splicing is regulated by both *cis*-elements (ESE, ESS, ISS, and ISE) and *trans*-acting splicing factors (e.g. SR proteins and hnRNPs) (Wang and Burge, 2008). The ability of HEK293T cells to process hGRIN2A cDNA in this manner suggests conservation of these regulatory elements, despite HEK293T cells not endogenously expressing hGluN2A protein. This conservation provides an opportunity for future studies to identify the splicing factors involved in the generation of hGluN2A-S in the human brain. For instance, overexpressing specific splicing factors could reveal their roles by altering the proportion of hGluN2A-S relative to hGluN2A-L. Such finding may enable the modulation of hGluN2A-S expression if its role in GRIN2A-associated disorders is found to be protective or pathogenic.

To enable the exclusive study of hGluN2A-L, we modified the splicing acceptor site to mimic the rat's version. Specifically, we substituted the adenine at position 4114 with guanine in the hGRIN2A sequence within the pcDNA3.1+ plasmid construct. This substitution alters the intraexon acceptor splice site dinucleotide, preventing its recognition by the spliceosome. As a result, only hGluN2A-L is generated. However, this mutation also introduces an amino acid change from

arginine to glycine at position 1372 (R1372G). Since glycine occupies this position in the rGluN2A protein and rodent and human NMDARs share highly conserved sequences and similar pharmacological properties (Hedegaard *et al.*, 2012), we do not anticipate any significant functional consequences of this substitution. To distinguish between the WT form of hGluN2A-L and the mutant hGluN2A^{R1372G} arising from modifying hGluN2A splice acceptor from human to the rat's version (r) to obtain hGluN2A-L expression only hGluN2A^{R1372G}, we refer to the latter as h(r)GluN2A-L or h(r)GRIN2A-L.

By generating a pcDNA3.1+ expression construct that produces h(r)GluN2A-L, we have developed a novel tool to study the functional significance of hGluN2A-S relative to hGluN2A-L in heterologous cell lines and neurons. At the mRNA level, our results indicate that the A4114G substitution effectively prevents alternative splicing of the recombinant hGRIN2A transcript, ensuring the exclusive synthesis of the long transcript. However, at the protein level, the prevention of hGluN2A-S generation remains unclear due to background antibody immunoreactivity and the consistent presence of a double banding pattern corresponding to both isoforms.

One possible explanation for this double banding pattern is the post-translational modification of the synthesised protein in HEK293T cells. GluN subunits contain multiple *N*-glycosylation sites (consensus: N-X-S/T) which regulate NMDAR trafficking and function. Studies have shown that exogenously expressed GluN subunits exhibit two immunoreactive bands on western blots, corresponding to glycosylated and non-glycosylated variants (Chazot, Cik and Stephenson, 1995; Everts, Villmann and Hollmann, 1997; Kaniakova *et al.*, 2016). Treating protein extracts with peptide-N-glycosidase F or endoglycosidase H reduces the immunoreactive band size, indicating the removal of N-glycans. The presence of N-glycans is critical for releasing functional NMDARs from the ER (Lichnerova *et al.*, 2015), and their inhibition significantly reduces NMDAR surface expression and steady-state currents without affecting ligand binding (Everts, Villmann and Hollmann, 1997; Lichnerova *et al.*, 2015).

To confirm the absence of hGluN2A-S protein following A4114G mutation, pretreatment with glycosidases could be employed in future studies. However, due to time constraints, we relied on mRNA-level evidence to demonstrate that the A4114G substitution successfully prevents alternative splicing, allowing the exclusive synthesis of the long hGRIN2A transcript.

3.4.1.2 Rat Grin2A splice site mutagenesis suggests more complex mechanisms of splicing for human GluN2A-S generation

As a secondary objective of this chapter, we aimed to investigate whether the determinants of hGRIN2A alternative splicing—and the absence of splicing in rodent Grin2A—hinge solely on differences at the splice site dinucleotides. This line of inquiry holds potential for generating a second, shorter rodent Grin2A isoform, which could enable the study of its endogenous function in mouse or rat models. Such studies could, in turn, shed light on the role of hGluN2A-S within the human brain.

However, the single nucleotide change at the acceptor splice site in rGrin2A was insufficient to generate two rGrin2A mRNA transcripts. Specifically, substituting the guanine at position 4114 with adenine resulted in a sequence mimicking the donor and acceptor splice site dinucleotides found in hGRIN2A. Despite this, HEK293T were unable to synthesise a second shorter mRNA transcript.

While rodent and human NMDARs share highly conserved sequences and exhibit near-identical pharmacological properties (Hedegaard *et al.*, 2012), additional sequence disparities beyond the splice site dinucleotides may contribute to the alternative splicing observed in human and primate brains (Warming *et al.*, 2019; Herbrechter *et al.*, 2021). As reviewed by Wang and Burge (2008), alternative splicing involves more than the recognition of the 5' splice site, 3' splice site, and branch site. The process is extensively regulated by *cis*-regulated elements, including exonic and intronic splicing enhancers (ESE and ISE) and silencers (ESS and ISS). These elements, located in the exonic and intronic regions flanking the splice sites, function through the recruitment of *trans*-acting splicing factors, which regulate spliceosome assembly and site recognition.

These critical regulatory elements are likely absent or diverged in rGrin2A mRNA, thereby precluding the synthesis of a second protein isoform. This finding underscores the importance of considering disparities between human and rodent nucleotide and protein sequences when using rodent models to study molecular mechanisms relevant to the human brain. Such disparities can limit the direct translation of findings made in rodents to human systems.

For this work, we continue to focus on investigating whether hGluN2A-L and hGluN2A-S contribute distinct functional properties to NMDARs. The novel tool developed to enable the isolated expression of h(r)GluN2A-L provides a valuable resource for studying the isoform-specific effects of hGluN2A-L and hGluN2A-S on NMDAR function.

3.4.2 Future perspectives

Several experimental approaches and considerations could enhance and expand the findings presented in this chapter. A critical question remains whether the A4114G nucleotide substitution completely prevents the generation of the hGluN2A-S protein isoform. While the data suggest this mutation abolishes the production of hGRIN2A-S mRNA transcripts, technical challenges limited our ability to quantify the corresponding reduction in hGluN2A-S protein expression using Western blot – the bands were not clear cut and therefore not quantifiable.

To address this, further optimisation of the SDS-PAGE separation, protein transfer, and western blot procedures could provide a more definitive assessment of the mutagenesis effect on hGRIN2A alternative splicing. Specifically, pretreatment of the protein extract with a glycosidase, as discussed earlier, could help distinguish between glycosylated and non-glycosylated variants, reducing confounding double banding patterns. Additionally, longer separation times on a lower-percentage polyacrylamide gel may improve band resolution.

Another key consideration is the selection of the primary antibody used in western blot analysis. Using an anti-GFP antibody that targets an epitope within the N-terminal eGFP tag may yield a cleaner banding pattern, minimising background immunoreactivity. This approach would increase confidence in distinguishing the effects on h(r)GluN2A-L and hGluN2A-S expression at the protein level.

Implementing these optimisations would enhance our ability to draw robust conclusions about the effects of the A4114G substitution on hGluN2A-S expression. Furthermore, these refinements would ensure that future comparisons of the functional properties of h(r)GluN2A-L and hGluN2A-S reflect their distinct roles in isolation, providing deeper insight into their contributions to NMDAR function and dysfunction.

We have demonstrated that, despite the absence of intronic regions, HEK293T cells possess the capacity to recognise intra-exon splice sites and consequently generate both hGluN2A isoforms. This conservation of splice factors within HEK cells presents an opportunity to investigate the specific splice factors involved in GluN2A-S generation in the human brain. One potential approach is the overexpression of individual candidate splice factors, followed by measurement of resulting hGluN2A-S protein synthesis. This exploratory method has proven valuable in other fields, such as cancer biology, to elucidate splice factors driving alternative splicing. For instance, Zheng et al. (2023) demonstrated that overexpression of USP39, a component of the U4/U6.U5 tri-snRNP complex, enhances hepatocarcinogenesis and tumour proliferation in transgenic mice and human liver cancer cells. Similarly, Liu et al. (2024) reported that overexpression of PQBP1

promotes BAX exon 2 skipping, resulting in increased apoptosis resistance in ovarian cancer cells. Employing such approaches to study hGluN2A-S could provide valuable insight into the splicing mechanisms underlying this primate-specific isoform.

The HEK293 human cell line appears to contain the appropriate spliceosome machinery to generate both hGluN2A isoforms. An unanswered question, however, is whether a rodent cell line—such as PC12—can perform alternative splicing of the hGRIN2A transcript. It is hypothesised that sequence differences between rat and human GRIN2A may partially explain the lack of alternative splicing of rGrin2A. That raises an important question: does the splicing machinery in rodent cells have the capacity for hGluN2A-S generation, but sequence disparities prevent its recognition. Exploring whether rodent cell lines can perform alternative splicing of hGRIN2A may help identify critical splice factors or sequences involved in hGluN2A-S generation.

Previous work by Warming et al. (2019) confirmed the presence of hGluN2A-S in human and primate brains. However, while hGluN2A-S is detectable in whole-brain extracts, it remains unclear whether its expression is region-specific or neuron-type specific. Investigating this question could provide key insights into its functional role in the human brain. One method to address this involves single-cell PCR. By isolating the nucleus from specific, identifiable neuron subtypes and performing PCR on these extracts using primers designed to specifically amplify the hGRIN2A and hGRIN2A-S transcripts, it may be possible to determine neuron-specific expression patterns of hGluN2A-S.

A better understanding of hGluN2A-S generation, expression, and function could pave the way for developing novel strategies to address GRIN2A-associated disorders, such as epilepsy. The ability to manipulate hGluN2A-S expression or activity may offer therapeutic potential, especially if its contribution to dysfunction in such conditions can be elucidated.

Chapter 4 Investigating differences in the current-voltage relationship between Human GluN2A, Rat GluN2A, and Human GluN2A-S

4.1 Introduction

Voltage dependence is a critical feature of NMDARs, underpinning their role in synaptic communication, learning and memory. Any functional divergence between hGluN2A-L and hGluN2A-L—isoforms present in the human brain but absent in rodent models—could reveal mechanisms unique to human synapses. Understanding the functional properties of hGluN2A-S may also shed light on unexplored pathways involved in NMDAR-associated neurological disorders, potentially identifying novel therapeutic targets.

Preliminary electrophysiological recordings by H. Warming and myself examined HEK293T cells transfected with plasmids encoding rGrin1-1a in combination with hGRIN2A or hGRIN2A-S. Interestingly, the data hinted at potential differences in the I-V relationship between these cells. However, cells transfected with hGRIN2A expressed a mixture of hGluN2A-L and hGluN2A-S and thus were difficult to interpret (Hannah, 2018; Houghton, 2019).

This preliminary finding was unexpected, as the Mg²⁺ binding site within the NMDAR channel pore is located far from the C-terminal sequences differences that distinguish the hGluN2A isoforms. Therefore, we aimed to independently assess the voltage-dependent Mg²⁺ blockade of NMDARs containing either hGluN2A-L or hGluN2A-S. This approach would provide evidence for isoform-dependent NMDAR function in hGluN2A diheteromeric receptors.

Using the plasmid generated in the previous chapter for exclusive expression of GluN2A-L, h(r)GluN2A-L, (expressed by the plasmid pcDNA3.1+eGFP-hGluN2A^{A4114G}), we could selectively express the long or short isoforms of hGluN2A in HEK293T cells. This allowed us to isolate and compare the electrophysiological properties of NMDARs containing these isoforms independently.

4.2 Aims and Objectives

The overarching aim of this chapter is to investigate preliminary findings suggesting that hGluN2A-S affects the voltage dependency of NMDARs. Utilising the approach described in Chapter 3 to express h(r)GluN2A-L isolation, we aim to examine the current-voltage relationship

of rodent and human NMDARs. We will measure NMDAR-mediated currents in response to voltage steps in the presence of a locally applied NMDA agonist.

To achieve this, we will first develop a method for measuring stationary NMDAR conductance during local NMDA application, minimising baseline changes caused by activation, deactivation and desensitisation by reaching equilibrated state conditions. Next, we will analyse the voltage-dependence of human and rat NMDARs (rGluN2A, h(r)GluN2A-L and hGluN2A-S) expressed in HEK293T cells and will assess Mg²⁺ sensitivity under physiological and low Mg²⁺ conditions. Finally, we will isolate and compare the effects of h(r)GluN2A-L and hGluN2A-S on NMDAR responses during voltage steps and action potential waveforms.

The aims of this chapter are as follows:

- Develop a method for recording stationary NMDAR-mediated conductance in transfected HEK293T cells during NMDA application.
- 2. Investigate the current-voltage relationship of NMDARs containing rGluN2A, h(r)GluN2A-L or hGluN2A-S during instantaneous block and unblock.
- 3. Explore Mg²⁺ blockade in hGluN2A-S-containing NMDARs during non-instantaneous block and unblock.

4.3 Results

4.3.1 Stationary NMDAR-mediated conductance during local application of NMDA via iontophoresis

To establish a method for recording stationary NMDAR-mediated conductance with minimal desensitisation, we transfected HEK293T cells with expression vectors expressing eYFP-rat GluN1-1a and eGFP-h(r)GluN2A-L. The fluorescent eYFP and eGFP tags facilitated the identification of successfully transfected cells. Our objective was to activate NMDAR currents and achieve stationary conductance over several seconds. Enabling the subsequent assessment of voltage dependence across rodent and human NMDAR subunits.

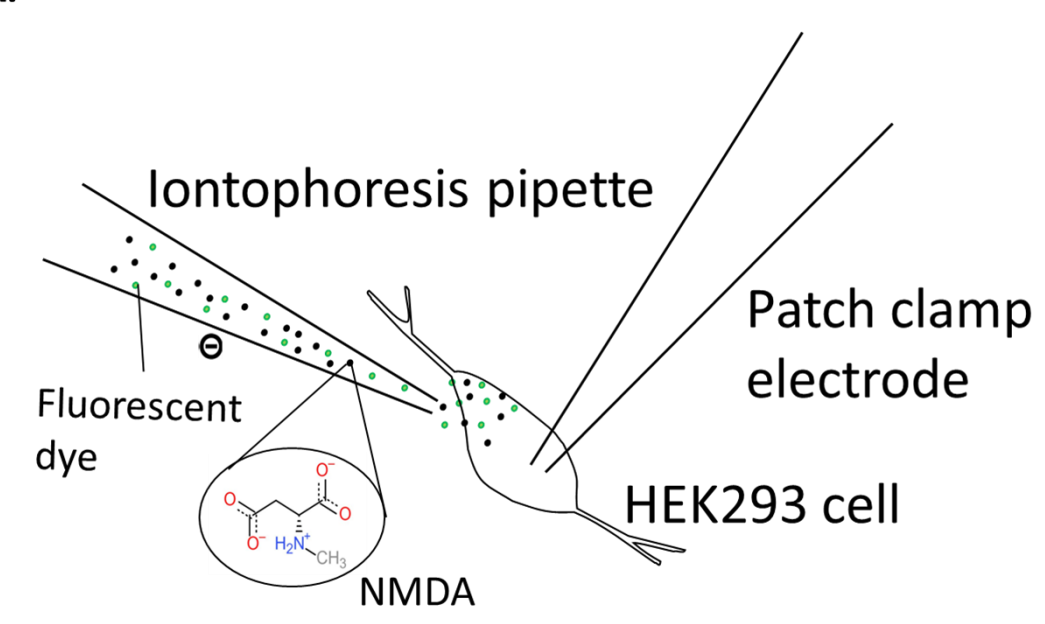
Whole-cell patch-clamp recordings were performed in voltage-clamp mode, where HEK cells were subjected to a voltage step from -80 mV to +50 mV. To elicit NMDAR-mediated currents, a saturating glycine concentration (10 μ M) was present in the extracellular solution and an iontophoresis pipette containing NMDA (150 mM) was used. Iontophoresis provided rapid, localised NMDA exposure via controlled retain or eject currents. Additionally, Alexa 488 or Lucifer

yellow dyes were included in the pipette to visualise NMDA ejection, confirm retention, and detect potential pipette blockages (Figure 4.1A).

Current responses during the voltage step were recorded in the absence of local NMDA perfusion to account for leak currents. These leak currents were subtracted from the responses recorded during NMDA application to isolate NMDAR-mediated currents.

Consistent with previous findings by Nahum-Levy et al. (2001), the resultant NMDAR-mediated currents showed no observable desensitisation over several seconds at a constant membrane potential (Nahum-Levy et al., 2001). This observation, replicated across multiple independent recordings, confirmed stationary NMDAR activation at equilibrium (Figure 4.1B). Achieving this stable activation allowed us to proceed with measuring and comparing the current-voltage relationship across rodent and human NMDAR subunits during a slow voltage ramp.

A.



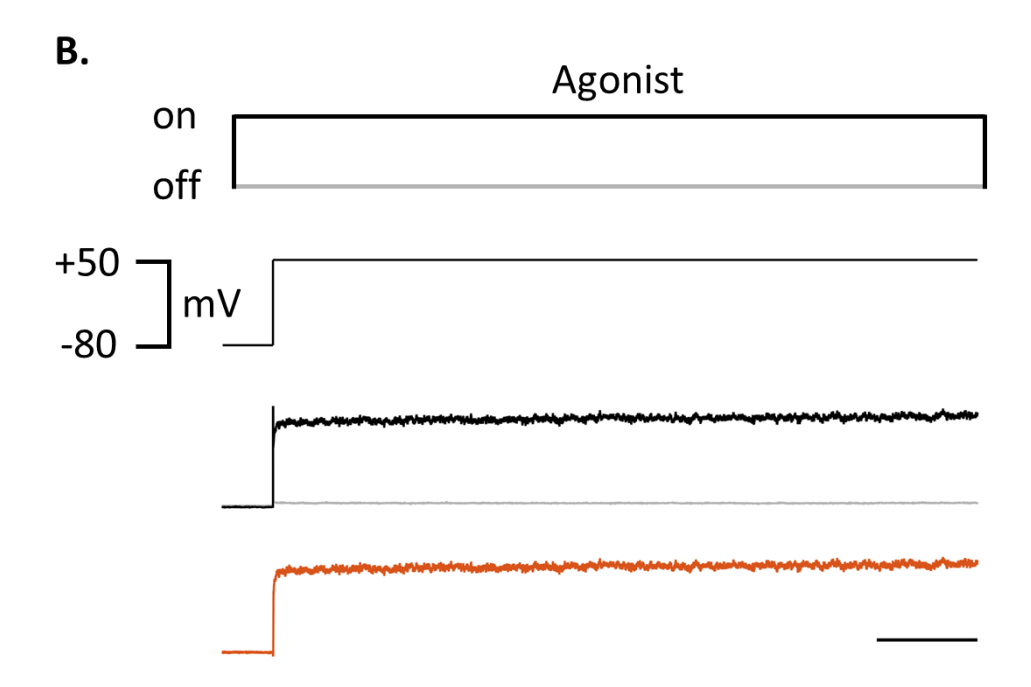


Figure 4.1 - Establishing a stationary NMDA receptor conductance.

A) Cartoon depicting whole-cell patch-clamp recording of HEK293T cells with simultaneous local perfusion of NMDA agonist using iontophoresis to activate exogenously expressed NMDA receptors and obtain stationary NMDA receptor conductance. A negatively charged fluorescent dye (represented by green dots) is present to allow the visualisation of NMDA (represented by black dots) application during negative eject current and cessation of agonist application during positive retain current. B) (top) HEK293T cells exogenously expressing h(r)GluN2A-L were

subjected to either no application of NMDA (grey line) or constant local application of NMDA (black line) indicating negative charge applied via iontophoresis. (middle) Cells were voltage-clamped from -80mV to +50mV. (bottom) The corresponding current was recorded in the absence (grey trace) or presence of an agonist (black) trace. Leak subtraction from the raw trace was performed to obtain the NMDAR-mediated current response to agonist application (red). Sample trace representative of an average of 2 recording sweeps from N = 9 cells. Scale bar = 500 ms.

4.3.2 Analysis of voltage-dependence of rGluN2A, h(r)GluN2A-L and hGluN2A-S-containing NMDARs during instantaneous Mg²⁺ unblock.

To investigate the equilibrium I-V relationship of NMDARs containing rGluN2A, h(r)GluN2A-L, or hGluN2A-S, HEK293T cells were subjected to a slow voltage ramp from -80 mV to +50 mV during stationary NMDAR activation using local NMDA application via iontophoresis. This produced typical non-linear J-shaped I-V curves, with reversal potentials near -4 mV and maximal inward currents around -20 mV. Responses recorded in the absence of NMDA were subtracted from those with NMDA to isolate the NMDAR-mediated currents (Figure 4.2Ai-iii).

To minimise noise effects, we calculated a moving average with a sliding window of 25 ms, allowing a more accurate determination of the maximum current at +49-50 mV. Current amplitudes varied across NMDAR subtypes (Figure 4.2Aiv).

To compare voltage dependence, we normalised individual I-V curves to the current at +49-50 mV, where maximal Mg²⁺ unblock is expected. While rGluN2A and h(r)GluN2A-L displayed similar normalised I-V curves, hGluN2A-S-containing NMDARs exhibited a noticeable shift showing a smaller fraction of current unblocked at negative membrane potentials, particularly between -20 mV and -30 mV (Figure 4.2Bi, Bii). Despite this shift, the membrane potential corresponding to the maximal inward current obtained was consistent across all subtypes (Figure 4.2C).

Previous work by Garashuk et al. (1996) showed that maximal Ca²⁺ influx through NMDARs occurs at around -10 mV, rather than at the membrane potential for maximal inward current. To explore this although we did not measure Ca2+ directly, as a proxy, we compared the fraction of unblocked current at -10 mV across NMDAR subtypes (Garaschuk *et al.*, 1996). Moving averaged I-V curves revealed no significant differences in current at this potential between rGluN2A, h(r)GluN2A-L, and hGluN2A-S-containing NMDARs (Figure 4.2D).

These findings suggest that hGluN2A-S alters the voltage dependence of NMDARs at negative potentials while retaining similar current characteristics at potentials associated with maximal

 Ca^{2+} influx. This highlights potential functional differences in Mg^{2+} sensitivity and gating between the subunits.

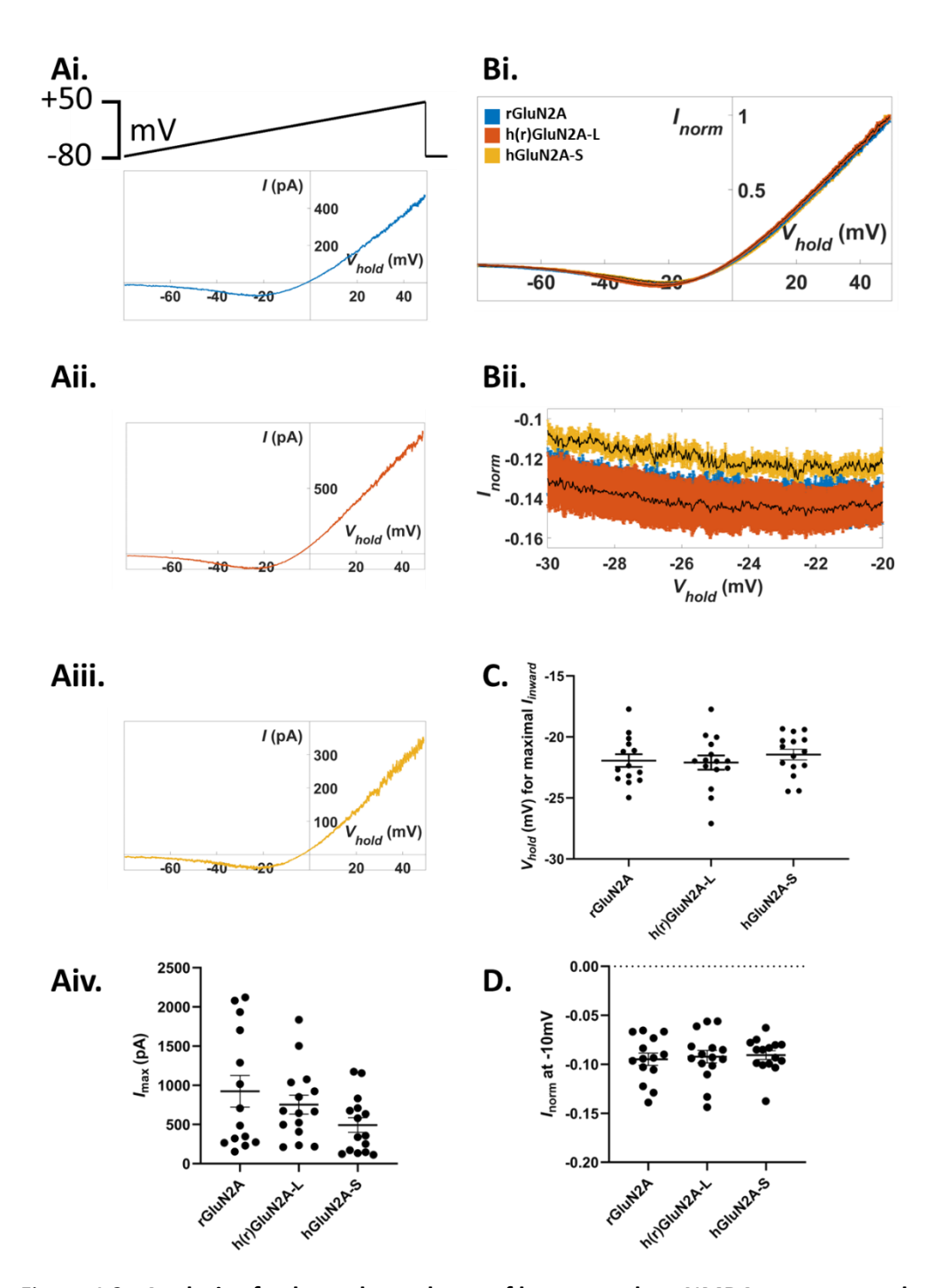


Figure 4.2 - Analysis of voltage dependence of human and rat NMDA receptors: subtracted and normalised.

Ai-iii) During the local application of NMDA, HEK293T cells were subjected to a slow voltage ramp (4 sec) from -80mV to +50mV. Representative sample traces of current-voltage relationships from HEK293T cells expressing rGluN1-1a alongside rGluN2A (blue), h(r)GluN2A-L (red) or hGluN2A-S (yellow), respectively. Endogenous currents in the absence of an NMDA were subtracted from currents in the presence of NMDA.

Traces averaged from one cell per condition. **Aiv, C + D)** A moving average of subtracted data was calculated with a sliding window size of 25 ms to remove noise. **Aiv)** The maximum current at +49-50 mV was then extracted. **Bi)** Leak subtracted data for each condition were averaged from rGluN2A N = 14 cells, h(r)GluN2A-L N = 15 cells, hGluN2A-S N = 15 cells and normalised to the current at +49-50 mV where maximal Mg²⁺ unblock is achieved. This allowed comparisons of behaviour at negative membrane potentials. Data is displayed as mean (black) with SEM (blue, red and yellow respectively). **Bii)** A zoomed view of the current-voltage relationship at holding potentials between -20mV and -30mV. **C)** The holding potential required for maximum inward current extracted from normalised current-voltage relationship recordings. **D)** Normalised current at -10mV as relevant to Ca²⁺ entry, extracted from normalised current-voltage relationship recordings. rGluN2A N = 14 cells. h(r)GluN2A-L N = 15 cells. hGluN2A-S N = 15 cells. Current-voltage curves from each cell are averaged from 2 recording sweeps.

4.3.2.1 Voltage Dependence of Mg²⁺ Block and Conductance-Voltage Analysis

The voltage dependence of NMDARs arises primarily from the Mg²⁺ block, which follows a Boltzmann distribution in the electric field (Woodhull, 1973; Wollmuth, Kuner and Sakmann, 1998). Current responses obtained during a slow voltage ramp were transformed into conductance-voltage (G-V) relationships by estimating the unblocked NMDAR current in the absence of Mg²⁺. This ohmic response was estimated by fitting a linear slope to the cord conductance at positive membrane potentials using least squares (Figure 4.3A). The actual current was divided by this estimated unblocked current to calculate the fraction of conductance as a function of membrane potential (Figure 4.3B), and the data were fitted to a Boltzmann distribution:

Equation 4.1 - Boltzmann distribution

$$B(V) = \frac{1}{1 + \exp\left(-\frac{(V - V_{0.5})z\delta F}{RT}\right)}$$

Where B is the fraction blocked, $V_{0.5}$ is the voltage for the half-maximal block, z is the valence of the blocking ion (+2), δ is the fraction of the electric field sensed by Mg^{2+} , T is the temperature in Kelvin (293.15 K) and R and G are physical constants.

To compare Mg^{2+} sensitivity between NMDAR subtypes, the Boltzmann equation was fitted to normalised G-V relationships for rGluN2A, h(r)GluN2A-L , and hGluN2A-S-containing NMDARs. Our analysis revealed that hGluN2A-S-containing receptors exhibited a significantly smaller δ value (0.87 \pm 0.02) compared to h(r)GluN2A-L (0.95 \pm 0.02, p = 0.004), while the δ value of rGluN2A (0.90 \pm 0.02) was intermediate and not significantly different from either isoform (Figure 4.3C).

Additionally, hGluN2A-S-containing receptors had a significantly less negative $V_{0.5}$ (-7.4 \pm 0.9 mV) compared to both h(r)GluN2A-L (-12.5 \pm 1.5 mV, p = 0.006) and rGluN2A (-11.6 \pm 1.2 mV, p = 0.009) (Figure 4.3D). This indicates a reduced voltage sensitivity and increased Mg²⁺ block for hGluN2A-S-containing NMDARs.

Finally, the percentage unblock at the membrane potential corresponding to the maximal inward current (Figure 4.2C) was extracted from individual G-V curves. hGluN2A-S-containing NMDARs showed a significantly smaller percentage unblocked (27.7% \pm 0.9) compared to both rGluN2A (32.6% \pm 1.5, p = 0.0099) and h(r)GluN2A-L (33.2% \pm 1.8, p = 0.012) (Figure 4.3E).

These findings indicate that hGluN2A-S-containing NMDARs exhibit increased sensitivity to Mg^{2+} blockade, with both δ and $V_{0.5}$ values reflecting distinct voltage-dependent properties. This suggests that the hGluN2A-S isoform alters Mg^{2+} binding or channel gating, potentially affecting synaptic function under physiological conditions.

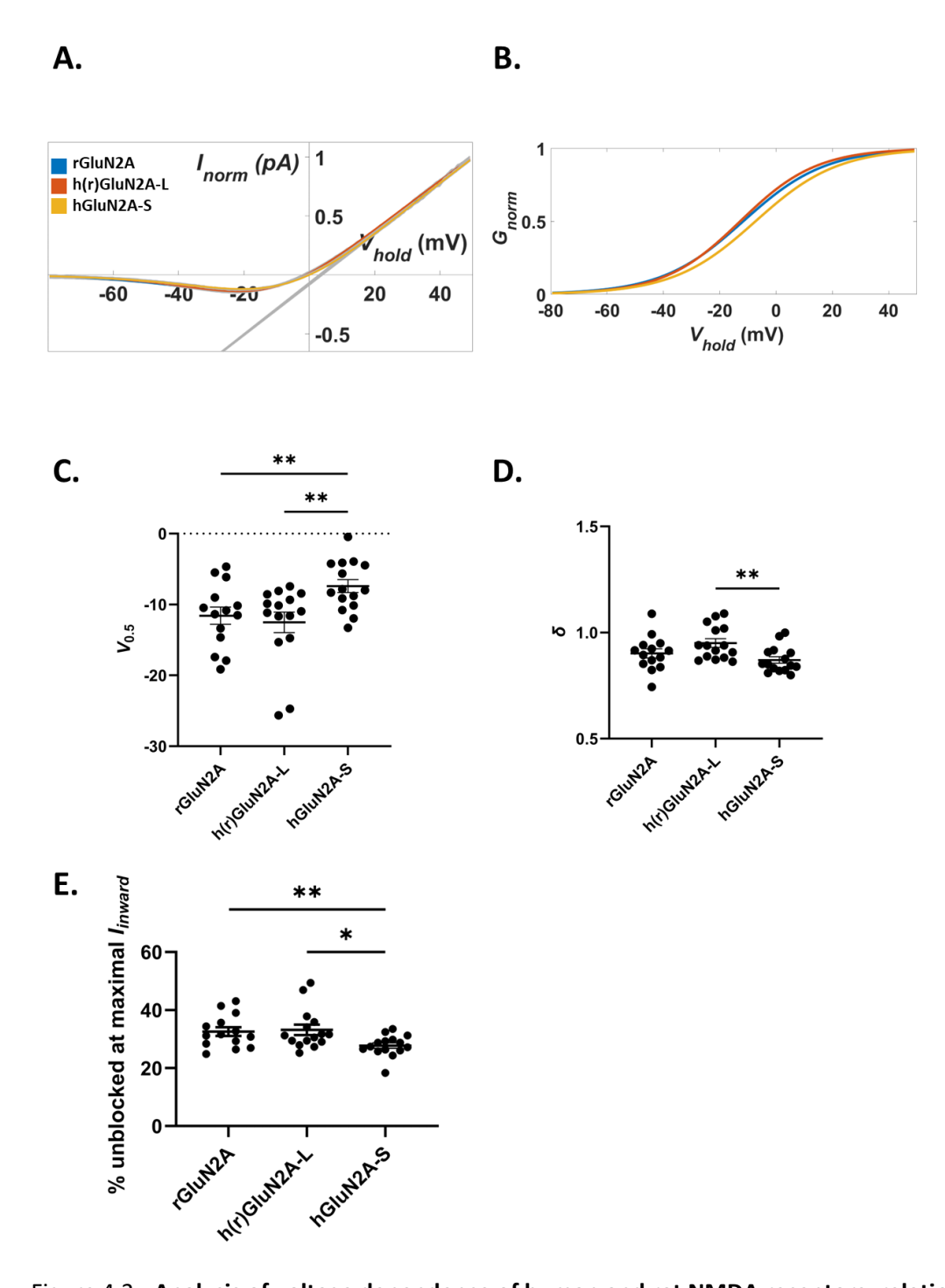


Figure 4.3 - Analysis of voltage dependence of human and rat NMDA receptors: relationship between expected linear and blocked current.

A) The cord conductance was calculated using the moving-averaged data. This was using a least square fitting (grey straight lines) to the linear portion of the normalised and averaged current-voltage data to model maximal expected current in the absence of Mg²⁺ antagonism. Subtracted and normalised current-voltage data (grey) were fitted using a Boltzmann-type equation (rGluN2A - blue, h(r)GluN2A-L - red, and hGluN2A-S - yellow). B) The fraction of the maximal slope G-V relationship is plotted as a function of membrane potential, fitted to a Boltzmann-type distribution. C) The

voltage for the half-maximal block ($V_{0.5}$) extracted from the Boltzmann-type equation summarised in B. rGluN2A vs. hGluN2A-S; unpaired t-test, P = 0.0099, two-tailed. h(r)GluN2A-L vs. hGluN2A-S; unpaired t-test, P = 0.0058, two-tailed. **D)** The fraction of the membrane potential sensed by the blocking site (δ) extracted from the Boltzmann-type equation summarised in B. h(r)GluN2A-L vs. hGluN2A-S; unpaired t-test, P = 0.0041, two-tailed. **E)** The percentage unblock at maximal inward current was extracted from individual G-V curves. rGluN2A vs. hGluN2A-S; unpaired t-test, P = 0.0099, two-tailed. h(r)GluN2A-L vs. hGluN2A-S; unpaired t-test, P = 0.012, two-tailed. Rat GluN2A N = 14 cells. Human h(r)GluN2A-L N = 15 cells. Human GluN2A-S N = 15 cells.

4.3.2.2 Current-voltage relationship of NMDARs under low Mg²⁺ conditions

To further investigate the differences in the current-voltage relationships of hGluN2A-S-containing NMDARs, we recorded responses at low external Mg²⁺ concentration (0.1mM). We hypothesised that NMDARs would display a more linear, ohmic current-voltage relationship due to reduced Mg²⁺ availability to block the channel pore at negative membrane potentials. As expected, local NMDA application during a slow voltage ramp produced J-shaped I-V curves with reversal potential around -4 mV across all subunits. To isolate NMDAR-mediated response, we subtracted I-V data recording in the absence of NMDA agonist from that recorded in its presence. Representative I-V curves for each subunit are shown in Figure 4.4Ai-iii.

As with physiological Mg^{2+} conditions, we applied a moving average with a 25 ms sliding window to minimise noise-driven artifacts and extracted the maximum current amplitude at +49-50 mV. Among the NMDAR subunits test, rGluN2A-containing NMDARs exhibited the largest variability in current amplitudes (1313 \pm 331 pA) and a significantly higher mean current compared to h(r)GluN2A-L-containing NMDARs (458 \pm 103 pA, p = 0.023), but not hGluN2A-S-containing receptors (550 \pm 175 pA) (Figure 4.4Aiv).

To compare voltage-dependence at negative membrane potentials, we normalised individual I-V curves to the current at +50 mV. While rGluN2A and h(r)GluN2A-L-containing receptor shifted towards a more linear response in low Mg²⁺ conditions, hGluN2A-S-containing NMDARs maintained a pronounced J-shaped curve, indicating persistent Mg²⁺ block (Figure 4.4Bi). This divergence in voltage dependence was most apparent at membrane potentials below -20 mV (Figure 4.4Bii).

To quantify these differences, we identified the membrane potential corresponding to the maximal inward current from individual normalised I-V curves. hGluN2A-S-containing NMDARs

exhibited a significantly more depolarised voltage for maximal inward current (-41.5 \pm 2.5 mV) compared to rGluN2A (-55.6 \pm 2.4 mV, p = 0.0021) and h(r)GluN2A-L (-50.9 \pm 2.5 mV, p = 0.023) (Figure 4.4C).

Finally, we examined normalised inward current at -10 mV, a critical membrane potential for NMDAR-mediated Ca²⁺ influx (Garaschuk *et al.*, 1996). hGluN2A-S-containing NMDARs exhibited significantly lower inward current (-0.13 \pm 0.01) than both rGluN2A (-0.17 \pm 0.01, p = 0.04) and h(r)GluN2A-L (-0.19 \pm 0.01, p = 0.0028) (Figure 4.4D). These results demonstrate that, unlike rGluN2A and h(r)GluN2A-L-containing receptors, hGluN2A-S maintains strong voltage-dependence and Mg²⁺ block even under low Mg²⁺ conditions, underscoring their unique functional profile.

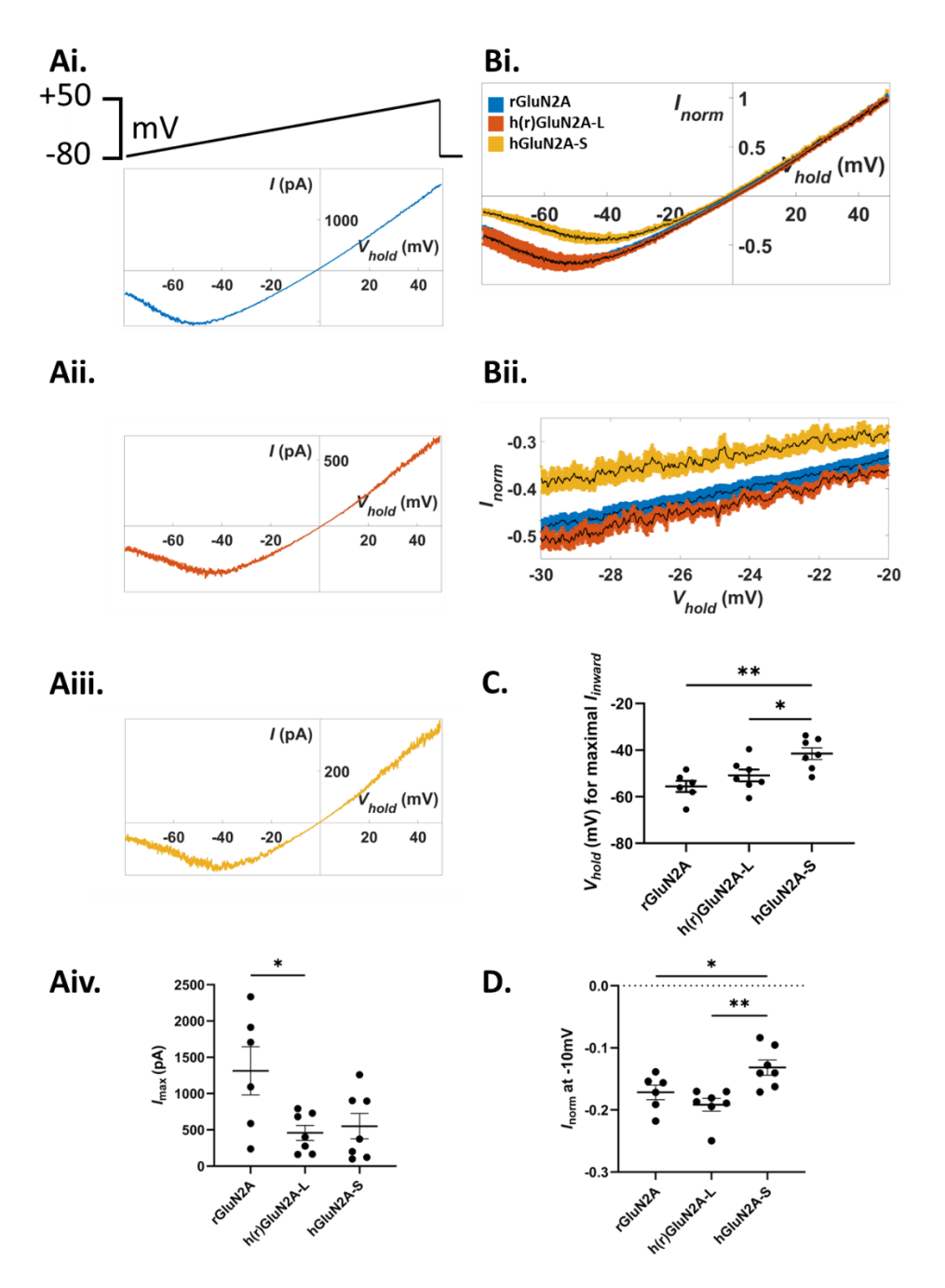


Figure 4.4 - Analysis of voltage dependence of human and rat NMDA receptors in low extracellular magnesium: subtracted and normalised.

Ai-iii) During local application of NMDA, HEK293T cells were subjected to a slow voltage ramp stimulus (4 sec) that voltage clamped the cell in increments from - 80mV to +50mV. Representative sample (liquid-junction potential corrected) traces of current-voltage relationships at low extracellular Mg²⁺ concentration (0.1mM) from HEK293T cells exogenously expressing rGluN1-1a alongside rGluN2A (blue), h(r)GluN2A-L (red) or hGluN2A-S (yellow), respectively. Endogenous currents in the absence of an agonist are shown in grey. **Aiv, C + D**) A moving average of subtracted

data was calculated with a sliding window size of 500 samples to remove noise. **Aiv**) The maximum current at +50mV was then extracted. rGluN2A vs. h(r)GluN2A-L, unpaired t-test, P = 0.02, two-tailed. **Bi**) Currents in the absence of NMDA were subtracted from currents in the presence of NMDA before being averaged and normalised. Data is displayed as mean (black) with SEM (blue, red and yellow respectively) **Bii**) A zoomed view of the current-voltage relationship at holding potentials between -20mV and -30mV. **C**) The holding potential required for maximum inward current extracted from normalised current-voltage relationship recordings. rGluN2A vs. hGluN2A-S; unpaired t-test, P = 0.0021, two-tailed. h(r)GluN2A-L vs. hGluN2A-S; unpaired t-test, P = 0.0225, two-tailed. **D**) Normalised current at maximal Ca²⁺ entry (-10mV) extracted from normalised current-voltage relationship recordings. rGluN2A vs. hGluN2A-S; unpaired t-test, P = 0.04, two-tailed. h(r)GluN2A-L vs. hGluN2A-S; unpaired t-test, P = 0.003, two-tailed. rGluN2A N = 6 cells. h(r)GluN2A-L N = 7 cells. hGluN2A-S N = 7 cells.

4.3.3 Investigation of Mg²⁺ blockade in hGluN2A-S-containing NMDARs during non-instantaneous block and unblock.

In the previous sections, we investigated the voltage-dependence of hGluN2A-S-containing NMDARs during a slow voltage ramp, modelling instantaneous Mg²⁺ unblock. However, in physiological conditions, Mg²⁺ unblock, and block are not instantaneous but exhibit distinct kinetics (Vargas-Caballero and Robinson, 2003). Moreover, although GluN2A-containing NMDARs exhibit faster Mg²⁺ unblock compared to GluN2B-containing NMDARs, we questioned whether there is an isoform-dependent difference in Mg²⁺ block and unblock between hGluN2A-L and hGluN2A-S (Qian, Buller and Johnson, 2005; Clarke and Johnson, 2006).

To isolate and compare non-instantaneous unblock and block kinetics of h(r)GluN2A-L and hGluN2A-S, we subjected transfected HEK293T cells to a voltage step protocol, transitioning from -70 mV to + 40 mV over 250 ms. We hypothesised that NMDAR current responses would exhibit asymmetry relative to the voltage step command, reflecting the kinetic processes underlying Mg^{2+} unblock and re-block.

We observed that during the depolarisation step from -70 mV to +40 mV, hGluN2A-S-containing receptors displayed a reduced rise in current before reaching the stationary phase compared to h(r)GluN2A-L. For example, at 20 ms following the depolarisation step hGluN2A-L receptors reached maximal normalised current (1.00 \pm 0.002) compared to the significantly reduced normalised current in hGluN2A-S-containing receptors (0.89 \pm 0.024, p = 0.032). Conversely,

during the repolarising step from +40 mV back to -70 mV, hGluN2A-S-containing receptors exhibited a modest but not statistically significant difference in recovery to resting current levels during repolarisation (-0.23 \pm 0.12) compared to hGluN2A-L (-0.03 \pm 0.02, p = 0.243). This pilot data may suggest a subtle difference in the characteristic hooked tail current in hGluN2A-S-containing receptors, allowing for a brief inward transient during Mg²⁺ re-block (Figure 4.5A).

To further explore these kinetic differences, we implemented a shorter voltage step protocol (5 ms duration), stepping from either -70 mV or 0 mV to +40 mV. Under these conditions, the reduced rise in current during the depolarising step and the faster recovery during the repolarising step of hGluN2A-S-containing NMDARs were more pronounced. For example, 1 ms following the depolarisation step there was a significantly increased normalised current in h(r)GluN2A-L-containing receptors (0.80 \pm 0.013) compared to hGluN2A-S receptors (0.74 \pm 0.005, p = 0.014). Notably, the reduced current rise during depolarisation was evident even when the initial holding potential was depolarised to 0 mV (h(r)GluN2A-L, 0.95 \pm 0.001 vs. hGluN2A-S, 0.89 \pm 0.009, p = 0.015). We again observed a potential difference in the hooked tail current during repolarisation for hGluN2A-S-containing receptors (-0.31 \pm 0.13) compared to hGluN2A-L (-0.04 \pm 0.02), although this difference was not statistically significant (Figure 4.5B).

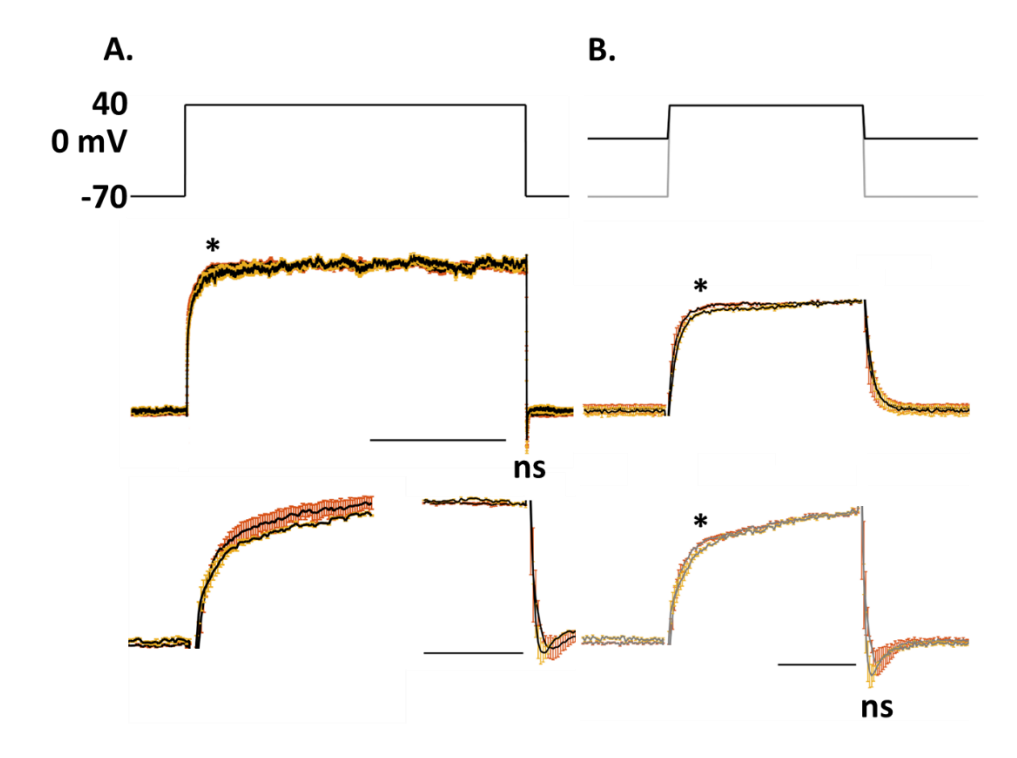


Figure 4.5 - NMDA-induced currents during voltage-steps.

During local application of NMDA, HEK293T cells were subjected to **A)** (top) a voltage step from -70 to +40 mV (250 ms). (middle) Leak subtracted data for each condition were averaged from hGluN2A-L-only (red) N = 2 cells, hGluN2A-S (yellow) N = 3 cells and the amplitude was normalised to the maximum (steady state) current. Data is

displayed as mean (black) with SEM (red and yellow respectively). Scale bar = 100 ms. hGluN2A-L-only vs. hGluN2A-S; unpaired t-test 20 ms following depolarisation, P = 0.032, two-tailed; unpaired t-test 0.25 ms following repolarisation, P = 0.24. (bottom) Expanded time scale from data above to highlight the current responses during depolarisation and repolarisation. Scale bar = 2 ms. B) (top) voltage steps to +40 mV starting from -70 (grey) and 0 mV (black) (5 ms). Leak subtracted data for each condition were averaged from hGluN2A-L-only N = 2 cells, hGluN2A-S N = 3 cells and the amplitude was normalised to the maximum (steady state) current. Data is displayed as mean (black, middle: 0 mV; grey, bottom: -70 mV) with SEM (red and yellow respectively). Scale bar = 2 ms. Stimulation artifacts have been removed averaged traces. Square wave from 0mV, hGluN2A-L-only vs. hGluN2A-S; unpaired t-test 1 ms following depolarisation, P = 0.015, two-tailed. Square wave from -70 mV hGluN2A-L-only vs. hGluN2A-S; unpaired t-test 1 ms following depolarisation, P = 0.014, two-tailed: unpaired t-test 0.25 ms following repolarisation, P = 0.15.

Lastly, to begin assessing the functional implications of differences in voltage dependence observed in hGluN2A-S during non-instantaneous Mg²⁺ block and unblock, we conducted a pilot study. HEK293T cells transfected with NMDAR subunits were subjected to action potential waveforms recorded from layer 5 pyramidal neurons by Larkum et al. (2001). Current responses during waveforms were normalised to the current during the voltage step at +40 mV. Current responses during these waveforms were compared to predicted currents derived from stationary I-V relationships obtained during slow voltage ramp stimulation, which simulate instantaneous Mg²⁺ unblock. Moving-averaged, leak-subtracted, and normalised stationary I-V curves were fitted with a Boltzmann-type distribution (Equation 4.1). These fitted curves were used to model expected instantaneous current responses for comparison with experimentally recorded currents during non-instantaneous Mg²⁺ unblock and block (Figure 4.6A, B).

We first examined current response during fast, somatic Na⁺ backpropagating action potentials. Consistent with previous findings by Vargas-Caballero and Robinson (2003), we observed reduced inward currents during the fast depolarisation phase of Na⁺ spikes compared to the predicted current from stationary I-V relationships (Vargas-Caballero and Robinson, 2003). Conversely, during the repolarisation phase, the measured current matches or exceeds that predicted by the stationary I-V curve, highlighting the influence of Mg²⁺ block and unblock mechanisms.

Relative to the expected current during instantaneous block and unblock, we observed a delayed current response from both h(r)GluN2A-L and hGluN2A-S-containing receptors. We observed this

delay during both the depolarisation and repolarisation phases of the action potential waveform, highlighting the non-instantaneous unblock and re-block of Mg²⁺ (Figure 4.6C+D).

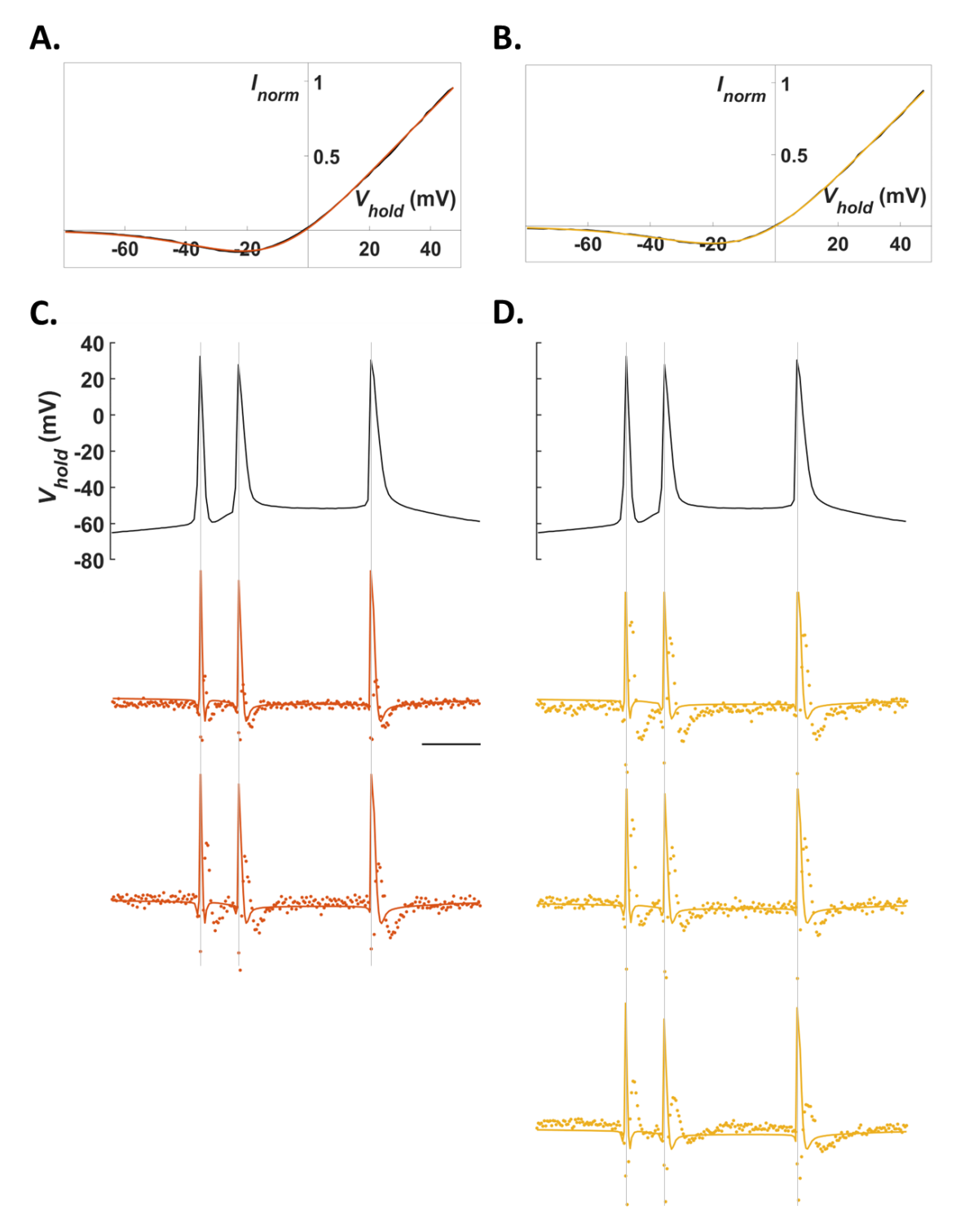


Figure 4.6 - NMDA-induced currents during action potential waveform stimulation: fast somatic Na+ backpropagating action potential.

HEK293T cells were transfected with rGluN1-1a with either h(r)GluN2A-L (red) or hGluN2A-S (yellow) **A+B)** Black traces show moving averaged, leak subtracted and normalised NMDAR current during a slow voltage ramp (4 sec) from -80 mV to +50

mV fitted using a Boltzmann-type equation (h(r)GluN2A-L- red; hGluN2A-S – yellow). **C+D)** Current responses (bottom) to fast somatic Na⁺ backpropagating action potential waveform (top) normalised to the current during the voltage step at +40 mV. The expected current from instantaneous block/unblock fitted in A and B is superimposed as solid lines in red and yellow, respectively. Each response is from an individual cell. Black grid lines mark the peak of each action potential. Scale bar = 2 ms.

We next examined current responses in HEK293T cells subjected to dendritic Na⁺/Ca²⁺ action potentials corresponding to the somatic backpropagating Na⁺ action potential described above. Both h(r)GluN2A-L and hGluN2A-S isoforms displayed similar response, consistent with prior observations by Vargas-Caballero and Robinson (2003). During the upstroke of the calcium action potential, the non-stationary NMDAR-mediated current closely followed the predicted stationary current. However, in all but one of the hGluN2A-S response, we observed a reduction in inward current compared to the predicted values following the short repolarisations at the plateau phase of the Ca²⁺ action potential (Figure 4.7)

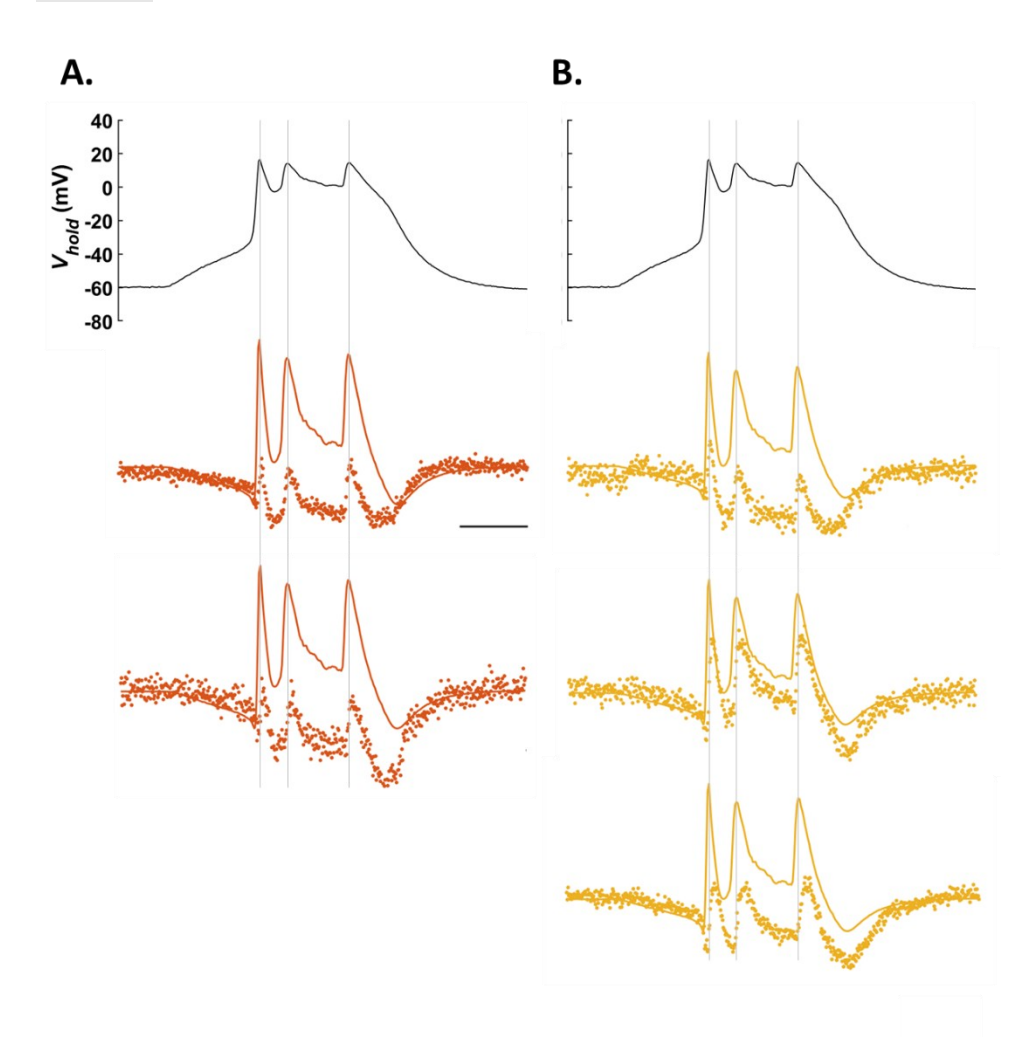


Figure 4.7 - NMDA-induced currents during action potential waveform stimulation: dendritic Na+/Ca+ action potential.

HEK293T cells were transfected with rGluN1-1a with either h(r)GluN2A-L (red) or hGluN2A-S (yellow) A+B) Current responses (bottom) to dendritic Na $^+$ /Ca $^+$ action potential waveform (top) normalised to the current during the voltage step at +40 mV. The expected current from instantaneous block/unblock fitted in A and B is superimposed as solid lines in red and yellow, respectively. Each response is from an individual cell. Black grid lines mark the peak of each action potential. Scale bar = 5 ms.

We next recorded current responses to a slow Na⁺ spikelet/boosted excitatory post-synaptic potential (EPSP). As anticipated, the NMDAR-mediated current closely matched the predicted stationary I-V relationship for both h(r)GluN2A-L and hGluN2A-S isoforms (Figure 4.8).

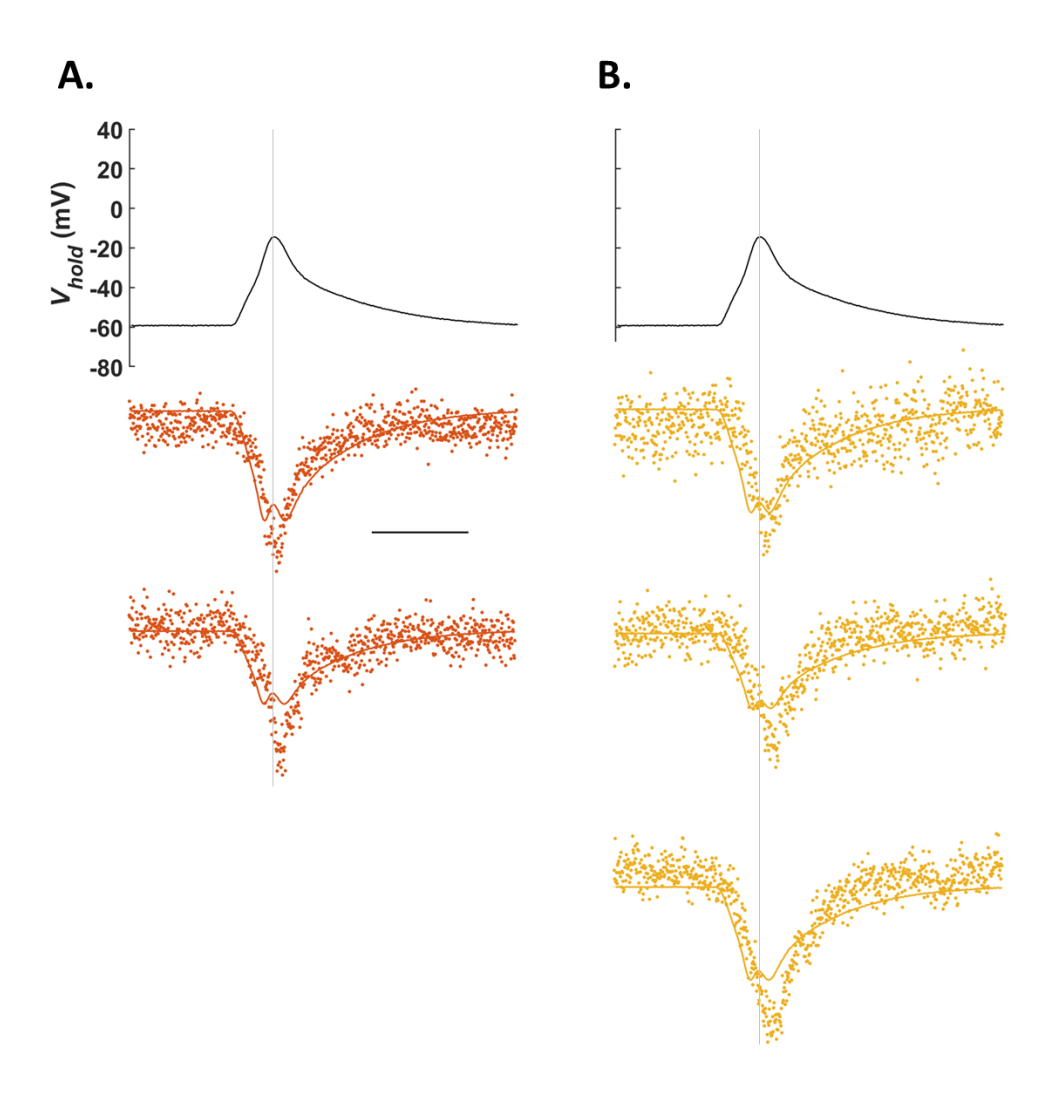


Figure 4.8 - NMDA-induced currents during action potential waveform stimulation: all-or-none dendritic Na+ action potential (boosted excitatory postsynaptic potential.

HEK293T cells were transfected with rGluN1-1a with either h(r)GluN2A-L (red) or hGluN2A-S (yellow) A+B) Current responses (bottom) to all-or-none dendritic Na⁺ action potential (boosted excitatory postsynaptic potential waveform (top) normalised to the current during the voltage step at +40 mV. The expected current from instantaneous block/unblock fitted in A and B is superimposed as solid lines in red and yellow, respectively. Each response is from an individual cell. Black grid lines mark the peak of each action potential. Scale bar = 10 ms.

Finally, we compared the I-V relationship obtained from slow voltage ramp response with those during the three action potential waveforms. Notable differences emerged between the expected instantaneous NMDAR current from stationary I-V curves and the observed non-instantaneous NMDAR current due to Mg²⁺ unblock kinetics. The non-stationary I-V relationship displayed greater variability, and for both h(r)GluN2A-L and hGluN2A-S isoforms, it mimicked the characteristic non-linear J-shaped curve observed in stationary I-V relationships at negative membrane potentials. However, at more depolarised membrane potentials we observed a

reduced current during non-instantaneous NMDAR currents, this was likely due to the slow unblocking kinetics of Mg²⁺ during depolarisation (Figure 4.9).

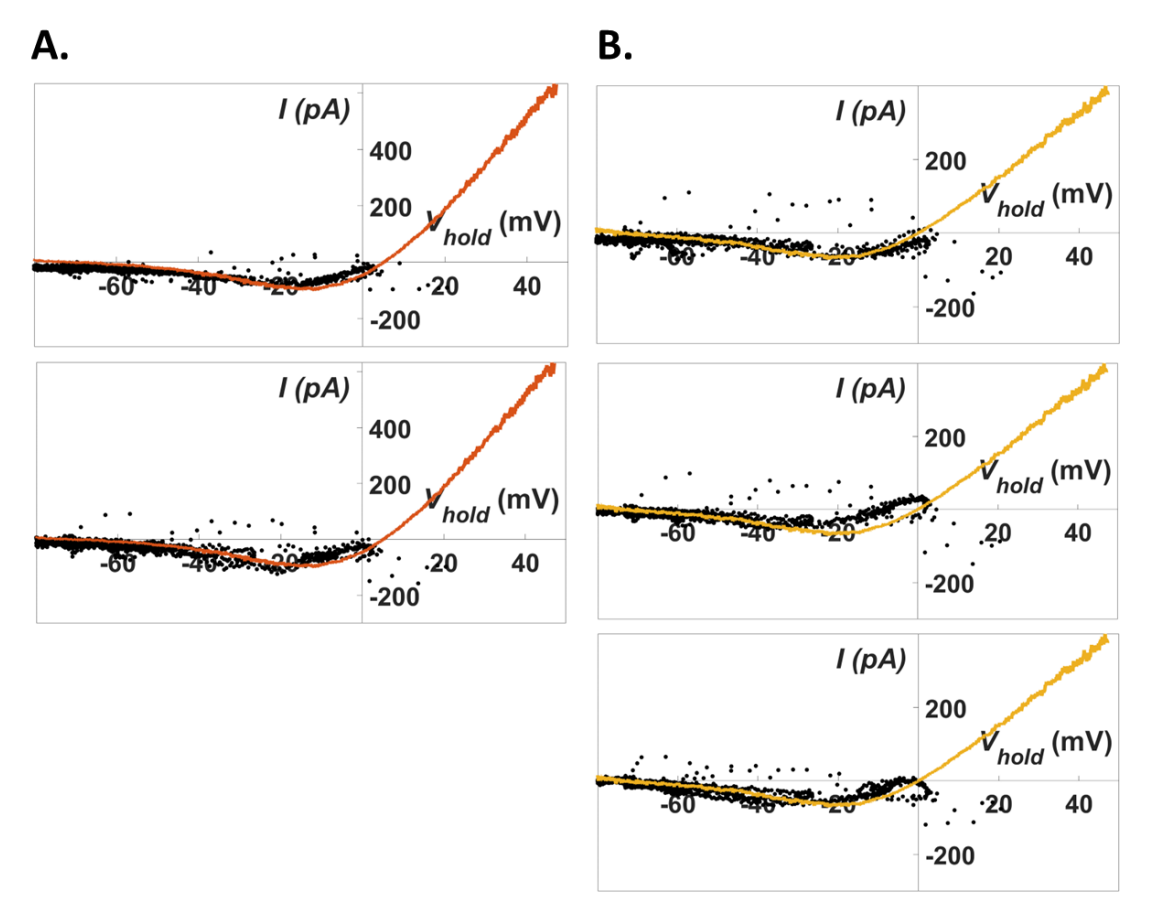


Figure 4.9 - NMDA-induced current-voltage relationship during either slow voltage ramp or during action potential waveform stimulation.

HEK293T cells were transfected with rGluN1-1a with either h(r)GluN2A-L (red) or hGluN2A-S (yellow) **A+B)** The red and yellow traces show a sample trace of current observed during a 4 second ramp in voltage from a cell transfected with either h(r)GluN2A-L and hGluN2A-S, respectively. The superimposed black dotted points represent the current observed during the AP-waveforms. Each trace of response during AP-waveforms is from an individual cell.

4.4 Discussion

4.4.1 Conclusions and Key Findings

4.4.1.1 hGluN2A-S increases magnesium sensitivity of exogenous NMDAR current in HEK293T cells.

In this chapter, we investigated a preliminary finding suggesting a divergence in the functional properties of hGluN2A-S. Using the tool described in Chapter 3, we selectively expressed h(r)GluN2A-L, allow direct comparisons of the voltage dependence of NMDARs containing rGluN2A, h(r)GluN2A-L, or hGluN2A-S. Our findings indicate that hGluN2A-S confers increased sensitivity to extracellular Mg²⁺ blockade at negative membrane potentials, resulting in greater voltage dependence compared to rGluN2A and h(r)GluN2A-L. This observation is intriguing given that the differences in primary protein sequence between hGluN2A-S and hGluN2A-L are confined to the C-terminal domain, whereas the Mg²⁺ binding site is located within the channel pore.

Although the difference in voltage dependence was subtle, further analysis of conductance at varying membrane potentials revealed that hGluN2A-S-containing NMDARs exhibited decreased sensitivity to incremental depolarisation compared to h(r)GluN2A-L, as indicated by a lower δ value. This suggests that while small depolarisations significantly reduce Mg²⁺ block in h(r)GluN2A-L-containing receptors, blockade in hGluN2A-S-containing receptors is more resistant to such changes. Consequently, hGluN2A-S-containing NMDARs may have a reduced capacity to respond to depolarisation through rapid increases in NMDAR activity.

This difference was further accentuated by lowering the extracellular Mg²⁺ concentration. Whereas rGluN2A and h(r)GluN2A-L adopted a more linear I-V relationship, as expected due to decreased Mg²⁺ availability, hGluN2A-S maintained strong voltage dependence at negative membrane potentials.

This finding contrasts with the study by Puddifoot et al. (2009), which examined the effects of C-terminal truncation on Mg²⁺ blockade in rGluN2A. They truncated rGluN2A at position I1098 and assessed extracellular Mg²⁺ effects on NMDAR-mediated currents in oocytes. At comparable Mg²⁺ concentrations (0.1 and 1 mM), they observed no significant change in voltage-dependent inhibition. Similarly, no significant difference was reported in memantine antagonism—a uncompetitive channel pore inhibitor that shares the QRN binding site with Mg²⁺ (Puddifoot *et al.*, 2009).

The unique Mg²⁺ sensitivity observed in hGluN2A-S suggests that differences within the C-terminal domain between hGluN2A-L and -S influence Mg²⁺ binding and/or kinetics within the channel

pore. For instance, C-terminal truncation or the unique sequence of hGluN2A-S may induce conformational changes that alter access to, or interactions with, key amino acids involved in Mg²⁺ binding.

4.4.1.2 Behaviour of h(r)GluN2A-L and hGluN2A-S-containing NMDARs during noninstantaneous changes in membrane potential

The final aim of this chapter was to isolate and compare the effects of h(r)GluN2A-L and hGluN2A-S on NMDAR-mediated currents during non-instantaneous changes in membrane potential. Vargas-Caballero and Robinson (2003) demonstrated that Mg²⁺ unblock as a slow component, challenging the traditional model of instantaneous voltage dependence in NMDARs. Earlier in this chapter, we examined the voltage dependence in NMDARs using a slow-voltage ramp designed to approximate instantaneous Mg²⁺ unblock. To further investigate this, we conducted a pilot study measuring NMDAR-mediated currents in response to voltage step and action potential waveforms.

We found that both h(r)GluN2A-L and hGluN2A-S-containing receptors exhibit a slow Mg^{2+} unblock during voltage step depolarisation before reaching maximal current. Notably, hGluN2A-S-containing NMDARs displayed a prolonged delay in reaching peak current, both from rest and from a pre-depolarised state (0 mV). This aligns with our previous findings that hGluN2A-S confers increased Mg^{2+} sensitivity and reduced responsiveness to membrane potential changes. Our results suggest that hGluN2A-S-containing receptors maintain Mg^{2+} blockade longer, despite the depolarisation-induced electrostatic repulsion of Mg^{2+} from the pore.

At the end of the depolarising step, we observed rapid but non-instantaneous Mg^{2+} re-block in both h(r)GluN2A-L and hGluN2A-S-containing NMDARs, as indicated by a tail inward current. This is consistent with Vargas-Caballero and Robinson (2003), who described the gradual restoration of Mg^{2+} blockade upon repolarisation.

Interestingly, the re-block appeared more pronounced in hGluN2A-S-containing NMDARs, suggesting enhanced extracellular $\mathrm{Mg^{2+}}$ access and binding within the channel pore, leading to stronger inward current suppression upon return to resting potential. Although no significant difference was found between the hooked tail currents following repolarisation, the observed response to repolarisation may hint at hGluN2A-S contributing to a potentially accelerated reblock of the channel by $\mathrm{Mg^{2+}}$.

Using the action potential waveforms described by Larkum et al. (2001), we observed current responses that aligned with the findings of Vargas-Caballero and Robinson (2003). During fast sodium action potentials, both receptor subtypes contributed minimally during the rapid

depolarising upstroke but exhibited a pronounced current response during repolarisation. This response either matched or exceeded the expected current based on instantaneous Mg²⁺ unblock. Furthermore, we noted a delayed response to each of the three backpropagating action potentials. While individual cell responses varied across both isoforms, hGluN2A-S appeared to confer a more consistent delay in response during backpropagating Na⁺ action potentials. This is consistent with the increased slow response to voltage change via Mg²⁺ unblock observed during the depolarising voltage step. A larger sample size for hGluN2A isoforms may reveal a reduced responsiveness of hGluN2A-S-containing NMDARs to rapid membrane potential changes.

Consistent with Vargas-Caballero and Robinson (2003), both h(r)GluN2A-L and hGluN2A-S-containing NMDARs displayed large inward currents during the repolarisation of dendritic Na⁺/Ca²⁺ action potentials. The deviation from the expected current during steady-state depolarisation suggests that unblocked NMDARs can facilitate inward Ca²⁺ conductance before complete Mg²⁺ re-block. While responses were consistent across the two repeats of h(r)GluN2A-L, we observed greater variability in NMDARs containing hGluN2A-S. In one sample, we observed a pronounced reduction in inward current during the short repolarisations observed at the plateau of the action potential that more closely matched the expected current during stationary NMDAR activation. This suggests an increased ability of Mg²⁺ to access and re-block the channel pore, as observed during the voltage step commands. A larger sample size may clarify whether hGluN2A-S-containing NMDARs have a reduced ability to contribute to Ca²⁺ influx during multiple dendritic spike activity.

In summary, we propose that hGluN2A-S confers greater Mg^{2+} sensitivity, reducing conductance during depolarisation in steady-state voltage measurements. While this difference may subtly affect non-instantaneous Mg^{2+} block kinetics during action potentials, our pilot data do not allow us to draw confident conclusions about how each isoform behaves independently during rapid Na^{+} and slower Ca^{2+} action potentials.

While this study provides insights into the behaviour of h(r)GluN2A-L and hGluN2A-S during non-stationary membrane potential changes, we acknowledge the limitation of our small sample size, particularly for h(r)GluN2A-L NMDARs. This constrains the robustness of our conclusions.

Nevertheless, our findings reinforce the non-instantaneous nature of Mg²⁺ blockade and highlight the importance of studying hGluN2A-S function under physiological conditions relevant to glutamatergic neurons. Despite variability in response to action potential waveforms, subtle differences may emerge with a larger sample size, warranting further investigation in future studies.

4.4.1.3 Implications of increased voltage dependence in hGluN2A-S-containing NMDARs

Our findings in this chapter suggest novel functional properties of NMDARs containing the hGluN2A-S subunit, with potential implications for synaptic communication and plasticity beyond what is currently understood. At resting membrane potentials, the increased Mg²⁺ sensitivity in hGluN2A-S-containing NMDARs results in a stronger blockade, requiring greater depolarisation to relieve this inhibition. This characteristic may limit receptor activation during low-level synaptic activity and preferentially activate hGluN2A-S-containing NMDARs during high-frequency synaptic events. As a result, these receptors may act as a filter, selectively contributing to synaptic strengthening during intense neuronal activity. Consequently, Ca²⁺ influx may be delayed or reduced except during stronger synaptic activity. Since NMDAR-mediated Ca²⁺ influx to crucial for initiating signalling cascades such as CaMKII activation, which is involved in synaptic plasticity, an aberrantly blocked hGluN2A-S-containing NMDAR may impact the induction threshold for long-term potentiation. Conversely, the pronounced Mg²⁺ blockade at negative membrane potentials might favour conditions leading to long-term depression, as lower synaptic activity may be insufficient to relieve the block, thereby reducing NMDAR-mediated signalling and promoting synaptic weakening (Lisman, Yasuda and Raghavachari, 2012; Collingridge, 2024).

An important subunit switch occurs during postnatal development. Before the second postnatal week, most synaptically localised NMDARs contain GluN2B as the additional subunit. However, following this turning point, NMDARs containing GluN2A begin to partially replace those GluN2B-containing NMDAR receptors (Kew *et al.*, 1998; Li *et al.*, 1998; Rumbaugh and Vicini, 1999; Tovar and Westbrook, 1999). Alongside the well-established developmental regulation of hGluN2A and hGluN2B, we now know that hGluN2A-S is also expressed in the human brain (Warming *et al.*, 2019). The presence of hGluN2A-S subunits with increased voltage-dependence may play a role in fine-tuning synaptic responses during critical periods of neural circuit formation. This study highlights a previously unaccounted-for receptor subunit that confers distinct functional properties compared to the longer hGluN2A isoform in the human brain.

While we have discussed potential physiological roles for hGluN2A-S, it is also important to consider its implications in neurological disorders. The unique properties of hGluN2A-S-containing NMDARs may contribute to the pathophysiology of GRIN2A-associated disorders, such as epilepsy. For example, Yuan et al. (2014) investigated the epilepsy-associated GRIN2A gain-of-function mutation L812M, reporting that this mutation decreases voltage-dependence in mutant NMDARs. However, their study did not distinguish between the individual effects of the L812M mutation on hGluN2A-L and hGluN2A-S isoforms. Here, we have demonstrated that hGluN2A-S confers increased voltage dependence, raising the question of how the L812M mutation affects

hGluN2A-S subunits in individuals with this epilepsy-associated variant. The increased voltage dependence conferred by hGluN2A-S subunits may significantly influence NMDAR function, affecting human synaptic transmission and plasticity.

The unique CTD-dependent voltage-dependent Mg²⁺ blockade in GluN2A-S may have implications for other NMDAR subunits. Simpkins et al. (2003) demonstrated that the CTD of GluN2 subunits can be cleaved by calpain following glutamatergic activation, playing a critical role in mechanisms of LTP, synaptic plasticity, and NMDAR overactivation. In hippocampal neurons, the primary subunit subjected to CTD cleavage is GluN2B, which may result in the removal of modulation sites, including those for protein kinase C, tyrosine kinase, CaMKII, and PSD95 (Simpkins *et al.*, 2003).

The present study suggests that the absence of a portion of the CTD in hGluN2A-S leads to an altered voltage-dependent Mg²⁺ block, requiring stronger depolarisation to relieve the Mg²⁺ blockade and thereby increasing channel conductance. This heighted Mg²⁺ blockade may also result from activity-dependent, calpain-mediated CTD cleavage of GluN2B subunits, potentially contributing to reduced NMDAR overactivation during synaptic communication.

Understanding the effects of CTD truncation through alternative splicing or proteolytic cleavage is essential for elucidating the role of NMDAR subunit diversity in neural circuit dynamics and for developing strategies to address NMDAR-related neuropathologies.

4.4.2 Future perspectives

Our findings indicate that hGluN2A-S confers increased Mg²⁺ sensitivity despite its structural differences being confined to the C-terminal domain. To elucidate the underlying mechanisms, future studies should employ high resolution structural techniques such as cryo-electron microscopy—like that used by Lü et al. (2017) to resolve triheteromeric NMDAR structures—to determine whether the unique C-terminal sequence of hGluN2A-S induces conformational changes affecting Mg²⁺ binding and kinetics (Lü *et al.*, 2017). Additionally, site-directed mutagenesis or targeted deletion of the unique region of hGluN2A-S could clarify their contribution to its increased voltage dependence.

Previous work by Warming et al. (2019) demonstrated that hGluN2A-S-containing receptors can localise and function at the cell surface in HEK293T cells. Our study builds on this by characterising their biophysical properties, yet their localisation and function within native neuronal networks remain unexplored. Future research should use whole-cell patch-clamp recordings in primary neuron cultures or brain slice preparation exogenously expressing hGluN2A-S to assess its synaptic function and its impact on synaptic transmission, plasticity, and excitatory input

integration. One potential method for exogenous expression is single-cell electroporation, which Elmasri et al. (2022) successfully applied to study neurons expressing either epilepsy-associated mutant or wild-type hGluN2A subunits within the same organotypic brain slice culture.

Lastly, our results suggest that hGluN2A-S-containing NMDARs may act as activity-dependent filters, preferentially activating during high-frequency synaptic events that have driven strong post-synaptic depolarisation. Future computational modelling of synaptic transmission could help predict how these receptors influence cortical circuit dynamics and information processing. Such models could provide insight into the role of hGluN2A-S in sensory processing, learning, and memory while circumventing the technical challenges of exogenous expression in rodent models.

Chapter 5 Investigating the isoform-specific effect of disease-associated *GRIN2A* missense mutations on NMDAR function.

5.1 Introduction

The disease relevance of NMDARs in humans is well established, with numerous mutations identified in genes encoding NMDAR subunits in patients with neurological disorders. Next-generation sequencing has facilitated the identification of several epilepsy-associated genes. NMDAR genes have been implicated including within *GRIN1*, *GRIN2A* and *GRIN2B* (Myers, Johnstone and Dyment, 2019b). In this thesis we focus on *GRIN2A* mutations which have a strong link to EAS disorders, presenting a range of clinical phenotypes from mild cases such as atypical benign partial epilepsy (ABPE) to more severe conditions like LKS and continuous spike-and-wave during slow-wave sleep syndrome (CSWSS) (Lemke et al., 2013; Strehlow et al., 2019). In more severe cases, epilepsy patients may exhibit comorbidities, including epileptic encephalopathy, intellectual disability, language impairments, and developmental delays (Strehlow et al., 2016, 2019). Current treatment options remain limited and often yield mixed outcomes depending on the specific *GRIN2A* mutations (Strehlow et al., 2016).

Missense *GRIN2A* mutations result in amino acid substitutions that can have diverse functional consequences, broadly classified as either gain-of-function (GOF) or loss-of-function (LOF). One mutation of focus in this present study is the disease-associated GOF mutation is L812M. We chose to study this mutation due to the striking pathophysiological effects on NMDAR function and therefore the clinical phenotype of the individual carrying the mutation. The L812M mutation was identified in a child with intractable seizures and early-onset epileptic encephalopathy accompanied by developmental delay (Table 5.1). This mutation resides in the linker region between the S2 agonist-binding domain and the M4 transmembrane domain (Figure 5.1) and is thought to interfere with key gating regions, including the M4 domain of GluN2A and the M3 transmembrane domain and pre-M1 helix of the GluN1 subunit. Yuan et al. (2014) reported that the L812M mutation reduces Mg²⁺ block while increasing glutamate potency, channel open probability and deactivation kinetics, leading to enhanced charge transfer during synaptic transmission.

A limitation of this study is the independent expression of hGluN2A-L in *Xenopus* oocytes and a mixed expression in HEK293 cells. In *Xenopus* oocytes—where increased glutamate potency and

decreased voltage dependence was observed—Yuan et al. (2014) synthesised circularised RNA from a linearised cDNA template of hGluN2A, resulting in the exclusive expression of the hGluN2A-L isoform.

In contrast, expression in HEK293 cells—where increased receptor deactivation kinetics were reported—would have involved a mixture of hGluN2A-L and hGluN2A-S due to exon-dependent alternative splicing of the hGluN2A expression vector. Consequently, their findings do not account for the independent effect of the mutation on the hGluN2A-S isoform (Yuan *et al.*, 2014).

To distinguish between GluN2A-L and GluN2A-S, we employed the isoform-specific expression tool described in Chapter 3 to investigate the functional consequences of the L812M mutation. Specifically, we examined its effects on voltage dependence and glutamate potency in both h(r)GluN2A-L and hGluN2A-S-containing NMDARs. Additionally, given our previous findings—described in Chapter 4—demonstrating a hGluN2A-S-specific increase in Mg²⁺ sensitivity, we explored whether the L812M-induced reduction in Mg²⁺ blockade is isoform specific. This investigation further informs the functional divergence between hGluN2A-L and hGluN2A-S in WT and mutant isoforms.

LOF mutations in *GRIN2A* are, by definition, associated with reduced current density, diminished surface expression, and decreased channel open probability, often profoundly impacting NMDAR function (Elmasri *et al.*, 2022). Addis et al. (2017) examined several notable LOF mutations (Figure 5.1), including C231Y and G483R, which were found to reduce agonist potency and surface expression significantly. The C231Y mutation, linked to the severe epilepsy-aphasia spectrum subtype LKS (Lemke et al., 2013) (Table 5.1), resides within a hydrophobic cavity of the NTD (Figure 5.1). The mechanism by which the cysteine to tyrosine substitution elicits its effect is yet to elucidated; Addis et al. (2017) speculate that this mutation may disrupt protein folding through replacement of a polar side chain with a bulky hydrophobic tyrosine residue. This may in-turn disrupt the agonist-binding site and therefore lead to protein degradation (Addis *et al.*, 2017). Similarly, the G483R mutation, identified in individuals with CSWSS (Lesca et al., 2013) (Table 5.1), occurs in a flexible loop of the S1 agonist-binding domain (Figure 5.1) and is thought to disrupt the structure of the glutamate-binding pocket due to the substitution of a large, positively charged arginine residue (Addis *et al.*, 2017).

Another *GRIN2A* LOF mutation, C436R, also investigated by Addis et al. (2017), results in a significant reduction in cell surface expression, thereby limiting receptor availability for glutamate signalling. This mutation, found in a child with ABPE (Lemke et al., 2013)(Table 5.1), is proposed to impair protein folding and stability by eliminating a key disulphide bridge-forming cysteine residue in the S1 agonist-binding domain (Figure 5.1) and replacing with a polar arginine. These

LOF mutations likely contribute to *GRIN2A* haploinsufficiency, leading to neural hyperexcitability, potentially due to the compensatory increase in hGluN2B expression. The slower deactivation kinetics of hGluN2B-containing NMDARs could disrupt the balance of excitation and inhibition in neuronal networks (Addis *et al.*, 2017).

As with Yuan et al. (2014), a major limitation of Addis et al. (2017) was the likely contribution of GluN2A-L and GluN2A-S to their functional outcome measures when expressing hGluN2A in HEK293 cells. To overcome this limitation, we investigated how these LOF mutations affect isolated hGluN2A-S-containing NMDARs. Furthermore, *GRIN2A*-associated EAS mutations are typically heterozygous, meaning individuals possess both wild-type and mutant subunits. Most studies, including that of Addis et al. (2017), have examined mutations in a homozygous state, which does not accurately reflect patient genotypes. We therefore explored whether coexpression of wild-type and mutant subunits results in a dominant-negative effect, which could explain the sometimes-severe clinical phenotypes observed in individuals with *GRIN2A*-related EAS (Lesca et al., 2013; Addis et al., 2017).

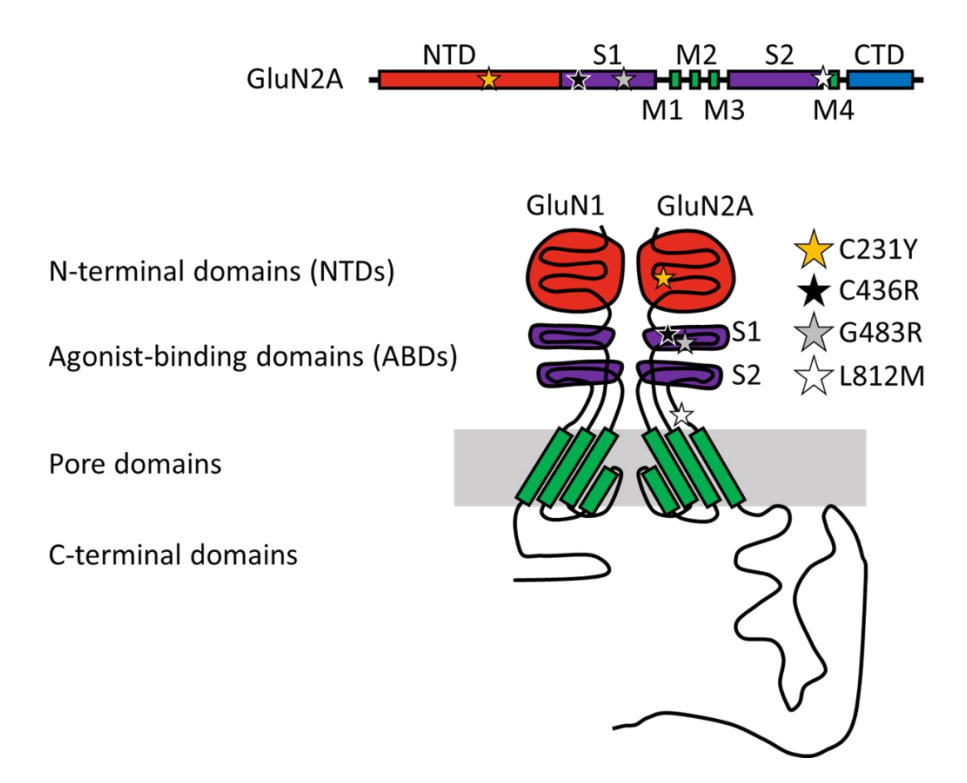


Figure 5.1 - Locations of loss-of-function and gain-of-function epilepsy-associated GRIN2A missense mutations.

Cartoon depicting the molecular domains of GluN1/GluN2A NMDA receptor in linear (top) and assembled/native (bottom) formats. One half of the tetrameric assembly is shown for simplicity. The plasma membrane is depicted as a grey box. The loss-of-function mutation locations are depicted by star-shaped markers (C231Y – yellow;

C436R – black; G483R – grey). The gain-of-function mutation (L812M) is depicted by a white star-shaped marker.

Table 5.1 GRIN2A missense mutations and clinical presentations

DNA mutation	Protein alteration	Clinical presentation	Inheritance	Reference
c.692G>A	C231Y	Landau-Kleffner syndrome	Maternal	(Lemke et al., 2013)
c.1306T>C	C436R	Atypical benign partial epilepsy	de novo	(Lemke et al., 2013)
c.1447G>A	G483R	Continuous spike- and-wave during slow-wave sleep syndrome, atypical Rolandic epilepsy, verbal dyspraxia	Maternal	(Lesca et al., 2013)
c.2434C>A	L812M	Early-onset epileptic encephalopathy, profound global developmental delay	de novo	(Yuan et al., 2014)

5.2 Aims and Objectives

The overarching aim of this chapter is to examine the functional effects of disease-associated GOF and LOF mutations on hGluN2A-L- and hGluN2A-S-containing NMDARs. Using the h(r)GluN2A-L expression system described in Chapter 3, we aimed to isolate and study the impact of these mutations on each isoform individually.

To achieve this, we will first introduce and validate the GOF missense mutation L812M in plasmid constructs encoding either h(r)GluN2A-L or hGluN2A-S. Site-directed mutagenesis will be employed to substitute cytosine at position 2434 with adenine in the transcript sequence. Once validated, we will assess the functional consequences of L812M on each isoform.

Next, we aim to employ a high-throughput method to measure Ca²⁺ influx following NMDAR activation. This will involve adapting an existing bioluminescence-based assay to establish a glutamate concentration that elicits a stable Ca²⁺ response with minimal desensitisation. Using this method, we will evaluate the effect of the L812M mutation on glutamate potency and voltage-dependence in h(r)GluN2A-L and hGluN2A-S-containing NMDARs. Based on previous findings by Yuan et al. (2014), we hypothesise that L812M will similarly increase glutamate potency in both isoforms (Yuan *et al.*, 2014). However, due to the isoform-specific differences in voltage-dependence (Chapter 4) we predict the mutation will have a reduced impact on the voltage-dependent Mg²⁺ block of hGluN2A-S. To test this, we will perform voltage-ramp experiments in transfected HEK293T cells, using iontophoresis to apply NMDA locally.

We will also investigate the effects of LOF mutations C231Y and C436R on hGluN2A-S and their interactions with wild-type NMDAR subunits. Previous work by Addis et al. (2017) has shown that these ER-retaining mutations significantly impair receptor function and surface expression when only mutant GluN2A subunits are expressed (Addis *et al.*, 2017). Here, we aim to isolate the specific impact of these mutations on hGluN2A-S and determine whether they exert a dominant-negative effect in a heterozygous context, where mutant and wild-type subunits are co-expressed.

Finally, we will examine the isoform-specific effects of the G483R LOF mutation. Although Addis et al. (2017) reported a borderline functional impact of this mutation, their experiments did not distinguish between hGluN2A isoforms. We will address this gap by studying the functional consequences of G483R in h(r)GluN2A-L versus hGluN2A-S-containing NMDARs to identify any isoform-specific differences.

The objectives of this chapter are to:

- 1. Introduce and validate the GOF mutation L812M in h(r)GluN2A-L and hGluN2A-S.
- 2. Develop a high-throughput method to measure Ca²⁺ influx through NMDARs.
- 3. Characterise the isoform-specific effects of the L812M mutation on glutamate potency and Mg²⁺ blockade.
- 4. Investigate the impact of the C231Y, C436R and G483R mutations on hGluN2A-S and their interactions with wild-type subunits.

5.3 Results

5.3.1 Investigating the effect of the epilepsy-associated GOF mutation L812M on h(r)GluN2A-L and hGluN2A-S-containing NMDARs.

5.3.1.1 Site directed mutagenesis of h(r)GRIN2A-L/hGRIN2A-S and sequence validation.

To introduce the epilepsy-associated GOF missense mutation L812M into h(r)GluN2A-L and hGluN2A-S, we targeted the pcDNA3.1+ eGFP-h(r)GRIN2A-L and eGFP-hGRIN2A-S plasmids for site-directed mutagenesis. Primers were designed (Table 2.1) to substitute cytosine with adenine at nucleotide position 2434 within the GRIN2A sequence, resulting in the desired L812M substitution.

Site-directed mutagenesis was performed using PCR to amplify the template plasmids with the intended base substitution. Following the PCR amplification, the products were ligated and transformed into DH5 α E. coli cells. Bacterial colonies were screened for successful transformation by selecting for ampicillin resistance (Figure 2.1).

To confirm the C2434A substitution, Sanger sequencing was performed using the Seq_Primer_Fwd_F sequencing primer (Table 2.2), which was designed to cover the target site. The chromatograms are shown in Figure 5.2A (for h(r)GluN2A-L) and Figure 5.3A (for hGluN2A-S) and confirm the successful substitution of cytosine with adenine. To ensure that no off-target mutations were introduced during mutagenesis, additional sequencing primers (previously used for the A4114G substitution; Table 2.2) were used to provide full coding sequence coverage. A 100% match was observed between the query sequence and the reference sequences for both h(r)GRIN2A-L^{C2434A} and hGRIN2A-S^{C2434A} plasmids.

The plasmid constructs resulting from these mutations are depicted in Figure 5.2B and Figure 5.3B, illustrating the presence of ampicillin and neomycin resistance genes and the coding sequence for eGFP-tagged h(r)GluN2A-L^{L812M} and hGluN2A-S^{L812M}, respectively. Sequence alignment confirmed the C2434A nucleotide substitution and the corresponding amino acid change at position 812 from lysine to methionine.

Expression of the mutated constructs was verified by transfection of HEK293T cells with pcDNA3.1+ eGFP-h(r)GRIN2A-L^{C2434A} or eGFP-hGRIN2A-S^{C2434A} plasmids. Successful expression was confirmed 48 hours post-transfection by visualising eGFP fluorescence at an excitation of 480 nm (Figure 5.4).

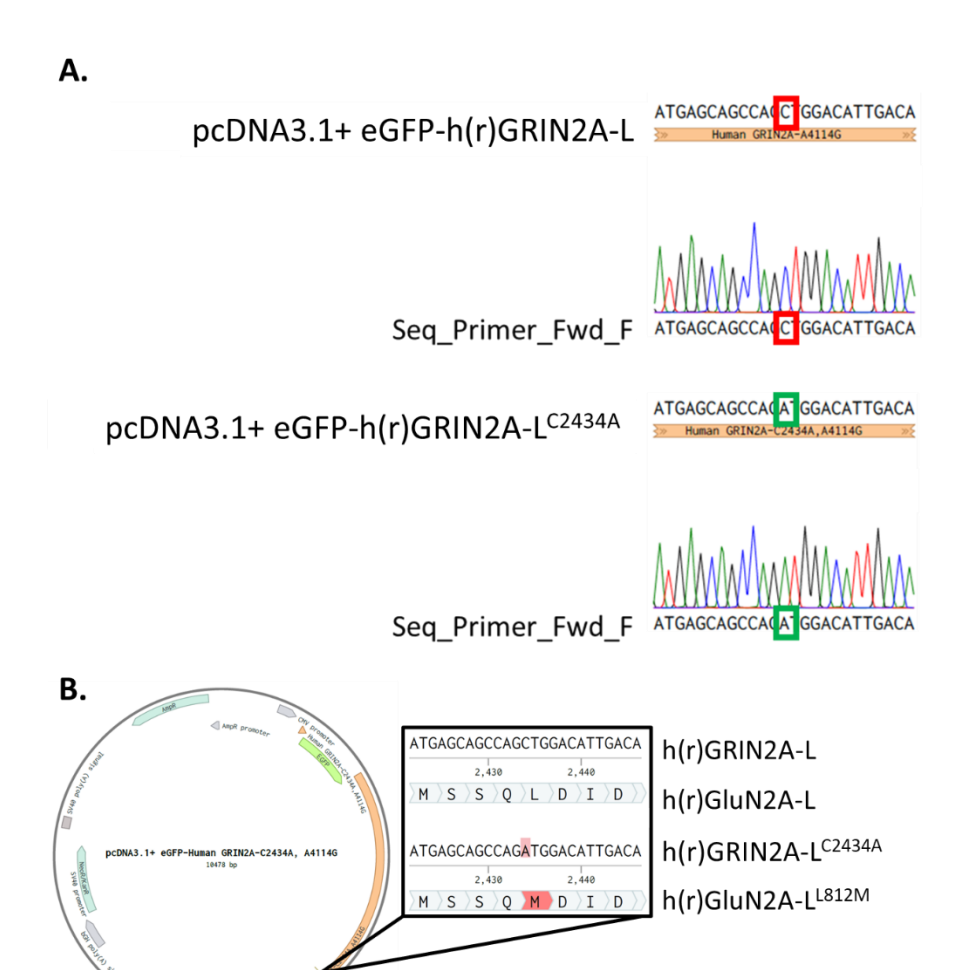


Figure 5.2 - Generation of pcDNA3.1+ eGFP-h(r)GRIN2A-L^{C2434A} using site-directed mutagenesis.

A) pcDNA3.1+ eGFP-h(r)GRIN2A-L and pcDNA3.1+ eGFP-h(r)GRIN2A-L^{C2434A} plasmids were sequenced using the Seq_Primer_Fwd_F primer to validate the success of the C2434A substitution. Sequencing chromatogram showing the presence of a cytosine (red box) in pcDNA3.1+ eGFP-h(r)GRIN2A-L which was mutated to an adenine in pcDNA3.1+ eGFP-h(r)GRIN2A-L^{C2434A} resultant from substitution of C2434A via site-directed mutagenesis (green box). B) (Left) Plasmid map of pcDNA3.1+ eGFP-h(r)GRIN2A-L^{C2434A} indicating locations of antibiotic resistance, promoter regions and polyA signal sequences. (Right top) Pairwise sequence alignment of the coding sequence of h(r)GRIN2A-L and h(r)GRIN2A-L^{C2434A}. As intended, a nucleotide mismatch can be observed at position 2434 due to C2434A substitution (red box). (Right bottom) Pairwise sequence alignment of the amino acid sequence of h(r)GluN2A-L and h(r)GluN2A-L^{L812M}. A mismatch can be observed at position 812, lysine for methionine respectively (red box). Sequences were aligned using EMBL-EBI, EMBOSS Needle, Pairwise Sequence Alignment; full-stop denotes sequence mismatches.

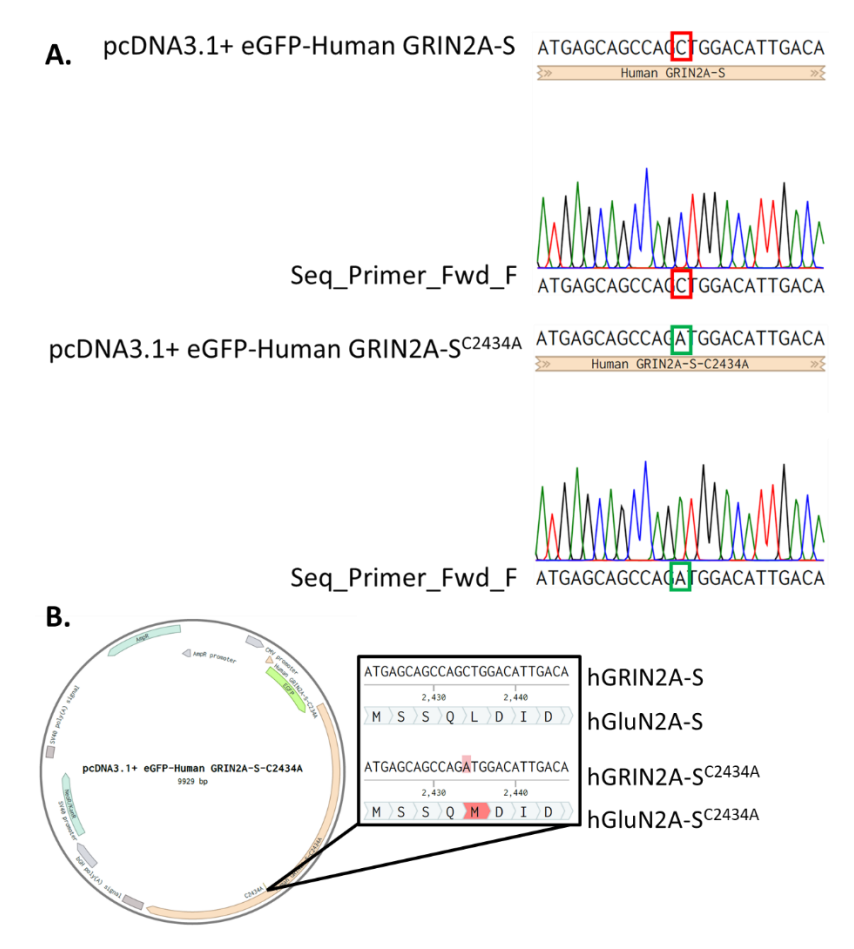


Figure 5.3 - Generation of pcDNA3.1+ eGFP-Human GRIN2A-S^{C2434A} using site-directed mutagenesis.

A) pcDNA3.1+ eGFP-Human GRIN2A-S and pcDNA3.1+ eGFP-Human GRIN2A-S^{C2434A} plasmids were sequenced using the Seq_Primer_Fwd_F primer to validate the success of the C2434A substitution. Sequencing chromatogram showing the presence of a cytosine (red box) in pcDNA3.1+ eGFP-Human GRIN2A-S which was mutated to an adenine in pcDNA3.1+ eGFP-Human GRIN2A-S^{C2434A} resultant from substitution of C2434A via site-directed mutagenesis (green box). B) (Left) Plasmid map of pcDNA3.1+ eGFP-Human GRIN2A-S C2434A indicating locations of antibiotic resistance, promoter regions and polyA signal sequences. (Right top) Pairwise sequence alignment of the coding sequence of human GRIN2A-S and human GRIN2A-S^{C2434A}. As intended, a nucleotide mismatch can be observed at position 2434 due to C2434A substitution (red box). (Right bottom) Pairwise sequence alignment of the amino acid sequence of human GluN2A-S and human GluN2A-S and human GluN2A-S land human GluN2A-S and human GluN2A-S land human

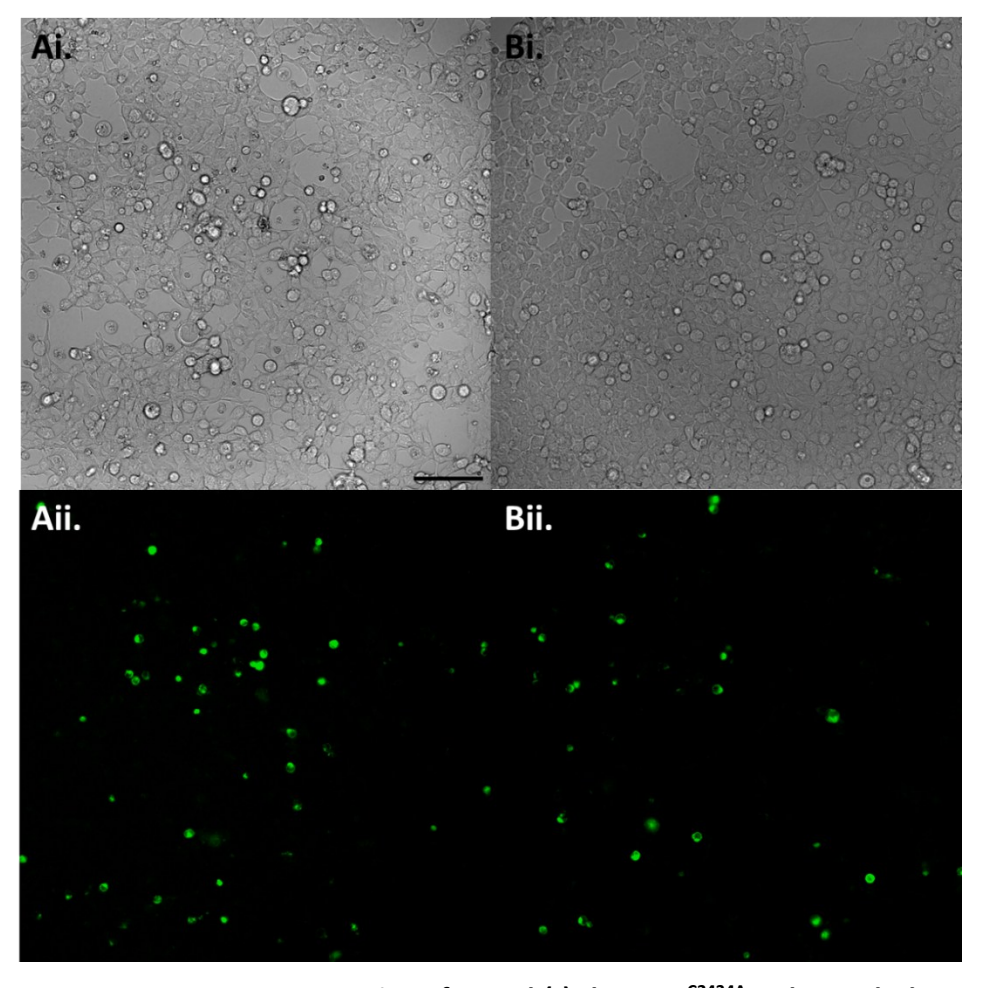


Figure 5.4 - Exogenous expression of eGFP-h(r)GluN2A-L^{C2434A} and eGFP-hGluN2A-S^{C2434A} in HEK293T cells.

Ai+Bi) Representative brightfield images of HEK293T cells plated and transfected in a 6-well plate with pcDNA3.1+ eGFP-h(r)GRIN2A-L^{C2434A} and eGFP-hGRIN2A-S^{C2434A} plasmids, respectively. Aii+Bii) As in Ai and Bi, fluorescence image at 488 nm excitation of eGFP-tagged protein. Images were taken at 48 hours post-transfection. Scale bar = $100\mu M$.

5.3.1.2 Testing mRNA transcripts produced by mutants.

To confirm that the pcDNA3.1+eGFP-h(r)GRIN2A-L^{C2434A} plasmid construct generated only the hGRIN2A-L mRNA transcript, we performed PCR amplification of cDNA synthesised from reverse-transcribed RNA extracted from transfected HEK293T cells. Using the primer pair GRIN2A Human F/GRIN2A Human R1, as previously described in Chapter 3.3.2, we aimed to amplify both hGRIN2A and hGRIN2A-S transcripts (Figure 5.5A).

We predicted the following amplicon sizes for each condition:

- h(r)GRIN2A-L^{C2434A}: a single larger amplicon of 0.474 kb.
- h(r)GRIN2A-S^{C2434A}: a single smaller amplicon of 0.131 kb.

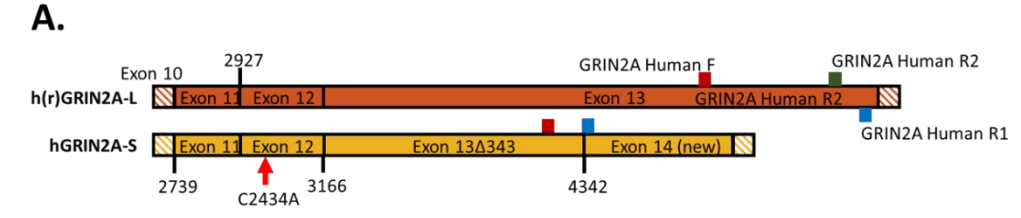
 hGRIN2A (positive control): two distinct amplicons at 0.474 kb and 0.131 kb, corresponding to hGRIN2A-L and hGRIN2A-S, respectively.

For cells transfected with h(r)GRIN2A-L^{C2434A}, we observed a single upper band between 0.4 kb and 0.5 kb on the ladder, consistent with the predicted 0.474 kb amplicon. For hGRIN2A-S^{C2434A}, we detected a lower band between 0.1 kb and 0.2 kb, matching the expected 0.131 kb amplicon. As expected, the positive control (hGRIN2A) yielded two distinct bands at 0.474 kb and 0.131 kb, confirming the presence of both isoforms.

To account for potential preferential amplification of the shorter cDNA and to verify the presence of the longer hGRIN2A-L transcript, we used a second primer pair (GRIN2A Human F/GRIN2A Human R2) that specifically amplifies the hGRIN2A-L transcript. Consistent with our predictions, this primer pair generated a single amplicon of 0.386 kb in both hGRIN2A and h(r)GRIN2A-L^{C2434A} samples, with no amplification observed in hGRIN2A-S^{C2434A} samples.

To ensure that the observed amplicons originated from exogenous cDNA rather than endogenous off-target templates, we included a negative control comprising RNA extracted from cells transfected with soluble eGFP. No amplification was detected in this control, as expected. Additionally, no bands were observed in the non-template control, where no cDNA was added, confirming that the amplification was not due to contamination of reagents (Figure 5.5A).

These observations were consistent across three independent experiments, confirming the specificity of the primer pairs and the successful expression of the intended mRNA transcripts from the mutant constructs.



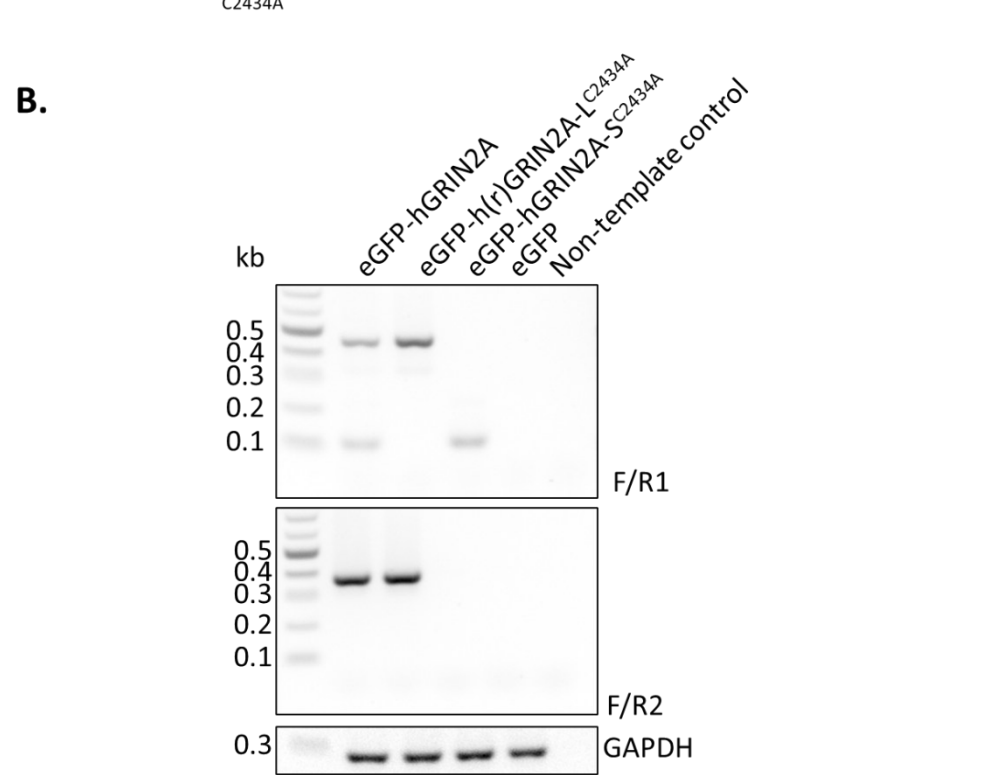


Figure 5.5 - Exogenous expression of recombinant h(r)GRIN2A-L^{C2434A} results in a single GRIN2A mRNA transcript in HEK293T cells.

A) Diagram depicting the h(r)GRIN2A-L and GRIN2A-S transcripts. Depicted by a red arrow is the location of C2434A (L812M) that is the epilepsy-associated GRIN2A mutation. The annealing locations of PCR primers are also depicted on their respective transcript (GRIN2A Human F – red; GRIN2A Human R1 – blue; GRIN2A Human R2– green). B) Gel electrophoresis of PCR products from amplification of cDNA from RNA extracted from HEK293T cells exogenously expressing plasmids encoding human GRIN2A, h(r)GRIN2A-L^{C2434A}, human GRIN2A-S^{C2434A} or eGFP. Primers GRIN2A Human F and GRIN2A Human R1 were used for the specific amplification of human GRIN2A and/or GRIN2A-S transcripts. GAPDH Human forward (F) and reverse (R) primers were used to control for the presence of cDNA. Image representative of two independent repeats. C) As in B but using primers GRIN2A Human F and GRIN2A Human R2 for the specific amplification of Human GRIN2A transcripts.

5.3.1.3 Establishing a method for high-throughput measurement of NMDAR activity

Previous work by colleague Luis Yañez-Guerra (Thiel et al. 2023) utilised a bioluminescence-based Ca²⁺ assay with HEK293 cells stably expressing the chimeric GFP-Aequorin protein G5A (HEK293G5A) to investigate ligands for G protein-coupled receptors (Thiel *et al.*, 2023). We sought to adapt this high-throughput method to measure Ca²⁺ influx through NMDARs containing h(r)GluN2A-L and hGluN2A-S wild-type and mutant subunits.

To test whether this assay could detect Ca²⁺ influx via NMDARs, we first transfected HEK293G5A cells with either soluble RFP or hGluN1-4a/hGluN2A-S. 48 hours post-transfection, these cells were then incubated with the aequorin substrate coelenterazine h, before measurement of the bioluminescence signal using a Flexstation 3 Multi-mode Microplate reader. This setup allowed timed exposure of cells to a range of glutamate concentrations—via a step change in glutamate concentration without washout— thereby activating the NMDARs and inducing Ca²⁺ influx, which was quantified by the bioluminescence emitted from the binding of Ca²⁺ to aequorin and the conversion of coelenterazine h to coelenteramide (Figure 5.6A).

Bioluminescence readings were processed using a moving average filter with a window size of two samples to reduce noise. Cells expressing only soluble RFP showed minimal to no bioluminescence signal across glutamate concentrations ranging from 100 nM to 1 mM (Figure 5.6B). In contrast, cells expressing either RFP or hGluN1-4a/hGluN2A-S responded to 1 mM MgATP, activating endogenous P2Y purinergic receptors as a control to assess cell viability post-culture and transfection. Similar levels of bioluminescence were detected following purinergic receptor activation, confirming cell survival (Figure 5.6C).

To account for background activity, we subtracted data from soluble RFP-expressing cells (which lacked glutamate sensitivity) from the readings of hGluN1-4a/hGluN2A-S-expressing cells (Figure 5.6D). This corrected for endogenous Ca^{2+} activity in cells and isolated the NMDAR-mediated response. The integral of the bioluminescence curves was calculated, and the data were normalised to the maximal response. The resulting values were plotted against the agonist concentration. As shown in Figure 5.6E, a dose-dependent increase in total Ca^{2+} activity was observed with glutamate binding, reaching a maximal response at 50 μ M. Further increases in glutamate concentration led to a dose-dependent decrease in the total detected bioluminescence, consistent with desensitisation or saturation of the NMDAR response.

This work established the method and associated parameters for a high-throughput approach to measure Ca²⁺ influx through NMDARs, which will be used in subsequent experiments to study the functional impact of mutations on NMDAR activity.

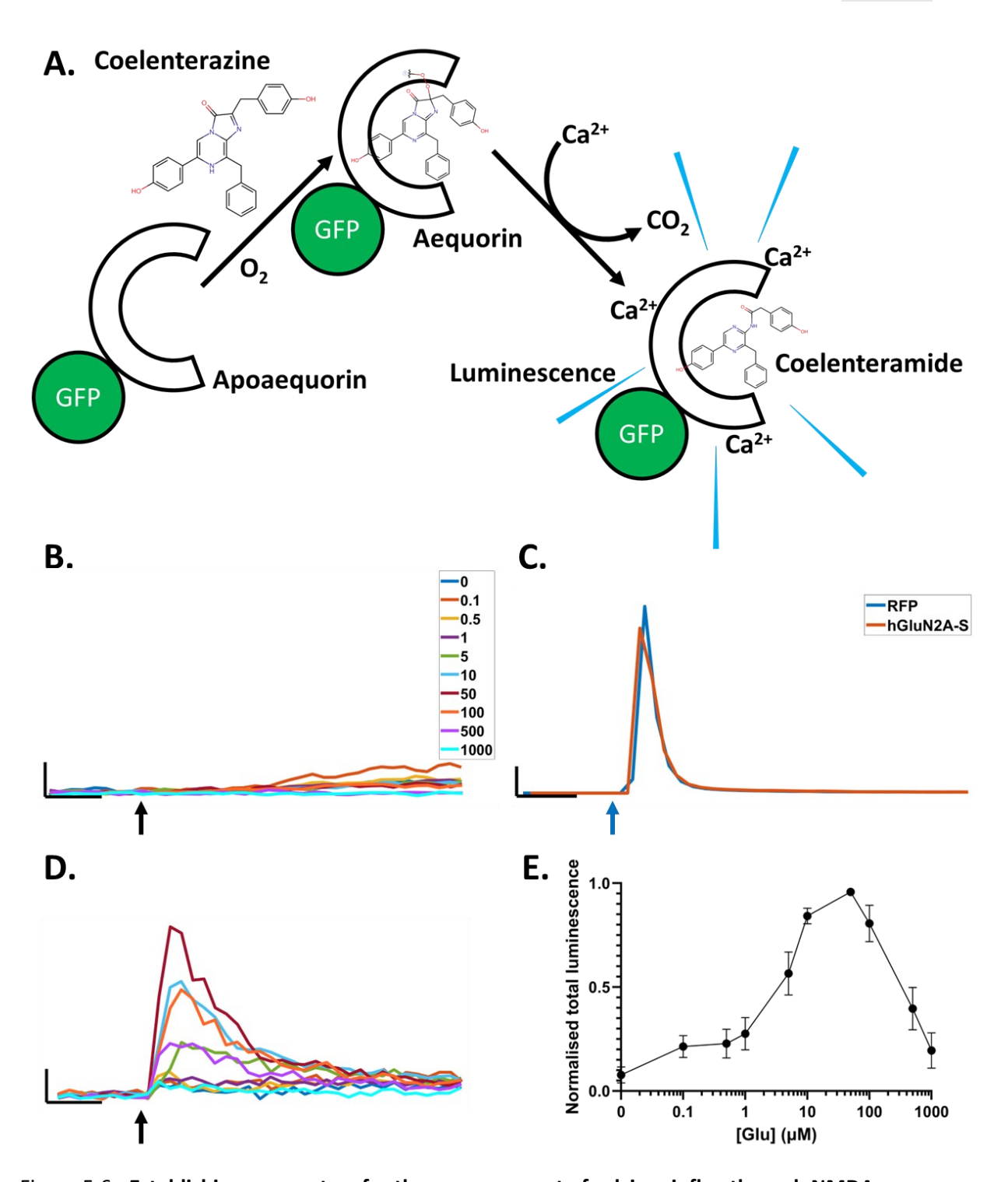


Figure 5.6 - Establishing parameters for the measurement of calcium influx through NMDA receptors using a bioluminescence-based assay on HEK293G5A cells with calcium-sensitive aequorin expression.

A) Cartoon depicting the luminescence reaction of aequorin. HEK293G5A expressing GFP-tagged (green) apo-aequorin are incubated with cell-permeant coelenterazine. This generates the functional aequorin. Ca^{2+} influxed via NMDA receptor activation binds to aequorin, triggering a conformational change which leads to the destabilisation of the peroxide group. This generates CO_2 and coelenteramide which,

now in its excited state, releases blue light. **B)** Moving averaged (window = 2) calcium responses from HEK293G5A cells transfected with RFP following application of increasing concentrations of glutamate (100nM – 1mM black arrow). Scale bar: Y-axis = 100 Relative Luminescence Units (RLU); X-axis = 10 sec. N = 8 wells. **C)** Averaged calcium responses from HEK293G5A cells transfected with either RFP (N = 8 wells) or hGluN2A-S (N = 8 wells) following application of 1mM MgATP (blue arrow – activation of endogenous P2Y receptors). Scale bar: Y-axis = 10'000 RLU; X-axis = 10 sec. **D)** As in B, HEK293G5A transfected with hGluN1-4a/hGluN2A-S. N = 8 wells. **E)** Dose-response curve of glutamate-induced calcium responses from HEK293G5A cells transfected with hGluN2A-S. Endogenous calcium activity in cells transfected with RFP was subtracted from calcium responses in cells transfected with hGluN2A-S. Data points represent the area under the curve of bioluminescence readings from 8 independent wells per concentration, normalised to the maximum response observed for each experiment. Each data point represents the mean ± SEM.

5.3.1.4 Analysis of the individual effect of L812M on h(r)GluN2A-L and hGluN2A-S glutamate pharmacology

Having established a method for high-throughput measurement of NMDAR activation via Ca²⁺ influx, we next aimed to investigate the effect of the L812M mutation on glutamate potency in h(r)GluN2A-L and hGluN2A-S subunits individually. Previous work by Yuan et al. (2014) identified an increased potency of glutamate when hGluN2A-L was expressed in isolation (Yuan *et al.*, 2014). To test for isoform-specific effects of the L812M mutation, we transfected HEK293G5A cells with hGluN1-4a and either h(r)GluN2A-L or hGluN2A-S, in both their wild-type and L812M mutant forms. As a negative control, we included cells transfected with soluble RFP.

After 48 hours following transfection, we incubated cells with coelenterazine h. Bioluminescence was measured following exposure to increasing glutamate concentrations—via a step change in glutamate concentration without washout ($100nM - 100\mu M$). Bioluminescence readings were processed using a moving average filter with a window size of two samples to reduce noise. Cells expressing soluble RFP showed minimal or no bioluminescence signal across all glutamate concentrations (Figure 5.7A). As a control for cell viability post-culture and transfection, all cell conditions were exposed to 1 mM MgATP to activate endogenous P2Y purinergic receptors, revealing comparable bioluminescence levels across conditions and thus confirming similar viable cell counts (Figure 5.7B).

During recordings without glutamate addition, a positive background bioluminescence signal was detected in conditions with no external glutamate addition. To measure the amount of

background measured RLU was due to NMDARs, we included a condition with 50 μ M APV, an NMDAR antagonist. In hGluN2A-S, NMDAR activity accounted for 9.8% of the measured RLU for WT receptors and 73.1% in L812M mutant receptors. In hGluN2A-L-containing receptors, NMDARs activity accounted for 0% of the measured RLU for WT receptors and 77.8% in L812M mutant receptors (Figure 5.7C-F). This was observed despite multiple washes to remove cell culture media and replace with extracellular solution before applying glutamate-free solution containing coelenterazine h. We speculate that this background signal could be due to background activation due to presence of cell debris containing glutamate.

Data recorded from cells expressing soluble RFP were subtracted from the measurements of cells expressing hGluN2A subunits, isolating the NMDAR-mediated response to glutamate. The integral of the bioluminescence curves was calculated, and we normalised the data to the maximal response. We then plotted these normalised values as a function of glutamate concentration.

We observed similar dose-response curves for glutamate activation in both h(r)GluN2A-L and hGluN2A-S WT subunits. The presence of the L812M mutant resulted in a leftward shift in the dose-response for both h(r)GluN2A-L and hGluN2A-S-containing NMDARs (Figure 5.7G+H).

At a glutamate concentration of 50 μ M, where we observed near-maximal bioluminescence, the bioluminescent signal from WT receptors was greater than that from L812M mutant receptors in averaged traces (Figure 5.7C-F). To investigate this difference, Figure 5.7I display the RLU integrals from individual well records. We did not observe a significant reduction in total bioluminescence between WT and mutant receptors. We did observe however, readings from a single well with markedly high total bioluminescence at 50 μ M for both WT h(r)GluN2A-L and hGluN2A-S (Figure 5.7I). The inclusion of this well may explain why we observed larger averaged traces from WT h(r)GluN2A-L and hGluN2A-S compared to that of L812M mutant receptors (Figure 5.7C-F).

To quantify the difference in dose-response, we extracted the RLU integrals from individual well recordings at 0.1 μ M, where the largest disparity in dose-response between WT and mutant receptors was observed. Figure 5.7J shows a significant increase in total bioluminescence detected from h(r)GluN2A-L^{L812M} (9246 ± 1180 RLU) compared to h(r)GluN2A-L WT (2188 ± 234 RLU, p < 0.0001). Similarly, we observed a significant increase when comparing hGluN2A-S^{L812M} (6263 ± 897 RLU) with hGluN2A-S WT (1776 ± 233 RLU, p = 0.0002). However, we did not find a significant difference between the WT receptors (p = 0.23) or between the L812M mutant receptors (p = 0.06).

These findings are consistent with Yuan et al. (2014), demonstrating that the L812M mutation increases glutamate potency. Furthermore, the L812M mutation exerts a similar effect on

glutamate potency across both hGlun2A isoforms, despite differences in the C-terminal domain of hGluN2A-S.

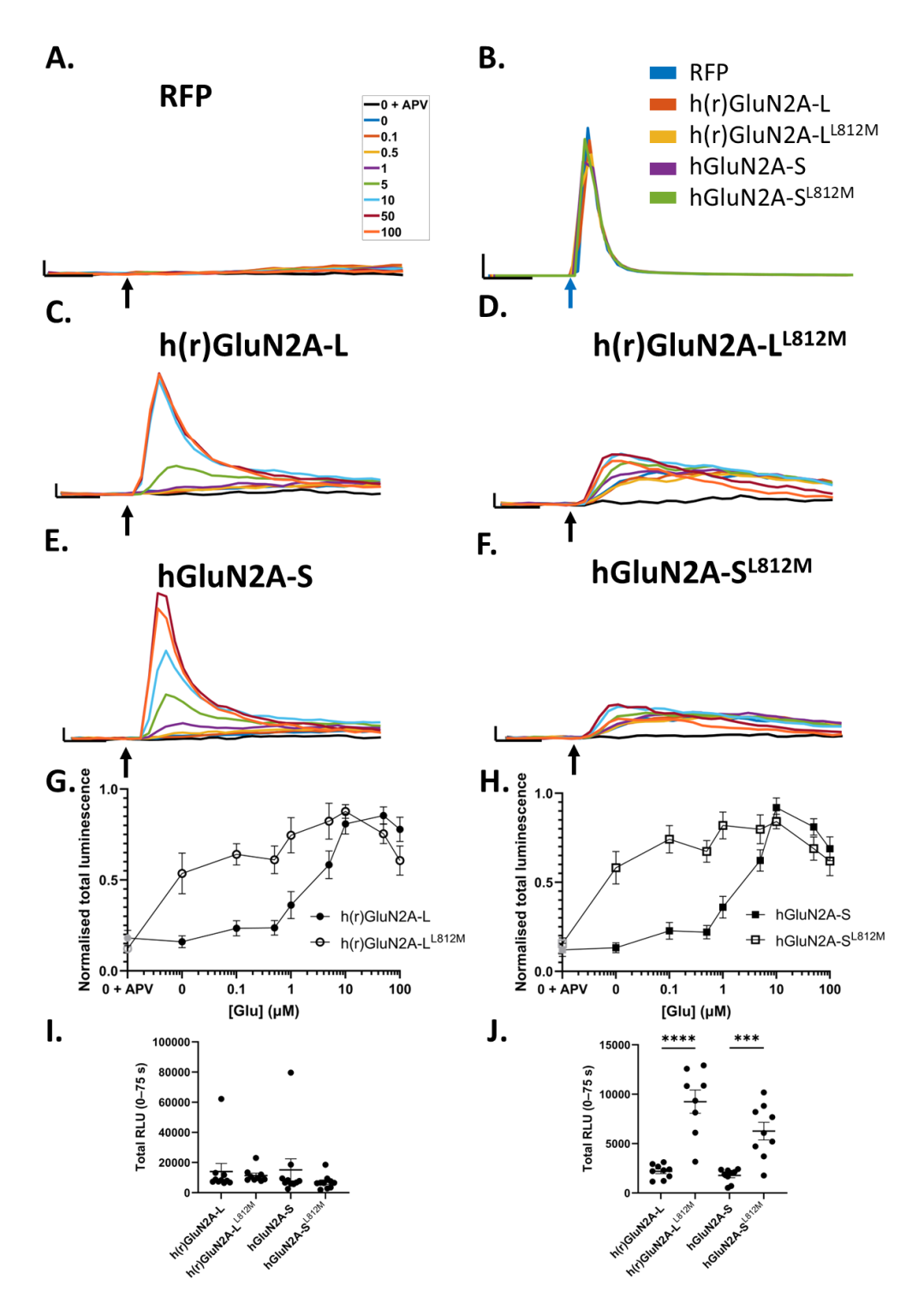


Figure 5.7 - Analysis of the individual effect of the epilepsy-associated L812M GRIN2A missense mutation on glutamate pharmacology in hGluN2A-L and hGluN2A-S-containing NMDA receptors.

A) Moving averaged (window = 2) calcium responses from HEK293G5A cells transfected with RFP following application of increasing concentrations of glutamate ($100 \text{nM} - 100 \mu\text{M}$ black arrow). Scale bar: Y-axis = 100 Relative Luminescence Units

(RLU); X-axis = 10 sec. N = 10 wells. B) Moving averaged (window = 2) calcium responses from HEK293G5A cells transfected with either RFP (N = 10 wells), hGluN1-4a/h(r)GluN2A-L wild-type (wt) (N = 10 wells), hGluN1-4a/h(r)GluN2A-L^{L812M} (N = 9 wells), hGluN1-4a/hGluN2A-S wt (N = 10 wells) or hGluN1-4a/hGluN2A-S^{L812M} (N = 10 wells) following application of 1mM MgATP (blue arrow – activation of endogenous P2Y receptors). Scale bar: Y-axis = 10'000 RLU; X-axis = 10 sec. C-F) As in A, HEK293G5A transfected with hGluN1-4a/h(r)GluN2A-L wt (N = 10 wells), L812M (N = 9 wells) and hGluN1-4a/hGluN2A-S wt (N = 10 wells), L812M (N = 10 wells), respectively. G) Dose-response curve of glutamate-induced calcium responses from HEK293G5A cells transfected with hGluN1-4a/h(r)GluN2A-L wt or L812M mutant. Endogenous calcium activity in cells transfected with RFP was subtracted from calcium responses in cells transfected with NMDA receptor subunits. Grey data points correspond to the addition of 50 µM APV. Data points represent the area under the curve of bioluminescence readings from independent wells per concentration, normalised to the maximum response. Each data point represents the mean ± SEM. H) As in G, for cells transfected with hGluN1-4a/hGluN2A-S wt or L812M mutant. I) Summary data for the area under the curve of bioluminescence readings from independent wells per condition following addition of 50 µM glutamate. Endogenous calcium activity in cells transfected with RFP were subtracted from calcium responses in cells transfected with NMDA receptor subunits. Data is displayed as independent repeats with mean ± SEM. J) As in I, for well recordings following addition of 0.1 μM glutamate. h(r)GluN2A-L vs. h(r)GluN2A-L^{L812M}; unpaired t-test, P < 0.0001, two-tailed. hGluN2A-S vs. hGluN2A-S^{L812M}; unpaired t-test, P = 0.0002, two-tailed.

5.3.1.5 Analysis of the individual effect of L812M on h(r)GluN2A-L and hGluN2A-S voltagedependence

We next investigated the isoform-specific effects of the L812M mutation on voltage-dependence in h(r)GluN2A-L and hGluN2A-S subunits. Previous studies by Yuan et al. (2014) and Elmasri et al. (2020) demonstrated a decrease in Mg²⁺ sensitivity and consequently reduced voltage-dependence, when either hGluN2A-L was expressed in isolation or when both isoforms were expressed together, respectively (Yuan *et al.*, 2014; Elmasri *et al.*, 2020). However, our earlier findings (Chapter 4) revealed isoform-specific differences in voltage-dependence, with hGluN2A-S-containing receptors exhibiting increased Mg²⁺ sensitivity and requiring stronger depolarisation to relieve the Mg²⁺ block for NMDAR conductance. Thus, we aimed to determine isoform specific effects on voltage dependent Mg²⁺ block in NMDARs with the L812M mutation.

To investigate the equilibrium, I-V relationship, HEK293T cells transfected with h(r)GluN2A-L^{L812M} or hGluN2A-S^{L812M} were subjected to a slow voltage ramp from -80 mV to +50 mV during stationary NMDAR activation in the presence of physiological Mg²⁺ concentrations (2 μ M), induced by local NMDA application via iontophoresis (Figure 5.8Ai). This protocol produced the characteristic J-shaped I-V curves, with reversal potentials near 0 mV (Figure 5.8Ai-ii).

To minimise noise effects, we calculated a moving average with a sliding window of 25 ms, allowing a more accurate determination of the maximum current at +49-50 mV. Current amplitudes varied but was comparable between h(r)GluN2A-L^{L812M} and hGluN2A-S^{L812M}-containing receptors (Figure 5.8Aiii).

To compare voltage-dependence, we normalised individual I-V curves to the current at +49-50 mV, where maximal Mg²⁺ unblock is expected. By comparing the mean normalised data and corresponding SEM of mutant subunits to the wild-type data from Chapter 4, we observed that h(r)GluN2A-L^{L812M}-containing receptors displayed reduced voltage-dependence at negative membrane potentials, particularly between -20 mV and -30 mV (Figure 5.8Bi, Bii). This finding aligns with previous reports from Yuan et al. (2014) and Elmasri et al. (2020) in receptors coexpressing both isoforms. Interestingly, hGluN2A-S^{L812M}-containing NMDARs exhibited I-V relationships closely resembling wild-type hGluN2A-S-containing receptors.

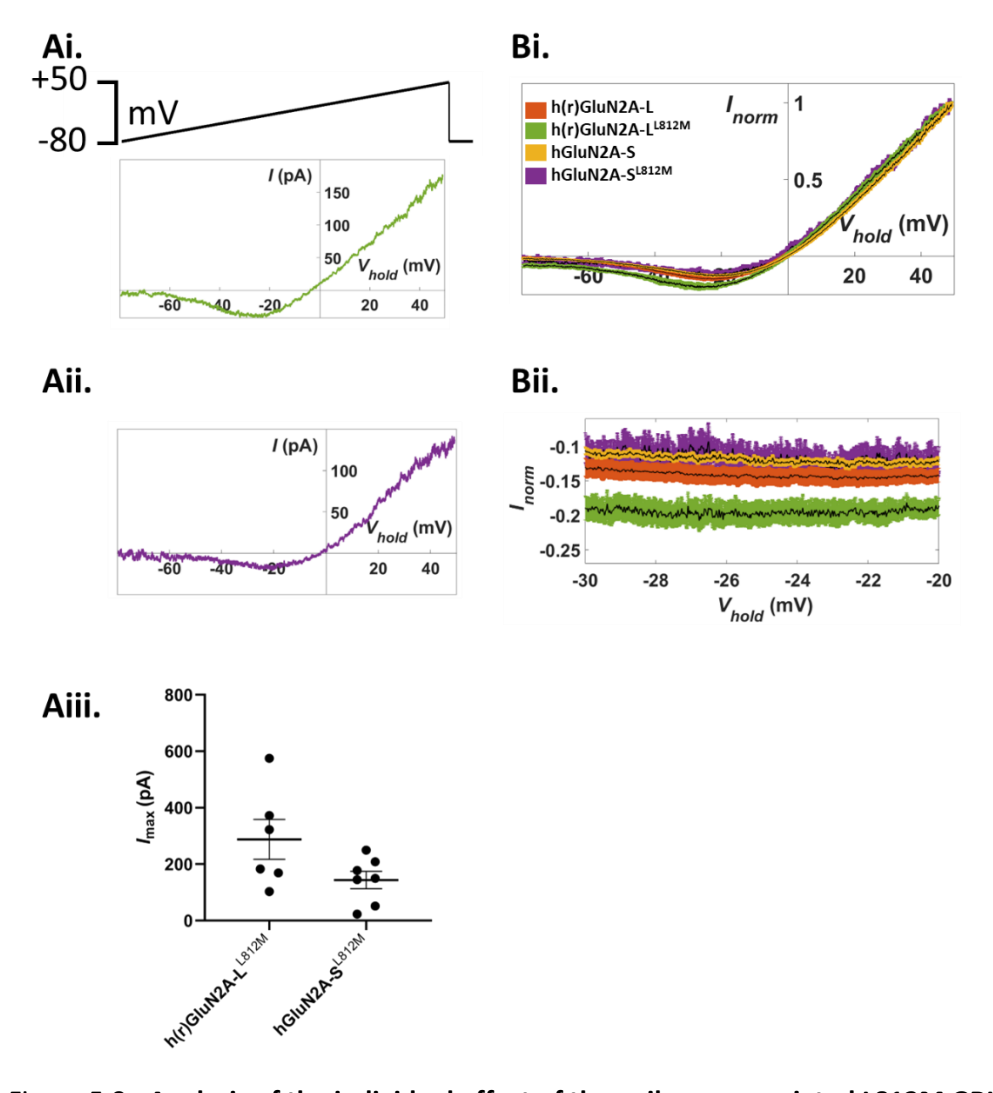


Figure 5.8 - Analysis of the individual effect of the epilepsy-associated L812M GRIN2A missense mutation on voltage-dependence in hGluN2A-L and hGluN2A-S-containing NMDA receptors.

A) During local application of NMDA, HEK293T cells were subjected to a slow voltage ramp (4 sec) from -80mV to +50mV. Representative sample traces of current-voltage relationships from HEK293T cells expressing rGluN1-1a alongside h(r)GluN2A-LL812M (green), or hGluN2A-SL812M (purple), respectively. Endogenous currents in the absence of an NMDA were subtracted from currents in the presence of NMDA. Traces averaged from one cell per condition. Aiv) A moving average of subtracted data was calculated with a sliding window size of 25 ms to remove noise. The maximum current at +49-50mV was then extracted. Bi) Leak subtracted data for each condition were averaged from h(r)GluN2AL812M N = 6 cells, hGluN2A-SL812M N = 7 cells normalised to the current at +49-50 mV where maximal Mg²⁺ unblock is achieved. This allowed comparisons of behaviour at negative membrane potentials. Data is displayed as mean (black) with SEM (green and purple, respectively). Data from wild-type h(r)GluN2A-L (red) and hGluN2A-S are shown for comparison. Bii) A zoomed

view of the current-voltage relationship at holding potentials between -20mV and - 30mV. Current-voltage curves from each cell are averaged from 2 recording sweeps.

To further investigate the isoform-dependent effect of the L812M mutation current responses obtained during a slow voltage ramp were transformed into conductance-voltage (G-V) relationships by estimating the unblocked NMDAR current in the absence of Mg²⁺. The ohmic response was estimated by fitting a linear slope to the cord conductance at positive membrane potentials using least squares (Figure 5.9A). The actual current was divided by this estimated unblocked current to calculate the fraction of conductance as a function of membrane potential (Figure 5.9B), and the data were fitted to the Boltzmann distribution (Equation 4.1).

To compare Mg^{2+} sensitivity between NMDAR subtypes, the Boltzmann equation was fitted to normalised G-V relationships for h(r)GluN2A-L^{1812M}, and hGluN2A-S^{1812M}-containing NMDARs. Our analysis revealed that hGluN2A-S^{1812M}-containing receptors had a significantly less negative V_{0.5} (-11.4 ± 1.8 mV) compared to h(r)GluN2A-L^{1812M} (-26.2 ± 2.9 mV, p = 0.0087) (Figure 5.9C). This indicates that hGluN2A-S maintains its increased Mg²⁺ block despite the presence of the L812M mutation. Conversely, we found that hGluN2A-S^{1812M}-containing receptors exhibited a similar δ value (0.53 ± 0.08) compared to h(r)GluN2A-L^{1812M} (0.65 ± 0.07) (Figure 5.9D). This is suggestive of similar sensitivity to changes in membrane potential.

Finally, we extracted the percentage unblock at the membrane potential corresponding to the maximal inward current from individual G-V curves. hGluN2A-S^{L812M}-containing NMDARs showed a significantly smaller percentage unblocked (25.9 \pm 2.6%) compared to h(r)GluN2A-L^{L812M} (42.5 \pm 2.0%, P = 0.0004) (Figure 5.9E). In summary, these results indicate an isoform-specific effect of the L812M mutation, with a resistance to the mutation-induced decrease in Mg²⁺ sensitivity in the hGluN2A-S isoform. This suggests that the increased Mg²⁺ sensitivity of hGluN2A-S mitigates the impact of the L812M mutation on voltage-dependence.

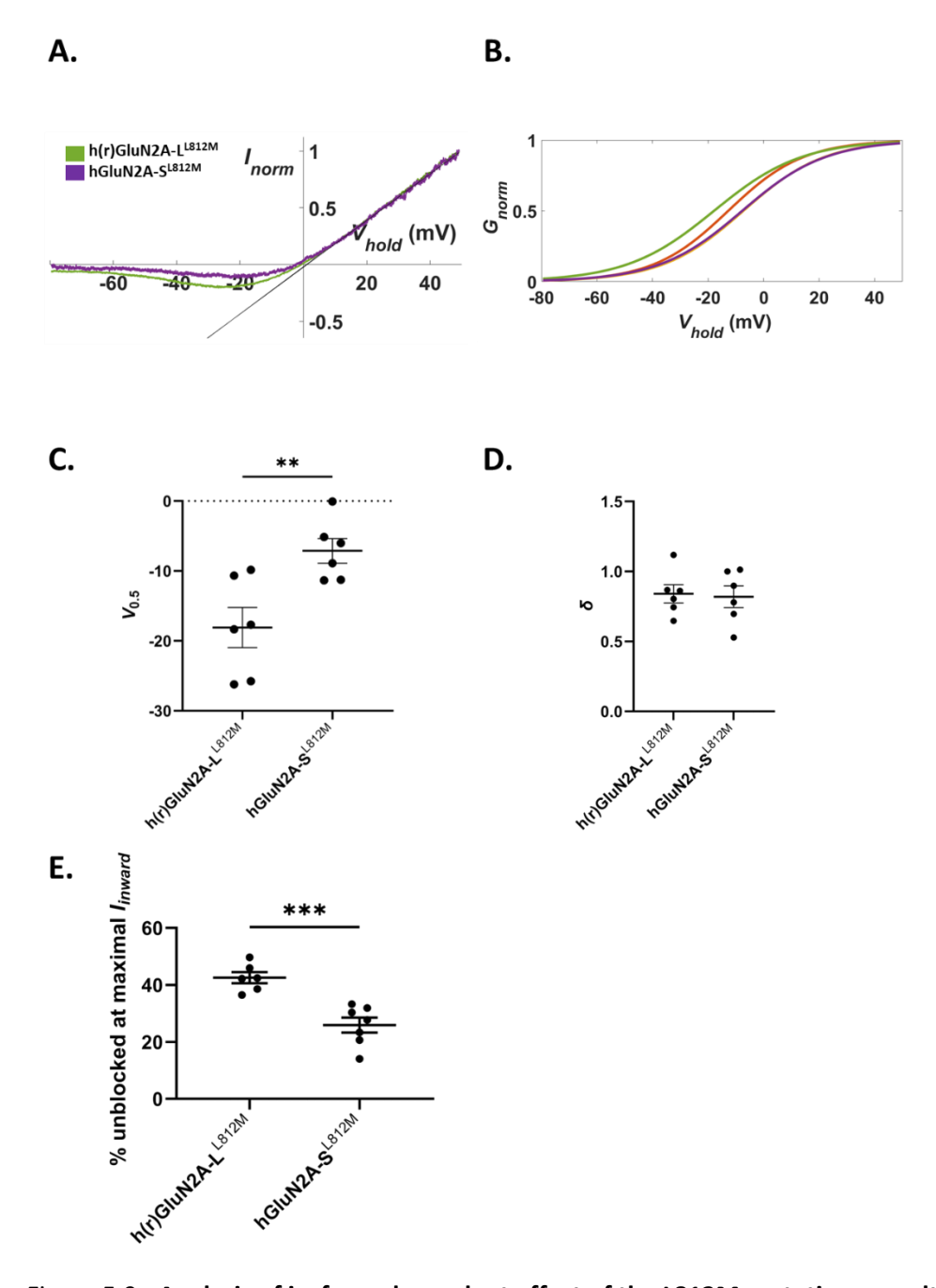


Figure 5.9 - Analysis of isoform-dependent effect of the L812M mutation on voltage dependence of NMDA receptors: relationship between expected linear and blocked current.

A) The cord conductance was calculated using the moving-averaged data. This was by means of a least square fitting (grey straight lines) to the linear portion of the normalised and averaged current-voltage data to model maximal expected current in the absence of Mg²⁺ antagonism. Subtracted and normalised current-voltage data (grey) were fitted using a Boltzmann-type equation (h(r)GluN2A-L^{L812M} – green and hGluN2A-S^{L812M} – purple). B) The fraction of the maximal slope conductance (G-V relationship) is plotted as a function of membrane potential, fitted to a Boltzmann-type distribution. Data from wild-type h(r)GluN2A-L (red) and hGluN2A-S are shown for comparison. C) The voltage for the half-maximal block (V_{0.5}) extracted from the

Boltzmann-type equation summarised in B. h(r)GluN2A-L^{L812M} vs. hGluN2A-S^{L812M}; unpaired t-test, P = 0.0087, two-tailed. **D)** The fraction of the membrane potential sensed by the blocking site (δ) extracted from the Boltzmann-type equation summarised in B. **E)** The percentage unblock at maximal inward current was extracted from individual G-V curves. h(r)GluN2A-L^{L812M} vs. hGluN2A-S^{L812M}; unpaired t-test, P = 0.0004, two-tailed. h(r)GluN2A-L^{L812M} N = 6 cells. GluN2A-S^{L812M} N = 7 cells.

5.3.2 Investigating the effect of the disease-associated LOF mutations on hGluN2A-S and its effect on wild-type receptor function.

We next investigated the isoform-specific effects of three epilepsy-associated LOF *GRIN2A* mutations that have pronounced effects on NMDAR function: C231Y, C436R, and G483R (Addis *et al.*, 2017). In this chapter, we present the experimental data in two parts. We first present the C231Y and C436R mutants, which did not exhibit isoform-specific effects on NMDAR function. We then present the data obtained from the G483R mutant, which displays an isoform-dependent effect on NMDAR function, causing a LOF in hGluN2A-L-containing NMDARs and a GOF in hGluN2A-S-containing receptors.

5.3.2.1 C231Y and C436R

Among the LOF mutations analysed by Addis et al. (2017), C231Y and C436R were reported to have pronounced effects on receptor function, hypothesised to result—at least in part—from retention of mutant receptors in the endoplasmic reticulum (Addis *et al.*, 2017). However, a previously unappreciated caveat of this study is that the expression of hGluN2A constructs in HEK293 cells would have resulted in a mixed expression of the two hGluN2A protein isoforms. Consequently, the work presented by Addis et al. (2017) does not investigate the independent contribution of hGluN2A-L and hGluN2A-S isoforms to NMDAR dysfunction in these disease-associated mutants. To build on these findings, we aimed to isolate the effects of these mutations specifically on hGluN2A-S-containing NMDARs.

Given that these mutations are heterozygous in affected individuals, we also sought to examine whether mutant hGluN2A-S exerts a dominant-negative effect on hGluN2A-S wild-type-containing receptors by potentially interfering with their trafficking to the cell surface.

We used the bioluminescence-based Ca²⁺ assay (described in chapter 5.3.1.3) to evaluate the impact of these LOF mutations on glutamate-induced NMDAR Ca²⁺ conductance. HEK293G5A cells were transfected with hGluN1-4a and either wild-type hGluN2A-S or mutant subunits (C231Y or C436R. As a negative control, some cells were transfected with soluble RFP. After 48 hours, cells

were incubated with a glutamate-free HEPES solution containing coelenterazine h, as substrate for the stable expression of aequorin.

To confirm cell viability after transfection and culture, we exposed cells to 1 mM MgATP to activate endogenous P2Y receptors. Bioluminescence responses to MgATP were comparable across all conditions, indicating similar cell numbers in the cultures (Figure 5.10A). Additionally, cells transfected with soluble RFP showed minimal bioluminescence in response to 50 μ M glutamate (Figure 5.10B).

Figure 5.10C-E show representative and averaged bioluminescence responses for cells expressed wild-type hGluN2A-S, hGluN2A^{C231Y}, and hGluN2A^{C436R}. The integrals of bioluminescence signals for each condition are summarised in Figure 5.10F.

For cells expressing hGluN2A-S^{C231Y}, we observed a significant reduction in Ca²⁺-dependent bioluminescence (2305 \pm 218 RLU) compared to wild-type hGluN2A-S (8569 \pm 447.2 RLU, p < 0.0001). This reduction was consistent with previous findings by Addis et al. (2017) when mixed hGluN2A isoforms were expressed. However, when hGluN2A-S wild-type and C231Y mutant subunits were co-expressed (9454 \pm 389 RLU), Ca²⁺-dependent bioluminescence returned to levels similar to those of wild-type hGluN2A-S alone and significantly increased from the hGluN2A-S^{C231Y} expressed in isolation (p < 0.0001).

A similar pattern was observed for the hGluN2A^{C436R} mutation. Receptors containing this mutation displayed a marked reduction in activity (920.8 \pm 85.84 RLU, p < 0.0001) compared to wild-type hGluN2A-S. However, when hGluN2A-S wild-type and C436R mutant subunits were co-expressed (11'388 \pm 518 RLU), we observed bioluminescence activity comparable to wild-type hGluN2A-S and significantly increased compared to hGluN2A-S^{C436R} (p < 0.0001).

In summary, we found that the C231Y and C436R mutations caused significant reductions in NMDARs activity in hGluN2A-S-containing receptors. These results are consistent with previous findings by Addis et al. (2017) for mixed isoform expression. However, when co-expressed with wild-type hGluN2A-S, the mutant subunits did not impair wild-type receptor function at the cell surface. This suggests that the C231Y and C436R mutations do not exert dominant-negative effects on wild-type NMDARs, despite their LOF properties when expressed in isolation.

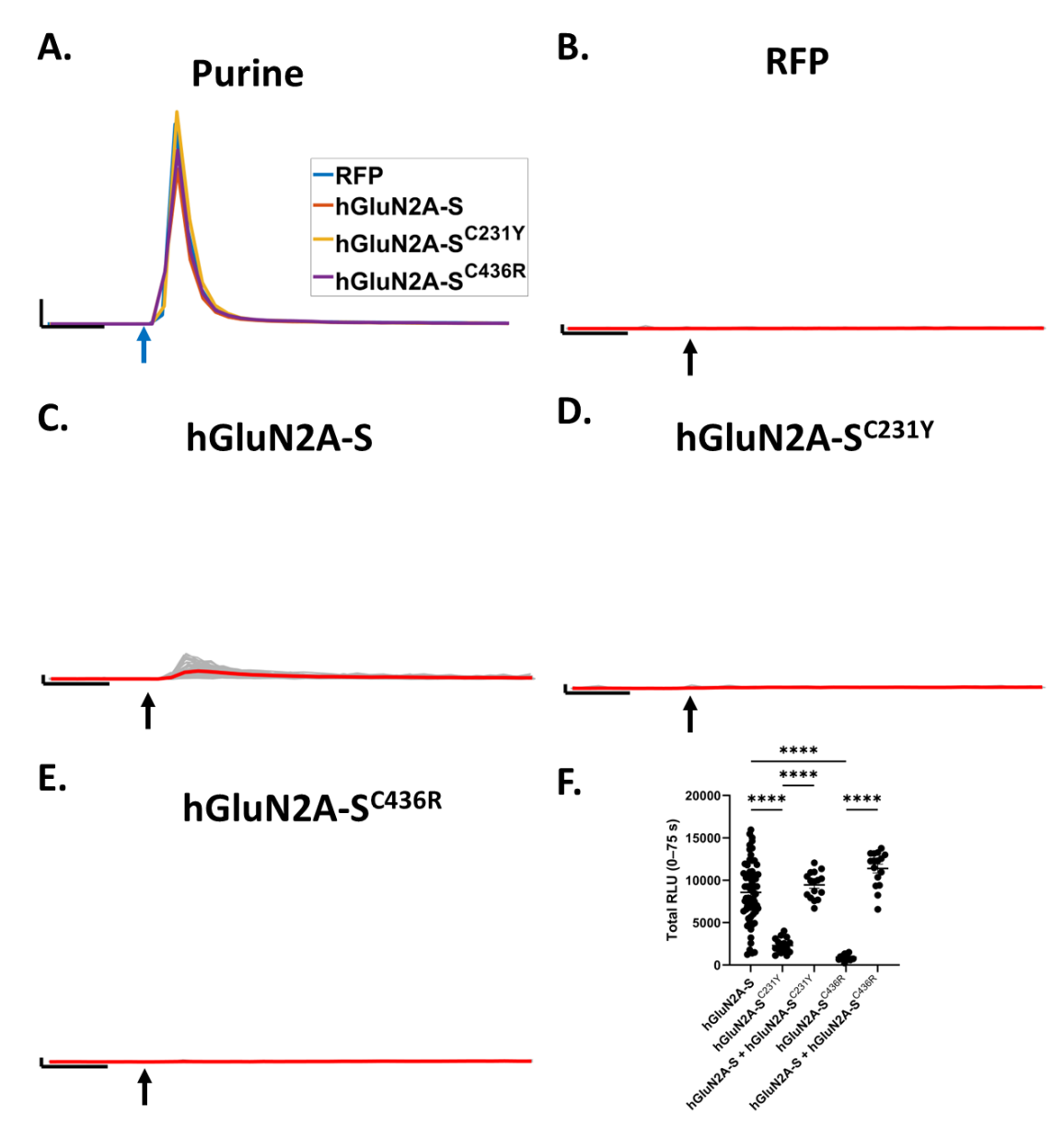


Figure 5.10 - Investigating the effect of epilepsy-associated GRIN2A loss-of-function missense mutations in GluN2A-S and its effect on wild-type receptor function.

A) Averaged calcium responses from HEK293G5A cells transfected with either RFP (N = 15 wells), hGluN1-4a/hGluN2A-S (N = 8 wells), hGluN1-4a/hGluN2A-S^{C231Y} (N = 2 wells) or hGluN1-4a/hGluN2A-S^{C436R} (N = 2 wells) following application of 1mM MgATP (blue arrow – activation of endogenous P2Y receptors). Scale bar: Y-axis = 10′000 RLU; X-axis = 10 sec. **B-E)** Calcium responses from HEK293G5A cells transfected with RFP (N = 120 wells), hGluN1-4a/hGluN2A-S (N = 53 wells), hGluN1-4a/hGluN2A-S^{C231Y} (N = 16 wells) or hGluN1-4a/hGluN2A-S^{C436R} (N = 16 wells) following application of 50 μ M glutamate (black arrow). Scale bar: Y-axis = 100 Relative Luminescence Units (RLU); X-axis = 10 sec. Individual well traces displayed in grey, and the mean response shown in red. **F)** Summary data concerning the effect of the C231Y and C436R missense mutations on receptor function and its effect on co-

expressed hGluN2A-S wt. Area under the curve of bioluminescence readings from independent wells per condition. Endogenous calcium activity in cells transfected with RFP was subtracted from calcium responses in cells transfected with NMDA receptor subunits. Data is displayed as independent repeats with mean \pm SEM. hGluN2A-S vs. hGluN2A-S^{C231Y}; unpaired t-test, P < 0.0001, two-tailed. hGluN2A-S^{C231Y} vs. hGluN2A-S + hGluN2A-S^{C231Y}; unpaired t-test, P < 0.0001, two-tailed. hGluN2A-S vs. hGluN2A-S^{C436R}; unpaired t-test, P < 0.0001, two-tailed. hGluN2A-S^{C436R} vs. hGluN2A-S + hGluN2A-S^{C436R}; unpaired t-test, P < 0.0001, two-tailed.

5.3.2.2 G483R

Lastly, we turned our attention to the disease-related G483R LOF GRIN2A mutation. Addis et al. (2017) reported a borderline functional impact of this mutation; however, their experiments involved the expression of a mixture of the hGluN2A-L and hGluN2A-S isoforms. We first aimed to replicate their findings using our bioluminescence-based assay before investigating whether the mutation exhibited an isoform-specific effect that was not previously distinguished.

Additionally, we explored whether the G483R mutation exerted a dominant-negative effect when co-expressed with wild-type hGluN2A receptor subunits. To do this, we transfected HEK293G5A cells with hGluN1-4a alongside either hGluN2A, h(r)GluN2A-L, or hGluN2A-S wild-type or mutant subunits. As previously observed, cells exposed to 1 mM MgATP exhibited similar bioluminescence signals, confirming comparable cell viability across all transfection and culture conditions (Figure 5.11A). Figure 5.11B-G present representative traces from individual cultures along with averaged responses.

We calculated the integrals of bioluminescence responses and subtracted data from cells expressing soluble RFP to eliminate contributions from endogenous activity, isolating NMDAR-mediated responses to 50 μ M glutamate-induced activation. These data are summarised in Figure 5.11H.

For cells transfected with hGluN2A^{G483R}—expressing a mixture of hGluN2A-L^{G483R} and hGluN2A-S^{G483R}—we observed a significant reduction in Ca²⁺-dependent bioluminescence (7028 \pm 366 RLU) compared to wild-type hGluN2A (10960 \pm 983.1, p = 0.0005). This reduction was more pronounced than the borderline LOF previously reported by Addis et al. (2017). Curiously, when wild-type hGluN2A and hGluN2A^{G483R} were co-expressed (15580 \pm 1020 RLU), we observed a

significant increase in activity compared to both hGluN2A^{G483R} alone (p < 0.0001) and wild-type hGluN2A alone (p = 0.0021).

When examining cells expressing h(r)GluN2A-L^{G483R}, we observed a significant reduction in bioluminescence (7903 \pm 1143 RLU) compared to hGluN2A-L wild-type (12'621 \pm 611 RLU, p = 0.0002). However, co-expression of wild-type h(r)GluN2A-L with mutant h(r)GluN2A-L subunits restored activity to levels comparable to h(r)GluN2A-L wild-type (12'549 \pm 976 RLU) and significantly increased activity compared to h(r)GluN2A-L^{G483R} alone (p = 0.0034).

Interestingly, co-expression of h(r)GluN2A-L with mutant hGluN2A-S^{G483R} resulted in a significant increase in activity (17'445 \pm 1728 RLU, p = 0.0016). This suggests a potential isoform-specific effect of the G483R mutation on hGluN2A-S.

When comparing the activity of hGluN2A-S wild-type (8569 \pm 447 RLU) to hGluN2A-S^{G483R}, we observed a significant increase in bioluminescence for the mutant (29'327 \pm 1907 RLU, p < 0.0001). Co-expression of wild-type hGluN2A-S with mutant hGluN2A-S^{G483R} resulted in a partial rescue of activity (15'112 \pm 1597 RLU). This activity was significantly reduced compared to hGluN2A-S^{G483R} alone (p < 0.0001) but significantly higher than that of wild-type hGluN2A-S (p < 0.0001)

In summary, we found that the G483R missense mutation adopts a GOF role in hGluN2A-S, with a notable dominant-positive effect when co-expressed with wild-type hGluN2A-S or h(r)GluN2A-L.

By contrast, the G483R mutation assumes a LOF role when present in h(r)GluN2A-L, with no significant dominant-negative effects observed when co-expressed with wild-type h(r)GluN2A-L.

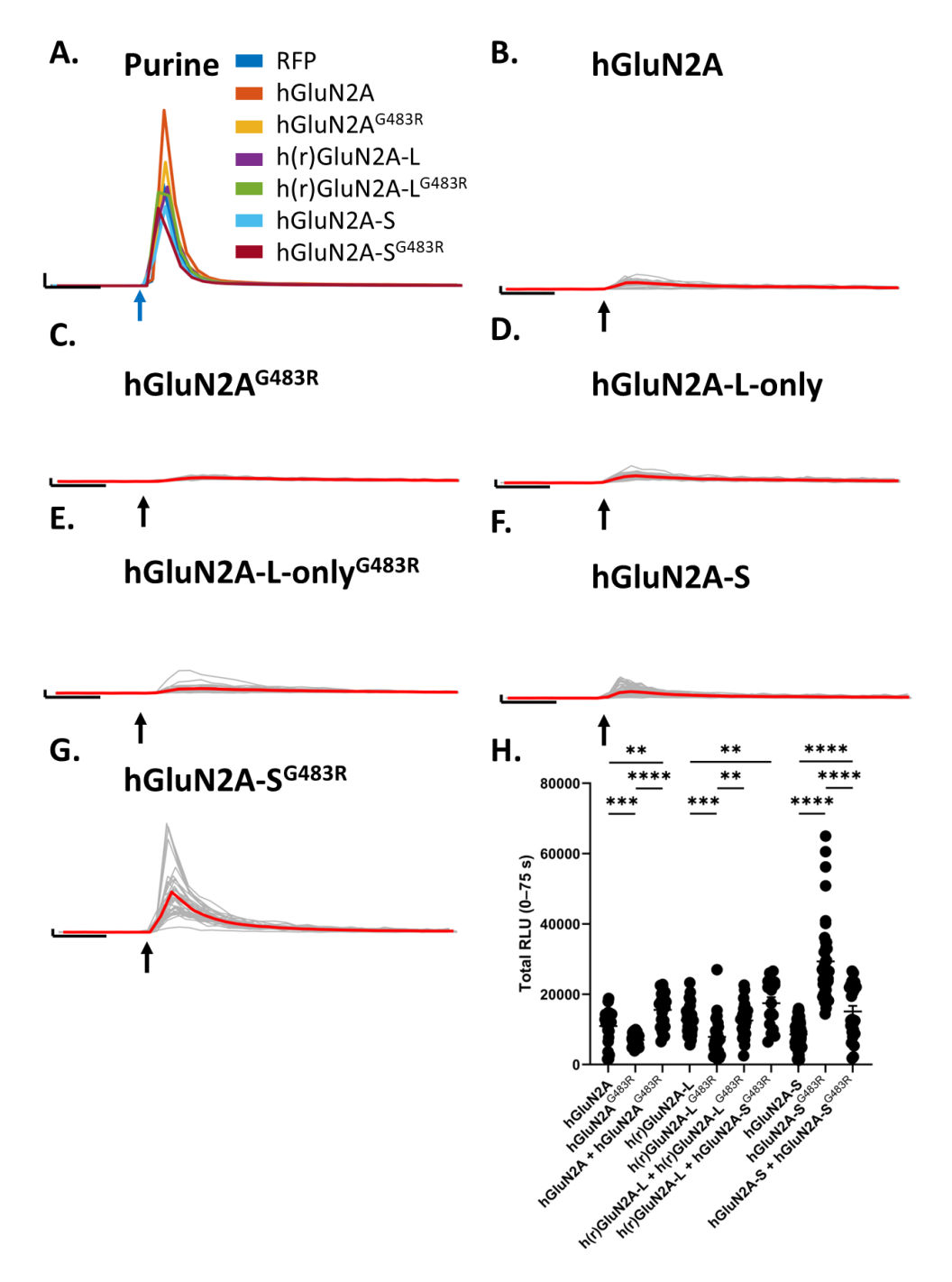


Figure 5.11 - Investigating whether the effect of the G483R missense mutation on hGluN2A-S is isoform-specific.

A) Averaged calcium responses from HEK293G5A cells transfected with either RFP (N = 15 wells), hGluN1-4a/hGluN2A (N = 3 wells), hGluN1-4a/hGluN2A G483R (N = 3 wells), hGluN1-4a/h(r)GluN2A-L (N = 5 wells), hGluN1-4a/h(r)GluN2A-L G483R (N = 3 wells), hGluN1-4a/hGluN2A-S (N = 8 wells) or hGluN1-4a/hGluN2A-S G483R (N = 5 wells)

following application of 1mM MgATP (blue arrow – activation of endogenous P2Y receptors). Scale bar: Y-axis = 10'000 RLU; X-axis = 10 sec. B-G) Calcium responses from HEK293G5A cells transfected with hGluN1-4a/hGluN2A (N = 24 wells), hGluN1- $4a/hGluN2A^{G483R}$ (N = 24 wells), hGluN1-4a/h(r)GluN2A-L (N = 40 wells), hGluN1-4a/h(r)GluN2A-L $4a/h(r)GluN2A-L^{G483R}$ (N = 24 wells), hGluN1-4a/hGluN2A-S (N = 53 wells) or hGluN1-4a/hGluN2A-S^{G483R} (N = 40 wells) following application of 50μM glutamate (black arrow). Scale bar: Y-axis = 100 Relative Luminescence Units (RLU); X-axis = 10 sec. Individual well traces displayed in grey, and the mean response shown in red. H) Summary data concerning the effect of the G483R missense mutation on receptor function and its effect on co-expressed wt receptor subunits. Area under the curve of bioluminescence readings from independent wells per condition. Endogenous calcium activity in cells transfected with RFP were subtracted from calcium responses in cells transfected with NMDA receptor subunits. Data is displayed as independent repeats with mean ± SEM. hGluN2A vs. hGluN2A^{G483R}; unpaired t-test, P = 0.0005, two-tailed. hGluN2A^{G483R} vs. hGluN2A + hGluN2A^{G483R}; unpaired t-test, P < 0.0001, two-tailed. hGluN2A vs. hGluN2A + hGluN2A^{G483R}; unpaired t-test, P = 0.0021, twotailed. h(r)GluN2A-L vs. $h(r)GluN2A-L^{G483R}$; unpaired t-test, P = 0.0002, two-tailed. $h(r)GluN2A-L^{G483R}$ vs. $h(r)GluN2A-L + h(r)GluN2A-L^{G483R}$; unpaired t-test, P = 0.0034, two-tailed. h(r)GluN2A-L vs. hGluN2A-L + hGluN2A-S^{G483R}; unpaired t-test, P = 0.0016, two-tailed. hGluN2A-S vs. hGluN2A-S^{G483R}; unpaired t-test, P < 0.0001, two-tailed. hGluN2A-S^{G483R} vs. hGluN2A-S + hGluN2A-S^{G483R}; unpaired t-test, P < 0.0001, twotailed. hGluN2A-S vs. hGluN2A-S + hGluN2A-S^{G483R}; unpaired t-test, P < 0.0001, twotailed.

5.4 Discussion

5.4.1 Conclusions and Key Findings

5.4.1.1 Bioluminescence-based Ca²⁺ assay as a suitable method for studying ion channel function

In this chapter, we aimed to repurpose a high-throughput bioluminescence assay to measure increases in intracellular Ca²⁺ concentration. This method relies on the stable genomic expression of the GFP-Aequorin fusion protein (G5A) in HEK293 cells. Traditionally, this approach has been used to identify ligands for G protein-coupled receptors (Thiel *et al.*, 2023). Here, we assessed whether exogenously expressed hGluN2A-S-containing NMDARs could generate a measurable bioluminescence signal upon activation with glutamate and glycine agonists.

We observed a robust and reproducible bioluminescence signal across a range of glutamate concentrations, with a maximal response between 50-100 μ M. At concentrations exceeding this, a concentration-dependent decrease in signal was consistently observed. Previous studies investigating the dose-response of NMDARs to glutamate agonist have used concentrations not exceeding 100 μ M (Hedegaard *et al.*, 2012; Stroebel *et al.*, 2014; Yuan *et al.*, 2014). This is likely due to the significant desensitisation and therefore non-conducting state of NMDARs in glutamate concentrations exceeding 100 μ M. We therefore chose to use a concentration of 50 μ M to analyse WT and mutant NMDAR function using the bioluminescence-based Ca²⁺ assay.

Interestingly, a low-level bioluminescence signal was detected even in the absence of added glutamate, despite careful removal of culture media and replacement with a glutamate-free HEPES-based extracellular solution. Glutamate is an abundant amino acid essential for cell metabolism. Residual glutamate, present in the media from dead HEK293 cells, could activate the exogenous hGluN2A-S-containing NMDARs, leading to detectable Ca²⁺-dependent bioluminescence signal. Our observation that APV reduced this background signal suggests that this is—at least in part—the case. We speculate that the remaining signal in the presence of APV constitutes recording noise. While this posed a minor limitation, it did not impede the robust detection of a dose-dependent response to increasing glutamate concentrations.

These findings demonstrate that the bioluminescence-based Ca²⁺ assay is a viable high-throughput method for investigating ion channel function, specifically the activity of wild-type and mutant NMDARs.

5.4.1.2 The GOF epilepsy-associated L812M mutation confers an isoform-independent effect on glutamate potency

We next sought to utilise the bioluminescence-based Ca²⁺ assay to isolate the specific effects of the epilepsy-associated GluN2A GOF missense mutation L812M on the two hGluN2A isoforms. Previous work by Yuan et al (2014) reported an increase in glutamate potency in mutant hGluN2A-containing NMDARs. However, their study did not distinguish between the individual expression of the hGluN2A-L and hGluN2A-S isoforms. We therefore investigated whether the L812M mutation exhibited an isoform-specific effect.

Consistent with Yuan et al. (2014), we found that the L812M mutation induced a leftward shift in the glutamate dose-response curve in both h(r)GluN2A-L and hGluN2A-S-containing NMDARs, indicative of increased glutamate potency. However, the dose-response relationship was comparable between wild-type and mutant receptors for both isoforms, suggesting that the L812M mutation exerts an isoform-independent effect. This finding suggests also suggests that

the C-terminal differences between the hGluN2A-L and hGluN2A-S isoforms don't influence the distal gating regions located between the M4 transmembrane domain of GluN2A and the M3/pre-M1 helix of GluN1 (Yuan *et al.*, 2014). Our findings therefore suggest that, in individuals carrying the L812M mutation, both hGluN2A-L and hGluN2A-S isoforms exhibit similarly enhanced sensitivity to glutamate release, indicative of an isoform-independent effect on NMDAR function.

As in our previous findings, we detected a measurable Ca^{2+} -dependent bioluminescence signal even in the absence of added glutamate, indicating basal NMDAR activation. This effect was more pronounced in the presence of the L812M mutation for both isoforms. We determined that this was, NMDAR-mediated, as the bioluminescence signal was reduced following the addition of 50 μ M APV, a competitive NMDAR antagonist. These results suggest that residue glutamate—potentially from HEK cell turnover—was sufficient to activate NMDARs, with the L812M further sensitising receptors to glutamate.

Despite the presence of APV, there existed a basal level of measurement noise. This was also apparent in wells containing HEK cells transfected with soluble RFP where there existed no NMDARs to respond to background glutamate. We speculate a contribution from endogenous Ca²⁺ signalling pathways. HEK cells express several receptors capable of increasing intracellular Ca²⁺, including P2Y G protein-coupled receptors and TRPC family ion channels (Schachter *et al.*, 1997; Bugaj *et al.*, 2005). While this background activity requires us to be cautions in interpreting small fluctuations, it did not obscure the dose-dependent glutamate-dependent effect of the L812M mutation in enhancing glutamate sensitivity for hGluN2A isoforms.

While our findings align with those of Yuan et al. (2014), a key difference in our approach lies in the method of quantification. Yuan et al (2014) reported a reduction in the half-maximal effective concentration of agonist (EC₅₀). However, the data we obtained from our bioluminescence-based Ca²⁺ assay using the L812M mutant receptors showed a sharp increase in activity at low external glutamate addition, rather than the characteristic sigmoidal (S-shaped) curve typically seen in dose-response data. This is resultant possibly due to background glutamate as discussed above. This deviation prevented the accurate fitting of our data to a sigmoidal curve and hindered EC₅₀ determination. As a result, we suggest that while the bioluminescence-based assay offers a high-throughput approach for studying NMDAR activity, more controlled techniques may be necessary for precise EC₅₀ measurements. Traditional methods, such as two-electrode voltage-clamping in *Xenopus* oocytes or patch-clamp recordings in HEK293 cells, provide better control over extracellular glutamate concentration and may yield further comparison of glutamate potency across the mutant hGluN2A isoforms.

In averaged traces, we observed a smaller peak bioluminescence from the L812M mutant receptors. However, this was not significantly different from the WT receptors. Analysis of individual well readings revealed that the reduction in bioluminescence was not representative of the overall data distribution. Notably, we identified a single outlier well in both the h(r)GluN2A-L and hGluN2A-S WT conditions. We speculate that conditions within these individual wells may have differed from the others, such as a higher number of cells or level of NMDAR expression present at the time of recording. A limitation of our methodology was that the position of conditions on the 96-well plate remained consistent across experiments. While temperature and CO₂ levels were regulated within the cell incubator and air circulation was maintained, there may have been a gradient of temperature of CO₂ concentration across the plate. This could have contributed to variability in the number of viable cells or the level of NMDAR expression across wells. Although we monitored cell viability by assessing activation of endogenous P2Y purinergic receptors, there may have existed disparities in the expression levels of NMDARs within the HEK293 cells. Lin et al. (2015) showed that whilst decreasing culture temperature from 37°C to 33°C 24 hours post-transfection led to a reduction in HEK293 cell growth, there was a marked increase both GFP and AMPARs expression (Lin et al., 2015). We therefore recommend that future experiments using this assay randomise the positioning of conditions on the 96-well plate. This would introduce variability across the conditions and help prevent unintentional bias between experimental groups.

5.4.1.3 The GOF epilepsy-associated L812M mutation confers an isoform-specific change in Mg²⁺ sensitivity

Previous studies by Yuan et al. (2014) and Elmasri et al. (2020) examined the effects of the L812M mutation on the voltage-dependent Mg²⁺ blockade of NMDARs, reporting a reduction in Mg²⁺-dependent inhibition. This was attributed to an increased proportion of unblocked channels and, consequently, enhanced conductance during depolarisation (Yuan *et al.*, 2014; Elmasri *et al.*, 2020). Here, we aimed to determine whether the L812M mutation exerts isoform-specific effects on h(r)GluN2A-L and hGluN2A-S-containing NMDARs.

Consistent with previous findings, we observed that the L812M mutation in h(r)GluN2A-L induced a shift in the current-voltage relationship indicative of reduced voltage-dependence and, therefore, decreased Mg²⁺ blockade at negative membrane potentials. This aligns with the notion that the L812M mutation in hGluN2A-L contributes a GOF effect via both increased glutamate potency and reduced extracellular Mg²⁺ blockade (Yuan *et al.*, 2014; Elmasri *et al.*, 2020).

Surprisingly, however, we found that the L812M mutation did not appear to alter the voltagedependence of Mg²⁺ blockade in hGluN2A-S-containing receptors, as the current-voltage

relationship remained comparable between wild-type and mutant receptors. This finding exceeded our expectations, particularly given our previous result in Chapter 4, which demonstrated that hGluN2A-S confers increased Mg²⁺ sensitivity. We hypothesised that this increased Mg²⁺ sensitivity might counteract the reduction in voltage dependence induced by the L812M mutation. However, our results suggest that hGluN2A-S retains wild-type-like voltage dependence, despite the presence of the mutation.

These findings indicate that the C-terminal differences between hGluN2A-L and hGluN2A-S not only influence voltage-dependent Mg²⁺ blockade but may also provide a partial compensatory effect against certain pathophysiological consequences of the L812M mutation. This supports the idea that the two hGluN2A isoforms have distinct functional roles and presents potential therapeutic opportunities. For example, selective targeting of hGluN2A-L may help mitigate the decrease in voltage dependent Mg²⁺ blockade imposed by the L812M mutation. Conversely, upregulating hGluN2A-S expression may partially rescue the detrimental effects of the L812M mutation. This may therefore rescue NMDAR function, and consequently, the clinical pathophysiology in individuals carrying this *GRIN2A* mutation. Notably, our results highlight the necessity of studying hGluN2A isoforms independently, as previous research that did not distinguish between hGluN2A-L and hGluN2A-S may have overlooked critical isoform-specific properties.

Warming et al. (2019) estimated that hGluN2A-S accounts for ~30% of total hGluN2A protein in the human brain. Therefore, increasing the hGluN2A-S to hGluN2A-L ratio could potentially mitigate some of the phenotypic effects of epilepsy-associated GOF mutations such as L812M. This finding underscores the importance of understanding isoform-specific contributions to NMDAR function in both physiological and pathological contexts.

5.4.1.4 Isoform-independent effect of disease-associated C231Y and C436R LOF mutations

We next investigated the effects of two epilepsy-associated LOF mutations, C231Y and C436R, on hGluN2A-S-containing NMDARs. Previous work by Addis et al. (2017) demonstrated that these mutations strongly impact hGluN2A-containing NMDAR expression and function, implicating them in the pathophysiology of EAS disorders. However, their study did not distinguish between hGluN2A-L and hGluN2A-S isoforms and did not account for the heterozygous genotype of affected patients (Addis et al., 2017). To address these limitations, we examined the independent effects of these mutations on hGluN2A-S and assessed whether their LOF effects persisted despite co-expression of wild-type hGluN2A-S subunits.

Consistent with Addis et al. (2017), we observed a significant reduction in NMDAR function, as indicated by decreased Ca²⁺ conductance, for both the C231Y and C436R mutations. This suggests that despite the differences in the C-terminal domain, these LOF mutations impose functional deficits on NMDARs containing mutant hGluN2A-S subunits.

Interestingly, despite the pronounced LOF effects of both mutations, overexpression of wild-type hGluN2A-S alongside the respective mutants restored Ca²⁺ conductance to levels comparable to wild-type hGluN2A-S-containing NMDARs. This indicates that, despite impairments in protein folding and NMDAR assembly caused by the mutations, HEK293 cells were able to synthesise, fold, assemble, and traffic functional wild-type hGluN2A-S-containing NMDARs to the plasma membrane. These findings suggest that the C231Y and C436R do not exert a dominant-negative effect on wild-type hGluN2A-S subunits. However, whether triheteromeric hGluN2A-S wild-type/mutant receptor co-exist alongside diheteromeric wild-type hGluN2A-S receptors remains undetermined. Future research is needed to explore whether wild-type hGluN2A-S subunits exert a compensatory effect within the NMDAR tetramer.

In summary, for individuals carrying the epilepsy-associated C231Y or C436R mutation, the presence of a wild-type allele expressing hGluN2A may provide partial compensation. However, the resulting haploinsufficiency of hGluN2A could still contribute to the phenotype observed in EAS disorders.

5.4.1.5 The LOF epilepsy-associated G483R mutation confers a GOF effect in hGluN2A-S

Lastly, we investigated the effects of the epilepsy-associated LOF mutation G483R on NMDARs containing either h(r)GluN2A-L or hGluN2A-S subunits. Addis et al. (2017) previously reported a borderline dysfunction hGluN2A-containing NMDARs carrying this mutation. We hypothesised that an isoform-specific effect may have been obscured due to the mixed expression of hGluN2A-L and hGluN2A-S subunits in their experimental conditions (Addis et al., 2017). Additionally, as with the previously examined LOF mutations, we assessed whether G483R exerted a dominant effect when co-expressed with wild-type receptor subunits.

When we expressed a mixture of hGluN2A-L and hGluN2A-S subunits, we observed a significant decrease in Ca^{2+} influx through NMDARs, suggesting a stronger dysfunction than the borderline effect reported by Addis et al. (2017). This discrepancy may be attributed to the increased statistical power in our study due to a larger sample size. Notably, the LOF effect was replicated when we examined the isolated expression of h(r)GluN2A-L, as evidenced by a significant reduction in total bioluminescence compared to wild-type h(r)GluN2A-L receptors.

Unexpectedly, we found that the G483R mutation within NMDARs containing hGluN2A-S resulted in a substantial GOF, characterised by a significant increase in NMDAR-mediated Ca²⁺ influx. This isoform-specific effect was not detected by Addis et al. (2017) and was likely masked in their measurements of mixed isoform expression. The opposing effects of G483R—LOF in hGluN2A-L and GOF in hGluN2A-S—may explain the previously reported borderline dysfunction, which our study resolved as an overall significant LOF due to increased statistical power.

Interestingly, when we co-expressed wild-type and mutant hGluN2A subunits—producing a combination of hGluN2A-L and hGluN2A-S, both mutant and wild-type—we observed a dominant-positive effect, reflected in a significant increase in receptor activity compared to wild-type. By separately analysing the two isoforms, we determined that this dominant-positive effect was driven by the G483R mutant hGluN2A-S subunit. In contrast, the mutant h(r)GluN2A-L subunit did not exert a dominant-negative effect. However, when mutant hGluN2A-S was co-expressed with either h(r)GluN2A-L or wild-type hGluN2A-S subunits, a dominant positive effect persisted.

In summary, our findings indicate that differences in the C-terminal domain of hGluN2A-S significantly influence the functional impact of the G483R mutation. While G483R induces a LOF effect in h(r)GluN2A-L receptors, it paradoxically confers a GOF effect in hGluN2A-S-containing NMDARs. Furthermore, the GOF effect in hGluN2A-S is sufficient to drive a dominant positive effect, when wild-type and mutant receptors are overexpressed together.

This work further highlights differences between hGluN2A-L and hGluN2A-S and underscores the necessity of studying these isoforms independently. The previous study has not distinguished these opposing effects of the G483R mutation, which could have important implications for understanding GRIN2A-associated neurological disorders. Other epilepsy-associated GRIN2A mutations may also contribute differently to pathophysiological dysfunction dependent on isoform-specific expression. Notably, the distinct roles of hGluN2A-L and hGluN2A-S in GRIN2A-associated epilepsy may partially explain the variable efficacy of current treatment strategies. We propose that in addition to considering whether a given mutation results in a GOF or LOF, future therapeutic approaches should account for isoform-specific contributions. In the case of patients carrying the G483R mutation, treatment strategies aimed at correcting LOF effects could inadvertently exacerbate the GOF effect in hGluN2A-S, potentially worsening disease outcomes.

In our experiments investigating the isoform-specific role of disease-associated mutations on NMDARs, we focused on exogenous overexpression in HEK293 cells. HEK293 cells are widely used due to their ease of culture, transient transfection efficiency, and experimental versatility (Thomas and Smart, 2005). Moreover, HEK293 cells do not endogenously express NMDARs, making them ideal for studying specific NMDAR compositions in isolation. In patients carrying

these mutations, there is a mixture of GluN1 and GluN2 subunits within the NMDAR, alongside heterozygosity for these mutations, resulting in a combination of WT and mutant receptors and subunits. These NMDARs are also under endogenous promoter control, leading to physiological levels of expression that are not accurately modelled in the context of exogenous overexpression in HEK cells. It is important therefore, to support our findings in models of NMDAR activity that are more physiologically accurate systems—for example studying these receptors at neuronal synapses under endogenous promoter control.

For our experiments, we chose to use the GluN1-1a or GluN1-4a isoforms of the obligatory GluN1 NMDAR subunit. Bioinformatic analysis by Herbrechter et al. (2021) revealed that GluN1-1 and GluN1-4 are the most common splice forms in humans, accounting for ~35% and 38%, respectively (Herbrechter et al., 2021). However, these are only two of the eight alternatively spliced isoforms present in the human brain. These isoforms can be incorporated into NMDARs with the five GluN2 subunits (GluN2A-L, GluN2A-S, GluN2B, GluN2C, and GluN2D), forming both di- and tri-heteromeric configurations. It is crucial, therefore, to recognise the complexity of NMDAR function, which cannot be fully modelled within heterologous cell lines. The functional roles of hGluN2A-L and hGluN2A-S in both physiological and disease-associated contexts may differ depending on the specific subunit combinations incorporated into the NMDAR.

Therefore, while exogenous overexpression systems provide a controlled environment for investigating the specific contributions of NMDAR subunits, the full complexity of NMDAR function, particularly in disease states, requires a more nuanced approach that considers the diverse subunit combinations and physiological contexts that exists *in vivo*.

5.4.2 Future perspectives

Our findings indicate an isoform-specific effect of the G483R epilepsy-associated *GRIN2A* mutation. However, it is important to acknowledge that this striking result stems from a single experimental method, repurposed from its use for the study of G-protein coupled receptors. A confirmatory approach yielding similar results would strengthen the hypothesis that the G483R mutation confers a GOF effect on hGluN2A-S while imparting a LOF effect on hGluN2A-L.

In chapter 4.3.2, we observed a similar distribution of maximal current at +50 mV between NMDARs containing either h(r)GluN2A-L or hGluN2A-S. Based on this, we propose that subjecting transfected HEK cells to a square voltage stimulus during local agonist perfusion via iontophoresis could provide a measure of the maximal stable current at +50 mV. We hypothesise that NMDARs containing h(r)GluN2A-L^{G483R} will exhibit reduced maximal current, whereas hGluN2A-S^{G483R} will

show an increase. Such findings would further support the notion that the G483R mutation enhances conductance in hGluN2A-S-containing NMDARs.

To elucidate the underlying mechanism by which G483R imposes a GOF effect on hGluN2A-S-containing receptors, we suggest assessing total synthesised hGluN2A-S^{G483R} protein and membrane trafficking. Following the approach by Addis et al. (2017), we propose performing western blot analysis on lysates of HEK293 cells transfected with either h(r)GluN2A-L or hGluN2A-S, in both wild-type and mutant forms. Additionally, immunocytochemistry on fixed and permeabilised cells would allow for the determination of the isoform-specific impact of the G483R mutation on membrane localisation (Addis et al., 2017). These analyses may provide a deeper understanding of the isoform-specific effects of hGluN2A-S in individuals carrying the G483R epilepsy-associated mutation. In turn, this may inform potential therapeutic strategies that specifically target the dysfunctional mechanisms in each hGluN2A isoform.

Beyond the G483R mutation, Addis et al. (2017) also reported a borderline effect of the P79R missense mutation on the number of cells responding to glutamate, despite observing reduced agonist potency and surface expression. Proline-79 is located within the NTD and is predicted to make extensive contact with the GluN1 subunit. It has been suggested that substituting proline for basic arginine disrupts this interaction, indirectly altering the glutamate and zinc binding sites in hGluN2A (Serraz, Grand and Paoletti, 2016). Given that we have developed a framework for investigating the individual function of hGluN2A-L isolated from hGluN2A-S, we propose that isolating the effects of P79R in these isoforms may reveal an unappreciated isoform-specific influence on glutamate agonism and zinc antagonism.

Overall, we advocate for future studies of hGluN2A function in neurological disorders to investigate the two isoforms separately. Our findings suggest that mutations like G483R may exert distinct, isoform-dependent effects that cannot be fully appreciated when hGluN2A-L and hGluN2A-S are studied together. By isolating these isoforms, we may gain a more nuanced understanding of their respective roles in disease pathology; therefore, providing more informed therapeutic intervention.

Chapter 6 General discussion and future directions

6.1 Overview of findings

Our research advances our understanding of how a previously unappreciated primate-specific GluN2A subunit within the NMDAR may confer a divergent function in both physiological and disease-relevant settings. Before the work presented in this thesis, work to investigate the function of the GluN2A subunit has either been performed on rodent GluN2A protein or in a mixed expression of hGluN2A-L and hGluN2A-S isoforms. Whilst rodent and human NMDARs share highly conserved sequences and functional properties (Hedegaard et al., 2012), the presence of a primate-specific GluN2A subunit not expressed in rodents presents an unexplored avenue of NMDAR function that cannot be studied using rodent GluN2A expression. Equally, we now suggest that studies that have driven exogenous hGluN2A expression are presenting an incomplete picture of hGluN2A function due to the mixed contribution of hGluN2A-L and hGluN2A-S isoforms. Exploiting a single nucleotide difference in the acceptor splice dinucleotide between human and rat Grin2A transcripts we have generated a tool to prevent the co-expression of both isoforms. This hence provides the field with a means of studying the functional properties of hGluN2A-L and hGluN2A-S in isolation.

We have begun to show how this tool can be used to extend the work of Warming et al. (2019) and begun to investigate how this shorter protein isoform is conferring different functional properties to the NMDAR. We have found that despite the difference existing within the C-terminal domain, there is an alteration of the voltage-dependence driven by Mg²⁺ blockade. Diheteromeric NMDARs with hGluN2A-S functional subunits present an increased Mg²⁺ sensitivity. These NMDARs therefore require a greater extent of depolarisation to remove their channel porebound Mg²⁺ and therefore flux Na⁺, K⁺ and Ca²⁺ ions across the plasma membrane. This therefore reveals a previously unappreciated subpopulation of NMDARs in the human brain that have incorporated hGluN2A-S and therefore may contribute a decrease in neuronal excitability. A stronger stimulus, providing a greater extent of depolarisation may be required to trigger NMDAR conductance when hGluN2A-S is highly represented at the plasma membrane.

Additionally, in this thesis we have begun to isolate the individual effect that certain epilepsy-associated *GRIN2A* mutations have on either hGluN2A-L or hGluN2A-S subunits within the NMDAR. We have found that for the GOF L812M mutation, whilst the glutamate potency is similarly increased for both isoforms, hGluN2A-S appears to negate the decrease in voltage-dependence. This isoform-specific absence of Mg²⁺ sensitivity decrease by hGluN2A-S was

previously masked in studies investigating the voltage-dependence of a mixture of L812M mutant hGluN2A isoforms (Yuan et al., 2014; Elmasri et al., 2020). This work highlights greater levels of complexity to the pathophysiology of epilepsy-associated mutations such as L812M than previously appreciated and proposes a potential target for therapeutic intervention to combat the dysfunction driven by hGluN2A in these patients.

Lastly, we have found another example of divergence in function between hGluN2A-L and hGluN2A-S in the context of neurological disease. Whilst previous work by Addis et al. (2017) presents the epilepsy-associated G483R *GRIN2A* missense mutation as conferring a LOF on the NMDAR. In work presented here, however, we suggest that this LOF effect is driven specifically by the hGluN2A-L isoform. We found, however, that when the G483R mutation is present in hGluN2A-S, there is a GOF effect present. This therefore provides more evidence of an unexplored avenue of understanding in the pathophysiology of some epilepsy-associated *GRIN2A* mutations. It raises the question of how a difference in the C-terminal domain can confer differences in distal sites in the NMDAR architecture, and what other mutations or neurological disorders hGluN2A-S may be contributing to a difference of effect. We propose that future studies need to appreciate the possibility that in the human brain there is a differing contribution to function and dysfunction from the long and short isoforms. Future studies and subsequent therapeutic interventions should treat the isoforms as separate entities that together may underpin a phenotype but individually may contribute very different functional effects.

6.2 Future research directions

6.2.1 Further investigation of the altered Mg²⁺ sensitivity in hGluN2A-S

The investigation into the functional properties of hGluN2A-S is far from complete. In Chapter 4, we found that at a physiological concentration of Mg²⁺ (2 mM), hGluN2A-S displays a subtle increase in voltage-dependency through an increased Mg²⁺ sensitivity. This sensitivity becomes more apparent when we decreased the Mg²⁺ availability (0.1 mM). Yet to be elucidated, however, is a measure of the potency of Mg²⁺ in inhibiting the channel pore. We therefore suggest a measure of hGluN2A-S-containing NMDAR activity in a dose-response manner to obtain an IC50 value. We have carried out a pilot study using the repurposed bioluminescence-based Ca²⁺ assay, however, we were unable to obtain a dose-response relationship with the experimental parameters used (See Appendix A). We found that the resting membrane potential of transfected HEK293 cells to be around -10 mV. It is suggested that at this membrane potential there is a large and near maximal influx of Ca²⁺ through the NMDAR (Garaschuk et al., 1996). This therefore prevents the measurement of the differences in Mg²⁺ inhibition in an assay relying on changes in

Ca²⁺ influx. We propose that a method to alter the resting membrane potential of the HEK293 cells to a more negative value may allow a dose-response relationship to be uncovered. For example, the co-expression of an inward rectifying K⁺ channel such as IRK1 may drive the resting membrane potential to a value at which we have observed the changes in current-voltage relationship in our electrophysiology studies (Kubo et al., 1993).

Alternatively, we propose the repeating of our current-voltage relationship measurements using a slow voltage ramp stimulus at a greater range of external Mg²⁺ concentrations. Although a lower throughput method, the measurement of the current through the hGluN2A-S-containing NMDARs across a range of membrane potentials may provide more of an understanding of the relationship between Mg²⁺ availability and the voltage-dependency of hGluN2A-S receptors.

Additionally, the exact nature by which the shorter C-terminal domain and/or unique C-terminus is affecting the channel pore Mg²⁺ binding site is yet to be investigated. We predict that subtle changes in the structural conformation resulting from the shorter C-terminal domain may be conferring changes in the interaction of Mg²⁺ with its binding site—thereby leading to an alteration of Mg²⁺ bind/unbind kinetics during depolarisation. Previous work by Karakas and Furukawa (2014) resolved the crystal structure of the GluN1/GluN2B NMDAR, allowing exploration of intersubunit and interdomain interactions—in particular, the residues involved in Ca²⁺ permeability and Mg²⁺ binding within the channel pore. We propose that adopting a similar technique to resolve the crystal structure of hGluN2A-S-containing NMDARs may provide some insight into differences that exist within the channel pore that may explain the changes in Mg²⁺ binding and unbinding (Karakas and Furukawa, 2014).

6.2.2 Developing rodent models to explore GluN2A-S function

In Chapter 3, we investigated whether introducing the acceptor splice site present in hGRIN2A could generate a second, shorter rGluN2A isoform. This approach aimed to establish a rodent model for studying GluN2A-S function. However, we found that a single nucleotide change was insufficient to produce two rGrin2A mRNA transcripts.

We hence propose an alternative approach to achieve endogenous expression of a shorter mouse GluN2A (mGluN2A) isoform. This strategy avoids caveats associated with transient overexpression, such as non-physiological protein levels, abnormal localisation, and potential artifacts due to altered binding or non-specific interactions. By placing expression under endogenous promoter control, we aim to more accurately replicate physiological conditions.

A promising method for precise genomic editing is Targeted Knock-In with Two (TKIT) guides, developed by Fang et al. (2021). This CRISPR/Cas9-based approach employs two guide RNAs (gRNAs) targeting non-coding regions flanking the coding region of interest. This strategy protects the coding sequence from insertion and deletion (INDEL) mutations and allows greater flexibility in gRNA selection, improving target specificity and reducing off-target effects (Fang et al., 2021).

We propose using TKIT to target gRNAs to the non-coding regions flanking exon 13 of mouse Grin2A (mGrin2A). The gRNA, delivered via a U6 dual-promoter expression vector with *Streptococcus pyogenes* Cas9, would direct the removal of exon 13 from the genomic DNA. A donor DNA fragment would then be inserted containing: the excised portion of intron 12-13, a truncated mGrin2A exon 13 incorporating the region of hGRIN2A-S encoding the unique hGluN2A-S C-terminus and the removed portion of the 3'-untranslated region (UTR) of exon 13 (Figure 6.1A).

To ensure correct integration, we propose the use of a switch-and-flip strategy as developed by Fang et al. (2021), where gRNAs in the donor DNA are arranged in reverse orientation. If the donor fragment is inserted incorrectly, Cas9 will continue cutting the intact gRNA recognition sites until the correct orientation is achieved through loss of gRNA recognition or INDEL-induced activation (Figure 6.1B). This method is expected to produce three possible outcomes: wild-type GRIN2A, a truncated mGrin2A or exon 13 deletion without donor insertion. The knock-in process can be validated via gDNA extraction, RT-PCR, and cDNA sequencing (Fang et al., 2021).

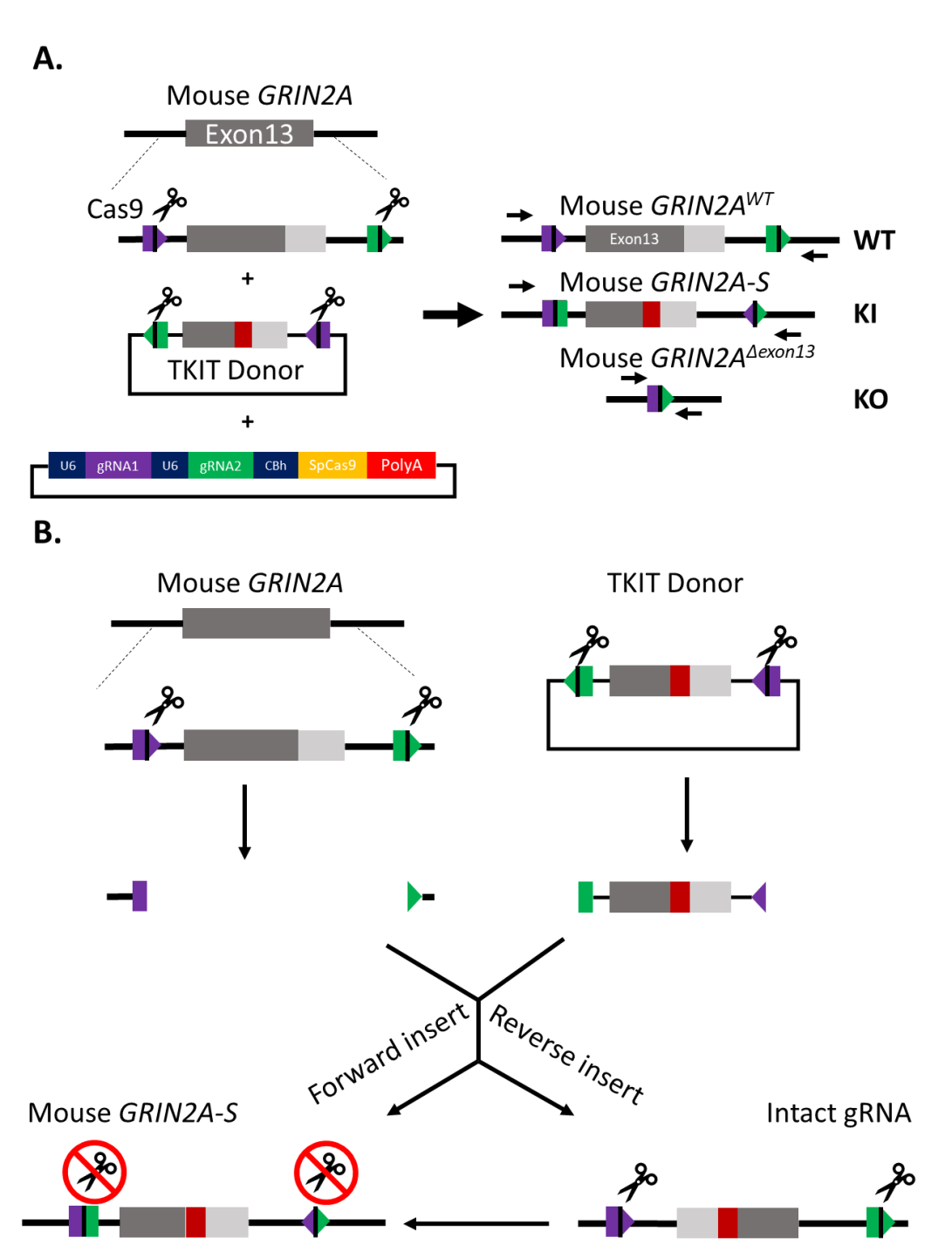


Figure 6.1 - TKIT design for the generation of a mouse GluN2A-S isoform.

A) Graphical representation of the proposed design of Targeted Knock-In with Two (TKIT) guides to allow the precise replacement of exon 13 of mGrin2A gDNA with the unique region of hGRIN2A. (left) Depiction of the target site, donor DNA fragment and dual-promoter guide RNA pX330 expression vector. Exon 13 is depicted in dark grey whilst the 3'UTR is depicted in light grey. The purple and green pentagons indicate gRNA target sequences. The black vertical lines within the pentagons indicate the Cas9 cleavage site. (right) Schematic of gDNA following knock-in with TKIT. Arrows indicate primers for RT-PCR and cDNA sequencing for knock-in validation. B) Graphical representation of the switch-and-flip design. The two gRNAs

within the donor will have opposite locations and flipped sequences compared to the gDNA. Following Cas9 cleavage and randomised non-homologous end-joining. If the donor gDNA is inserted into the reverse orientation, the gRNAs and PAMs will remain intact, allowing continued cleavage and insertion until the donor DNA fragment is inserted in the correct orientation; hence removing the gRNA recognition sites.

In vivo, TKIT-mediated knock-in could be achieved through in utero electroporation, in which gRNAs and donor DNA are introduced into the embryonic mouse brain via injection into the lateral ventricles, followed by electrical pulses to facilitate DNA uptake into neural progenitor cells. This would allow expression of a mGluN2A-S under endogenous promoter control, carrying the truncated CTD characteristic of hGluN2A-S.

A key challenge of this approach is the mosaic expression of knock-in products, as neurons may express either wild-type mGluN2A (failed donor insertion), mGluN2A-S (successful knock-in), or no exon 13 (failed repair). To distinguish successfully modified neurons, a visual selection marker, such as GFP, could be integrated into the donor DNA. This would enable the identification of neurons expressing the truncated mGluN2A-S, facilitating downstream functional analyses.

Developing a rodent model that endogenously expresses a truncated GluN2A-S isoform would provide a crucial tool for studying its function in the brain. By leveraging TKIT-mediated CRISPR/Cas9 editing, we could overcome limitations with transient overexpression and create a physiologically relevant model system for investigating the function of GluN2A-S in synaptic function and neurological disorders.

6.2.3 Investigating the synaptic localisation of hGluN2A-S

As introduced in Chapter 1.1 GluN2A binds to the scaffolding protein PSD-95, facilitating the clustering and stabilisation of GluN2A-containing NDMARs within the PSD of neuronal synapses. This interaction occurs via the SH3 and PDZ2 domains of PSD-95, which bind to the SH3- and PDZ-binding motifs of the GluN2A CTD (Cousins, Kenny and Stephenson, 2009; Cousins and Stephenson, 2012). The CTD of hGluN2A-S, however, lacks both the PSDPYK SH3-binding motif (positions 1383-1388) and ESDV PDZ-binding motif (1460-1464) (Figure 6.2). It remains unclear whether hGluN2A-S can associate with PSD-95 and localise to the synapse despite lacking these binding sites.

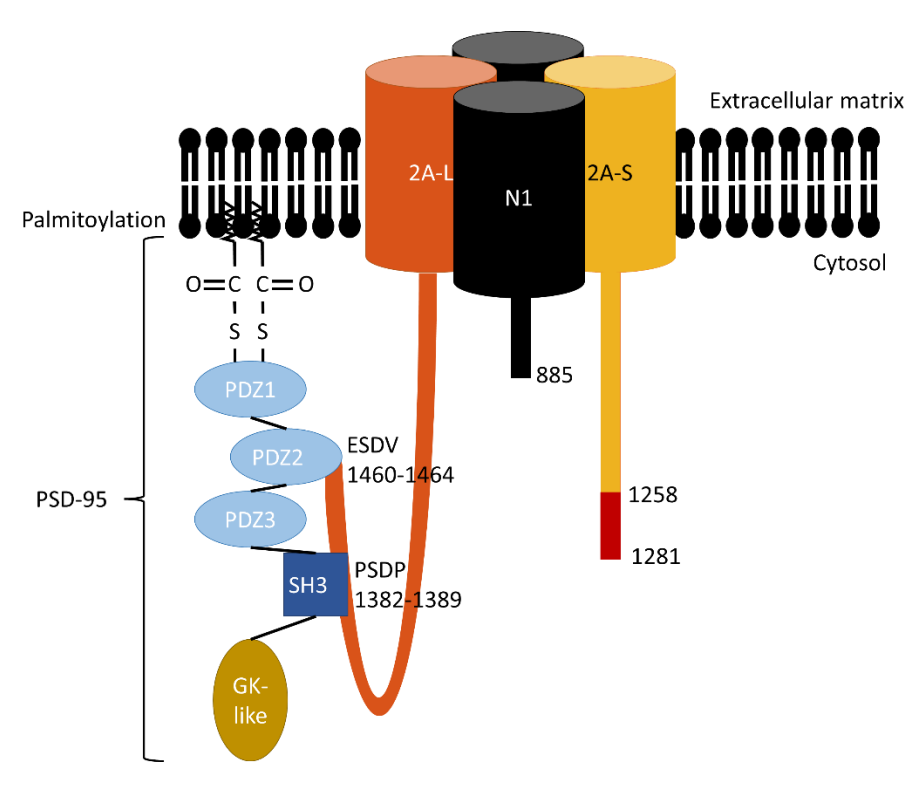


Figure 6.2 - Human GluN2A-S lacks both the C-terminal binding regions for PSD-95.

Graphical representation of PSD-95 binding to the C-terminal domain of hGluN2A. A GluN1/GluN2A-L/GluN2A-S triheteromer is displayed for comparison, showing the absence of the PSD-95 ESDV PDZ-binding and the PSDPYK SH3-binding regions in hGluN2A-S. The unique region of hGluN2A-S is shown in red.

We hypothesise that while diheteromeric hGluN2A-S-containing NMDARs may not be present at the synapse, hGluN2A-S could still localise and stabilise within triheteromeric configurations. The presence of PSD-95 binding sites in hGluN2A-L or hGluN2B may be sufficient to facilitate the localisation and function of GluN1/GluN2A-L/GluN2A-S or GluN1/GluN2B/GluN2A-S triheteromers at the synapse.

To test this, we propose an experimental approach to determine whether hGluN2A-S can localise at the synapse and whether its synaptic presence depends on a triheteromeric configuration with a subunit such as hGluN2B. Previous studies (Akashi et al., 2009; Gray et al., 2011) have generated GluN2A and GluN2B floxed mice using the Cre-loxP system, which enables conditional knockout of GluN2A and/or GluN2B expression. Crossing *GRIN2A*^{fl/fl} and *GRIN2B*^{fl/fl} mice allows selective deletion of these subunits upon Cre-recombinase expression, excising loxP-flanked regions within *GRIN2A* and *GRIN2B* gDNA (Akashi et al., 2009; Gray et al., 2011). By first removing endogenous GluN2A and GluN2B expression (*GRIN2A*^{fl/fl}*GRIN2B*^{fl/fl}), we can exogenously express hGluN2A-S and measure its contribution to synaptic NMDAR function. Electrophysiological recordings of NMDAR-mediated current in neurons expressing Cre-recombinase and hGluN2A-S will help determine whether diheteromeric hGluN2A-S NMDARs can localise and function at the synapse

despite lacking PSD-95 binding sites. We can exploit the characteristic differences in deactivation kinetics between GluN2A- and GluN2B-containing receptors. As discussed in Chapter 1.1, GluN2A confers a more rapid deactivation time course to NMDAR-mediated current compared to GluN2B (Vicini et al., 1998). This may therefore act as a marker for synaptic hGluN2A-S function in a GluN2A/GluN2B knockout background.

This approach assumes that the CTD truncation and unique C-terminus of hGluN2A-S do not affect NMDAR channel kinetics. Stroebel et al. (2014) demonstrated that replacing the GluN2A CTD with the C-terminal region of GABA-B receptors presented deactivation kinetics comparable to wt GluN2A-containing NMDARs.

To further investigate the potential requirement of a triheteromeric configuration for synaptic hGluN2A-S localisation, we can further exploit the differences in GluN2A and GluN2B deactivation kinetics. Hansen et al. (2014) showed that GluN1/GluN2A/GluN2B triheteromeric NMDARs exhibit deactivation kinetics intermediate between GluN2A and Glun2B diheteromers (Hansen et al., 2014). Using the Cre/loxP system we can conditionally knockout endogenous GluN2A while preserving GluN2B expression (*GRIN2A*^{fl/fl}*GRIN2B*^{wt/wt}). hGluN2A-S can then be exogenously expressed which may drive incorporation into GluN1/GluN2B/GluN2A-S triheteromers. If hGluN2A-S contributes to synaptic NDMARs in a triheteromeric configuration with GluN2B, electrophysiological recording should reveal an intermediate deactivation time course. This would suggest that synaptic localisation of hGluN2A-S depends on hGluN2B, providing further insight into the role of hGluN2A-S in human excitatory neurotransmission.

Appendix A Bioluminescence-based calcium assay for the analysis of NMDA receptor magnesium pharmacology

A.1 Introduction

Building on our success in repurposing the bioluminescence-based Ca²⁺ assay to investigate glutamate-induced NMDAR activity, we explored whether this technique could also be applied to study Mg²⁺ inhibition in hGluN2A-S-containing NMDARs. To assess this, we conducted a pilot study measuring Ca²⁺ influx through NMDARs across a range of external Mg²⁺ concentrations. Our goal was to generate an inhibition curve to estimate the IC₅₀ value for hGluN2A-S-containing NMDARs compared to those containing either rGluN2A or h(r)GluN2A-L. This approach aimed to provide a deeper insight into the role of the hGluN2A-S subunit in Mg²⁺ blockade.

A.2 Methods

A.2.1 Bioluminescence assay

HEK cell media was removed, and the cells were gently washed with a magnesium-free HEPES-based extracellular solution containing (in mM): 140 NaCl, 2 CaCl2, 10 glucose, 3 KCl, 0.1mM glycine, 10mM HEPES, with the pH adjusted to 7.4 using 1M NaOH. The cells were then incubated in the same solution supplemented with 3mM Coelenterazine h (Cat# BT10110-2) for 2 hours at 37°C, protected from light by wrapping the 96-well plate in aluminium foil.

A reagent plate was prepared with $MgCl_2$ diluted in magnesium-free HEPES-based extracellular solution containing 50 μ M glutamate. $MgCl_2$ was diluted at the following concentrations (in mM): 0.001, 0.01, 0.1, 1, 5, 10, and 50. A magnesium-free condition served as negative control, while a 1 mM ATP condition was included as a positive control to activate endogenous P2Y1 and P2Y2 purinoreceptors.

After incubation, bioluminescence corresponding to calcium influx in response to agonist exposure was measured using a FlexStation 3 Multi-Mode Microplate Reader. Data was exported as definite integrals and normalised by subtracting bioluminescence readings from RFP-transfected cells.

A.2.2 Measuring resting membrane potential

Resting membrane potential was recorded using whole-cell patch clamp in bridge mode with a caesium-based intracellular solution. The membrane potential was displayed in Axon MultiClamp Commander software and recorded manually.

A.3 Results and discussion

HEK293G5A cells were transfected with rGluN1-1a alongside either rGluN2A, h(r)GluN2A-L, or hGluN2A-S, and Ca²+-dependent bioluminescence was measured following exposure to 50 μ M glutamate in the presence of varying extracellular Mg²+ concentrations (1 μ M – 50 mM). The integral of bioluminescence was recorded for each condition and normalised by subtracting data from RFP-transfected cells to account for endogenous Ca²+ activity. Additionally, the data were normalised to the maximal bioluminescence signal for each receptor subunit condition. As shown in Figure A. 1A, the results were highly variable, and no clear dose-inhibition relationship was observed.

We hypothesised that the absence of a dose-inhibition relationship may be due to the resting membrane potential of transfected HEK cells, which would allow a significant proportion of NMDARs to remain unblocked by Mg^{2+} . To investigate this, we measured the resting membrane potential of untransfected HEK293 cells and those transfected with RFP or rGluN1-1a with either rGluN2A, h(r)GluN2A-L, or hGluN2A-S. Untransfected cells exhibited a resting membrane potential of -37.8 \pm 5.9 mV, consistent with a membrane potential of -40 mV suggested by Thomas and Smart (2005) (Thomas and Smart, 2005). However, transfected cells showed significant more depolarised resting membrane potentials: RFP (-8.1 \pm 1.1 mV, p < 0.0001), rGluN2A (-16.6 \pm 4.7 mV, p = 0.0007), hGluN2A-L-nly (-10.5 \pm 3.7 mV, p < 0.0001) and hGluN2A-S (-9.9 \pm 1.4 mV, p < 0.0001) (Figure A. 1B).

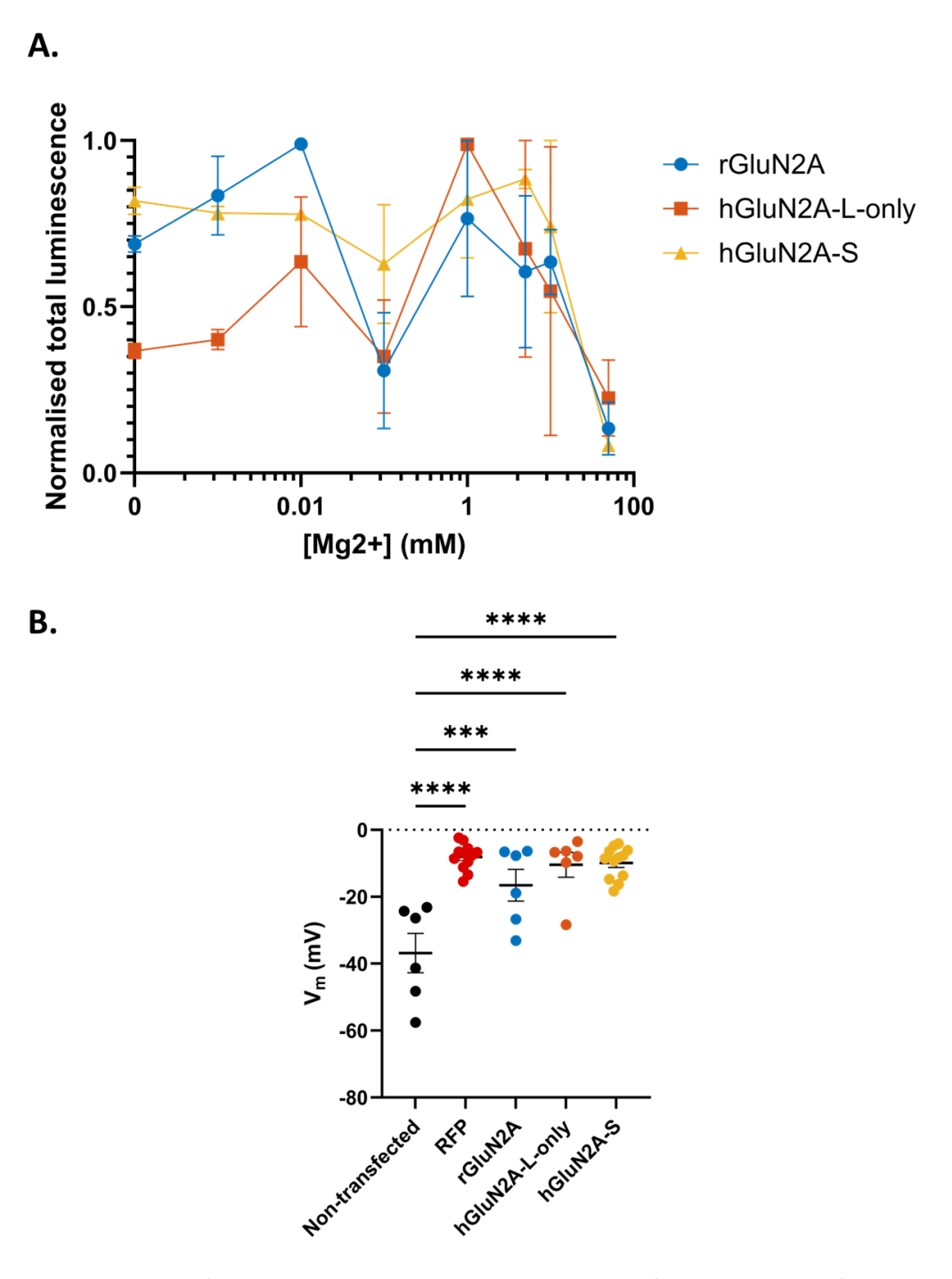


Figure A. 1 – Use of a bioluminescence-based calcium assay for the analysis of NMDA receptor magnesium pharmacology.

A) Dose-response curve of glutamate-induced (50 μ M) calcium responses to increasing concentrations of Mg²⁺ (1 μ M – 50mM). HEK293G5A cells were transfected with rGluN1-1a alongside rGluN2A, h(r)GluN2A-L or hGluN2A-S. Data points represent the area under the curve of bioluminescence readings from 2 independent wells per concentration, normalised to the maximum response. Each data point represents the mean± SEM. B) Resting membrane potential (V_m) obtained from either non-transfected HEK293T cells or cells transfected with RFP, rGluN1-1a/rGluN2A, rGluN1-1a/h(r)GluN2A-L or rGluN1-1a/hGluN2A-S. Comparisons made

using ordinary one-way ANOVA with Tukey's multiple comparisons test. Non-transfected (n = 6 cells) vs. RFP (n = 12 cells), P < 0.0001; rGluN2A (n = 6 cells), P = 0.0007; h(r)GluN2A-L (n = 6 cells), P < 0.0001; hGluN2A-S (n = 12 cells), P < 0.0001.

At these membrane potentials, Ca²⁺ influx through NMDARs is expected to be substantial and near maximal (Garaschuk et al., 1996), limiting our ability to detect Mg²⁺-dependent inhibition in an assay based on Ca²⁺ influx. To address this, we propose modifying the resting membrane potential of HEK293 cells to a more negative value, which may enable the detection of a dose-response relationship. One approach could involve co-expressing an inward-rectifying K⁺ channel such as Kv2.1, which may hyperpolarise the cells to a level where Mg²⁺-dependent blockade is more pronounced (Kubo et al., 1993). Alternatively, performing I-V relationship measurements using a slow voltage ramp stimulus across a broad range of external Mg²⁺ concentrations could provide more suitable information in further investigating the Mg²⁺-dependent inhibition of hGluN2A-S-containing NMDARs. While lower in throughput, this electrophysiological approach may offer a more detailed understanding of the relationship between Mg²⁺ availability and the voltage dependency of hGluN2A-S-containing receptors.

List of References

Addis, L. et al. (2017) 'Epilepsy-associated GRIN2A mutations reduce NMDA receptor trafficking and agonist potency-molecular profiling and functional rescue', *Scientific Reports*, 7(1).

Akashi, K. *et al.* (2009) 'NMDA receptor GluN2B (GluRε2/NR2B) subunit is crucial for channel function, postsynaptic macromolecular organization, and actin cytoskeleton at hippocampal CA3 synapses', *Journal of Neuroscience*, 29(35), pp. 10869–10882.

Akazawa, C. *et al.* (1994) 'Differential Expression of Five N-Methyl-D-Aspartate Receptor Subunit mRNAs in the Cerebellum of Developing and Adult Rats', *Journal of Comparative Neurology*, 347(1), pp. 150–160.

Barria, A. and Malinow, R. (2007) 'Subunit-Specific NMDA Receptor Trafficking to Synapses', *Protein Trafficking in Neurons*, 35, pp. 203–221.

Bar-Shira, O., Maor, R. and Chechik, G. (2015) 'Gene Expression Switching of Receptor Subunits in Human Brain Development', *PLOS Computational Biology*, 11(12), p. e1004559.

Bayer, K.U. *et al.* (2001) 'Interaction with the NMDA receptor locks CaMKII in an active conformation', *Nature*, 411(6839), pp. 801–805.

Berg, A.T. *et al.* (2010) 'Revised terminology and concepts for organization of seizures and epilepsies: Report of the ILAE Commission on Classification and Terminology, 2005-2009', *Epilepsia*, 51(4), pp. 676–685.

Beyer, A.L. and Osheim, Y.N. (1988) 'Splice site selection, rate of splicing, and alternative splicing on nascent transcripts.', *Genes & Development*, 2(6), pp. 754–765.

Bruno, V. et al. (2001) 'Metabotropic glutamate receptors as targets for neuroprotective drugs', Journal of Cerebral Blood Flow & Metabolism., 21(9), pp. 1013–1033.

Bugaj, V. *et al.* (2005) 'Functional properties of endogenous receptor- and store-operated calcium influx channels in HEK293 cells', *The Journal of biological chemistry*, 280(17), pp. 16790–16797.

Burnashev, N. *et al.* (1992) 'Control by asparagine residues of calcium permeability and magnesium blockade in the NMDA receptor', *Science*, 257(5075), pp. 1415–1419.

Carvill, G.L. *et al.* (2013) 'GRIN2A mutations cause epilepsy-aphasia spectrum disorders', *Nature Genetics*, 45(9), pp. 1073–1076.

List of References

Chazot, P.L., Cik, M. and Stephenson, F.A. (1995) 'An investigation into the role of n-glycosylation in the functional expression of a recombinant heteromeric NMDA receptor', *Molecular Membrane Biology*, 12(4), pp. 331–337.

Chen, L. *et al.* (2000) 'Stargazin regulates synaptic targeting of AMPA receptors by two distinct mechanisms', *Nature*, 408(6815), pp. 936–943.

Clarke, R.J., Glasgow, N.G. and Johnson, J.W. (2013) 'Mechanistic and Structural Determinants of NMDA Receptor Voltage-Dependent Gating and Slow Mg2+ Unblock', *The Journal of Neuroscience*, 33(9), p. 4140.

Clarke, R.J. and Johnson, J.W. (2006) 'NMDA Receptor NR2 Subunit Dependence of the Slow Component of Magnesium Unblock', *Journal of Neuroscience*, 26(21), pp. 5825–5834.

Collingridge, G.L. (2024) 'Long-term potentiation in the hippocampus: From magnesium to memory', *Neuroscience* [Preprint].

Consortium, T.U. (2023) 'UniProt: the Universal Protein Knowledgebase in 2023 - Google Scholar', 51(November 2022), pp. 523–531.

Cousins, S.L., Kenny, A. V. and Stephenson, F.A. (2009) 'Delineation of additional PSD-95 binding domains within NMDA receptor NR2 subunits reveals differences between NR2A/PSD-95 and NR2B/PSD-95 association', *Neuroscience*, 158(1), pp. 89–95.

Cousins, S.L. and Stephenson, F.A. (2012) 'Identification of N-Methyl-D-aspartic acid (NMDA) receptor subtype-specific binding sites that mediate direct interactions with scaffold protein PSD-95', *Journal of Biological Chemistry*, 287(16), pp. 13465–13476.

Cull-Candy, S.G. and Leszkiewicz, D.N. (2004) 'Role of distinct NMDA receptor subtypes at central synapses.', *Science's STKE*: signal transduction knowledge environment, 2004(255), pp. 1–10.

Dingledine, R. *et al.* (1999) 'The glutamate receptor ion channels', *Pharmacological Reviews*, 51(1), pp. 7–61.

Ehlers, M.D., Tingley, W.G. and Huganir, R.L. (1995) 'Regulated subcellular distribution of the NR1 subunit of the NMDA receptor', *Science*, 269(5231), pp. 1734–1737.

Elmasri, M. *et al.* (2020) 'Common synaptic phenotypes arising from diverse mutations in the human NMDA receptor subunit GluN2A', *bioRxiv*.

Elmasri, M. *et al.* (2022) 'Common synaptic phenotypes arising from diverse mutations in the human NMDA receptor subunit GluN2A', *Communications Biology*, 5(1), pp. 1–17.

Everts, I., Villmann, C. and Hollmann, M. (1997) 'N-glycosylation is not a prerequisite for glutamate receptor function but is essential for lectin modulation', *Molecular Pharmacology*, 52(5), pp. 861–873.

Fang, H. et al. (2021) 'An optimized CRISPR/Cas9 approach for precise genome editing in neurons', pp. 1–25.

Forrest, D. et al. (1994) 'Targeted disruption of NMDA receptor 1 gene abolishes NMDA response and results in neonatal death', *Neuron*, 13(2), pp. 325–338.

Francis, P.T. (2003) 'Glutamatergic systems in Alzheimer's disease', *International Journal of Geriatric Psychiatry*, 18(SUPPL. 1).

Frankish, A. *et al.* (2023) 'GENCODE: reference annotation for the human and mouse genomes in 2023', *Nucleic Acids Research*, 51(D1), pp. D942–D949.

Furukawa, H. *et al.* (2005) 'Subunit arrangement and function in NMDA receptors', *Nature*, 438(7065), pp. 185–192.

Garaschuk, O. *et al.* (1996) 'Fractional Ca2+ currents through somatic and dendritic glutamate receptor channels of rat hippocampal CAI pyramidal neurones', *Journal of Physiology*, 71(6), pp. 757-772.

Gray, J.A. *et al.* (2011) 'Distinct Modes of AMPA Receptor Suppression at Developing Synapses by GluN2A and GluN2B: Single-Cell NMDA Receptor Subunit Deletion In Vivo', *Neuron*, 71(6), pp. 1085–1101.

Hall, R.A. and Soderling, T.R. (1997) 'Differential surface expression and phosphorylation of the N-methyl-D- aspartate receptor subunits NR1 and NR2 in cultured hippocampal neurons', *Journal of Biological Chemistry*, 272(7), pp. 4135–4140.

Hamada, S. et al. (2014) 'The glutamate receptor GluN2 subunit regulates synaptic trafficking of AMPA receptors in the neonatal mouse brain', *European Journal of Neuroscience*, 40(8), pp. 3136–3146.

Hannah, W. (2018) *Electrophysiological investigation of a primate-specific putative isoform of the NMDA receptor GluN2A subunit.* University of Southampton.

Hansen, K.B. *et al.* (2014) 'Distinct functional and pharmacological properties of triheteromeric GluN1/GluN2A/GluN2B NMDA receptors', *Neuron*, 81(5), pp. 1084–1096.

List of References

Hawkins, L.M. *et al.* (2004) 'Export from the endoplasmic reticulum of assembled N-methyl-D-aspartic acid receptors is controlled by a motif in the C terminus of the NR2 subunit', *Journal of Biological Chemistry*, 279(28), pp. 28903–28910.

Hedegaard, M. et al. (2012) 'Molecular pharmacology of human NMDA receptors', Neurochemistry International, 61(4), pp. 601–609.

Herbrechter, R. *et al.* (2021) 'Splicing and editing of ionotropic glutamate receptors: a comprehensive analysis based on human RNA-Seq data', *Cellular and Molecular Life Sciences*, 78(14), pp. 5605–5630.

Herring, B.E. and Nicoll, R.A. (2016) 'Long-Term Potentiation: From CaMKII to AMPA Receptor Trafficking', *Annual Review of Physiology*, 78, pp. 351–365.

Horak, M. and Wenthold, R.J. (2009) 'Different roles of C-terminal cassettes in the trafficking of full-length NR1 subunits to the cell surface', *Journal of Biological Chemistry*, 284(15), pp. 9683–9691.

Houghton, S. (2019) *Investigating the functional properties of a novel NMDAR subunit* (GluN2A_iso2) in Human Embryonic Kidney cells. University of Southampton.

Jurica, M.S. and Moore, M.J. (2003) 'Pre-mRNA splicing: Awash in a sea of proteins', *Molecular Cell*, 12(1), pp. 5–14.

Kaniakova, M. *et al.* (2016) 'Biochemical and electrophysiological characterization of N-glycans on NMDA receptor subunits', *Journal of Neurochemistry*, pp. 546–556.

Karakas, E. and Furukawa, H. (2014) 'Crystal structure of a heterotetrameric NMDA receptor ion channel', *Science*, 344(6187), pp. 992–997.

Karakas, E., Simorowski, N. and Furukawa, H. (2009) 'Structure of the zinc-bound amino-terminal domain of the NMDA receptor NR2B subunit', *EMBO Journal*, 28(24), pp. 3910–3920.

Katoh, K. and Standley, D.M. (2013) 'MAFFT multiple sequence alignment software version 7: Improvements in performance and usability', *Molecular Biology and Evolution*, 30(4), pp. 772–780.

Kew, J.N.C. *et al.* (1998) 'Developmental Changes in NMDA Receptor Glycine Affinity and Ifenprodil Sensitivity Reveal Three Distinct Populations of NMDA Receptors in Individual Rat Cortical Neurons', *Journal of Neuroscience*, 18(6), pp. 1935–1943.

Kubo, Y. *et al.* (1993) 'Primary structure and functional expression of a mouse inward rectifier potassium channel', *Nature* 1993 362:6416, 362(6416), pp. 127–133.

Kumar, S. and Kumar, S.S. (2021) 'A Model for Predicting Cation Selectivity and Permeability in AMPA and NMDA Receptors Based on Receptor Subunit Composition', *Frontiers in Synaptic Neuroscience*, 13, pp. 1–14.

Laube, B., Schemm, R. and Betz, H. (2004) 'Molecular determinants of ligand discrimination in the glutamate-binding pocket of the NMDA receptor', *Neuropharmacology*, 47(7), pp. 994–1007.

Lee, C.H. et al. (2014) 'NMDA receptor structures reveal subunit arrangement and pore architecture', *Nature*, 511(7508), pp. 191–197.

Lemke, J.R. et al. (2013a) 'Mutations in GRIN2A cause idiopathic focal epilepsy with rolandic spikes', *Nature Genetics*, 45(9), pp. 1067–1072.

Lemke, J.R. *et al.* (2013b) 'Mutations in GRIN2A cause idiopathic focal epilepsy with rolandic spikes', *Nature Genetics 2013 45:9*, 45(9), pp. 1067–1072.

Lesca, G. *et al.* (2012) 'Epileptic encephalopathies of the Landau-Kleffner and continuous spike and waves during slow-wave sleep types: Genomic dissection makes the link with autism', *Epilepsia*, 53(9), pp. 1526–1538.

Lesca, G. *et al.* (2013a) 'GRIN2A mutations in acquired epileptic aphasia and related childhood focal epilepsies and encephalopathies with speech and language dysfunction', *Nature Genetics 2013 45:9*, 45(9), pp. 1061–1066.

Lesca, G. *et al.* (2013b) 'GRIN2A mutations in acquired epileptic aphasia and related childhood focal epilepsies and encephalopathies with speech and language dysfunction', *Nature Genetics*, 45(9), pp. 1061–1066.

Lesca, G. et al. (2019) 'Update on the genetics of the epilepsy-aphasia spectrum and role of GRIN2A mutations', Epileptic Disorders, 21(S1), pp. S41–S47.

Li, J.H. *et al.* (1998) 'Developmental changes in localization of NMDA receptor subunits in primary cultures of cortical neurons', *European Journal of Neuroscience*, 10(5), pp. 1704–1715.

Lichnerova, K. *et al.* (2015) 'Two N-glycosylation sites in the GluN1 subunit are essential for releasing N-methyl-D-aspartate (NMDA) receptors from the endoplasmic reticulum', *Journal of Biological Chemistry*, 290(30), pp. 18379–18390.

List of References

Lin, C.Y. et al. (2015) 'Enhancing Protein Expression in HEK-293 Cells by Lowering Culture Temperature', *PLoS ONE*, 10(4), p. e0123562.

Lisman, J., Yasuda, R. and Raghavachari, S. (2012) 'Mechanisms of CaMKII action in long-term potentiation', *Nature Reviews Neuroscience*, 13(3), pp. 169–182.

Lü, W. *et al.* (2017) 'Cryo-EM structures of the triheteromeric NMDA receptor and its allosteric modulation', *Science*, 355(6331).

Lussier, M.P., Sanz-Clemente, A. and Roche, K.W. (2015) 'Dynamic regulation of N-methyl-D-aspartate (NMDA) and α -amino-3-hydroxy-5-methyl-4-isoxazolepropionic acid (AMPA) receptors by posttranslational modifications', *Journal of Biological Chemistry*, 290(48), pp. 28596–28603.

Mayer, M.L., Westbrook, G.L. and Guthrie, P.B. (1984) 'Voltage-dependent block by Mg2+ of NMDA responses in spinal cord neurones', *Nature*, 309(5965), pp. 261–263.

McIlhinney, R.A.J. *et al.* (1998) 'Assembly intracellular targeting and cell surface expression of the human N-methyl-D-aspartate receptor subunits NR1a and NR2A in transfected cells', *Neuropharmacology*, 37(10–11), pp. 1355–1367.

Meddows, E. *et al.* (2001) 'Identification of Molecular Determinants That Are Important in the Assembly of N-Methyl-D-aspartate Receptors', *Journal of Biological Chemistry*, 276(22), pp. 18795–18803.

Meldrum, B.S., Akbar, M.T. and Chapman, A.G. (1999) 'Glutamate receptors and transporters in genetic and acquired models of epilepsy', *Epilepsy Research*, 36(2–3), pp. 189–204.

Myers, K.A., Johnstone, D.L. and Dyment, D.A. (2019a) 'Epilepsy genetics: Current knowledge, applications, and future directions', *Clinical Genetics*, 95(1), pp. 95–111.

Myers, K.A., Johnstone, D.L. and Dyment, D.A. (2019b) 'Epilepsy genetics: Current knowledge, applications, and future directions', *Clinical Genetics*, 95(1), pp. 95–111.

Nahum-Levy, R. *et al.* (2001) 'Desensitization of NMDA receptor channels is modulated by glutamate agonists', *Biophysical Journal*, 80(5), pp. 2152–2166.

Nicoll, R.A. (2017) 'A Brief History of Long-Term Potentiation', Neuron, 93(2), pp. 281–290.

Nilsen, T.W. (2003) 'The spliceosome: The most complex macromolecular machine in the cell?', *BioEssays*, pp. 1147–1149.

Okabe, S., Miwa, A. and Okado, H. (1999) 'Alternative splicing of the C-terminal domain regulates cell surface, expression of the NMDA receptor NR1', *Journal of Neuroscience*, 19(18), pp. 7781–7792.

Pan, Q. *et al.* (2008) 'Deep surveying of alternative splicing complexity in the human transcriptome by high-throughput sequencing', *Nature genetics*, 40(12), pp. 1413–1415.

Paoletti, P. (2011) 'Molecular basis of NMDA receptor functional diversity', *European Journal of Neuroscience*, 33(8), pp. 1351–1365.

Paoletti, P., Ascher, P. and Neyton, J. (1997) 'High-affinity zinc inhibition of NMDA NR1-NR2A receptors', *Journal of Neuroscience*, 17(15), pp. 5711–5725.

Paoletti, P. and Neyton, J. (2007) 'NMDA receptor subunits: function and pharmacology', *Current Opinion in Pharmacology*, 7(1), pp. 39–47.

Pegasiou, C.-M. (2018) 'Glutamate receptor composition in ageing human brain and in mouse models of synaptic degeneration'. University of Southampton, School of Biological Sciences, PhD Thesis.

Phillips, B.P., Gomez-Navarro, N. and Miller, E.A. (2020) 'Protein quality control in the endoplasmic reticulum', *Current Opinion in Cell Biology*, 65, pp. 96–102.

Puddifoot, C.A. *et al.* (2009) 'Pharmacological characterization of recombinant NR1/NR2A NMDA receptors with truncated and deleted carboxy termini expressed in Xenopus laevis oocytes', *British Journal of Pharmacology*, 156(3), pp. 509–518.

Qian, A., Buller, A.L. and Johnson, J.W. (2005) 'NR2 subunit-dependence of NMDA receptor channel block by external Mg2+', *The Journal of Physiology*, 562(2), pp. 319–331.

Rauner, C. and Köhr, G. (2011) 'Triheteromeric NR1/NR2A/NR2B receptors constitute the major N-methyl-D-aspartate receptor population in adult hippocampal synapses', *Journal of Biological Chemistry*, 286(9), pp. 7558–7566.

Retchless, B.S., Gao, W. and Johnson, J.W. (2012) 'A single GluN2 subunit residue controls NMDA receptor channel properties via intersubunit interaction', *Nature Neuroscience 2012 15:3*, 15(3), pp. 406–413.

Rumbaugh, G. *et al.* (2000) 'Exon 5 and spermine regulate deactivation of NMDA receptor subtypes', *Journal of Neurophysiology*, 83(3), pp. 1300–1306.

List of References

Rumbaugh, G. and Vicini, S. (1999) 'Distinct synaptic and extrasynaptic NMDA receptors in developing cerebellar granule neurons', *Journal of Neuroscience*, 19(24), pp. 10603–10610.

Schachter, J.: B. et al. (1997) HEK293 Human Embryonic Kidney Cells Endogenously Express the P2Y1 and P2Y2 Receptors, Two.

Serraz, B., Grand, T. and Paoletti, P. (2016) 'Altered zinc sensitivity of NMDA receptors harboring clinically-relevant mutations', *Neuropharmacology*, 109, pp. 196–204.

Sheng, M. et al. (1994) 'Changing subunit composition of heteromeric NMDA receptors during development of rat cortex', *Nature*, 368(6467), pp. 144–147.

Simpkins, K.L. *et al.* (2003) 'Selective activation induced cleavage of the NR2B subunit by calpain', *The Journal of neuroscience : the official journal of the Society for Neuroscience*, 23(36), pp. 11322–11331.

Sobolevsky, A.I. and Yelshansky, M. V. (2000) 'The trapping block of NMDA receptor channels in acutely isolated rat hippocampal neurones', *The Journal of Physiology*, 526(Pt 3), p. 493.

Standley, S. *et al.* (2000) 'PDZ domain suppression of an ER retention signal in NMDA receptor NR1 splice variants', *Neuron*, 28(3), pp. 887–898.

Strausberg, R.L. *et al.* (2002) 'Generation and initial analysis of more than 15,000 full-length human and mouse cDNA sequences', *Proceedings of the National Academy of Sciences of the United States of America*, 99(26), p. 16899.

Strehlow, V. et al. (2016) GRIN2A-Related Disorders.

Strehlow, V. *et al.* (2019) 'GRIN2A-related disorders: genotype and functional consequence predict phenotype', *Brain*, 142(1), pp. 80–92.

Stroebel, D. *et al.* (2014) 'Controlling NMDA receptor subunit composition using ectopic retention signals', *Journal of Neuroscience*, 34(50), pp. 16630–16636.

Sun, Y. et al. (2002) 'Mechanism of glutamate receptor desensitization', *Nature*, 417(6886), pp. 245–253.

Thiel, D. *et al.* (2023) 'Large-scale deorphanization of Nematostella vectensis neuropeptide G protein-coupled receptors supports the independent expansion of bilaterian and cnidarian peptidergic systems', 12, p. 90674.

Thomas, P. and Smart, T.G. (2005) 'HEK293 cell line: A vehicle for the expression of recombinant proteins', *Journal of Pharmacological and Toxicological Methods*, 51(3 SPEC. ISS.), pp. 187–200.

Tovar, K.R. and Westbrook, G.L. (1999) 'The incorporation of NMDA receptors with a distinct subunit composition at nascent hippocampal synapses in vitro', *Journal of Neuroscience*, 19(10), pp. 4180–4188.

Traynelis, S.F. *et al.* (2010) 'Glutamate receptor ion channels: Structure, regulation, and function', *Pharmacological Reviews*, 62(3), pp. 405–496.

Vance, K.M., Hansen, K.B. and Traynelis, S.F. (2012) 'GluN1 splice variant control of GluN1/GluN2D NMDA receptors', *Journal of Physiology*, 590(16), pp. 3857–3875.

Vargas-Caballero, M. and Robinson, H.P.C. (2003) 'A slow fraction of Mg2+ unblock of NMDA receptors limits their contribution to spike generation in cortical pyramidal neurons', *Journal of Neurophysiology*, 89(5), pp. 2778–2783.

Vicini, S. *et al.* (1998) 'Functional and pharmacological differences between recombinant N-methyl-D-aspartate receptors', *Journal of Neurophysiology*, 79(2), pp. 555–566.

Vyas, Y. and Montgomery, J.M. (2016) 'The role of postsynaptic density proteins in neural degeneration and regeneration', *Neural Regeneration Research*, 11(6), pp. 906–907.

Wang, Z. and Burge, C.B. (2008) 'Splicing regulation: From a parts list of regulatory elements to an integrated splicing code', *RNA*, pp. 802–813.

Warming, H. et al. (2019) 'A primate-specific short GluN2A-NMDA receptor isoform is expressed in the human brain', *Molecular Brain*, 12(1), pp. 1–8.

Watanabe, M. *et al.* (1992) 'Developmental changes in distribution of NMDA receptor channel subunit mRNAs', *Neuroreport*, 3(12), pp. 1138–1140.

Wetterberg, I. *et al.* (2001) 'In situ transcription and splicing in the Balbiani ring 3 gene', *The EMBO Journal*, 20(10), pp. 2564–2574.

WHO (2024) World Health Organisation.

Williams, K. *et al.* (1998) 'The selectivity filter of the N-methyl-D-aspartate receptor: A tryptophan residue controls block and permeation of Mg2+', *Molecular Pharmacology*, 53(5), pp. 933–941.

List of References

Wollmuth, L.P., Kuner, T. and Sakmann, B. (1998) 'Adjacent asparagines in the NR2-subunit of the NMDA receptor channel control the voltage-dependent block by extracellular Mg2+', *Journal of Physiology*, 506(1), pp. 13–32.

Wollmuth, L.P. and Sobolevsky, A.I. (2004) 'Structure and gating of the glutamate receptor ion channel', *Trends in Neurosciences*, 27(6), pp. 321–328.

Woodhull, A.M. (1973) *Ionic Blockage of Sodium Channels in Nerve, THE JOURNAL OF GENERAL PHYSIOLOGY*.

Yang, Xiaoping et al. (2011) 'A public genome-scale lentiviral expression library of human ORFs', *Nature methods*, 8(8), p. 659.

Yuan, H. *et al.* (2014) 'Functional analysis of a de novo GRIN2A missense mutation associated with early-onset epileptic encephalopathy', *Nature Communications*, 5(1), pp. 1–12.

Zhou, Y. and Danbolt, N.C. (2014) 'Glutamate as a neurotransmitter in the healthy brain', *Journal of Neural Transmission*, 121(8), pp. 799–817.

Zhou, Z. et al. (2002) 'Comprehensive proteomic analysis of the human spliceosome', *Nature 2002* 419:6903, 419(6903), pp. 182–185.

Zito, K. and Scheuss, V. (2009) 'NMDA Receptor Function and Physiological Modulation', *Encyclopedia of Neuroscience*, pp. 1157–1164.